DTU Mechanical Engineering
Department of Mechanical Engineering

State-of-the-art laser Doppler systems development for turbulence measurements

Mohd Rusdy Bin Yaacob

PhD Thesis

Contents

List of papers

I. * Mohd Rusdy Yaacob, Rasmus Korslund Schlander, Preben Buchhave and Clara Marika Velte. (2018) Experimental Evaluation of Kolmogorov's -5/3 and 2/3 Power Laws in the Developing Turbulent Round Jet. *Journal of Advanced Research in Fluid Mechanics and Thermal Sciences 45*(1), 14-21.

II. Mohd Rusdy Yaacob, Rasmus Korslund Schlander, Preben Buchhave and Clara Marika Velte. (2018) Mapping of the Turbulent Round Jet Developing Region Using a Constant Temperature Anemometer (CTA). *Malaysian Journal of Fundamental and Applied Sciences: Special Issue on Natural Sciences and Mathematics (ESCon 2018)*, 443-446

III. ** Mohd Rusdy Yaacob, Rasmus Korslund Schlander, Preben Buchhave and Clara Marika Velte. Validation of improved laser Doppler anemometer (LDA) based on the fully developed turbulent round jet (two-page abstract). *Symposium Proceeding on Electrical, Mechatronics and Applied Science 2018, 89-90. e-ISBN: 978-967-2145-58-5*

IV. Mohd Rusdy Yaacob, Rasmus Korslund Schlander, Preben Buchhave and Clara Marika Velte. (*manuscript*) A novel laser Doppler anemometer (LDA) for high-accuracy turbulence measurements.

V. ***Mohd Rusdy Yaacob, Preben Buchhave and Clara Marika Velte. Statistical description of the round turbulent jet developing region along its centerline. *(under review*) *Journal of Advanced Research in Fluid Mechanics and Thermal Sciences.*

VI. Mohd Rusdy Yaacob, Preben Buchhave and Clara Marika Velte. (*manuscript*) Mapping of the Energy Cascade in the Developing Region of a Turbulent Round Jet.

* Best Oral Presenter (Physics track) when being presented in the Emerging Scientists Conference 2018.

** The Best Paper Award when being presented in the Symposium of Electrical, Mechatronics and Applied Science 2018.

*** Best Poster Award when being presented in the 6th Mechanical Engineering Research Day 2019 from a two-pages abstract: "Turbulence measurements in the centerline region of a turbulent round jet using a software-driven laser Doppler system"

Author contributions

I. C.M.V. and M.R.Y. contributed to the planning of the investigation. M.R.Y and P.B. carried out the experiments. M.R.Y. processed and analyzed the data and drafted the manuscript. R.K.S, P.B. and C.M.V. contributed critical revision of the manuscript. All authors granted final approval for publication. M.R.Y presented the work in the 1st International Symposium on Fluid Mechanics and Thermal Sciences 2018.

II. C.M.V. and M.R.Y contributed to the planning of the investigation. M.R.Y carried out the experiments, analyzed the data and drafted the manuscript. R.K.S., P.B. and C.M.V contributed critical revision of the manuscript. All authors granted final approval for publication. M.R.Y presented the work in Emerging Scientists Conference 2018.

III. C.M.V. and P.B. contributed to the planning of the investigation. M.R.Y., P.B. and C.M.V. developed the experimental setup. M.R.Y and P.B. carried out the experiments. M.R.Y. processed and analyzed the data. M.R.Y. and R.K.S. drafted the manuscript. P.B. and C.M.V. contributed critical revision of the manuscript. All authors granted final approval for publication. R.K.S. presented the work in the Symposium of Electrical, Mechatronics and Applied Science 2018.

IV. C.M.V. and P.B. contributed to the planning of the investigation. M.R.Y and P.B. carried out the measurements. M.R.Y. processed and analyzed the data. M.R.Y. drafted the whole manuscript. R.K.S drafted the signal processing part. P.B. and C.M.V. contributed critical revision of the manuscript. All authors granted final approval for publication.

V. C.M.V. contributed to the planning of the investigation. M.R.Y carried out the measurements, processed and analyzed the data. M.R.Y. drafted the manuscript. P.B. and C.M.V. contributed critical revision of the manuscript. All authors granted final approval for publication. M.R.Y presented the two-pages abstract in the 6th Mechanical Engineering Research Day 2019.

VI. C.M.V. contributed to the planning of the investigation. M.R.Y carried out the measurements, processed and analyzed the data. M.R.Y. drafted the manuscript. P.B. and C.M.V. contributed critical revision of the manuscript. All authors granted final approval for publication.

Abstract

This thesis, as stated in the title, emphasizes on the development of a novel, software-driven laser Doppler anemometer (LDA) system followed by the experimental investigation on the turbulence in a round jet. The former has been driven by the practical limitations suffered by the commercial LDA system, which affect the accuracy of the difficult turbulence measurement. The latter has been inspired by the unsolved and underexplored developing turbulence, which is more difficult to measure than the fully developed counterpart. The challenge is to measure high intensity and high shear turbulence. This will be further elaborated in Chapter 1. The novel LDA system comprising the state-of-the-art, off-the-shelf hardware and a novel software for signal and data processing, which will be described in detail in Chapter 2. This chapter will also demonstrate the procedures for measurements and data analysis using the software, while highlighting some challenges that arose before obtaining the desired outcomes, which are later presented in Chapter 3. Some of the outcomes have already been published in two indexed journals and a conference proceeding, while the rest have been properly documented in three completed manuscripts. The ultimate aim of this thesis is to enhance the understanding of the underlying physics of turbulence and investigate whether the existing turbulence models need be corrected. This thesis is also intended to provide comprehensive information and thorough guidance for anyone who is going to operate the herein described LDA system independently in the future.

Resumé

Som det fremgår af titlen, omhandler denne afhandling udviklingen af et nyt, software baseret laser Doppler anemometer (LDA) efterfulgt af en eksperimentel undersøgelse af turbulensen i en rund jet. Det første formål er drevet af de praktiske begrænsninger, som kommercielle LDA-systemer lider under, og som begrænser nøjagtigheden af den vanskelige måling i turbulente strømninger. Det andet formål er inspireret af det uløste og lidet undersøgte problem, som omhandler turbulens under udvikling, som udgør et langt sværere måleproblem end fuldt udviklet turbulens. Udfordringen er at måle turbulens med høj turbulensintensitet og høj forskydningsspænding. Dette vil blive yderligere uddybet i Kapitel 1. Det nye LDA-system består af state-of-the-art, kommercielle hardware komponenter og et nyt program til signal- og databehandling, hvilket vil blive beskrevet i Kapitel 2. Dette kapitel vil også beskrive proceduren for måling og dataanalyse ved benyttelse af softwaren samtidigt med at det understreger nogle af de udfordringer, der opstod før de ønskede resultater blev opnået. Dette er beskrevet i Kapitel 3. Nogle af resultaterne er allerede blevet publiceret i to indekserede tidsskrifter og i en konference beretning, medens resten er dokumenteret i tre færdige manuskripter. Det ultimative formål med denne afhandling er at uddybe forståelsen af den underliggende fysik for turbulens og at undersøge om det er nødvendigt at korrigere de eksisterende turbulensmodeller. Afhandlingen er også beregnet på at levere en fyldestgørende information og en grundig vejledning til enhver, som planlægger at betjene det her beskrevne LDA-system på egen hånd i fremtiden.

1 Introduction

1.1 Research gap, Motivation and Objective

Although there have been a vast amount of studies over the century that provide so many different ways in defining turbulence, it still remains an undefined and unsolved problem of classical physics (Davidson 2004; L'vov and Procaccia 2007). Despite of that, turbulence is still and becoming more relevant in many important applications such as combustion engines, weather forecast, aerodynamics and oceanography. It also occurs in common natural phenomena such as river flows, natural convection and atmosphere streams.

Substantial debates and challenges have in recent years arisen among the experts on the foundation for understanding the turbulence, which is known as the K41 theory. Serious questionings on this theory has become the ultimate research gap to help fill in our study, with its association to the developing region of a turbulent round jet where high shear and intensity are very likely to occur as demonstrated in Paper II.

Technical difficulties to accurately measure the turbulence in this challenging yet interesting region has become our strong motivation to develop a novel and robust measurement system employing the laser Doppler technique. The final goal of this study is to unveil new findings from a series of accurate turbulence measurements that will be favorable for further improvement and understanding of the theory of non-equilibrium turbulence, which is an increasingly important branch of turbulence research. Moreover, since the vast majority of existing turbulent flow simulations have been based on the K41 theory (in one way or another), the new findings can be notably useful for turbulence modelers to improve their computational models also for non-equilibrium turbulence.

1.2 K41 Theory

The underlying assumptions of the classical K41 theory have been merely based on the equilibrium and universality of the intermediate and small turbulent scales, which for sufficiently high Reynolds number, should own the same statistical properties (Batchelor 1953; Kolmogorov 1941c, 1962). This so-called local equilibrium has been experimentally proven to occur in the fully developed region of a stationary round jet (Gibson 1962; Panchapakesan N. R. and Lumley 1993), leaving some ambiguity during which turbulence is still developing, especially on the cascade of turbulent kinetic energy from large to small scales.

A relevant question may then arise whether the so-called local interactions as postulated from the Richardson's energy cascade (see Figure 1-1) is also valid in the developing region of the jet (Richardson 1922). These concerns have been clearly addressed in Paper VI, listing key evidences from (Anselmet, Antonia, and Danaila 2001; Frisch, Sulem, and Nelkin 1978; Tsinober 2009) that would lead to the contradiction and misconception of the K41 theory, including one from Kolmogorov himself (Kolmogorov 1962).

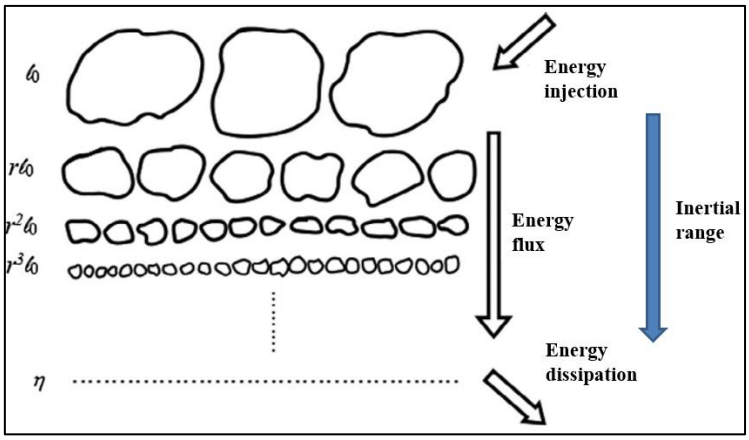

Figure 1-1 Sketch of Richardson cascade process across the inertial range (Liu, Yan, and Lu 2014). This cascade is assumed to be local since an eddy of size $r^n\ell_0$ receives energy only from its neighboring eddy of size $r^{n-1}\ell_0$.

The cornerstone of this theory comprises three different power laws viz. the -5/3 law for turbulence kinetic energy spectra, the 2/3 law for the spatial second-order structure functions and the 4/5 law for the spatial third-order structure functions (McDonough 2007). The empirical definition of the first two have been shown in Paper I and Paper VI, followed by the measurements across the jet (in radial direction) within the developing region, where turbulent is not necessarily in equilibrium. These experimental studies will therefore disclose whether or not, the non-equilibrium turbulence follow the classical turbulence theories, as initially shown in Figure 1-2. Meanwhile, Paper V has elaborated the 4/5 law, which is only valid for local homogeneity, isotropy and equilibrium (Frisch 1995). The non-equilibrium turbulence is therefore not relevant, or at least, of the least interest in this case. This experimental study however, has allowed us to determine the mean energy dissipation rate per unit mass, ε, which is the most important parameter in turbulent field (Stewart 1959), from the third-order structure functions plotted for measurements along the jet centerline throughout the fully developed region. Similar measurements throughout the developing counterpart will still unveil the range where the 2/3 and -5/3 power laws are valid or vice versa, as valuable additions to the study made in Paper I and VI.

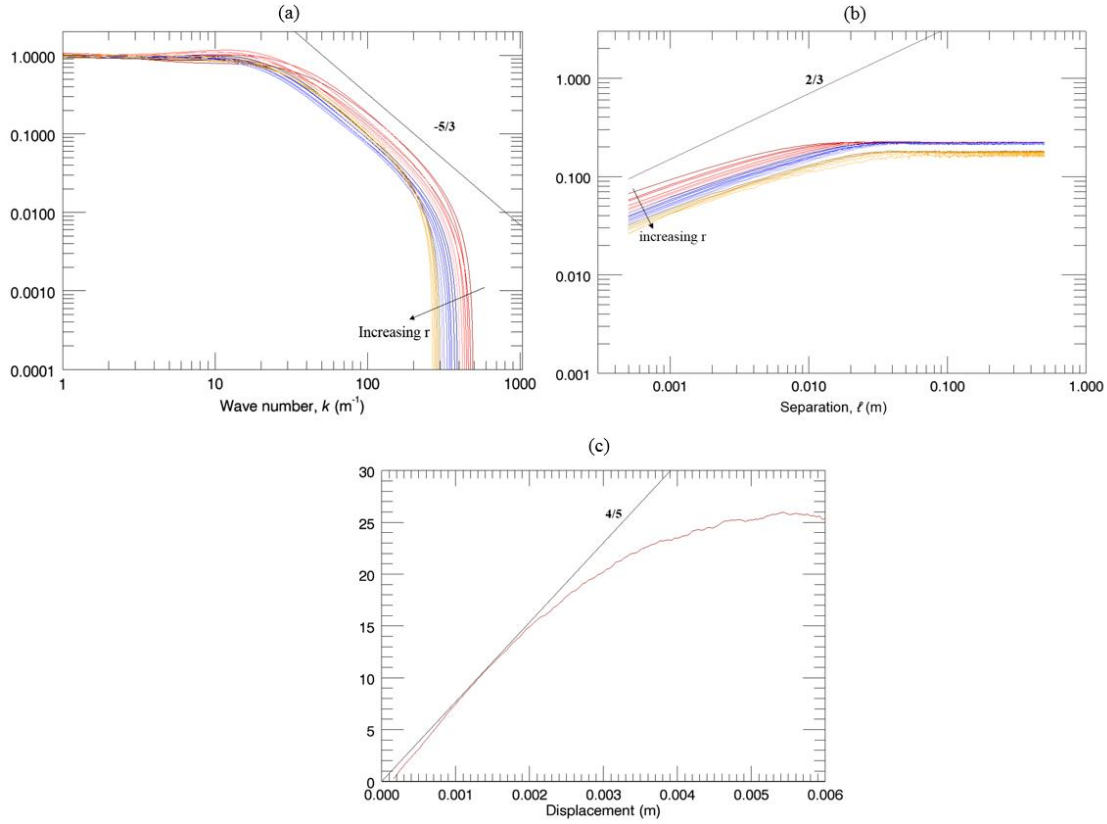

Figure 1-2 Some of the experimental results retrieved from Paper VI at 10 jet diameters downstream (a) Normalized spatial kinetic energy spectra (convection record) variations with radial distance. (b) Second order spatial structure functions variations with radial distance. (c) Spatial third order structure function at the jet centerline. Full results are disclosed in the same paper and to be discussed further in the Results & Discussions chapter.

1.3 Stationary Turbulent Round Jet

A stationary turbulent round jet (see Figure 1-3) has been chosen as the test bed for validation of turbulence measurements in this study, based on many practical reasons elaborated in all the papers attached. Firstly, the jet itself is a classical turbulent flow that exhibits an extensive range of dynamical variations (Capp 1983a) and therefore opens up a high interest for fundamental investigations (Hinze 1975), as mentioned in Paper V and II, respectively. Meanwhile in Paper I, III and IV, some previous experimental investigations have been listed, which results have demonstrated good agreement with the K41 theory (Gibson 1962; Panchapakesan N. R. and Lumley 1993). In fact, the turbulent round jet was the very first flow to display the nearly -5/3 slope on the kinetic energy spectrum (nearly equilibrium), at least in the fully developed region (Gibson 1962). Since then, the turbulent round jet has become a popular subject in turbulence research for many years, offering a wide variation in terms of the shear and turbulence intensities across its downstream and radial directions. With the fully developed turbulence to have been extensively studied (Hussein, Capp, and George 1994), investigation on the developing counterpart will be of the great interest.

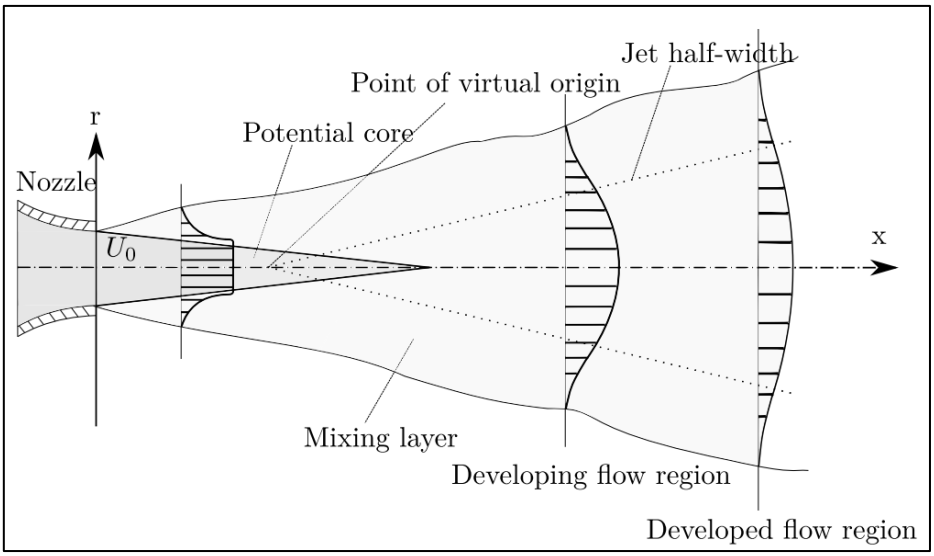

Figure 1-3 Sketch of turbulent round jet indicating the developing and fully developed regions (Hodzic 2014). The coordinate system is similar to the one used in our measurements.

Paper VI has also clearly stated our motivation in extending an investigation on the turbulent round jet. It is basically driven by the previous investigations on the dissipation anomaly during the streamwise development of turbulence (Seoud and Vassilicos 2007) and spectral discrepancy on the -5/3 law of a decaying grid turbulence flow (Danaila, Anselmet, and Antonia 2002). Moreover, the turbulent round jet, as a type of a free shear flow, can be easily accessed in an optical way, which perfectly suits for measurements using the laser Doppler technique. The interference on the largest scales may also be reduced with the absence of lateral boundaries on the flow (Burattini and Danaila 2005). The round jet is also one of few flow for which measurements of the dissipation, ε are possible (Hussein et al. 1994; Panchapakesan N. R. and Lumley 1993). This is because, the turbulence scales are growing and slowing down downstream (Ball, Fellouah, and Pollard 2012; Fellouah and Pollard 2009) and therefore can be resolvable in a high dynamic range and spatial resolution measurements. Finally, it is also worth to mention that air has been chosen as the working fluid for the jet since it is free from contaminations and easy to maintain in the long run.

1.4 The chosen technique: Laser Doppler Anemometer (LDA)

Another critical question to the turbulence theory has evolved around the unreliability of the flow measurement techniques and instruments that can measure turbulence accurately without bias and resolve the small scales of turbulence (high resolution or dynamic range) (Champagne 1978). These requirements have become more critical in our case since measurements needed to be performed in the outer part of the jet (Paper I, III, IV and V), which are by nature very challenging and demanding a sufficiently high dynamic range. Hot-wire anemometry (HWA), which has classically been employed in turbulence research (Gibson 1962, 1963; Janssent, Ensingt, and Vaan Erp 1959), may offer this feature but is restricted to measurements with low shear and turbulence intensities only due to the directional ambiguity of the detected flow (Jensen 2004). This limitation has even been

experimentally demonstrated through the turbulence measurements in the jet developing region by using a constant temperature anemometer (CTA) throughout Paper II. Though those high shear and intensity flows can be accurately measured with the particle image velocimetry (PIV) (Hodzic 2014), this technique is limited by the low dynamic range that refrain it from measuring the small velocity changes accurately (Jensen 2004). The limitations suffered from those two techniques have made it so apparent for us to opt to LDA (see Figure 1-4) as the principal measurement technique for our study, which can measure turbulence correctly even under the most challenging flow conditions.

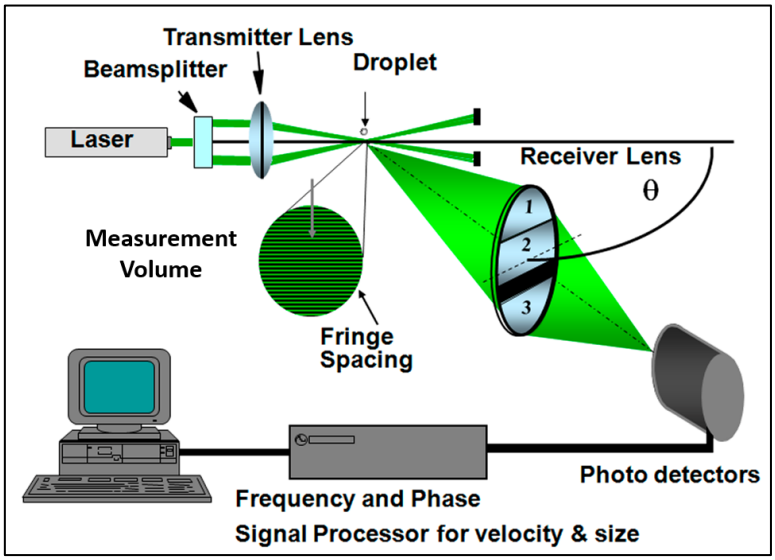

Figure 1-4 Measurement principle of LDA (source: *https://www.smart-piv.com/en/techniques/ldv-pdi/index.php*)

LDA has been used since almost half a century, starting around 1970s and 1980s (Barker 1973; Buchhave, George, and Lumley 1979; Capp 1983a; Hsu 1989; Ronald 1975; Xiong et al. 1984), to 1990s and the new millennium (Buchhave and Velte 2015; Falcone and Cataldo 2003; Hussein et al. 1994; Kassab, Bakry, and Warda 1996; Peiponen, Myllylä, and Priezzhev 2009; Velte, George, and Buchhave 2014). The general advantages of LDA has been mentioned repeatedly in every paper attached in this thesis, which also provide several prior investigations that has employed the same technique on their turbulent flow measurements. In summary, the main advantages are listed as below:

- Non-intrusive technique (no interruption to the flow)
- Can truly distinguish the spatial velocity components from each other, even at high turbulence intensities
- High dynamic range and spatial resolution to resolve correlations for the smallest scales of turbulence
- Absolute measurement technique requiring minimal calibration

1.4.1 Shortcomings of the commercial LDA system

It is worth to mention that the previously listed LDA measurements have been performed just by using the commercially available systems. They are apparently hardware-driven and have been suffering from some practical limitations, which in turn, has become our biggest motivation as highlighted in Paper III and IV. Each commercial system comes with a built-in processor, which is essentially just a black box with no detailed functions being disclosed, making it hard to understand any ambiguity resulted from the measurements. An example of the ambiguity is the dead time (see Figure 1-5), during which the processor is not able to register new measurements (Velte, Buchhave, and George 2014). A finite time for data transfer in each different processor causing them to display different behavior with respect to the dead time effect (Buchhave, Velte, and George 2014). Having a functionally open processor will be of the great interest for a transparent understanding and clear tracking on what has happened throughout the computation for a possible elimination of the dead time effect.

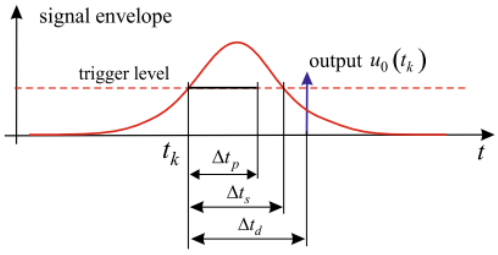

Figure 1-5 Dead time, Δt_d in the signal sampled by the burst detector (Buchhave et al. 2014). Δt_s and Δt_p are the residence time and processing time, respectively

The dead time effect in LDA measurement has been repeatedly addressed by Velte and Bucchave, who are apparently the supervisors of this PhD project, through a series of publications (Buchhave and Velte 2015; Buchhave et al. 2014; Velte, Buchhave, et al. 2014; Velte, George, et al. 2014). This effect is visible in the high frequencies part of the resulting power spectrum as an oscillation, which is unphysical since energy cannot again increase after being dissipated. If the dead time effect becomes dominant, a distorted power spectrum will be resulted (see Figure 1-6), which may compromise all the valuable information that can be obtained from it.

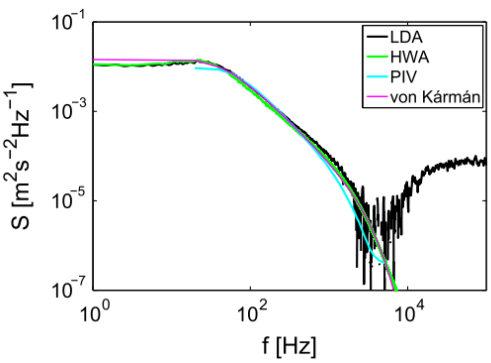

Figure 1-6 The dead time effect represented by the dip on the LDA spectrum, causing the spectrum to distort (Velte, Buchhave, et al. 2014)

The main contribution to the dead time in some commercial systems has been a finite data transfer time after each burst, during which no new measurements could be registered (see Figure 1-7). This problem should have been alleviated in the new generation of LDA burst processors according to one of the main manufacturers (private communication with Clara Velte). On the optics side, the dead time effect can be significantly minimized by reducing the size of the measurement volume (the region where two coherent laser beams intersect). The deadtime limitation arises here since the LDA in burst mode cannot measure more than one seeding particle at a time. Having to design and develop our own LDA setup will allow us to go for an optimum optical configuration that can result in a sufficiently small effective volume compared to the flow scales. This option could not be done, or might at least require additional hardware adjustment, with the commercial LDA systems that usually come in a fixed configuration mode, e.g., scattering angle, focal length and beam spacing, which will be further discussed in Chapter 2.

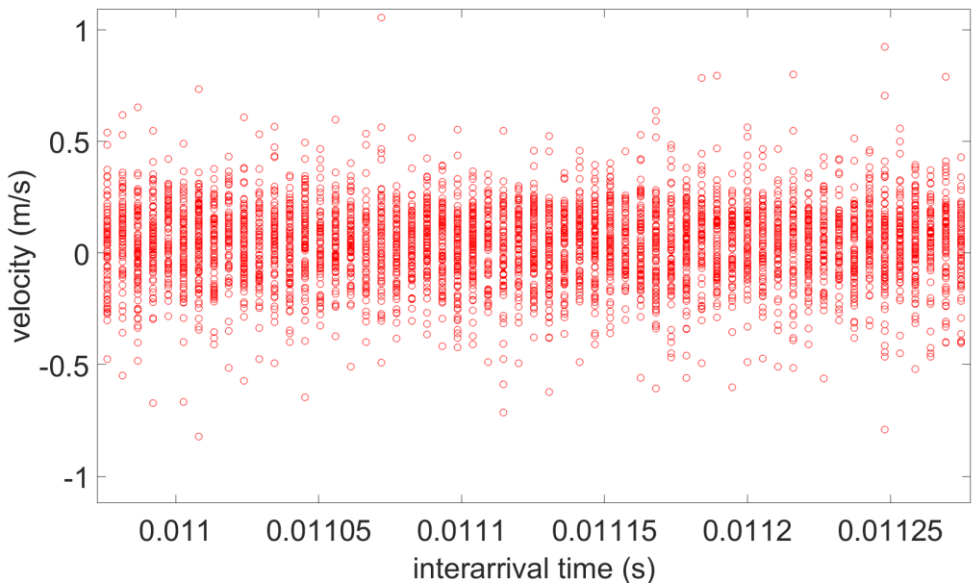

Figure 1-7 Digitization effect due to finite data transfer time in one of the commercial processors, for measurements conducted at the outermost axis position. Photo is from the diagnosis performed in Paper IV for LDA measurement at 30 jet diameters in the outermost off-axis position.

Performance comparison of the two leading commercial processors, e.g., Dantec (DISA) counter and TSI correlation processor, have also been made by (Velte, George, et al. 2014). The study highlights an issue regarding the unreliable values of arrival time, which is the time taken by a particle to travel through the measurement volume, by the Dantec processor. This discrepancy was due to buffer overflow when using much larger data sets, making the data to skip a certain number of realizations. Meanwhile, the TSI processor was reported to read the residence time (the time particle resides in the measurement volume) data registers wrongly, causing the reassembling of the binary data to be also incorrect. Almost all commercial processors seem to suffer from various problems with measuring the residence times. A valid example can again be seen from the diagnosis done on the processed signal of one of the commercial processors in Paper VI (see Figure 1-8). This problem has not been acknowledged by the manufacturers, but accurate representation of the residence time is of central importance in being able to produce unbiased statistics, as will be discussed later. To the best of our

knowledge prior to the beginning of this PhD project, this problem was yet to be solved. This has driven us to develop our own software-driven LDA system, which processor can better cope with problems encountered and thus allowing us to accurately measure the turbulence power spectra.

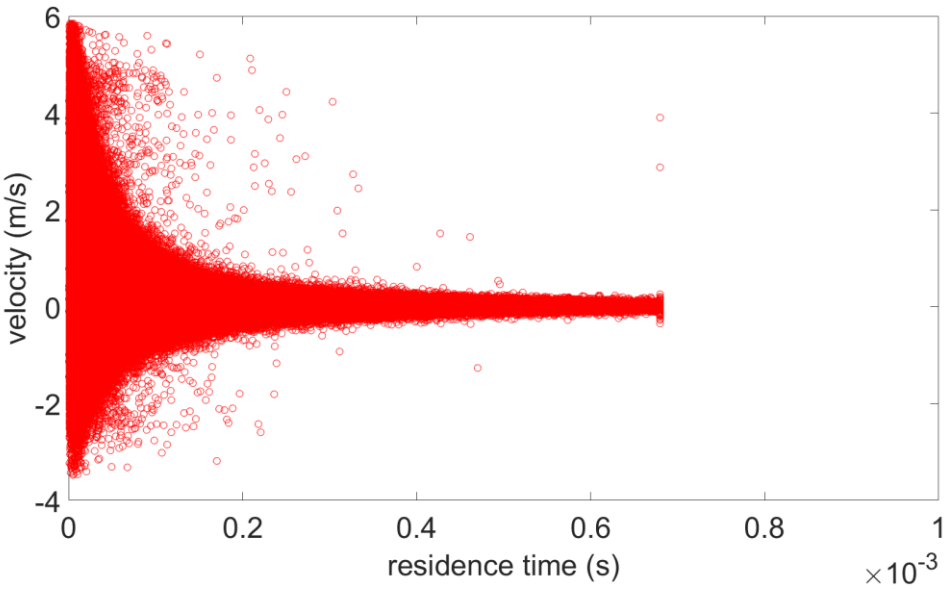

Figure 1-8 Abrupt limit on the maximum value of the residence times in one of the commercial processors, for measurements conducted in the outermost axis position. Photo is from the diagnosis performed in Paper IV.

1.4.2 Applied concepts

The important methods or concepts for computing the turbulence statistics have been briefly explained and recurrently employed throughout all papers attached in this thesis, except for Paper II which measurements were performed with hot-wire. This chapter will therefore provide a supplementary detail on those concepts and point out the significant advantages of using them, as opposed to the classical ones. Furthermore, these methods have been previously introduced and devotedly used in a series of relevant works, which strongly support our reasons to also apply the same methods for the turbulence statistics computations.

1.4.2.1 Convection record vs. Taylor hypothesis

Turbulence measurements with LDA is by default based on the time history of the velocity signal at a fixed point in space, which is contradictory with the founding turbulence theory that is formulated by the spatial correlations (in space domain) (Batchelor 1953; Kolmogorov 1941a, 1962). To measure large turbulence scales, one can just simply sample the records long enough but the resulted power spectrum will be unreliable towards the fluctuating convection velocity of the large scales (Lumley 1965). This problem has been overcome by the convection record method proposed and documented by (Buchhave and Velte 2017a, 2017b) that performs the mapping from time to spatial records. This

method is valid only for stationary flow and providing an exact mapping by taking into account the magnitude of the instantaneous velocity (see Figure 1-9).

$$s(t) = \int_0^t \bar{u}(x_0, t')dt' \tag{1.1}$$

where s is the scalar length of accumulated convection elements for fluid passing through the spatial record, or the convection record, $\bar{u}$ is the instantaneous velocity at an instantaneous time, t' and x_0 is the location of the fixed measurement volume.

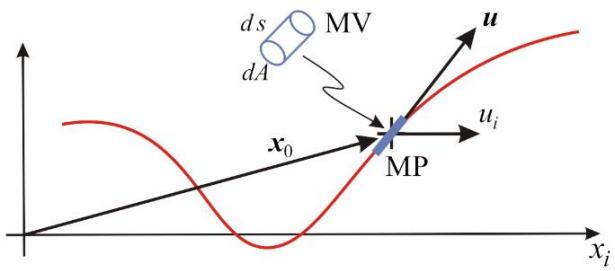

Figure 1-9 Time to spatial records mapping by the convection of the magnitude of the instantaneous velocity, u through the measurement volume (MV) (Buchhave and Velte 2017b)

This mapping does in an exact way what has only been approximated by Taylor's hypothesis based on the streamwise local mean velocity (Taylor 1938). Taylor's hypothesis was proven to be invalid in high intensity flow (Buchhave and Velte 2017b; Lin 1953; Wyngaard and Clifford 1977), which region is of the main interest in our investigation. This invalidity is clearly demonstrated from the spectra obtained by (Buchhave and Velte 2017b) and shown in Figure 1-10(b), which estimation was based on Taylor's hypothesis. The spectra for the two outermost position fail to collapse, as compared to the spectra estimated by the convection record method as in Figure 1-10(a). Due to this reason, the convection record method has been faithfully used for computing the static and dynamic statistical moments, including the turbulence energy spectra in all the papers attached (except for Paper II with hot-wire measurements) and second- and third-order structure functions (in Paper I, V and VI).

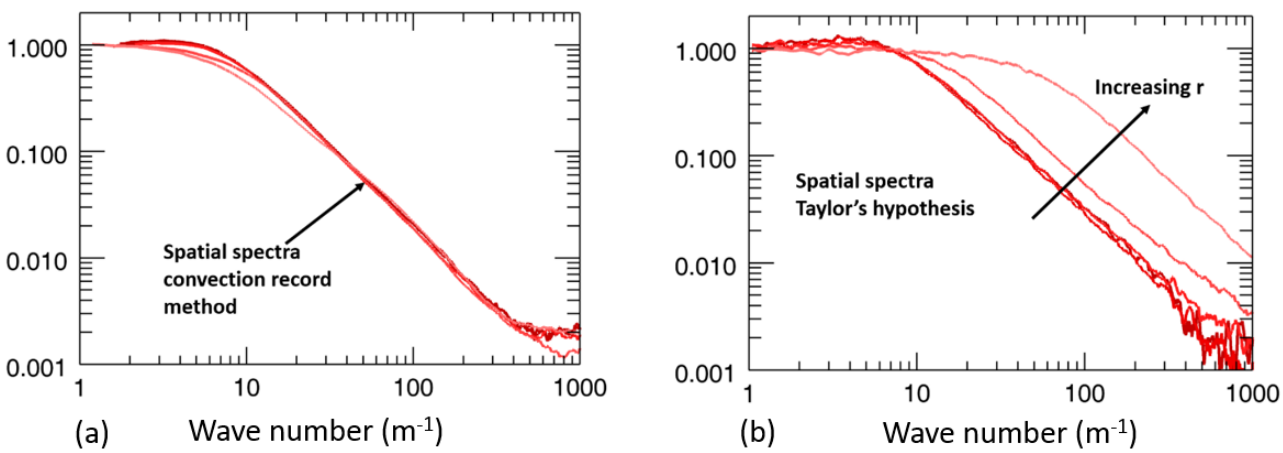

Figure 1-10 Normalized spatial kinetic energy spectra variations with radial distance, estimated by: (a) convection record method (b) Taylor's hypothesis (Buchhave and Velte 2017b)

1.4.2.2 Residence Time Weighting

A simple arithmetic mean of the measured velocities has been challenged, whether or not, the measured static and dynamic moments obtained were really based only during the time the particles spend in the measurement volume. This classical method has later been proven to be inappropriate in the case of LDA since the sampling rate and therefore, the arrival rate of Doppler bursts fluctuates in time with the variations of the velocity (Buchhave 1979; Buchhave et al. 1979; George 1988). Pursuing this will simply result in biased velocities of the true ones (Lading, Wigley, and Buchhave 1994).

As a solution to this, a residence time weighting method has been derived from first principles (Buchhave 1979; Buchhave et al. 1979) and further developed and validated by (Velte 2009; Velte, George, et al. 2014). This method is able to process the LDA data correctly regardless of the arrival time statistics, provided that the particle seeding is statistically constant and uniform (Capp 1983a). In this method, the measured mean velocity $\bar{u}$ and velocity variance, $\overline{u^2}$ are weighted by the measured residence times

$$\bar{u} = \frac{\sum_{n=0}^{N-1} \boldsymbol{u_i(t_n)\Delta t_n}}{\sum_{n=0}^{N-1} \boldsymbol{\Delta t_n}} \tag{1.2}$$

$$\overline{u^2} = \frac{\sum_{n=0}^{N-1} [\boldsymbol{u_i(t_n)} - \boldsymbol{\bar{u}_i}]^2 \boldsymbol{\Delta t_n}}{\sum_{n=0}^{N-1} \boldsymbol{\Delta t_n}} \tag{1.3}$$

where Δt_n is the residence time for the nth realization.

This method has then been extensively used in previous LDA measurements (Abdel-Rahman, Al-Fahed, and Chakroun 1996; Buchhave and Velte 2017b; Hussein et al. 1994; Velte, Buchhave, and Hodzic 2017), which provides reliable and bias-free results of the measured moments.

1.4.2.3 Correlation and spectrum computation

Since our software-driven LDA system is essentially optimized for the estimation of turbulence energy spectra, a proper and practical algorithm has been developed, which also takes both the residence time weighting and convection record method into account (Velte, George, et al. 2014). The convection record method (see Equation (1.1)) provides a correct representation of the spatial structures, which allow us to estimate the energy spectrum either by using the direct method (from the correlation function), or the slotted autocovariance function (SACF) invented by (Buchhave and Velte 2017b). With the former one, the spatial energy spectrum for the ith velocity component is estimated by

$$S_i(k) = \frac{1}{L} \hat{u}_i(k) \hat{u}_i(k)^* \tag{1.4}$$

where $\hat{u}_i(k)$ is the Fourier transform of $u_i(s)$ over the finite length of the convection record, s. However, due to random sampling, the discrete Fourier transform (DFT) must be used to compute the Fourier transform. The direct method provides a sufficiently fast computation time but gives the "dip" at the high end of the spectrum due to dead time effect (see Figure 1-11), which however can

be compensated by using deconvolution (Buchhave and Velte 2015). Note that, this deconvolution method was developed prior to the convection record method.

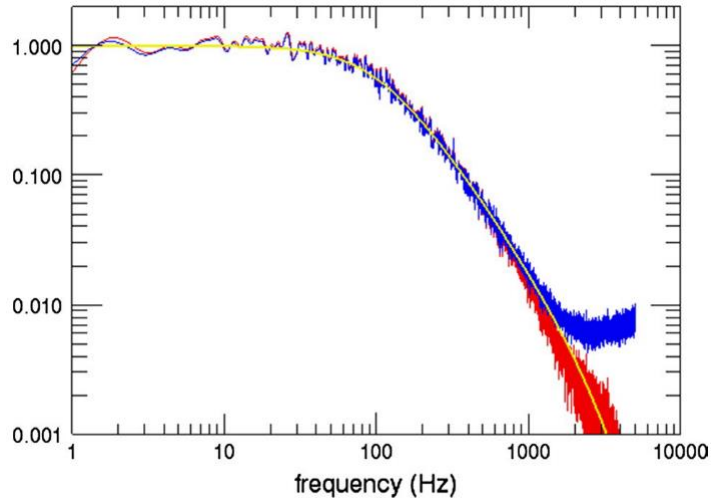

Figure 1-11 Removal of dead time effect and reduction in noise level on a the *red* spectrum after applying deconvolution, compared to the direct method (*blue*). The *yellow* spectrum is from Von Karman model.

Meanwhile, with the SACF method, the spatial energy spectrum for the ith velocity component is defined by

$$S_i(k) = \int_{-\infty}^{\infty} e^{-i2\pi k_i r} C_{ui}(r) dr \tag{1.5}$$

where C_{ui} is the autocovariance function of $u_i(s)$. This method is slower but can directly compensate for the dead time effect and noise, provided that the number of slots used in the ACF is at least two times the highest frequency in the spectrum. The SACF method has been demonstrated and proven to essentially eliminate the effect of dead time and random sampling noise on the energy spectrum (Buchhave and Velte 2015) . Naturally, great care has to be taken to compute these estimates correctly so that additional windowing or aliasing or similar is not imposed.

1.4.2.4 Noise reduction in LDA

Much information from an LDA measurement can be retained by reducing the noise level appearing in the Doppler signals. Among all types of noise, the most dominant one is the random sampling noise, which is due to the random arrival times (Durrani and Greated 1973; Lumley, Kobashi, and George 1969). As mentioned earlier, this spectrally white (flat) noise has been compensated through deconvolution of the spectral estimators.

Other noise sources, of which addition raises the constant noise floor are the thermal and shot noise (Velte, Buchhave, et al. 2014). This electronic noise arise during the conversion from the incident

light to the electrical signal by the detector. The thermal noise has been minimized by using a large value of load resistor, R_L, based on its definition

$$\overline{i_{n,T}^2} = \frac{4k_B T}{R_L}\Delta f \tag{1.6}$$

where k_B is the Boltzmann's constant, T is the absolute temperature and Δf is the bandwidth of the detector circuit. A resistance of 270 Ω has been chosen, which is not too big that may otherwise cut off the maximum Doppler frequency of the measured signal. The shot noise, which is highly proportional to the light power received by the detector (see Equation (1.7)), has been limited with the use of photomultiplier as our detector. This device comes with an internal gain that allows us to amplify the current internally before passing through the load resistor, while keeping a moderate level of the light power at the first place.

$$\overline{i_{n,q}^2} = 2e\overline{i_s}\Delta f \tag{1.7}$$

where $\overline{i_s}$ is the mean signal current and e is the electron charge.

Apart from above, we have also minimized the effect of optical noise by creating a larger beam angle (Gerosa and Romano 1994), through replacement of the focusing lens with a shorter focal length (see Section 2.1.1.3). Finally, though the fluid dynamic noise was claimed to be negligible (Durrani 1972), we have still taken a precaution step by using seeding particles (glycerin) of size 1 to 5μm, which is smaller than the fringe spacing (5.331μm).

2 Instrumentations and Measurements

This chapter particularly describes our state-of-the-art laser Doppler anemometer (LDA), which is based on off-the-shelf hardware and software. The hardware part of the setup is depicted in Figure 2-1, supported by the block diagram for data acquisition in Figure 2-2. Operating in the forward-scattering detection configuration, which advantages over the back-scattering configuration are illustrated in (Johnson 1988), the transmitting and receiving optics are mounted on two separate mountings. The transmitting optics is built of a laser source, a Bragg cell and a focusing lens, while the receiving optics comprises a detector head, which is connected to the electronic parts for data acquisition. Though this LDA system has been described briefly in each paper except for Paper II (hot-wire measurements), more detailed descriptions of each component/device listed in Figure 2-1 and Figure 2-2, will be covered in the following sections of this chapter, as well as the basic principle of LDA.

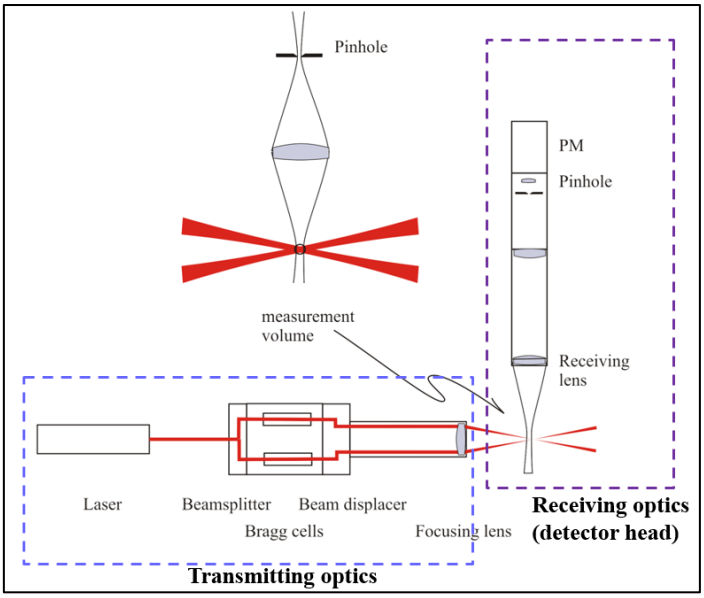

Figure 2-1 Schematic drawing (side view) of the LDA setup

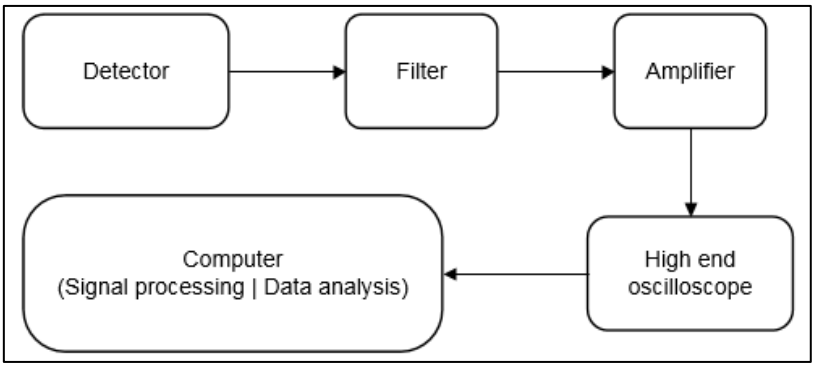

Figure 2-2 Block diagram for data acquisition of the LDA system

2.1 Burst-mode Laser Doppler Anemometer (LDA)

The LDA operates in burst-mode (Roberts, Downie, and Gaster 1980) and employs a dual-beam LDA configuration (Bartlett and She 1976) using a single laser source, from which the beam is split into a pair of coherent beams and passed through a Bragg cell, before they are focused and cross in a very small region where measurement is desired. This region is technically known as the measurement volume (MV in the following), which dimensions are calculable and is composed of interference fringes as illustrated in Figure 2-3. Since the system is indeed a 1D LDA, for the existing orientation of the beams and the detector, only one velocity component could be therefore measured at a time, which is the streamwise velocity component (in *x*-direction).

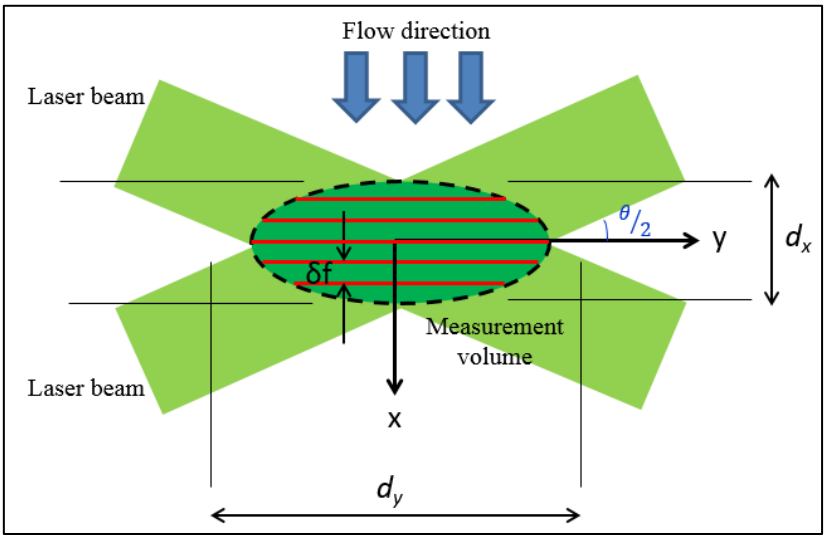

Figure 2-3 Top view of the measurement volume with its dimensions

The spatial resolution for an LDA measurements is ultimately limited by the size of the MV. The parameters listed in Figure 2-3 can be estimated based on the basic following formulae.

$$d_x = \frac{4f\lambda}{\pi E d_\iota \cos{}^{\theta}/_{2}} \tag{2.1}$$

$$d_y = \frac{4f\lambda}{\pi E d_\iota \sin{}^{\theta}/_{2}} \tag{2.2}$$

where λ is the laser wavelength, θ is the angle between the two beams, E is the beam expansion and d_l is the beam diameter. The dimension in the vertical direction, d_z, (not shown in Figure 2-3) should be equal to beam waist, d itself

$$d_z = d = \frac{4f\lambda}{\pi E d_\iota} \tag{2.3}$$

Fringe spacing, δ_f, or also known as the calibration factor:

$$\delta_f = \frac{\lambda}{2\sin\theta/_2} \tag{2.4}$$

In general, LDA works based on the Doppler effect due to the change of frequency in the laser light after being scattered by a moving seeding particle. In a dual-beam configuration, the measured Doppler shift, or frequency, f_D is obtained from the difference of the Doppler frequency by the two split beams.

$$f_D = f_{D1} - f_{D2} \tag{2.5}$$

In order to avoid the LDA from measuring a negative frequency resulted from Equation (2.5), a Bragg cell (BC in the following) has been introduced into the system. The measured Doppler frequency should now be obtained by

$$f_{D,m} = f_D + f_s \tag{2.6}$$

where f_s is the effective frequency shift from the BC. This shift in frequency makes it possible to distinguish the direction (sign) of the measured velocity component even in high intensity flows where reversed flow may occur.

With an assumption that the particle is to trace the flow (to a good approximation), the instantaneous streamwise velocity of a seeding particle (each detected burst) can be therefore calculated by

$$u_i = f_{d,m} d_f \tag{2.7}$$

This velocity, together with its respective values of arrival time, t, and residence time, Δt are obtained from signal processing by using our novel processor. By implementing the residence time-weighting method, the mean streamwise velocity and velocity variance at each measurement point can be determined by using Equation (1.2) and (1.3), respectively.

The performance and validation of the processor is briefly discussed in Paper III, but only for measurements in the fully developed region. The processor was then being tested for measurements in the challenging developing region, which results are presented in Paper IV. In this paper, a detailed explanation on the signal processing part can also be found (in Section 2.5), followed by the diagnosis of the processed signal (in Section 2.6) with a direct comparison to that of an existing commercial (hardware-driven) processor.

2.1.1 Transmitting Optics

Following the off-axis forward scatter configuration (Johnson 2016), our LDA setup has been built by mounting the transmitting and the receiving optics separately at two different locations, as shown earlier in Figure 2-1. Besides avoiding reflection, the essential purpose of having this configuration is to enhance the signal-to-noise ratio based on the Lorenz-Mie theory where the forward scattering angles yield higher light intensities (Fischer 2017). MV created from this configuration is also smaller and nearly spherical in establishing the highest possible spatial resolution (Buchhave and Velte

2017b). These technical reasons are also described in Paper IV. The whole transmitting optics are built of a laser source and an optical head equipped with a beam splitter, Bragg cells (frequency shifter) and a focusing lens, as illustrated in Figure 2-4 .

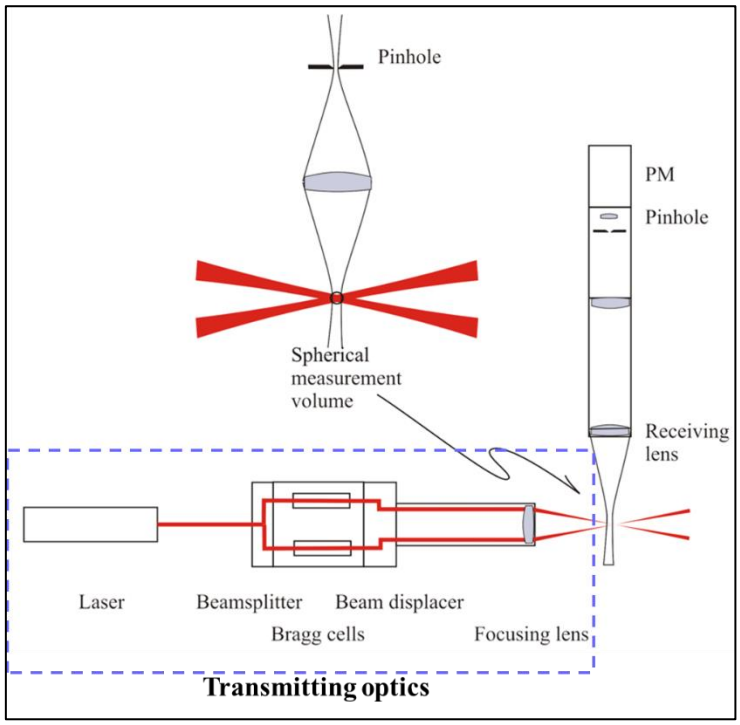

Figure 2-4 Overall schematic LDA setup showing the components of the transmitting optics

2.1.1.1 Laser Source

The continuous-wave green (532 nm) laser source used for the setup is from Laser Quantum Ltd, i.e., *excel 532 nm compact* laser. It is powered by the Power Supply Unit, *SMD6000*, which power can be regulated by a separate knob as shown in Figure 2-5. Detailed technical specifications of the laser source can be found in the **Appendix I**. The maximum laser intensity when the knob was turned to its maximum was measured to be 1.29 W. Even though the maximum intensity is considerably low, basic safety measures must still be adhered. The beam has always been safely projected to and collected in an appropriate beam stop. The intensity was set to minimum during the beams and optical alignment, before being levelled up to its maximum when measurements were acquired. Most importantly, the laser should be switched off completely when it was not in use. The beam coming out from the laser source is reflected on two small mirrors placed between the source and the optical head. Each mirror needs to be adjusted simultaneously to allow the beam entering the optical head through the center of an entrance hole as demonstrated in Figure 2-6. The beam is then directed through a beam splitter that split the beam into two beams of equal intensity, based on the dual-beam principle (Fingerson 1982).

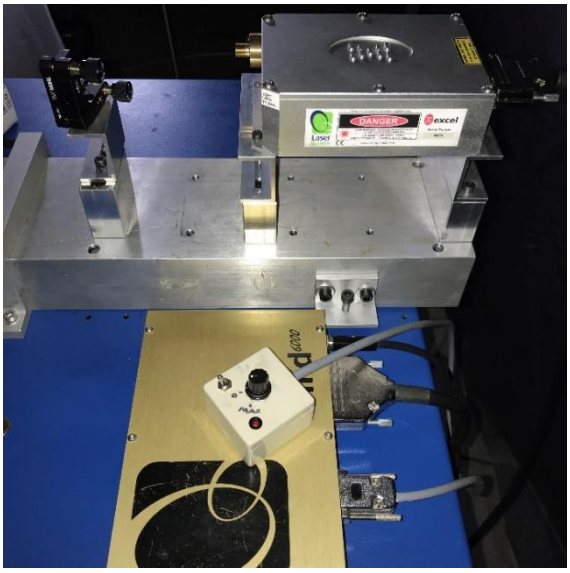

Figure 2-5 Excel 532 nm compact laser powered by the Power Supply Unit, SMD 6000

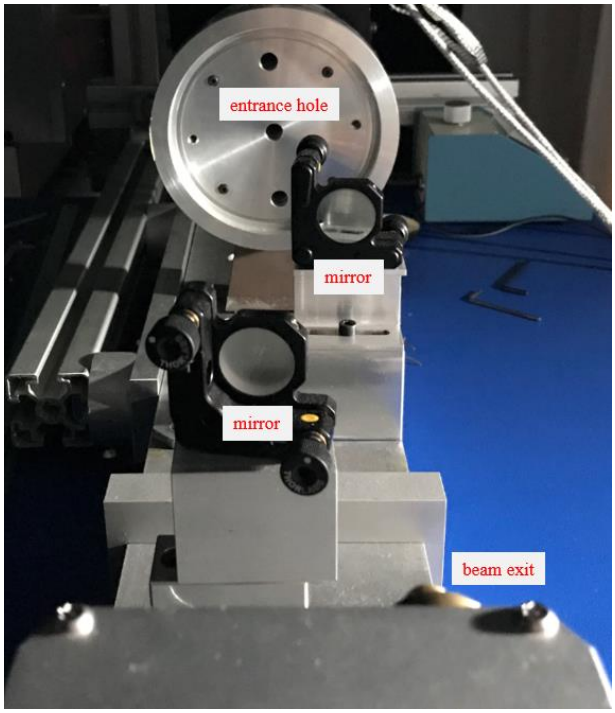

Figure 2-6 Beam alignment between laser source and optical head

2.1.1.2 Bragg Cell (Frequency Shifter)

Each beam is allowed to pass through a frequency shifter, or a Bragg cell (BC) to diffract the beam at the Bragg angle. A dual BC panel is opted to be able to get a much lower frequency difference that can be resolved by the digital oscilloscope, e.g., 3 MHz instead of 40 MHz from using only a single BC panel. Figure 2-7 shows one of the panels installed in the optical head, where the other one should

be seen from the other side of the optical head. Each is equipped with an acousto-optical modulator that inflects the light on an acoustic wave through the BC, which results in each beam to be divided into two (from each BC) as shown in Figure 2-8. Each panel is channeled to a BC module (see Figure 2-9), which allows us to set the desired value of the effective frequency shift (difference), f_s, e.g., 3 MHz as what has been consistently used in Paper I, III, IV, V and VI. To obtain this, one BC was set to up-shift of one beam by a known frequency, 40 MHz and the other BC was set to up-shift the frequency of the other by 37 MHz. With the shift, a higher frequency of the scattered light should be observed for particles moving in the opposite direction of the fringes, and vice versa. This effect can be demonstrated by slowly adjusting the value of the frequency shift on the BC module, while observing the change on the Doppler frequency from the oscilloscope.

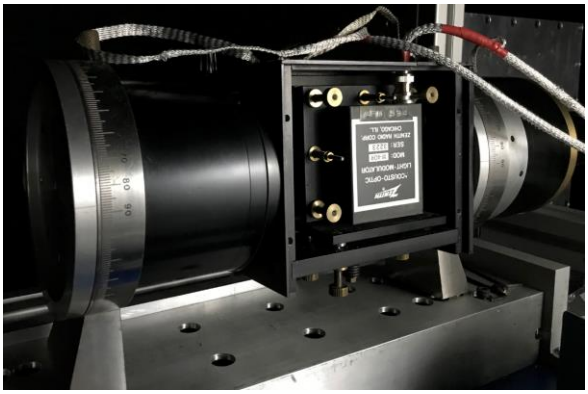

Figure 2-7 Acousto-optical modulator on one side of the optical head. The other side is also equipped with the same.

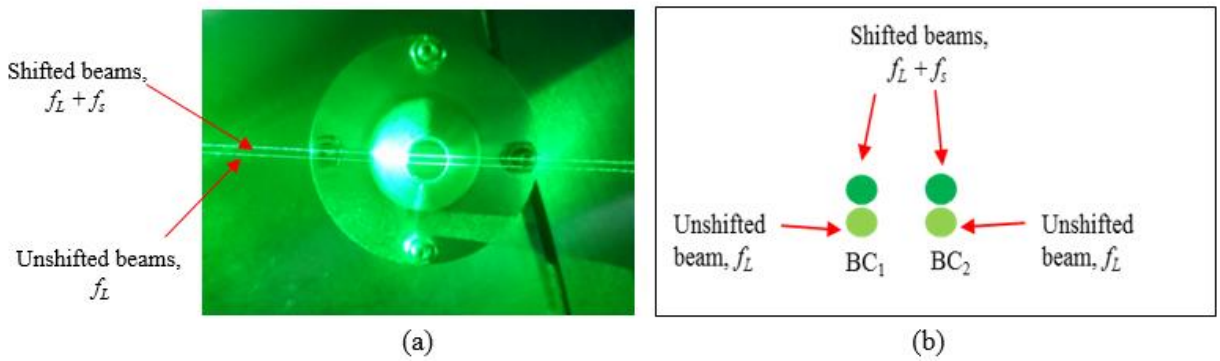

Figure 2-8 (a) Inflection of laser beams from each BC panel as seen by naked eyes (b) Illustration of the beam spots as seen on the wall, where f_L is the frequency of the laser. The shifted beams must be made higher in intensity than the unshifted ones.

Figure 2-9 DFE-A4 Series Dual BC module

The critical reason for including the BC in our setup is mentioned in the preceding section and fairly explained in Paper IV, which is to distinguish the moving direction of the particles along the measured component axis. It becomes more critical when the measurements are to be done in the shear region where the fluctuations and turbulence intensities are higher, as what we have experimentally shown in Paper II. However, it takes a lot of efforts and tedious jobs in configuring the BC prior to measurements. As can partly be seen from Figure 2-7, each BC panel comes with six different adjustment screws, e.g., three on the side and three underneath it. Each of them needs to be thoroughly and simultaneously adjusted until we get the shifted beams to be relatively brighter than the unshifted ones as demonstrated in Figure 2-8(b). The power knobs on the BC module may also need to be tuned optimally in getting the best output.

There may consequently exist two separated MV's, which are resulted from the intersection of two different pairs of the beams. The one that needs to be chosen for measurements is from the shifted beams, which appear as the upper beams in Figure 2-8(a). Bear in mind that both beam pairs do not necessarily intersect to form an MV. The height of the table where the optical head is lying needs to be adjusted until the chosen MV were at the same level with the center of the nozzle exit. This procedure has to be done simultaneously with the height adjustment of the other table where the jet box is lying. This can be simply done since both tables are equipped with a lifting mechanism. Meanwhile, the horizontal flatness of the tables was assured by measuring it with a spirit level.

On a separate note, we have also discovered that the BC radiates some waves to the surrounding, which can be seen from the unwanted spikes in the signals (see Figure 2-10). To minimize this, the BC panels have been covered with a black plate as shown in Figure 2-11. We have also replaced the normal BNC cables that connect the BC panel to the BC module with shielded copper cables, which have also been branched to a common grounding point. Having to do this, we have also taken an initiative to do a proper grounding for the other electrical equipment, e.g., digital and analog oscilloscopes, and preamplifier.

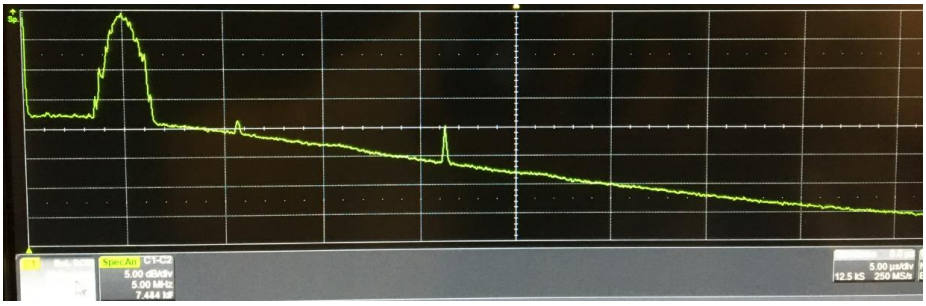

Figure 2-10 Unwanted spike from the BC radiation

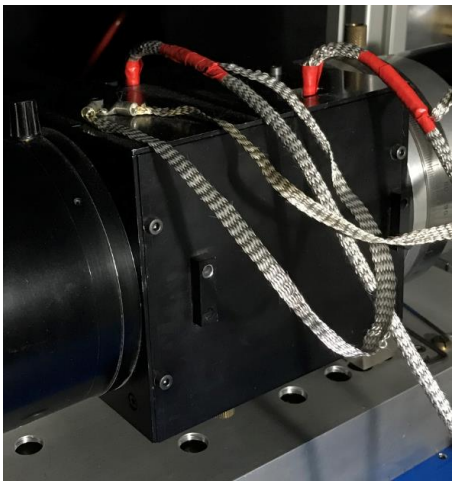

Figure 2-11 BC panel covered with a black plate to minimize radiation

2.1.1.3 Focusing Lens

The focusing lens used for the transmitting optics is a convex lens type that refracts and then converges the two parallel and coherent laser beams passing through it at a point called principal focus. In LDA, this is the point where a MV forms. The distance between this point and the center of the lens is known as the focal length. The lens surfaces are flat on one side and spherical on the other, which is widely known as the plano-convex lens (Sato 1979). The lens was mounted in a way that the flat side to be pointed away from optical head towards the MV since the beams passing the outer part of the lens should be refracted equally at the two surfaces. The outer part of the lens is like a prism, and the laser beams should hit both surfaces with approximately the same angle to result in a minimum aberration.

At the early stage of the setup development, we have initially opted to use a focusing lens having a focal length, f=300 mm as depicted. With a beam spacing set to be 22 mm, the beam angle and fringe spacing was found to be 4.2^{o} and 7.259 µm, respectively. Since the MV was expected to form at 300 mm from the outer surface of the lens, the detector head was also mounted in a way that the distance between its outer surface and the MV to be also at 300 mm, as demonstrated in Figure 2-12 where

L_1=L_2=300 mm. This was done to avoid the distortion of the image seen by the detector, which might compromise the image sharpness. The longest dimension of the MV, d_y, resulted from this arrangement is around 127 µm.

We later decided to replace the focusing lens with one having a shorter focal length, *f*=200 mm. The purpose of doing this was to enlarge the beam angle so that in the end it will result in a smaller fringe spacing and also a smaller size of the MV. The beams entering the lens are displaced through a pair of prisms, which space between them is 20 mm as illustrated in Figure 2-13. With this spacing, the new resulted beam angle and fringe spacing were 5.7^o and 5.331 µm, respectively. The longest dimension of the MV is now reduced to around 90 µm. In order to fit in the new lens, an adapter with a matched thread was fabricated in the workshop and later mounted to the optical head as shown in Figure 2-14. Having this, we also had to make an adjustment on the detector by mounting a receiving lens tube with *f*=200 mm to it (see Figure 2-15) so that its distance to the MV will be also the same as the new focal length. Both L_1 and L_2 of Figure 2-12 are now equal to 200 mm.

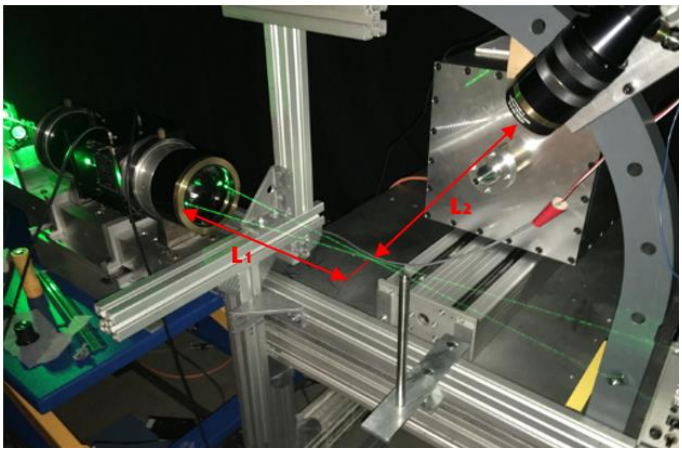

Figure 2-12 The initial setup when a focusing lens with f=300 mm was in used

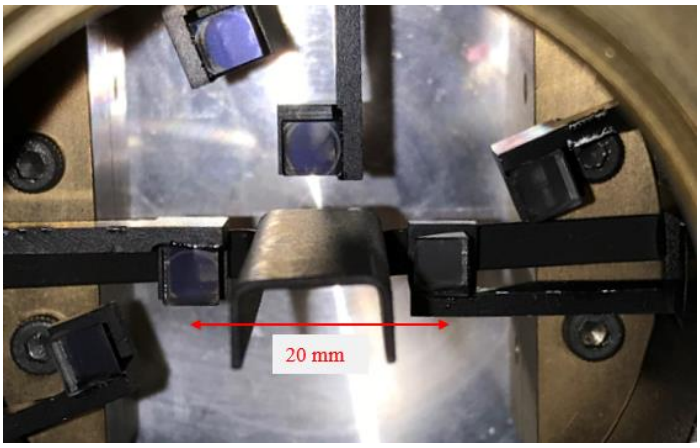

Figure 2-13 Prisms inside the optical head through which the beams from BC are displaced to the focusing lens

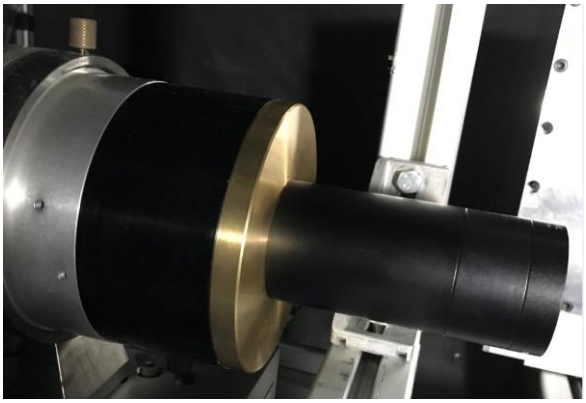

Figure 2-14 New focusing lens mounted to the optical head through an adapter

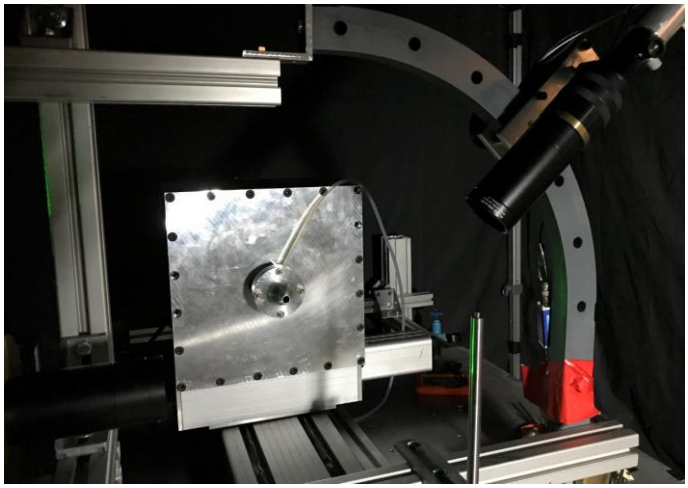

Figure 2-15 Modified setup with new focusing lens and a receiving lens tube on the detector head

The main purpose of decreasing the focal length is to reduce the size of the MV. This will allow us to obtain a higher seeding density and still avoid to a good degree the risk of having more than one particle in the MV at a time. Figure 2-16 clearly illustrates the overlapping bursts from two particles residing in the MV at the same time. The dead time effect can therefore be minimized (Velte, Buchhave, et al. 2014)(Buchhave et al. 2014) even with a sufficiently high data rate, by having a sufficiently small MV. Some preliminary measurements were done to investigate and demonstrate the effect of data rate on the noise level of the measured velocity power spectrum, *S(f)*, based on the following equation:

$$S(f) = \frac{\overline{u'^2}}{v} + S_{u'}(f) \tag{2.8}$$

where u' is the fluctuating velocity, v is the data rate and $S_{u'}(f)$ is the true power spectrum (Buchhave and Velte 2015). The second term in the equation is the (frequency independent) random sampling noise, which is by far the most dominating noise and smaller in the laminar flow for a higher data rate, η. Note that, these measurements were performed in side-scattering configuration, where the

receiving (detector) and the transmitting optics (optical head) were placed at 90° to each other as in Figure 2-17. This configuration demands less tedious alignment of the detector head (see *Detector* section), which was the main reason of opting it for this time.

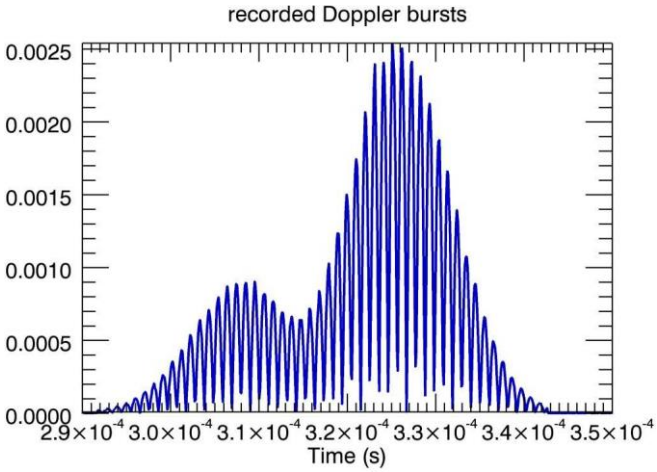

Figure 2-16 Two bursts are overlapping from two particles residing in the MV at a time

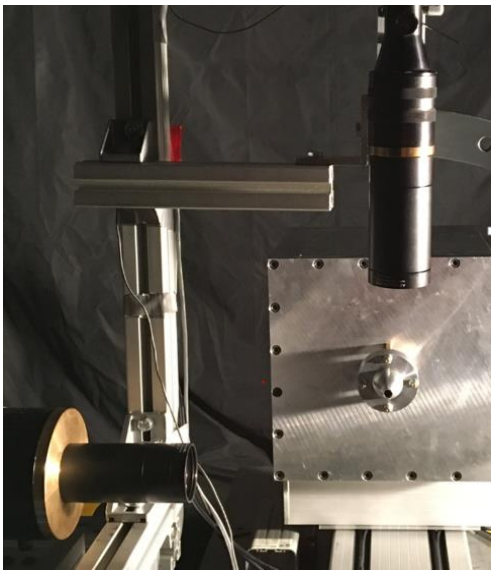

Figure 2-17 LDA setup showing a 90° side scattering configuration

Measurements were done by varying the pressure across the seeding generator at 1.1 bar, 1.2 bar and 1.3 bar, and by taking only 1 record at *x/D*=30 (centerline). The results shown in Figure 2-18 demonstrate that the noise level was diminished with the increment of the seeding pressure (data rate). The significant impact of having a higher data rate can also be demonstrated from the spatial second order structure function plot, as presented in Figure 2-19. The data is taken from one of our earliest long measurements, also at *x/D*=30 (centerline) for which 400 records were acquired to meet the statistical requirement. Measurement with the higher data rate (seeding pressure of 1.4 bar) results in much higher smoothness of the plot. Based on this diagnosis, this seeding pressure value was

therefore used in LDA measurements reported in all papers presented in this thesis, except for Paper II (hot-wire measurements).

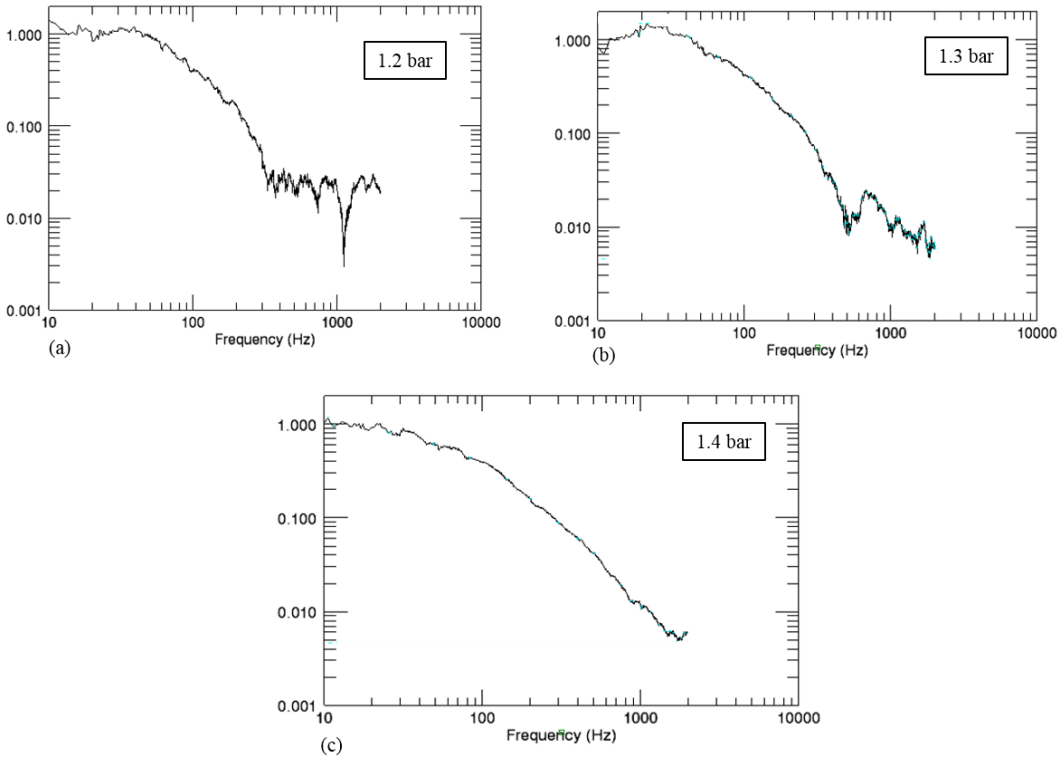

Figure 2-18 Data rate test at varied seeding pressure: (a) 1.2 bar, (b) 1.3 bar, (c) 1.4 bar. The data rate recorded for each case are 1552 Hz, 2929 Hz and 8989 Hz, respectively. The poor smoothness of the spectra is due to limited number of records taken for the measurements.

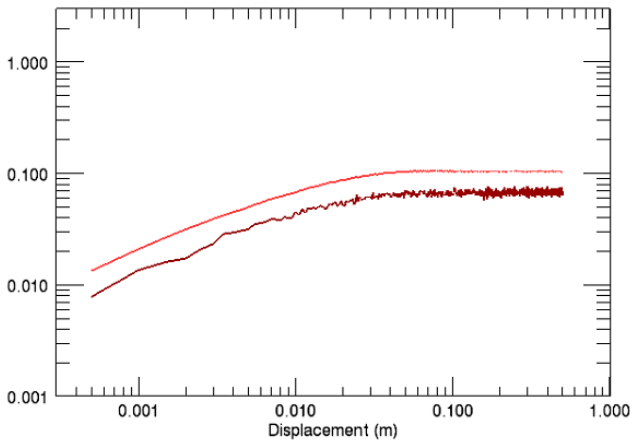

Figure 2-19 Spatial second order structure functions at *x/D*=30, centerline, from measurement with 1.2 bar (light red curve) and 1.4 bar (dark red curve). The curves are deliberately shifted vertically for a clear comparison.

2.1.2 Receiving Optics and Electronics

2.1.2.1 Detector

The main component of the receiving optics in an LDA system is the detector, which delivers an electronic signal modulated by the Doppler shift caused by the velocity of the seeding particles passing through the MV. The type of detector used in our case is a photomultiplier tube (Hamamatsu H10425), which also amplifies the photocurrent internally before it passes through the electronics parts, so that the noise amplification can be minimized (Albrecht et al. 2003). It is equipped with a custom-made power supply (see Figure 2-20) having a range of 0 – 100 µA, which suits the maximum output signal current by the PMT (refer **Appendix II** for its datasheet).

Figure 2-20 Customized and self-fabricated power supply for Hamamatsu H10425 PMT

As explained in the preceding section, the detector head is attached to a receiving lens tube with *f*=200 mm (see Figure 2-21) to suit the focal length of the new focusing lens. It is also properly mounted on a curved beam having seven different holes to offer a great flexibility in choosing the mounting angle following the side/forward-scattering configuration. The mounting mechanism consists of a holder that is slotted through the hole and tighten, and a ball joint holding the detector head to ease the pinhole alignment with the MV (see *Cookbook* section). The lower end part of the beam has been screwed to a frame, which has been locked to the table through a holder (see Figure 2-22) to avoid the detector from wobbling when measurements are acquired. The current configuration seen in Figure 2-21, i.e., at 45° forward-scatter, has been chosen for all LDA measurements presented in each paper except for Paper II (hot-wire measurements). It optimizes the demand for having sufficient amount of light by the detector and effective reduction of the detection volume to simultaneously uphold both the highest possible signal-to-noise ratio (Fischer 2017) and spatial resolution (Buchhave and Velte 2017b) throughout the measurements. Compared to the side-scattering, this configuration however demands more tedious alignment work as briefly described in Paper IV and in more detail in the *Cookbook* section in **Appendix III**.

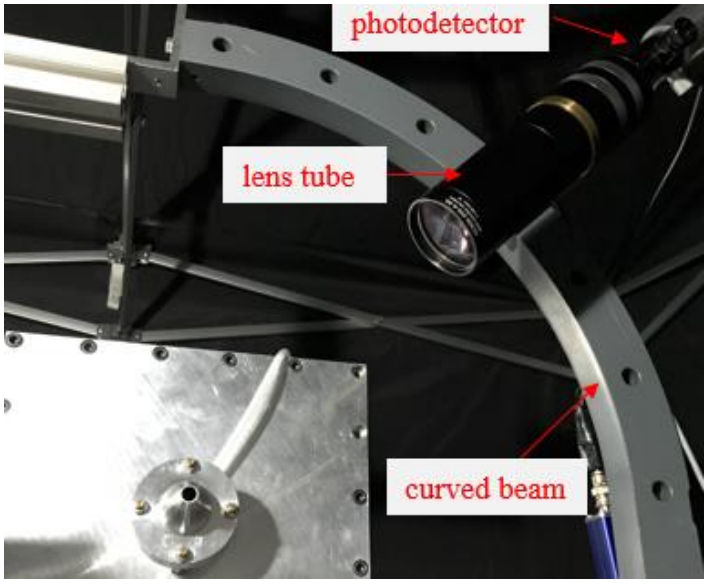

Figure 2-21 A part of the LDA setup showing the receiving optics with its mounting mechanism, and demonstrating a 45° forward-scattering configuration

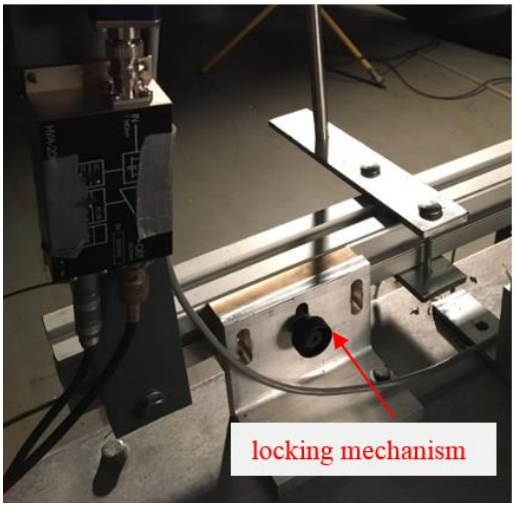

Figure 2-22 Locking mechanism for the frame holding the detector head

2.1.2.2 Filter and Preamplifier

The output of the photomultiplier (PM) is connected via a BNC cable to a SUCOBOX coaxial adapter (see Figure 2-23), in which a load resistor, R_L=270 Ω is in place. Together with a built-in capacitor, C=22 pF in the PM tube, a first-order RC low pass filter (see Figure 2-24) is constructed that results in a cut-off frequency, f_c=26 MHz. This frequency was tested and found out to be high enough in a way that the Doppler frequency will not be cut off by the front-end electronics. The analog signal coming out from the filter is then passed through a 200 MHz High Input Impedance Voltage

Preamplifier. The signal mode and the amplification gain are set to AC and 20 dB, respectively. The datasheet for the preamplifier can be found in **Appendix IV**.

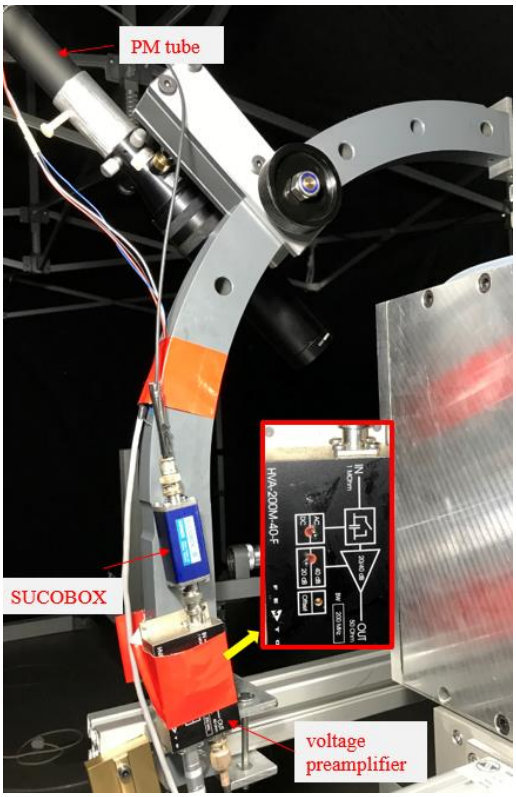

Figure 2-23 A part of the LDA setup showing the receiving optics and the electronics

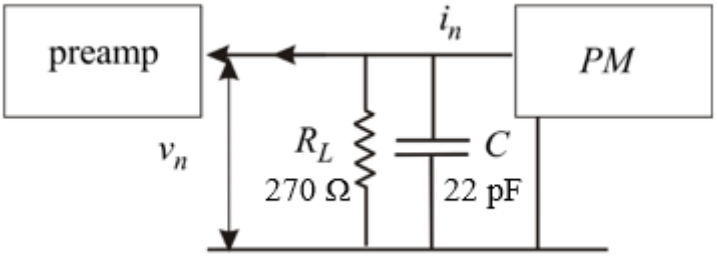

Figure 2-24 RC low pass filter between the photomultiplier and preamplifier

2.1.2.3 Digital Oscilloscope

The analog frequency modulated signal from the amplifier is then channeled via a BNC connection to an HDO6054 high-definition digital oscilloscope from Teledyne LeCroy. It has a large buffer memory, which can hold a record long enough to contain all the desired turbulence scales. An example of a good measured Doppler signal is visualized by the oscilloscope is shown in Figure 2-25. When the continuously captured signal exceeds the burst detection level, it undergoes a fast digitization and a subsequent FFT analysis provides a velocity data point from the digitized burst signal, which is saved and transferred to the computer for further processing with our self-developed software. Another useful feature of this oscilloscope is the *Spectrum Analyzer* that perform a simplified Fourier transform of the Doppler burst, from which the maximum Doppler frequency, f_D can be estimated (see Figure 2-26). This value will be used to estimate the sampling rate for data recording, which should fulfill the Nyquist sampling rate to avoid aliasing (Paper IV). From the same figure, the estimated values of the center frequency, f_{ctr} and frequency range, f_{wins} can also be obtained. These values are to be set later as the processing parameters in the software for signal processing.

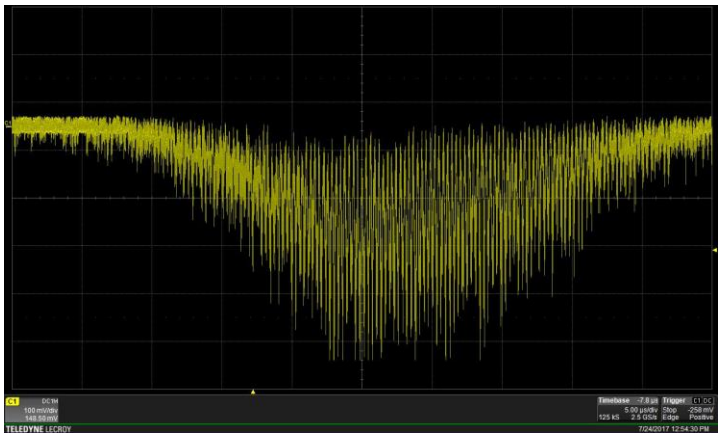

Figure 2-25 An example of a high-quality Doppler signal visualized on the oscilloscope

Figure 2-26 Simplified analysis of Fourier transform of the Doppler burst by the oscilloscope

2.1.3 In-house Software (Processor)

As mentioned earlier, our LDA system is driven by an in-house developed software package for signal and data processing, which is optimized for computing turbulence energy spectra and similar dynamic statistical moments. The package comprises three different software (programs), which algorithms have been developed in IDL from Harris Geospatial Solutions:

ldapro_17_02_19_sdtw

This program processes the digital (binary) records saved from the digital oscilloscope. Prior to the processing, few important settings need to be set, e.g., validation parameters, sampling parameters, frequency settings (f_{ctr} and f_{wins}), Hilbert window, gain and trigger level. To begin with, the number of records can be temporarily set to 1 while trying to optimize all those parameters since processing all the 400 records may take around 8 hours to finish. The program finally generates and saves a set of Gaussian's validated data that includes the arrival times, residence times, mean and RMS velocities at one particular measurement point. The signal processing performed throughout this program is described in Paper IV.

ldaps_tts_sacf_1

This program computes the kinetic energy spectrum in spatial domain (wave number, *k*-domain). It first reads the data generated by the previous program and converts the temporal records to spatial records by employing the convection record principle proposed by (Buchhave and Velte 2017a). The subsequent computation of spatial kinetic energy spectrum is done by implementing the slotted autocovariance function (SACF) method proposed by (Buchhave and Velte 2015), which has been proven to remove the dead time effect (Velte, Buchhave, et al. 2014)(Buchhave et al. 2014). For this method, the number of slots chosen should be big enough (or, correspondingly, the slots should be narrow enough) in order to avoid aliasing of the spectrum. For spectra computation at radial points along one particular downstream position, the diameter of the measurement volume, *dmv* in the program needs to be calibrated until it gives the same spatial record length for the convection record and the Taylor Hypothesis record. This calibration must be done in a region where turbulence intensity is less than 30%, e.g., at the centerline. For computing the spectra for the other outer points along the same downstream position, the same *dmv* value may only be used if the measurements were done with an equally long time records, which what we have done for our measurements. Besides, the gain setting in the program was also kept to be the same. The spectrum is obtained by performing the FFT of the averaged autocovariance function, for which the plot data will be finally saved for use in the following plot program.

plot_ldaps_tts_sacf_1

Though the preceding program may already provide the energy spectrum for one particular measurement point, this separated plot program allows us to replot and best present the spectrum with the optimized plot parameters. For each spectrum, the plot parameters need to be adapted, e.g., for normalizing the spectrum to 1 in the low wave number asymptote and subtracting a suitable constant noise level to best display the slope of the spectrum as comparison to -5/3. Having the plot data saved earlier, computation of an energy spectrum will just need to be done once, whenever the plot parameters are to be changed, which will save us a substantial amount of time.

All in all, this self-developed software offers many significant advantages compared to the commercial hardware-driven processor. Besides being transparently functioning with a highly flexible functionality, it allows much more sophisticated signal processing with possibility to resample the raw data, perform filtering and FFT analysis based on a selected optimum sample rate. The available signal will therefore be much better utilized to improve the dynamic range of the measured turbulence. These advantages are also highlighted in Paper III and IV, which are even supported with valid experimental results.

Other than the three previously mentioned main programs, a few other programs have also been developed to compute the spatial second-order and third-order structure functions, which plots and computation methods are presented in Paper I (without the latter one), V and VI.

lda_structure_function_2
This program computes both the spatial second-order and third-order structure functions from the data generated by the *ldapro_17_02_19_sdtw* program. Since it also employs the convection record method, calibration of the *dmv* value is again demanded by doing it with the same way as in the *ldaps_tts_sacf_1* program. Upon computation, this program will save the plot data for the structure functions.

plot_lda_structure_function_2
This program reads the plot data from the preceding software and separately replots the spatial second-order and third-order structure functions for one particular measurement point. The 2/3 and 4/5 slopes are also plotted on top of the second-order and third-order structure functions, respectively. In this program, the parameter *ffconst* is fine-tuned to best-fit the 4/5 slope with a third-order structure function, which value represent the mean energy dissipation rate per unit mass, ε, as presented in Paper V and VI.

2.2 Flow Generation Facility

Most of the mechanical parts of the experimental setup were fully designed and fabricated in the DTU Mechanical workshop, including the air jet and the nozzles fitted with it. The jet itself is made of a cubic Aluminum box of dimensions 58 x 58.5 x 59 cm^3 (see Figure 2-27), which interior is stacked with foam-coated baffles to damp out large disturbances from the pressurized air, and screens to eliminate remaining fluctuations in the stream.

The jet is fitted with a trumpet nozzle (Figure 2-28 (a)) tooled through a connecting pipe into an outer nozzle (Figure 2-28 (b)) of a fifth-order polynomial contraction with an inner diameter of 32 mm and exit diameter, D=10 mm, respectively. The order of polynomial was chosen based on the contraction design study conducted by (Bell and Mehta 1988) on a low-speed wind tunnel, which has been proven to output a uniform velocity distribution, or a top-hat velocity profile on a the air jet used in (Jung 2001). The exact dimensions of the two nozzles can be found in the 2D drawing with Solidworks in **Appendix VI**. The outer nozzle is jutted out of the jet box as shown in Figure 2-29. Different series of measurements were done on the jet to validate its characteristics based on the previous jet studies.

In Paper IV, the jet was proven to satisfy the momentum conservation test in an (to a fair approximation) infinite environment, based on the almost similar values of the momentum flux per unit mass obtained at the jet exit and *x/D*=30. Furthermore, based on the Strouhal Number obtained from our measurements, Paper VI demonstrates that the jet is in good agreement with the preferred operating mode defined by Gutmark (Gutmark 1983), which represent the specific range of shedding frequency for an axisymmetric jet. Meanwhile in Paper V, we could see that the ratio between the RMS and mean velocity (turbulence intensity) of the jet flow exhibits an asymptotic value, which is close to the previous investigations on the jets of similar type (Mi, Nathan, and Nobes 2001).

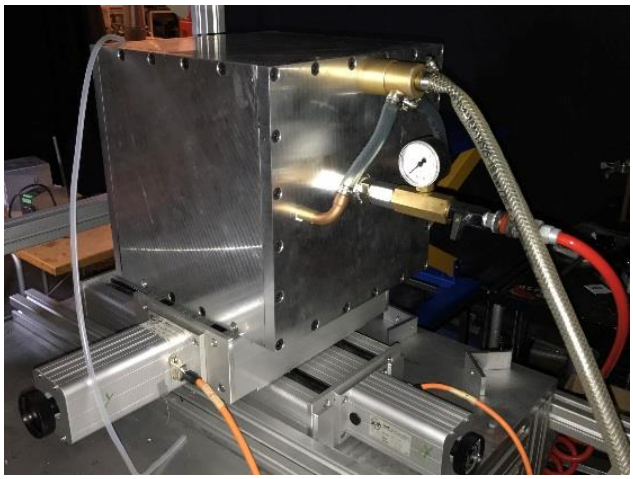

Figure 2-27 Jet box with a pressure gauge and an adjustable valve at its input port

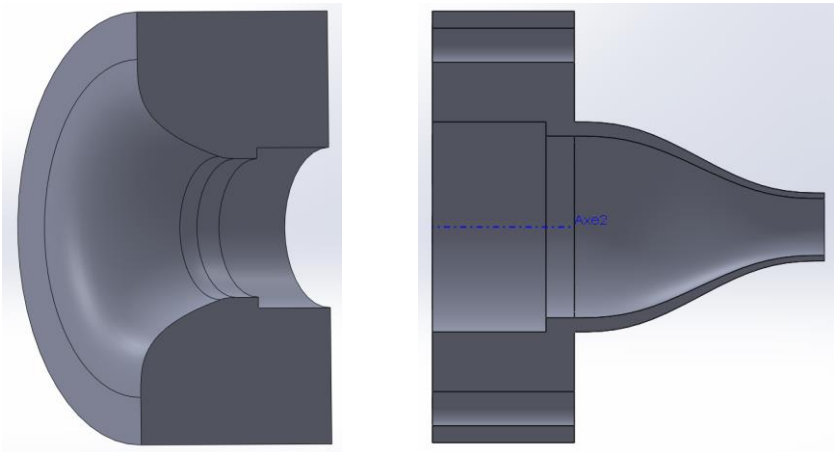

(a) (b)

Figure 2-28: (a) Trumpet nozzle. (b) Outer nozzle with fifth-order polynomial contraction

A pressure gauge is located just right before the input port of the jet (see Figure 2-27) with an adjustable valve to control the pressure amount of the incoming air supplied. In order to obtain the desired jet exit velocity, the supplied pressure needs to be regulated, which will vary the pressure difference between the point before the contraction and the atmosphere. This pressure difference

needs to be monitored whenever the opening valve is regulated to give a value that is corresponding to the desired jet exit velocity based on the Bernoulli's principle. Pressure taps were then made before the contraction to allow this pressure difference measurement with a digital pressure meter, as demonstrated in Figure 2-30. The jet exit, u_{exit} and pressure difference, Δp are related by Equation (2.9)

$$u_{exit} = \sqrt{\frac{2\Delta p}{\rho\left[1-\left(\frac{r_{exit}}{r_{inlet}}\right)^4\right]}} \tag{2.9}$$

where ρ is the density of air, r_{exit} is the jet exit radius *and* r_{inlet} is nozzle inner radius.

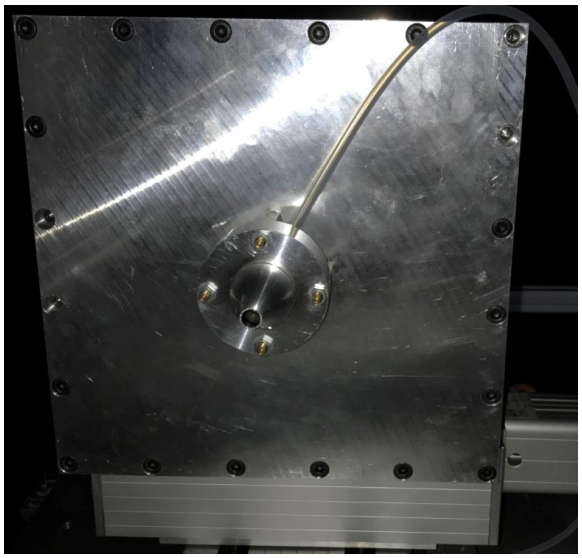

Figure 2-29 Outer nozzle jutted out of the jet box

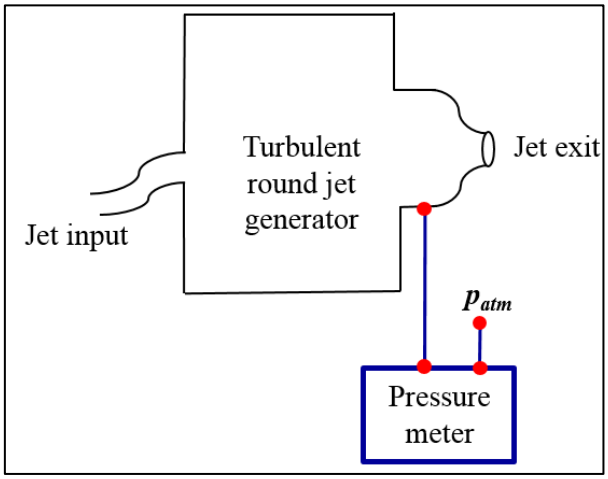

Figure 2-30 Pressure difference monitoring

2.2.1 Seeding particles and Generator

Seeding particles are the medium that allows an air flow to be optically traced by the LDA, or to be specific, the detector. Since air is invisible to our naked eyes at the atmospheric pressure, seeding particles must be fed into the air flow to scatter some amount of light to the detector once it moves across the measurement volume. In principle, a smaller particle is expected to track the flow with insignificant slip but may reduce the signal-to-noise ratio, if it is too small (Fischer 2017). Meanwhile, a larger particle scatters higher amount of light to the detector that will increase the signal-to-noise ratio but will also limit its ability to respond to the variations in the mean flow (Reeks 2011) and be uniformly distributed in the flow (Johnson 1988), if it is inappropriately large. Therefore, one must be careful in choosing the seeding particle having an optimum size (Melling and Whitelaw 1973). Glycerin of size 1 to 5 µm has been chosen since it was proven to be small enough to travel in an identical velocity with the flow and observed to be large enough to scatter the light adequately (Capp 1983b). The size is also still smaller than the fringe spacing (5.331µm) calculated from Equation (2.4), which is an important requirement for obtaining a maximum visibility of the oscillating part of the Doppler signal (Righini, Antonella, and Cutolo 2009), as seen earlier in Figure 2-25 .The same type of particle has been consistently used for all LDA measurements done throughout the study (Paper I, III, IV, V and VI).

A seeding generator is used to continuously supply seeding particles into the air flow. Glycerin is usually generated by the atomization method (Jensen 2004) and so is for our LDA setup as shown in Figure 2-31. This method is capable of maintaining a steady concentration of the oil droplets particles generation (Melling 1997). Before performing each LDA measurements, the particles were allowed to distribute uniformly through the ambient air inside a large tent (3 x 5.8 x 3.1 m^3) for at least half an hour to obtain homogeneous seeding. This will avoid having incorrect representation of the flow due to conditional seeding, i.e., only some parts of the flow are seeded. In other words, only the high velocities are measured since the slower fluid entrained is yet to contain any particles just after the jet is seeded.

Figure 2-31 Seeding generator based on atomization method

The size of the tent was chosen to allow the jet flow to correspond to a free jet up until 70 jet exit downstream (Hussein et al. 1994), which is more than enough for our purpose, e.g., up to 37 jet exit downstream, corresponding to the fully developed region. Since mostly half of the area of the tent was not in use based on the scope of our measurements, a curtain was installed inside the tent as a separator to narrow down the effective seeded area. This is acceptable, as thin shear layers obey marching solutions, so downstream conditions barely affect the upstream flow (White 1991). The steady particle concentration can also be achieved faster in this way. In order to avoid the glycerin smoke from being exhausted to the whole laboratory, a portable ventilator filter is placed at one corner of the tent as illustrated in Figure 2-32.

Figure 2-32: (a) Portable ventilator filter placed inside the tent. (b) Exhaust to the outside of the tent

2.2.2 Linear Traversing System

A traversing system plays an important role in maneuvering the MV to the desired positions throughout the jet, e.g., in the streamwise, *x*- and radial, *y*-directions (Figure 2-33). Paper IV and V briefly describe both the hardware and the software parts of this linear traversing system. Each traversing unit was fabricated by ISEL Automation and equipped with a stepper motor (MS110 and MS160) and limit switches. Both were found in the old laboratory aging more than 20 years, together with an old controller by Targus Group International. There was a problem in interfacing the controller with the computer as the driver was no being able to be detected. The detailed specifications of the stepper motors were also missing, which made it even harder for further configuration. Manufacturer of the motors, isel Germany AG was contacted to get access to the datasheets (attached in **Appendix VI**). They later came out with a worthy suggestion to use the latest three-axis stepper motor controller, *iMC-S8* to drive the motors at a higher precision, e.g., in micro stepping mode. Each motor is connected to the controller using the *M23 12-pin Plug - SubD9-pin Connector* cable.

We decided to operate the stepper motor controller in Direct Numerical Control (DNC) mode by connecting it permanently to a computer via *RS232* serial interface as illustrated in Figure 2-34. To operate the controller in such mode, the isel control software *RemoteWin* was installed to the computer. This software allows controlling the stepper motors in a manual execution, which detailed procedures are described in **Appendix VII**. According to the manual for those particular traversing units, the number of steps per revolution and spindle elevation have been set to 800 steps/rev and 5 mm, respectively. A test run was executed to compare 6 different positions traversed on the hardware

with the ones executed in the software for both axes. From the test, all positions were verified to match well with each other. Another challenge in making the traversing system to work was the difficulty in setting the right direction of the linear movement of one of the traversing units. After having a virtual consultation with the technical support from the manufacturer via *Teamviewer*, we agreed to ship out both traversing units to Germany for further inspection and troubleshooting. One of the limit switches was discovered switching in a wrong way, which was then being fixed and tested on their site before being they return the units back to us.

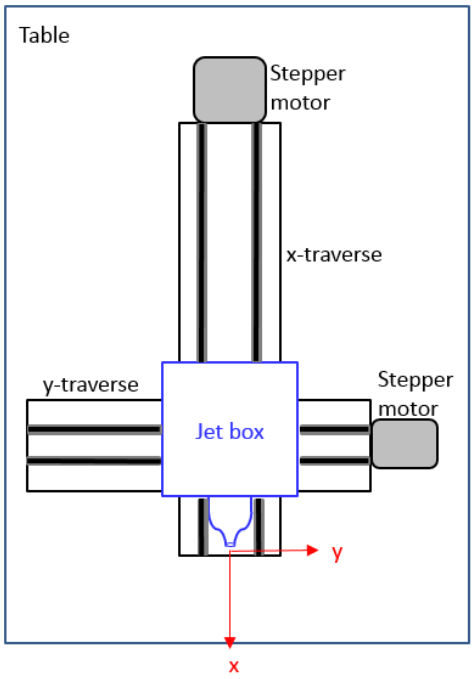

Figure 2-33 Top view of traversing units setup on the jet box

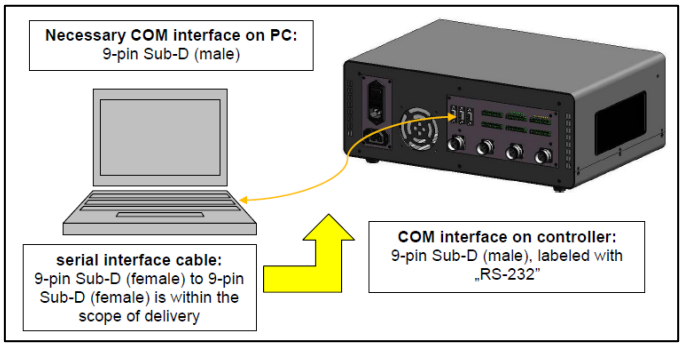

Figure 2-34 Serial connection between iMC-S8 stepper motor controller and computer (source: *https://www.isel.com/en/mwdownloads/download/link/id/4249/*)

At the beginning of the construction of the setup, each traversing unit was initially attached to the jet box (Figure 2-35(a)) and the optical head (Figure 2-35(b)) in order to traverse them in streamwise and radial direction, respectively. However, we later discovered that mounting the optical head on the traversing unit would lead to instability due to wobbling issue on the MV, which is the most sensitive part for acquiring a good and accurate Doppler burst. This may potentially happen when

big measurements are carried out, within which the MV needs to be moved from one position to another along or across the jet, if we do not allow a certain amount of delay for the optical head to become stable, before recording the data. Therefore, to be on the safe side, both traversing units were stacked to each other and attached to the jet box (see Figure 2-36), leaving the optical head fixed to the table. This solution is more reliable since the jet box is heavy enough to assure its stability while being operated.

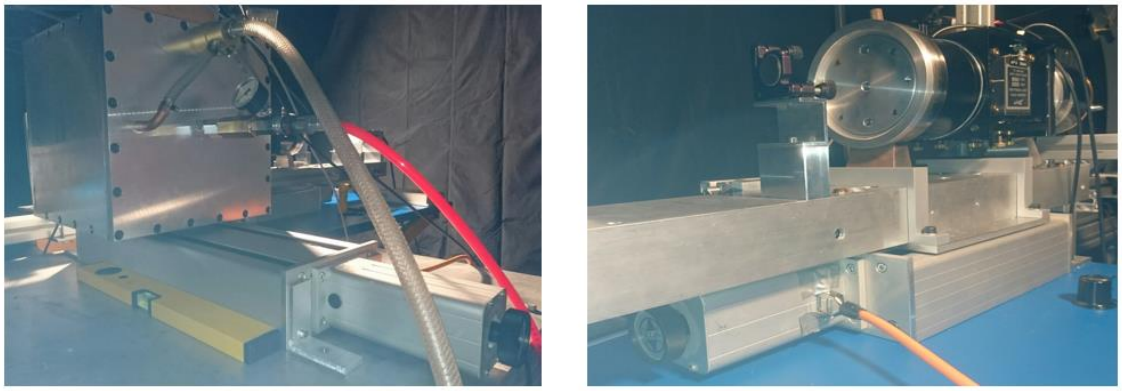

(a) (b)

Figure 2-35: Traversing unit attached to (a) the jet box. (b) the optical head

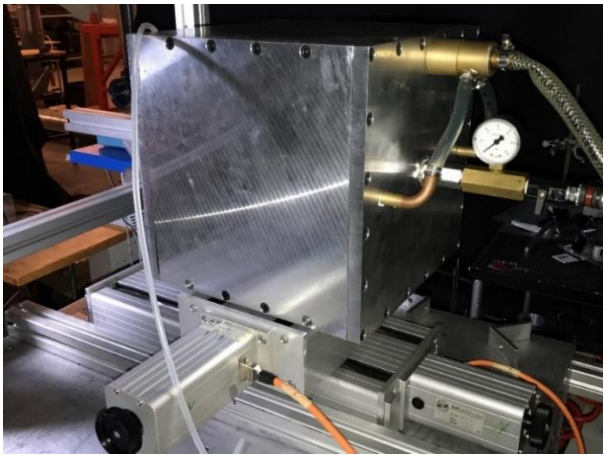

Figure 2-36 Attachment of both traversing units to the jet box

2.3 Overview of Experimental Campaigns

Three different sets of final turbulence measurements have been carried out using the LDA system (Paper I, III, IV, V and VI) and one using the Dantec mini constant temperature anemometer (CTA) system. The measurement points and settings are summarized in Table 2-1. For the convection record method to work correctly, the same setting of PM voltage, laser power, gain in the oscilloscope and sampling parameters must be used for measurements along the same radial direction. A step-by-step procedure with few important tips and cautions in attending the LDA setup for a typical turbulence measurement can be found in the *Cookbook* section in **Appendix III**.

Table 2-1: Summary of turbulence measurements

Paper	Measurement Settings	Link to the processed data
I	exit velocity ≈ 43 m/s (Re ≈ 29000) seeding pressure=1.4 bar PM setting = 60 µA laser power=90% of full power f_{shift}=3 MHz no. of records = 400 Configuration: 45° forward scattering Measurement points and processing parameters are listed in **Appendix VIII(a)**	https://www.dropbox.com/sh/b41fwua4gfq0csj/AADf9t0A0qPx9sLkiDZGwdMta?dl=0
II	Sampling frequency = 10 kHz Sampling time = 10 s Number of samples = 100 kS P_{atm} = 1018.7 hPa Temperature = 21.6°C at 9.30AM Measurement points and data are listed in **Appendix VIII(b)**	https://www.dropbox.com/sh/s4kyr0b3n41jpp2/AAB53xD0qQD8mbcVvctbHkd9a?dl=0
III, IV, and VI	Exit velocity = 35 m/s (Re≈22000) Laser power=full PM setting=60 µA f_{shift}=3 MHz No. of records= 400 records Configuration: 45° forward scattering seeding pressure varies Seeding pressure = (refer **Appendix VIII(c)**) Measurement points and processing parameters are listed in **Appendix VIII(c)**	https://www.dropbox.com/sh/bs5i64bnmocaliq/AAAtuuIhPBD6pvrEMWT2WP_Ya?dl=0
V	Exit velocity = 40 m/s (Re≈25000) Seeding pressure = 1.4 bar Laser power=full PM setting=70µA f_{shift}=3MHz No. of records= 400 records Configuration: 45° forward scattering Measurement points and processing parameters are listed in **Appendix VIII(d)**	https://www.dropbox.com/sh/by8cpgq6xte2usj/AAA1AfiNMvGpURfyDAY3gd4Qa?dl=0

3 Results and Discussions

3.1 Overview of Papers

This chapter summarizes all the scientific findings presented in each paper, which are closely interrelated and attached in the order from the least challenging yet important investigation to the most difficult and central one. Measurement wise, the papers advance from a low to a higher resolution that allow us to obtain higher degree of results towards the end. Several tests and measurements were also done earlier while getting the LDA system to fully work but only those with convincing results are herein reported. It took us almost one and a half years until we obtained a high-quality Doppler signal, from where we decided to go for more thorough data processing and deeper analysis.

Paper I presents a pilot investigation to validate the functionality of our LDA system based on turbulence measurements off the jet axis in the fully developed region (x/D=30), which results are expected to follow the Kolmogorov -5/3 and 2/3 laws. Within the same time frame and experimental conditions, measurements were also performed in the developing counterpart (x/D=10 and x/D=15) in a low resolution yet significant enough to unveil some initial and interesting observations. Throughout the preparation stage of this paper, we also noted down the amount of time needed for measuring the raw data at one measurement point and also for processing it using our developed software. For a statistically significant data, tt took us almost 45 to 60 minutes and 7 to 8 hours of measurement and computation time, respectively.

Knowing the amount of time demanded by our LDA system, preliminary turbulence measurements were conducted using the hot-wire technique, e.g., the Constant Temperature Anemometer (CTA) in Paper II. This classical yet broadly commercialized technique is much faster and straightforward, thanks to its automated calibration. A series of high-resolution measurements were performed off the jet axis in both developing and fully developed regions across the jet, e.g., x/D=10, 15, 20 and 30 to estimate the boundary of the jet with the surrounding air and to identify the high-fluctuation region. Knowing the limitation of the hot-wire technique in high intensity and high shear flow, the results obtained were used only to aid the upcoming high-resolution LDA measurements rather than to describe the actual turbulence phenomena in the jet.

The high-resolution LDA measurements are reported in Paper III, IV and VI. The last of these were written upon completion of Paper III and IV since it requires a deeper look into the governing theory of turbulence especially in the developing region. Paper III, which is just a two-pages extended abstract, is aimed to validate our LDA system but only in a brief way based on the measurements in the fully developed region. Paper IV is the extended version of Paper III describing in detail, the operation and functionality of our LDA system. It emphasizes on the novelties of our system compared to a hardware-driven (commercial) one, supported by a thorough diagnosis of the processed signal.

Paper VI is actually a major extension of the study made earlier in Paper I, covering many more measurement points off the jet axis in a higher resolution, within a downstream range of $5 \leq x/D \leq 30$, e.g., at x/D=5, 10, 15, 20 and 30. The main purpose of this paper is to vigorously test the central

assumptions of Richardson-Kolmogorov's theory in the developing and outermost regions of the jet, which are challenging to measure due to high shear and turbulence intensity. The results presented encompass the radial development of the same and higher order statistics than that of in Paper I, as well as the time and length scales of the turbulence cascade development.

Paper V is aimed to study how the state in the fully developed region is achieved by conducting measurements within the range of $10 \leq x/D \leq 37$ but only along the jet centerline. The region covered is less challenging compared to the shear region yet of significant interest in mapping the energy cascade of the jet centerline. Same statistics are presented similar to those in Paper VI but focusing on the downstream development, which are expected to support our findings in Paper VI.

3.2 Diagnosis of processed signal

The processed signal from both our novel processor and the commercial one is simultaneously diagnosed to evidently highlight the novelties of our processor, which at the same time, overcome the practical limitations suffered by the commercial counterpart. The data acquired from the commercial (hardware-driven) LDA is courtesy of Clara Velte who performed the measurements at 30 jet diameters on an identical jet but with different jet generator (Velte, George, et al. 2014). Results are solely presented and reported in Paper IV, using a simple diagnostic tool for LDA data quality, e.g., the scatter plots.

The misinterpretation of the residence times by the commercial processor and the flexibility of ours are visibly demonstrated by the scatter plot of the instantaneous velocities against their respective residence times as shown in Figure 3-1. Our novel processor is proven to capture much longer residence times at the lowest (almost zero) velocities compared to that of the commercial one. The deficiency by the commercial processor can already been seen in the shear region (see Figure 3-1(a)), and is even pretty more noticeable in the outermost off-axis positions where the abruption occurs at a residence time of 6 times smaller than the longest one detected by our processor, (see Figure 3-1(b)). The poor quality of the low mean velocity is due to the fixed value of the longest measurable burst defined in the commercial hardware, which setting can be flexibly optimized in our software-driven processor.

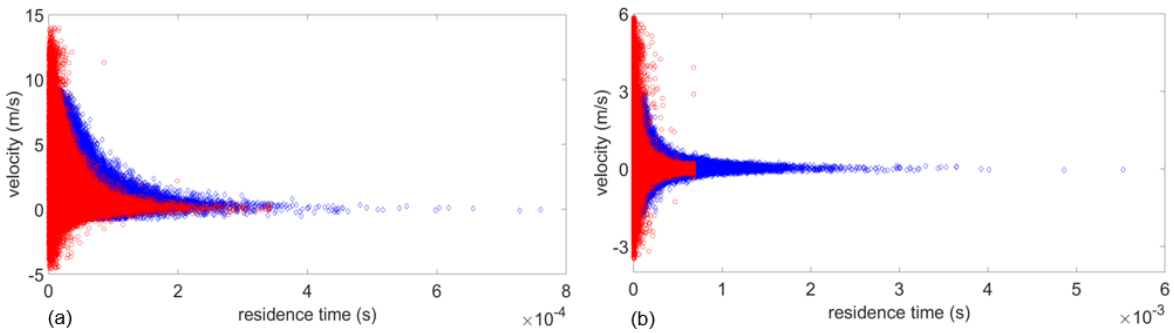

Figure 3-1 Scatter plots of instantaneous velocity vs. residence time for (a) r = 26 and 27 mm, (b) r = 52 and 51 mm. *Red* circle ○: hardware-driven LDA processor, *Blue* diamond ◇: software-driven LDA processor

Meanwhile, the zoomed-in scatter plot of the instantaneous velocities against the difference in arrival time (interarrival time) in Figure 3-2 evidently demonstrates the effect of the digitization (vertical lines) and dead time (separation between lines) in the commercial processor. It shows that the commercial processor suffers from having a finite data transfer rate for each measured burst, which strictly limits the minimum attainable time between measurement. This does not mean that our processor is totally free from the dead time effect caused by the finite measurement volume, which is limited by the optics itself. However, this problem has been significantly minimized by making the processor software based and by reducing the effective size of measurement volume in the forward scattering configuration as previously described in Chapter 2.

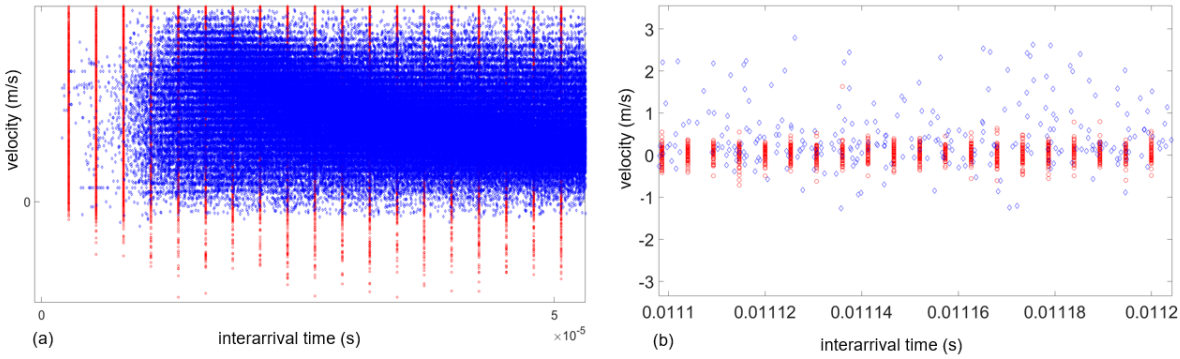

Figure 3-2 A zoom-in of the velocity and interarrival time between neighboring points for (a) r = 26 and 27 mm, (b) r = 52 and 51 mm. *Red* circle ○ : hardware driven LDA processor at r = 52 mm, *Blue* diamond ◇ : software driven LDA processor at r = 51 mm

3.3 Velocity static moments

3.3.1 Mean streamwise velocity

In Paper II, the mean streamwise velocities, $\bar{u}$ presented are computed just by using the simple arithmetic averaging since the measurements were performed using the hot-wire technique. The radial profiles are not normalized or fitted to any polynomial (see Figure 3-3) to retain the direct flow results. Even though the magnitudes can be not as accurate as that of from the LDA measurements, especially in high shear and intensity region, the profiles still seem to follow a nearly Gaussian shape (Hussein et al. 1994), as expected from the theory.

The non-bias values of $\bar{u}$ determined from the residence time weighting (RTW) method in Equation (1.2) are presented in Paper I, IV, V and VI, which profiles are plotted with different curve-fit and normalization approaches. The radial profiles presented in Paper I are fitted with cubic spline interpolation due to the small number of measurement points for the preliminary LDA measurements (see Figure 3-4). Meanwhile, the radial profiles presented in Paper IV and VI, which data are from the same measurements, are fitted with the fifth-order polynomial (see Figure 3-5). The radial distance, r is also normalized with the jet diameter, D, for a fair comparison with the profiles obtained from the previous studies (Ball et al. 2012; Buchhave and Velte 2017b; Fellouah, Ball, and Pollard 2009; Hussein et al. 1994). As expected, each profile tends to follow nearly Gaussian shape with the

maximum velocity at the centerline (r=0) before it spreads out and tapers with downstream development. From the overall profiles, the local (centerline) mean velocity is also maximum at the jet most upstream position.

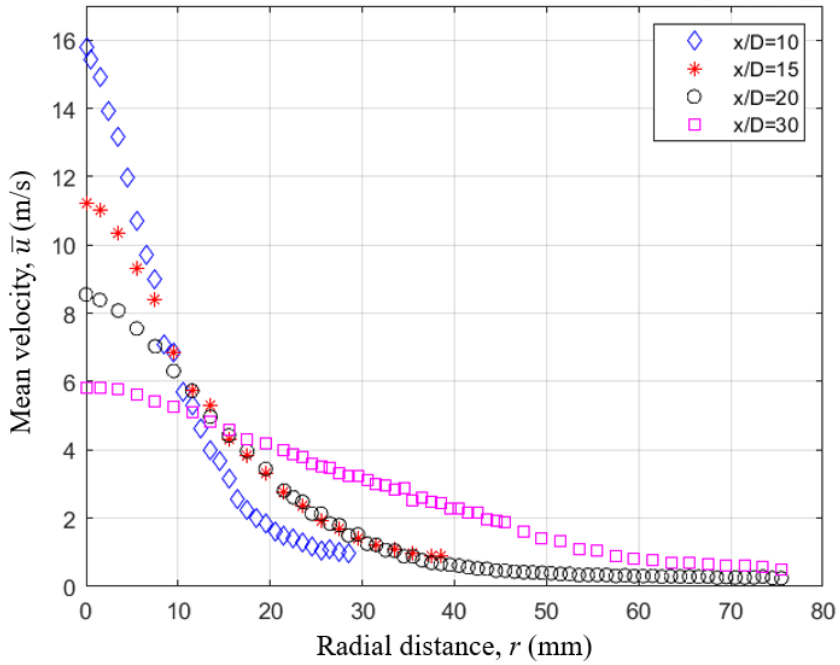

Figure 3-3 Radial profiles of the mean streamwise velocity at different downstream positions *x/D*=10, 15, 20 & 30

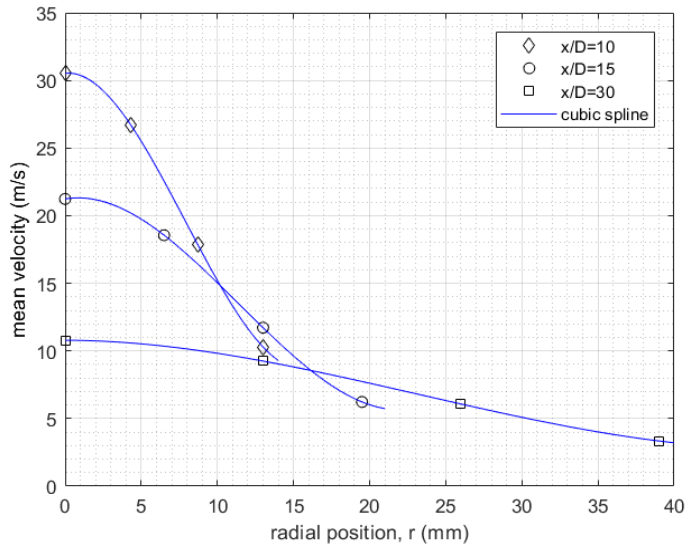

Figure 3-4 Radial profiles of mean streamwise velocity at *x/D*=10, 15 and 30 with cubic spline data interpolation

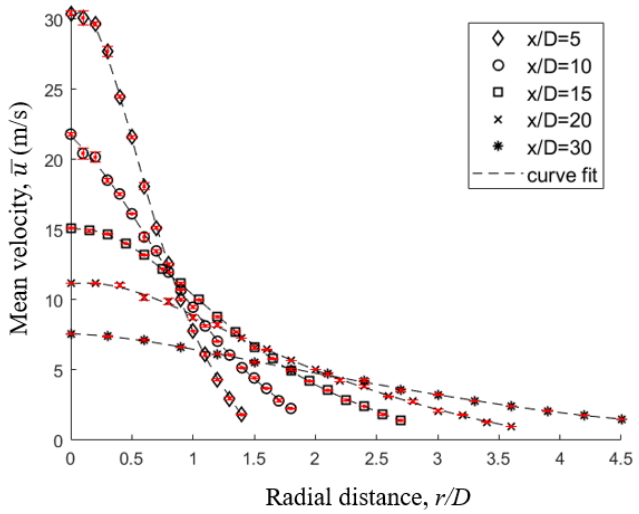

Figure 3-5 Radial profiles of mean streamwise velocity at *x/D*=5, 10, 15, 20 and 30 with fifth-order polynomial curve fits and error bars (in *red*)

Further manipulation on the radial profiles is also done in Paper VI, by normalizing *r* with the downstream distance, *x*, and also $\bar{u}$ with the local mean velocity, U_C, as depicted in Figure 3-6. Except for *x/D*=10, a convincing collapse is observed that agrees well with the previous results presented by (Khashehchi et al. 2013), in which they found the collapse to occur within the same developing jet (near field) range, e.g., at *x/D*=15, 18 and 20. Note that, for this manipulation, the profile for *x/D*=5 is excluded since we believe the flow is still in the laminar region. Same thing applies for velocity variance and turbulence intensity profiles in the following subsections. The slight deviation of the *x/D* =10 profile may be either due to measurement technical reasons (the scales become too small to obtain a fair representation of the energy in the flow) or that the collapse is not valid in that region.

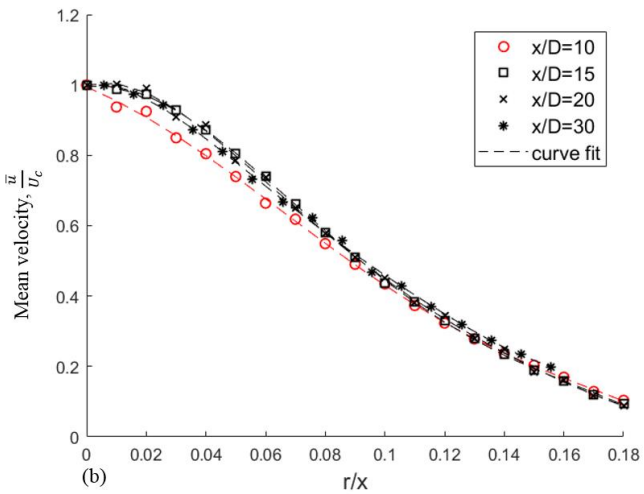

Figure 3-6 Radial profiles of normalized mean streamwise velocity at *x/D*=10, 15, 20 and 30 with fifth-order polynomial curve fits

In Paper V, the downstream profile of the local mean streamwise velocity is fitted with the fourth-order polynomial, in which *x* is normalized by *D* as depicted in Figure 3-7(a). As what has already been observed in Figure 3-4 and Figure 3-5 earlier, and presented in (Grandchamp, Van Hirtum, and

Pelorson 2013), the local mean streamwise velocity decays downstream. With the higher-resolution measurements along the centerline this time, different decay rates are observed between the developing and fully developed regions. A faster decay occurs in the former compared to the latter, as also being observed in (Ball et al. 2012; Fellouah et al. 2009).

To further investigate on this decay, the local mean streamwise velocity is inversely normalized by the jet exit velocity, U_0 as in Figure 3-7 (b). Although this normalization has immediately resulted in a nearly linear behavior, a linear curve fit is made only within the crudely assumed fully developed region, e.g., $20 \leq x/D \leq 37$. Upon extrapolating the linear fit line until it cuts the x-axis, the virtual origin, x_0 is found to be 2.3D. This value and the resulted decay constant, B_u are compared with the values obtained in the previous studies, which are summarized in Table 3-1. While B_u has been shown to be independent to the Reynolds number (S. B. Pope 2000), the small deviations are very likely caused by the different nozzle geometries and measurement techniques applied.

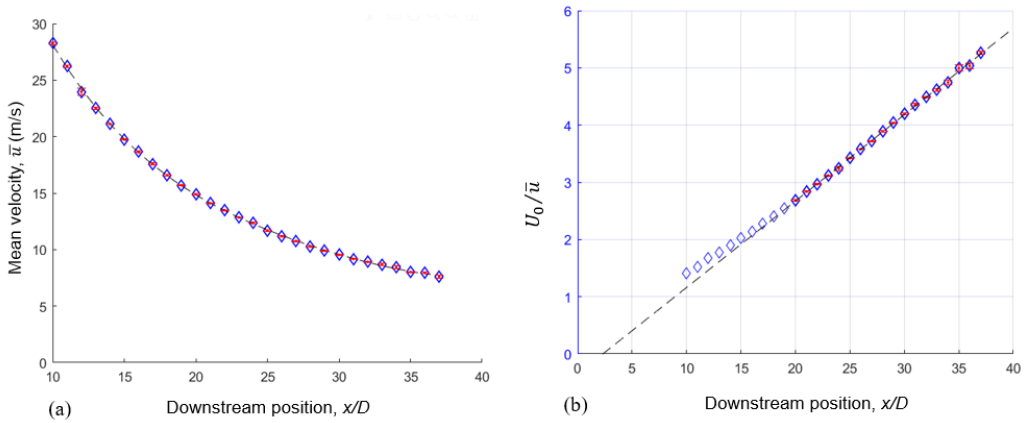

Figure 3-7 Downstream profiles (with error bars) of (a) the local mean streamwise velocity, with fourth-order polynomial curve fit, (b) the normalized inverse of the mean streamwise velocity, with linear fits covering the points within the estimated linear regions. U_0 is the jet exit velocity around 40 m/s.

Table 3-1 Measured round jet mean velocity development parameters

Authors	***Re***	x_0/D	B_u	***x/D***	**Technique**
Present study	25000	2.3	6.6	20-37	LDA
(Weisgraber and Liepmann 1998)	16000	-	6.6	17-27	PIV
(Ferdman, Otugen, and Kim 2000)	24000	2.5	6.7	15-80	Hot-wire
(Hussein et al. 1994)	100000	4	5.8	15-100	LDA
(Hodzic 2014)	20000	3.1	5.9	30-105	PIV
(Panchapakesan N. R. and Lumley 1993)	11000	-	6.06	30-160	Hot-wire

3.3.2 Velocity variance

Similar for $\bar{u}$, the velocity variance, $\overline{u^2}$ of the LDA measurements is also computed using the RTW method as in Equation (1.3), which profiles are also plotted and fitted in the same way as for the corresponding mean velocity counterpart in Paper I, IV, V and VI. The cubic spline interpolations of the radial profiles from Paper I are depicted in Figure 3-8, showing a crude visualization of the variance development across the shear layer of the jet.

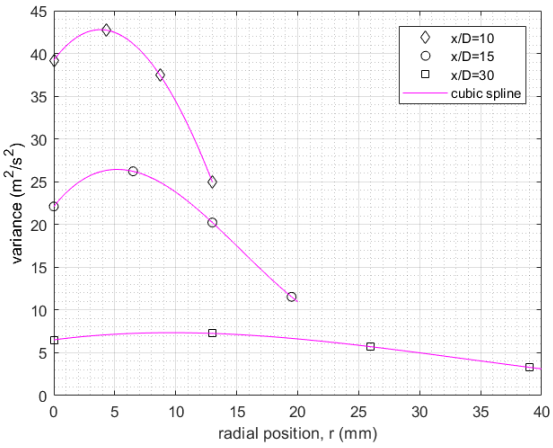

Figure 3-8 Radial profiles of velocity variance at *x/D* = 10, 15 and 30 with cubic spline data interpolation

The fifth-order polynomials of the radial profiles from Paper IV and VI are shown in Figure 3-9, which exhibit the same yet more defined development of the velocity variance across the shear layer. The peak is most dominant at *x/D*=5 before the profiles spread and taper with the downstream development. It demonstrates that the shear region becomes wider with the spreading of the jet downstream, centering at the point where the variance is peaking. The radial profiles in Paper VI (except for *x/D*=5) are then normalized with the local velocity variance, $\overline{u^2}_C$, as depicted in Figure 3-10. Similar to the case for the mean velocity, the profile at *x/D*=10 is the most unlikely to collapse while for the rest, the collapse is more dominant at larger radial positions.

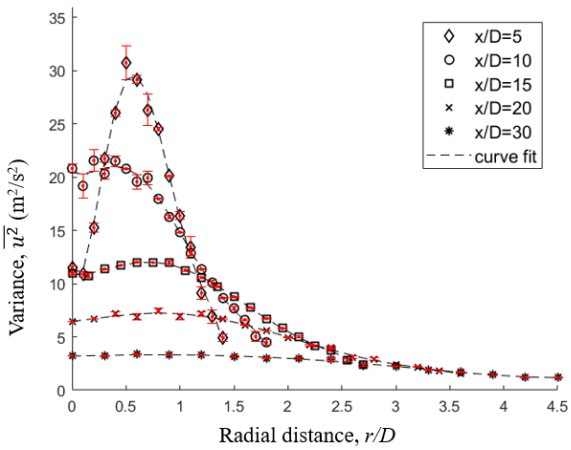

Figure 3-9 Radial profiles of velocity variance at *x/D*=5, 10, 15, 20 and 30 with fifth-order polynomial curve fits and error bars (in red)

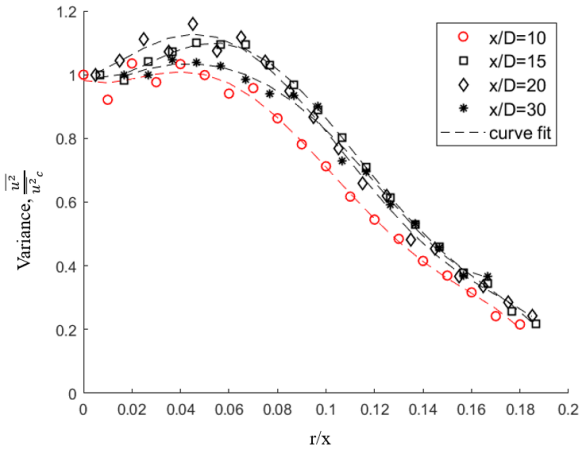

Figure 3-10 Radial profiles of normalized velocity variance at *x/D*=10, 15, 20 and 30 with fifth-order polynomial curve fits

In Paper V, the downstream profile of the velocity variance (see Figure 3-11(a)) is fitted in the same way as for the corresponding mean streamwise velocity. It also exhibits an inversely proportional development with the downstream distance. The profile is further inversely normalized by the square of U_0 as in Figure 3-11(b). In this case, the corresponding range for the linear self-preserving region only starts from *x/D*=24 onwards, which is a bit shorter than that of for the mean velocity. On top of this, the normalized inverse of the RMS velocity is also plotted with the linear self-preserving region of *x/D*≥20 (see Figure 3-11(c)). Upon extrapolation, the linear fit lines intercept at *x/D*=15.6 and 1.27 for the normalized inversed of the velocity variance and RMS velocity, respectively.

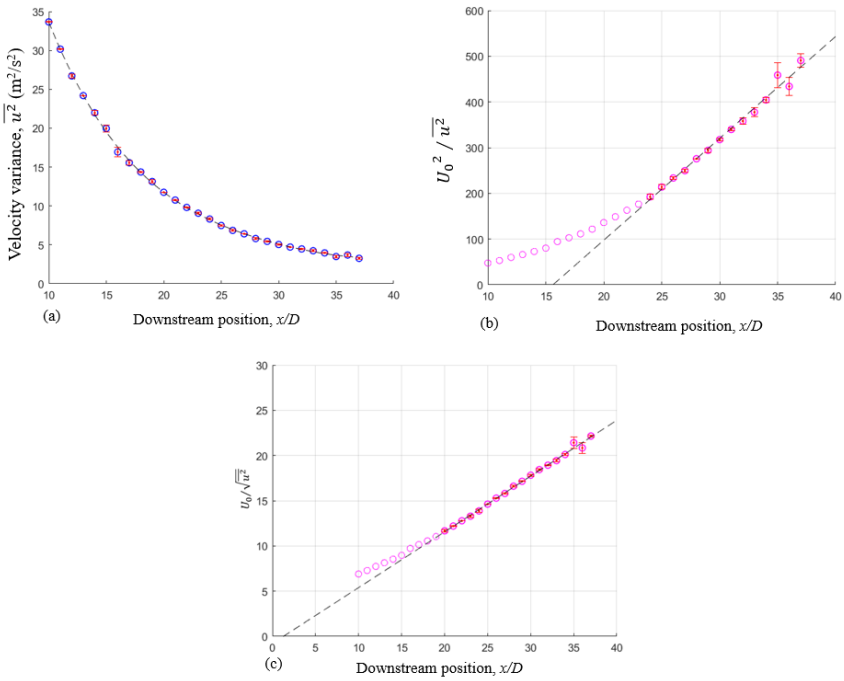

Figure 3-11 Downstream profiles (with error bars) of (a) the local velocity variance, with fourth-order polynomial curve fit, (b) the normalized inverse of the velocity variance, with linear fit covering the range of *x/D*≥24, (c) the normalized inverse of the RMS velocity , with linear fit covering the range of *x/D*≥20. U_0 is the jet exit velocity around 40 m/s.

3.3.3 Turbulence intensity

Despite having different empirical definitions, turbulence intensity basically represents the level of the velocity fluctuation in a flow in relation to the average velocity. Plotting both radial and downstream profiles of the streamwise turbulence intensity gives us a comprehensive overview on the velocity fluctuation in our jet flow. In Paper II, the radial profiles are first plotted (see Figure 3-12) from the hot-wire measurements at different downstream positions. To recall, these measurements were aimed to identify the regions of interest for the next LDA measurements, which is why the profiles do not go through any normalization or curve fitting. The profiles also provide only a crude description of turbulence especially in the shear region where velocity fluctuations dominate the streamwise convection. This approximation is, however, more acceptable outside the shear region where the fluctuations are dominated by the larger streamwise convection. From the profiles, the buildup of the turbulence intensity in the shear region highlights the need of having a suitable frequency shift (Buchhave 1984) in our LDA measurements in order to establish a highly accurate turbulence measurements especially in the high fluctuations region.

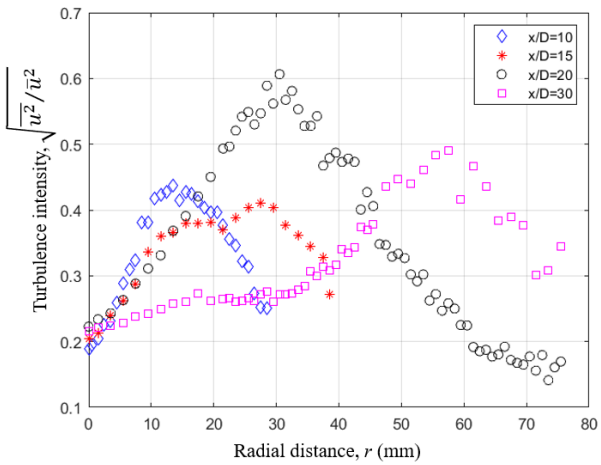

Figure 3-12 Radial profiles of streamwise turbulence intensity at *x/D*=10, 15, 20 and 30

The more rigorous measurements in Paper VI provide a more accurate description of turbulence from the resulted radial profiles plotted in Figure 3-13, with *r* being normalized by *D* on the horizontal axis. The measurements span from the laminar jet core, *x/D*=5, up to the fully developed region, *x/D*=30. The turbulence intensities are significantly lower at the jet core due to the early turbulence measurements. However, the buildup rate in this region is higher than that of in the downstream direction. These convincing profiles evidently demonstrate the robustness and capability of our software-driven LDA, which is uniquely suited for measurements in the challenging regions, e.g., outer part of the jet with limited dynamic range and shear region with high turbulence intensity. The results therefore validate the advantages of our LDA system over the hot-wire and PIV technique as discussed in Chapter 1.

Except for *x/D*=5, the radial profiles are replotted by normalizing *r* with the downstream distance, *x* as depicted in Figure 3-14. Compared to the centerline region, turbulence intensities in the shear layer counterpart are in general higher due to the highly energetic large turbulence structures generated by the mixing layer (Fellouah et al. 2009). A convincing collapse is also observed among the profiles

for the more downstream position i.e., *x/D*=15, 20 and 30, which is in good agreement with the results presented by (Panchapakesan N. R. and Lumley 1993; Wänström, George, and Meyer 2012). It is even more surprising in our case that, even the profile for *x/D*=10 seems to nearly collapse with the rest too.

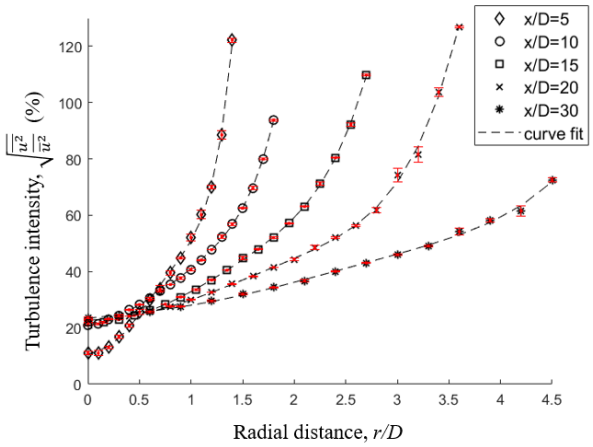

Figure 3-13 Radial profiles of streamwise turbulence intensity at *x/D*=5, 10, 15, 20 and 30, with fifth-order polynomial curve fits and error bars (in *red*)

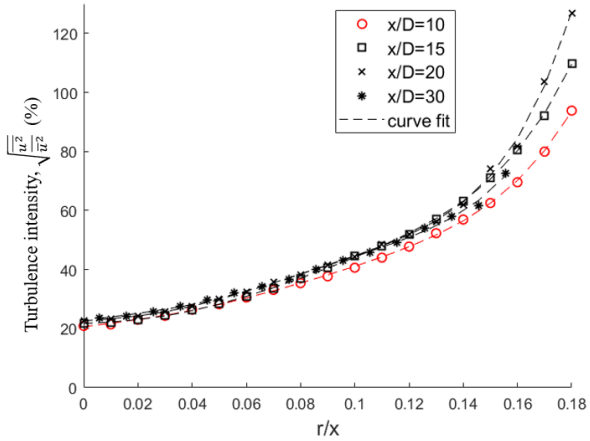

Figure 3-14 Radial profiles of the normalized streamwise turbulence intensity at *x/D*=10, 15, 20 and 30, with fifth-order polynomial curve fits

The downstream profile of the streamwise intensity presented in Paper V is shown in Figure 3-15, which is in term of the ratio between the RMS and the mean velocities. The significant buildup observed in the developing region (from 10 to around 15 jet diameters) is caused by the progressively larger influence of the large scale Kelvin-Helmholtz instability development in the shear layer (Ball et al. 2012; Fellouah et al. 2009). From here, the turbulence intensity continues to rise gradually before it asymptotes to a nominal value of around 0.23 in the fully developed region, which agrees well with most of the previous findings accumulated by (Mi et al. 2001).This asymptotic behavior is also assumed to remain further downstream (Kassab et al. 1996) based on the known similarity scalings provided by (Hodzic 2019) for the fully developed turbulent round jet.

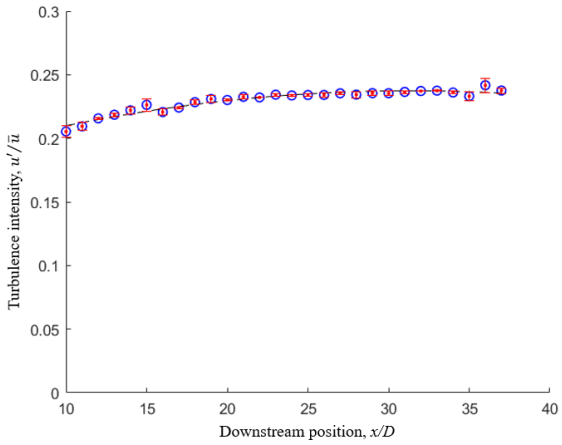

Figure 3-15 The downstream development of the streamwise turbulence intensity

3.4 Spatial kinetic energy spectrum

Velocity power spectrum, or herein referred as kinetic energy spectrum is an essential tool in turbulence research, which maps the energy across all the turbulence scales and provides information about the generation and development of turbulence. With the acquirement of our LDA measurements in time records, a corresponding temporal energy spectrum may display unfaithful distribution of the spatial scales due to the convection effect from the velocity fluctuations of the large scale (Lumley 1965). The energy spectra presented in our papers are therefore computed and plotted in the spatial or wave number, k-domain, where $k=2\pi/\lambda$. These spectra cater more comprehensive information on the spatial turbulence structure that is of the great interest in turbulence theory and modelling. It describes the distribution of spatial scales as well as the evolution from the larger scales to the smaller ones. Moreover, the -5/3 slope from the Kolmogorov power law is well predicted in the spatial spectra rather in the temporal ones (S. Pope 2000). To obtain a fairer comparison with this -5/3 slope, each spectrum in the the papers is deliberately normalized to 1 in the low wave number asymptote.

The radial developments of the spatial kinetic energy spectra for the fully developed region are first plotted in Paper I (see Figure 3-16(a)) to initially investigate the -5/3 power law and later to study the distribution of spatial velocity structures across the jet. As expected, and also previously being observed in (Buchhave and Velte 2015, 2017a, 2017b; Velte, Buchhave, et al. 2014; Velte et al. 2017), each spectrum in the fully developed region exhibits a clear -5/3 slope across a significant range. This observation indicates the possibility of local turbulence equilibrium in the (assumed) inertial subrange in the fully developed region, according to the central, yet implicit assumption of Kolmogorov's local equilibrium of the small scales (Batchelor 1953). Similar observation is obtained in the spectra computed and plotted from the other higher-resolution measurements at the same downstream position as reported in Paper IV and VI (see Figure 3-16(b)), which essentially helps in validating the equilibrium solution postulated by Kolmogorov and Batchelor. The spectra from both measurements also show a convincing collapse, which indicate a nearly equal distribution of turbulent kinetic energy across the scales, regardless of the jet off-axis positions. This consistency has made us to believe that

the second-order moments of turbulence have finally reached a state of self-similarity in this fully developed region.

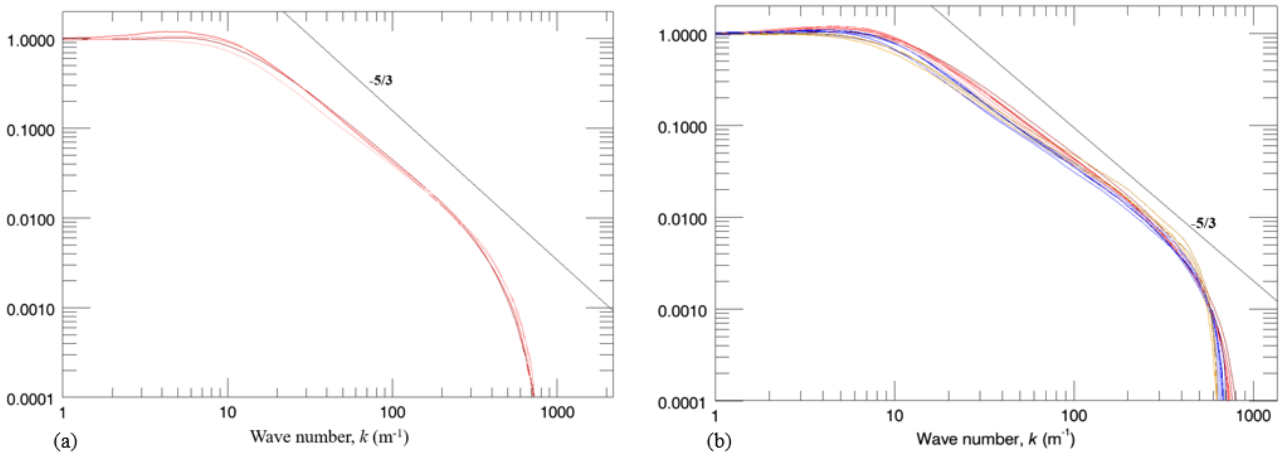

Figure 3-16 Radial developments of spatial kinetic energy spectra at *x/D*=30 as presented in (a) Paper I. From *heavy to light red*: *r/D*=0, 1.3, 2.6, 3.9 (b) Paper IV and VI. From *heavy to light red*: *r/D* = 0, 0.3, 0.6, 0.9, 1.2, 1.5. From *heavy to light blue*: *r/D* = 1.8, 2.1, 2.4, 2.7, 3, 3.3, 3.6. From *heavy to light brown*: *r/D* = 3.9, 4.2, 4.5.

In Paper VI, the radial developments at *x/D*=20 is also plotted (Figure 3-17) that surprisingly shows a good tendency for the spectra to already follow the -5/3 slope, yet within a narrower range since the jet is still not completely developed. The convincing collapse also appears to agree with our previous finding from the downstream profile of the normalized inverse of the local mean streamwise velocity as in Figure 3-7(a), through which the linear self-preserving region also starts from *x/D*=20 onwards.

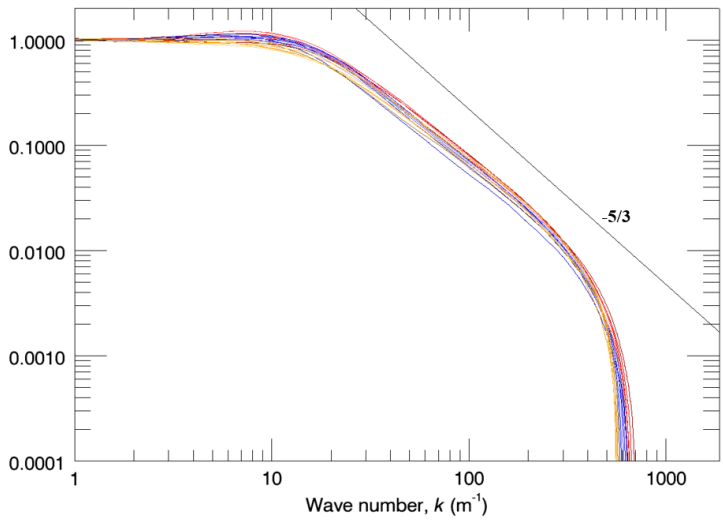

Figure 3-17 Radial developments of spatial kinetic energy spectra at *x/D*=20. From *heavy to light red*: *r/D* = 0, 0.2, 0.4, 0.6, 0.8, 1. From *heavy to light blue*: *r/D* = 1.2, 1.4, 1.6, 1.8, 2, 2.2, 2.4. From *heavy to light brown*: *r/D* = 2.6, 2.8, 3, 3.2, 3.4, 3.6

The radial developments for the more upstream measurement positions, or the developing region, e.g., *x/D*=10 and 15, are presented in Paper I and Paper VI, from the two different series of

measurements (see Figure 3-18). The variation in the shape of the spectra in this region shows that the spatial velocity structures are variously distributed along the radial direction and also downstream direction. At the higher wave number, the lowest tendency to follow the -5/3 slope is spotted at *x/D*=10 as in Figure 3-18(c) and (d), which indicates the invalidity of the local equilibrium assumption in the jet developing region. From the higher-resolution measurements in Paper VI, a clear shift from high to lower wave numbers with increasing radial distance is observed (denoted by the arrow in Figure 3-18(b) and (d)), which illustrates the growth of the smallest scales away from the jet exit.

The radial developments for the most upstream measurement position, e.g., *x/D*=5, is presented in Paper VI as depicted in Figure 3-19. A bump is spotted at around 800 Hz, which is suspected to result from the periodic shedding of vortex rings leading up to the Kelvin Helmholtz shear layer instability (Danaila, Jan, and Anselmet 1997). This effect is however coherent only for a short time before the vortex rings merge and lose their stability, which explains the gradual disappearance of the bump as the measurements progress further away from jet exit (see Figure 3-20) and also the jet centerline (see Figure 3-19). Based on the frequency where the bump occurs, the corresponding Strouhal number is found to be 0.25, which agrees well with the range of preferred mode for operating an axisymmetric turbulent jet, i.e., from 0.24 to 0.64 (Gutmark 1983).

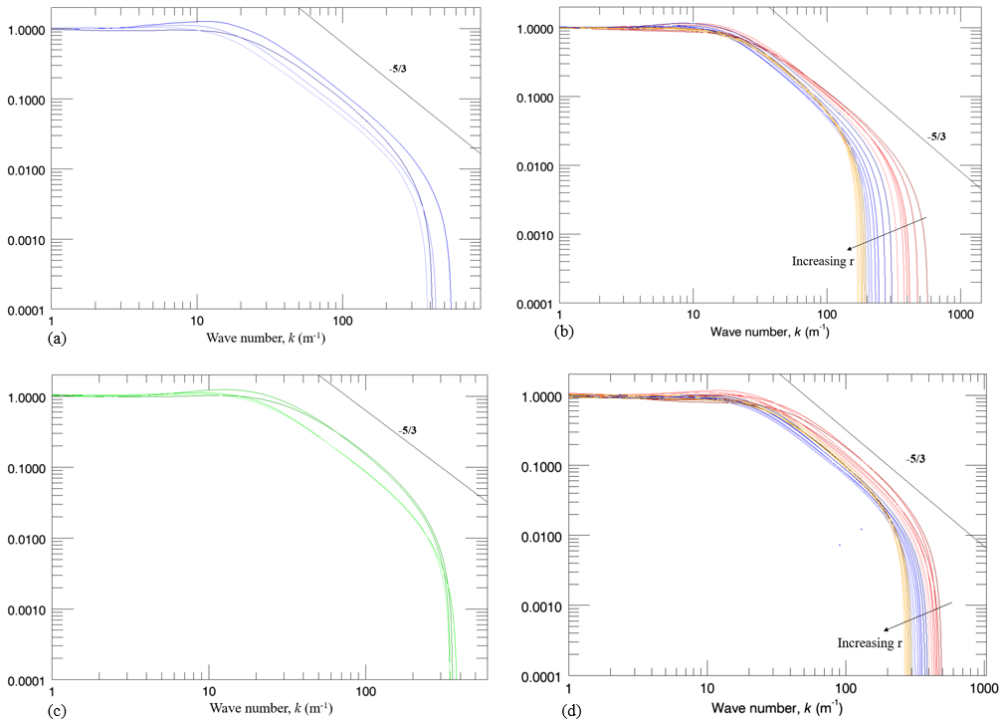

Figure 3-18 Radial developments of spatial kinetic energy spectra at (a) *x/D*=15 from Paper I. From *heavy to light blue*: *r/D*=0, 0.65, 1.3, 1.95 (b) *x/D*=15 from Paper VI. From *heavy to light red*: *r/D*=0, 0.15, 0.3, 0.45, 0.6, 0.75. From *heavy to light blue*: *r/D*=0.9, 1.05, 1.2, 1.35, 1.5, 1.65, 1.8. From *heavy to light brown*: *r/D*=1.95, 2.1, 2.25, 2.4, 2.55, 2.7 (c) *x/D*=10 from Paper I. *From heavy to light green*: *r/D*= 0, 0.43, 0.87, 1.3 (d) *x/D*=10 from Paper VI. From *heavy to light red*: *r/D*=0, 0.1, 0.2, 0.3, 0.4, 0.5, 0.6. From *heavy to light blue*: *r/D*=0.7, 0.8, 0.9, 1, 1.1, 1.2, 1.3. From *heavy to light brown*: *r/D*=1.4, 1.5, 1.6, 1.7, 1.8

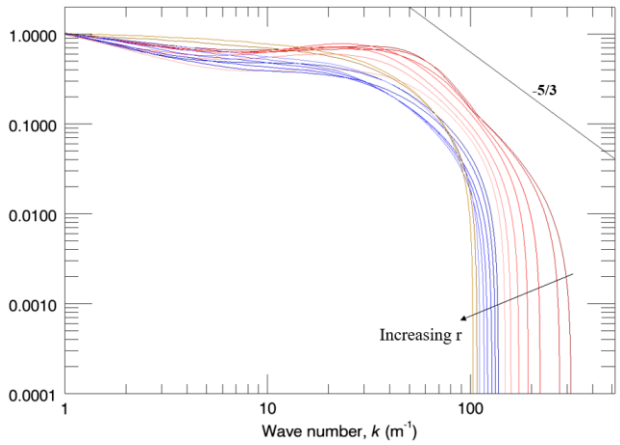

Figure 3-19 Radial developments of spatial kinetic energy spectra at *x/D*=5. From *heavy to light red*: *r/D*=0, 0.1, 0.2, 0.3, 0.4, 0.5, 0.6. From *heavy to light blue*: *r/D*=0.7, 0.8, 0.9, 1, 1.1, 1.2. From *heavy to light brown*: *r/D*=1.3, 1.4.

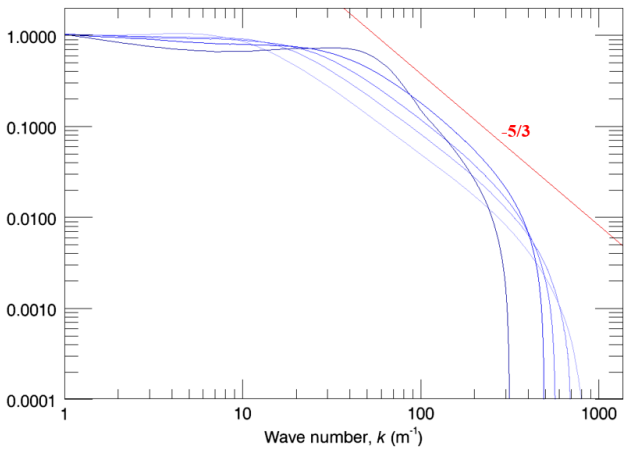

Figure 3-20 Downstream development of spatial turbulent kinetic energy spectra along the centerline (*r/D*=0) downstream. From *heavy to light blue*: *x/D*=5, 10, 15, 20, 30.

From the downstream developments depicted in Figure 3-20, a more rigorous version is presented in Paper V from the centerline turbulence measurements (see Figure 3-21). Again, as expected, the (assumed) inertial subrange is wider in the fully developed region (Batchelor 1953). A clear transition from a remarkable steep deviation is also observed from the developing region towards the fully developed counterpart (at $25 \leq x/D \leq 37$) where the spectra significantly resemble the -5/3 slope (Gibson 1962). The possibility of local equilibrium in the fully developed region is again herein indicated (Batchelor 1953), but it should be noted that this observation is based on averaged statistics.

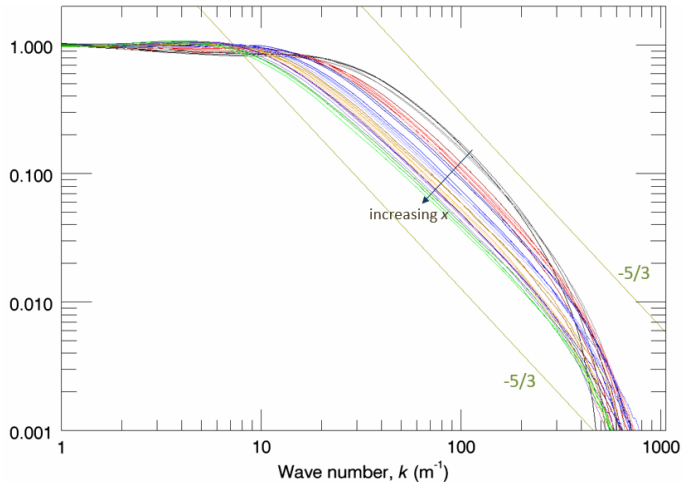

Figure 3-21 Downstream development of spatial turbulent kinetic energy spectra along the jet centerline. From *heavy to light black*: *x/D*=10, 11, 12, 13. From *heavy to light red*: *x/D*=14, 15, 16, 17, 18, 19. From *heavy to light blue*: *x/D*=20, 21, 22, 23, 24, 25. From *heavy to light brown*: *x/D*=26, 27, 28, 29, 30. From *heavy to light purple*: *x/D*=31, 32, 33, 34. From heavy to light green: *x/D*=35, 36, 37

3.5 Spatial second-order structure function

The spatial second-order structure function, S_2 is a useful tool in quantifying the turbulence scales based on the square of the velocity increment, which emphasizes the scales effect of the order of the separation, ℓ_s along the spatial records. Its empirical definition is given by

$$S_2(\ell_s) = \langle(\bar{u}(s+\ell_s) - \bar{u}(s))^2\rangle \tag{3.1}$$

where the < >-brackets denote ensemble averaging. The S_2 functions presented in Paper I, V and VI are all based on the convection record principle as described in Chapter 1. Each curve is shifted vertically at the small separation region for a clear comparison on the shape of the scales development.

The S_2 functions are first computed and plotted in Paper I (see Figure 3-22) for different off-axis positions to initially investigate the Kolmogorov 2/3 power law in the fully developed as well as the developing region. The greatest tendency for the S_2 functions to follow the expected 2/3 slope is observed in the fully developed region, i.e., at *x/D*=30 (Danaila et al. 2002; Frisch 1995; Romano and Antonia 2001). Meanwhile, significant deviations from the 2/3 slope are observed in the developing region, with the most dominant one occurs at the most upstream position, i.e., *x/D*=10. The lower slope in this region indicates that the large velocity increments is yet to be produced by the cascade process. Similar yet more significant observation is illustrated in Figure 3-23, for the S_2 functions resulted from the higher-resolution measurements as in Paper VI. The range within which each curve well approximates the 2/3 slope is observed to become larger in the downstream direction. Similar bump is also noticed at *x/D*=5 as what has been found in the corresponding energy spectra earlier.

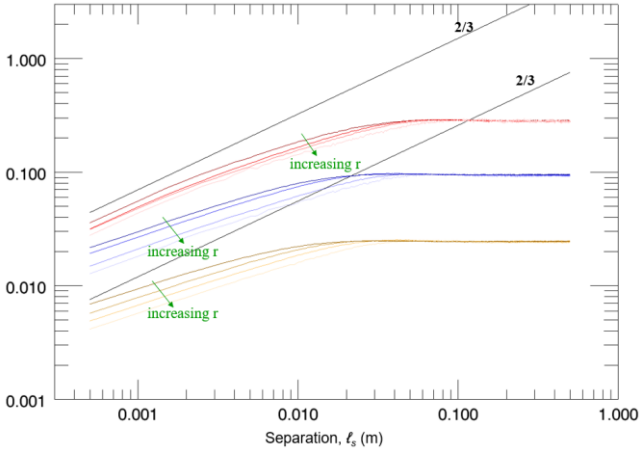

Figure 3-22 Second-order spatial structure functions variations with radial distance. From *heavy to light red*, *x/D*=30: 0, 1.3, 2.6, 3.9. From *heavy to light blue*, *x/D*=15: 0, 0.65, 1.3, 1.95. From *heavy to light brown*, *x/D*=10: 0, 0.43, 0.87, 1.3. Curves of the same downstream position, *x/D*, are shifted vertically at the small separation region to clearly differentiate the shape of the scales development.

As what goes by its definition, a lot of valuable information of the turbulence scales can be retrieved from the S_2 functions. Each curve demonstrates that most of the energy is dominated by the large scales and more large-scale activity is also relatively noticed in the outer part of the jet compared to in the centerline. The scales grow as they progress away from the jet exit, as denoted by the arrow in Figure 3-24 and Figure 3-25. The width of the variations in the small scales grows with the downstream position, corresponding to the development in the spectra as shown earlier in Figure 3-20 and Figure 3-21.

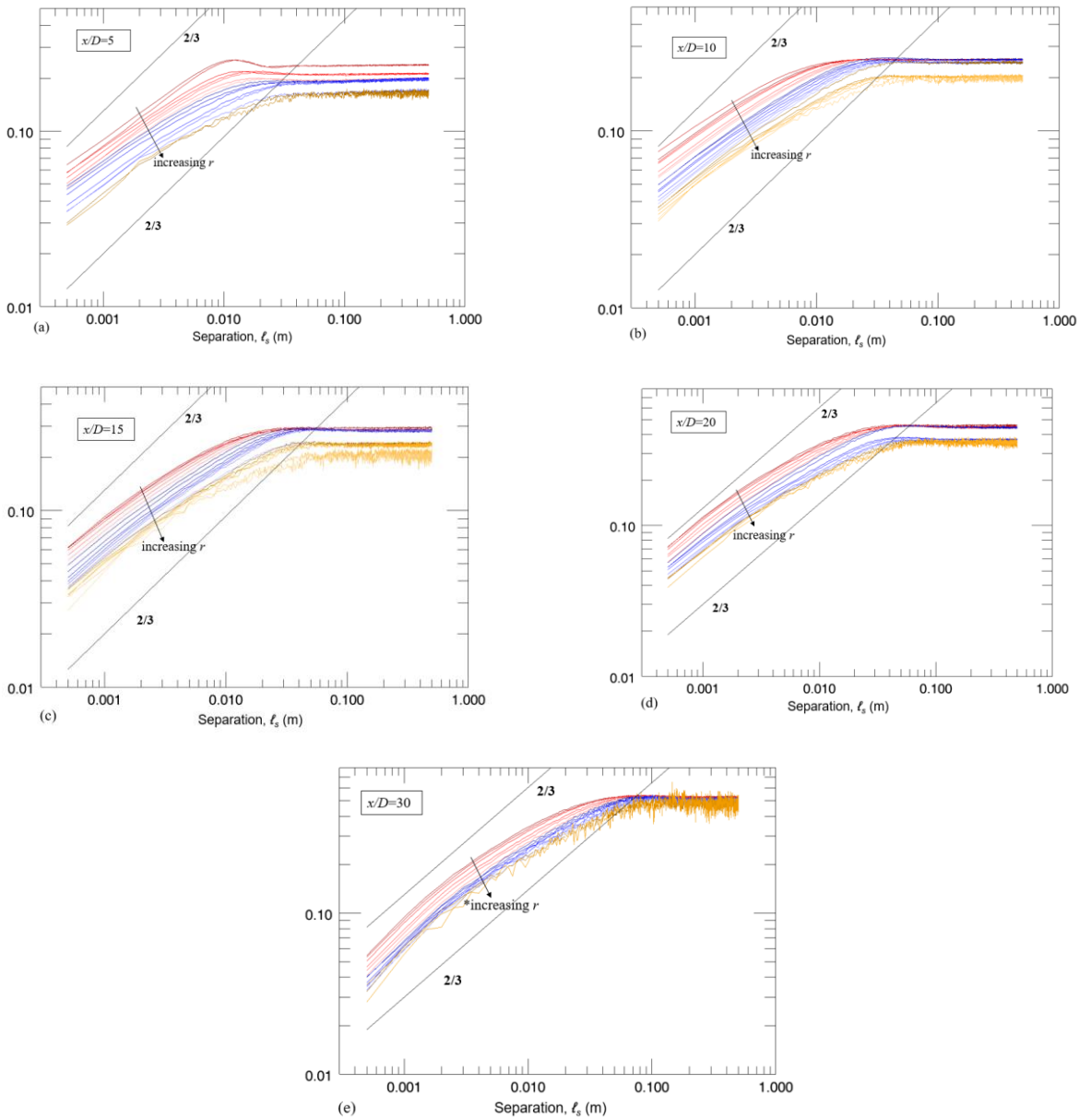

Figure 3-23 Second-order spatial structure functions variations with radial distance at: (a) *x/D*=5. From *heavy to light red*: *r/D*=0, 0.1, 0.2, 0.3, 0.4, 0.5, 0.6. From *heavy to light blue*: *r/D*=0.7, 0.8, 0.9, 1, 1.1, 1.2. From *heavy to light brown*: *r/D*=1.3, 1.4. (b) *x/D*=10. From *heavy to light red*: *r/D*=0, 0.1, 0.2, 0.3, 0.4, 0.5, 0.6. From *heavy to light blue*: *r/D*=0.7, 0.8, 0.9, 1, 1.1, 1.2, 1.3. From *heavy to light brown*: *r/D*=1.4, 1.5, 1.6, 1.7, 1.8 (c) *x/D*=15. From *heavy to light red*: *r/D*=0, 0.15, 0.3, 0.45, 0.6, 0.75. From *heavy to light blue*: *r/D*=0.9, 1.05, 1.2, 1.35, 1.5, 1.65, 1.8. From *heavy to light brown*: *r/D*=1.95, 2.1, 2.25, 2.4, 2.55, 2.7 (d) *x/D*=20. From heavy to light red: *r/D*=0, 0.2, 0.4, 0.6, 0.8, 1. From *heavy to light blue*: *r/D*=1.2, 1.4, 1.6, 1.8, 2, 2.2, 2.4. From *heavy to light brown*: *r/D*=2.6, 2.8, 3, 3.2. (e) *x/D*=30. From *heavy to light red*: *r/D*=0, 0.3, 0.6, 0.9, 1.2, 1.5. From *heavy to light blue*: *r/D*=1.8, 2.1, 2.4, 2.7, 3, 3.3, 3.6. From *heavy to light brown*: *r/D*=3.9, 4.2, 4.5. Each curve is shifted vertically at the small separation region to clearly differentiate the shape of the scales development (also in the next two following figures). *Note that the arrow indicating the increment of radial distance, *r*, is not applicable for the two outermost points due to high variation in the plots.

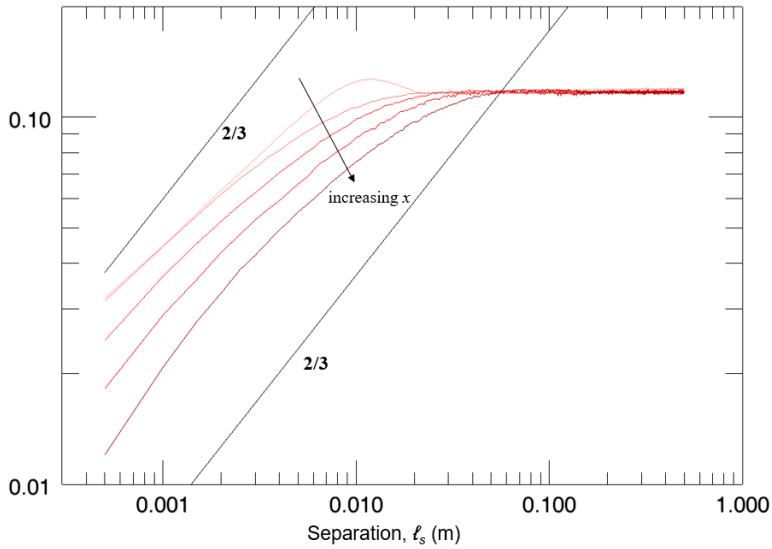

Figure 3-24 Downstream development of the second-order spatial structure functions along the jet centerline (*r*/*D*=0). From *heavy to light red*: *x*/*D*=30, 20, 15, 10, 5

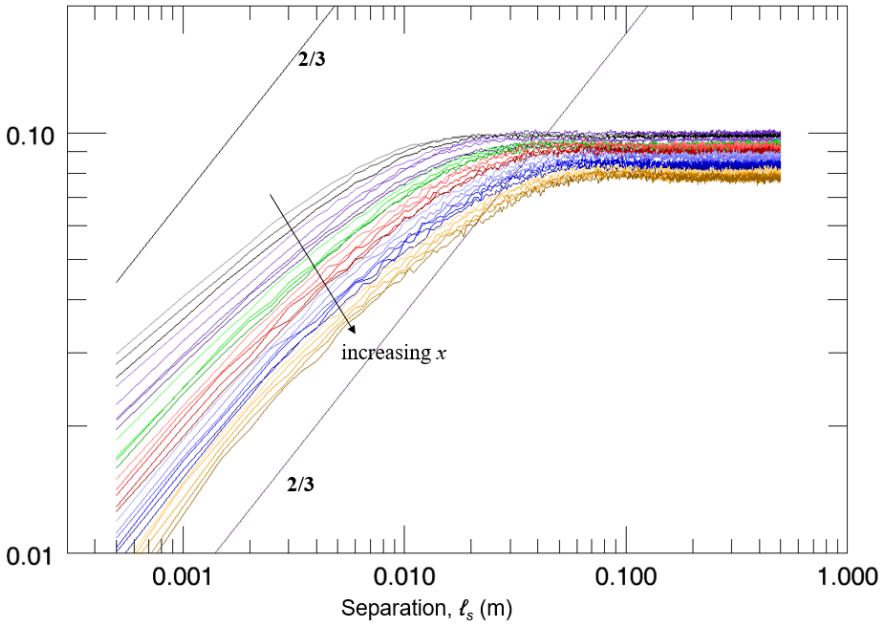

Figure 3-25 Spatial second-order structure functions for different downstream positions retrieved from Paper V. From *heavy to light brown*: *x*/*D*=37, 36, 35, 34, 33. From *heavy to light blue*: *x*/*D*=32, 31, 30, 29, 28, 27. From *heavy to light red*: *x*/*D*=26, 25, 24, 23, 22. From *heavy to light green*: *x*/*D*=21, 20, 19, 18. From *heavy to light purple*: *x*/*D*=17, 16, 15, 14, 13. From *heavy to light black*: *x*/*D*=12, 11, 10.

3.6 Spatial third-order structure function

Just like the lower order counterpart, the spatial third-order structure function, S_3 is also based on the velocity increment but in the third order, as a function of the spatial separation, ℓ_s, given by

$$S_3(\ell_s) = \langle(\bar{u}(s+\ell_s) - \bar{u}(s))^3\rangle \tag{3.2}$$

It is strongly associated with the Kolmogorov 4/5 law (Frisch 1995), which is given by

$$S_3(\ell_s) \sim -\frac{4}{5}\varepsilon\ell_s \tag{3.3}$$

where ε is the mean energy dissipation rate per unit mass. This reduced formula can be derived from the Navier-Stokes equation if these underlying assumptions are being implemented; that the flow must be locally equilibrium, locally homogeneous and isotropic (McDonough 2007).

The S_3 functions presented in Paper V and VI are also computed after employing the convection record principle and depicted in

Figure *3-26*, Figure 3-27 and Figure 3-28. The first two of these shows the S_3 functions for each off-axis position only at *x/D*=30 and 20, respectively. Although these could certainly not be credible in the more upstream region, the S_3 functions for *x/D*=15 and 10 are nevertheless attached in Appendix II and III of Paper VI, respectively. Meanwhile, Figure 3-28 represents S_3 function only at *x/D*=28 (centerline), while the rest , e.g., *x/D*=20, 21, 22 and so on, can be found in Appendix I of Paper V but only for 20≤*x/D*≤37.

Along with each S_3 function, a straight line having the 4/5 slope is also plotted for a direct comparison to the Kolmogorov 4/5 law. Note that the slope in this case is positive since the negative sign has been cancelled out by the ε. The S_3 functions are observed to follow the 4/5 slope at the lower separation region, as expected at *x/D*=30, which is in a good agreement with the simulation work by (Boratav and Pelz 1997). A significant tendency is also observed for the S_3 functions up to *x/D*=20, which agrees with the observation by (Van De Water and Herweijer 1999) in their turbulent round jet measurements at *x/D*=22.

A horizontal line tangent to S_3 function is drawn to intersect with the 4/5 slope in selected downstream positions of the centerline measurements (see Figure 3-29). The break in the curves is observed to occur at larger ℓ_s as the measurement progress away from the jet exit, which indicates that there are more large structures in the downstream region. Similar observation is also found at the centerline positions of *x/D*=10, 15, 20 and 30 in Paper VI (see Figure 3-30), excluding the plot at *x/D*=5 since we believe that the flow is still laminar at this region and therefore not possible to fit the 4/5 slope.

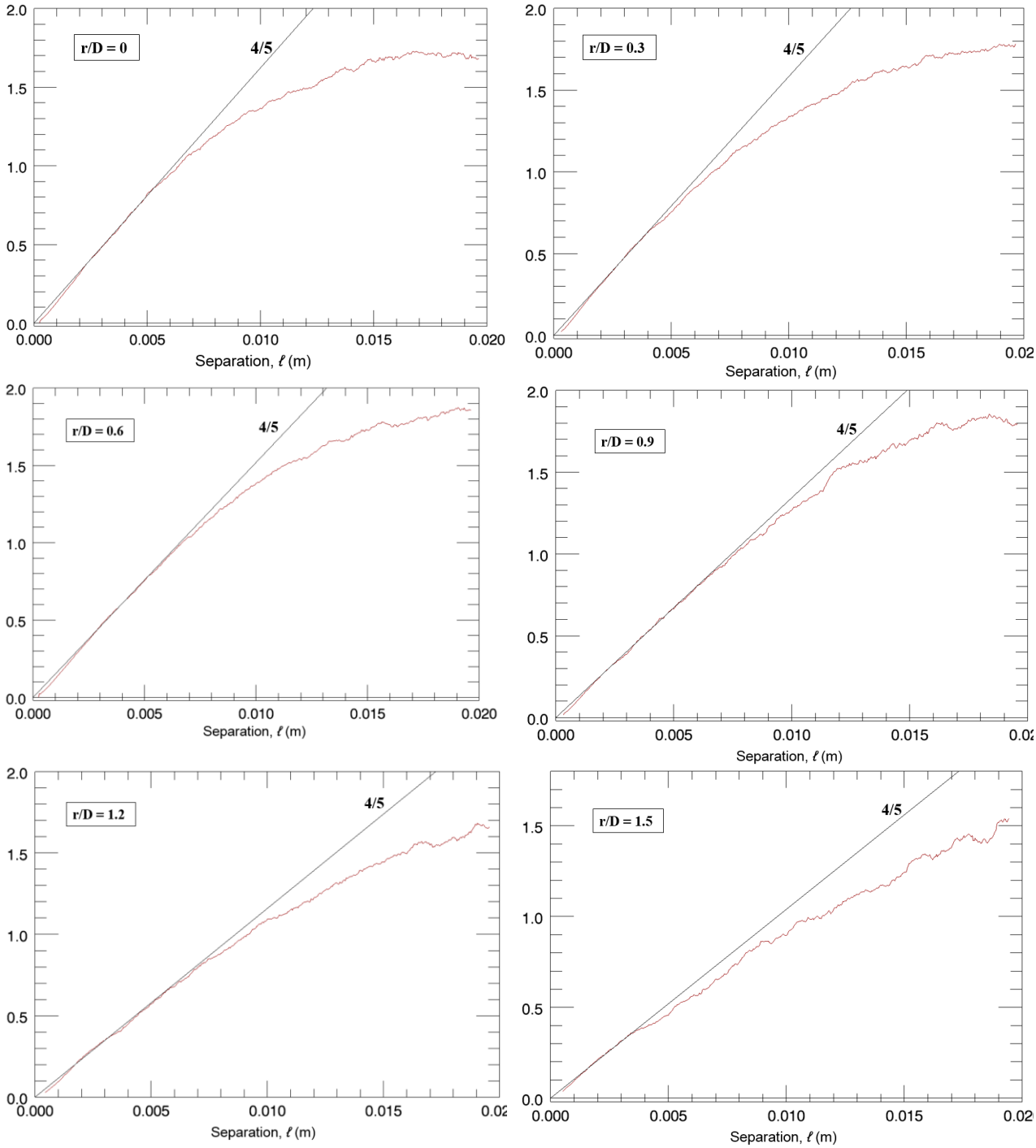

Figure 3-26 Spatial third order structure functions variations with radial distance at *x/D*=30, retrieved from Paper VI. Due to high variations in the plots beyond *r/D*=1.5, only functions up this position are presented. Separate plots are made to clearly show the coincidence between each function and the 4/5 slope.

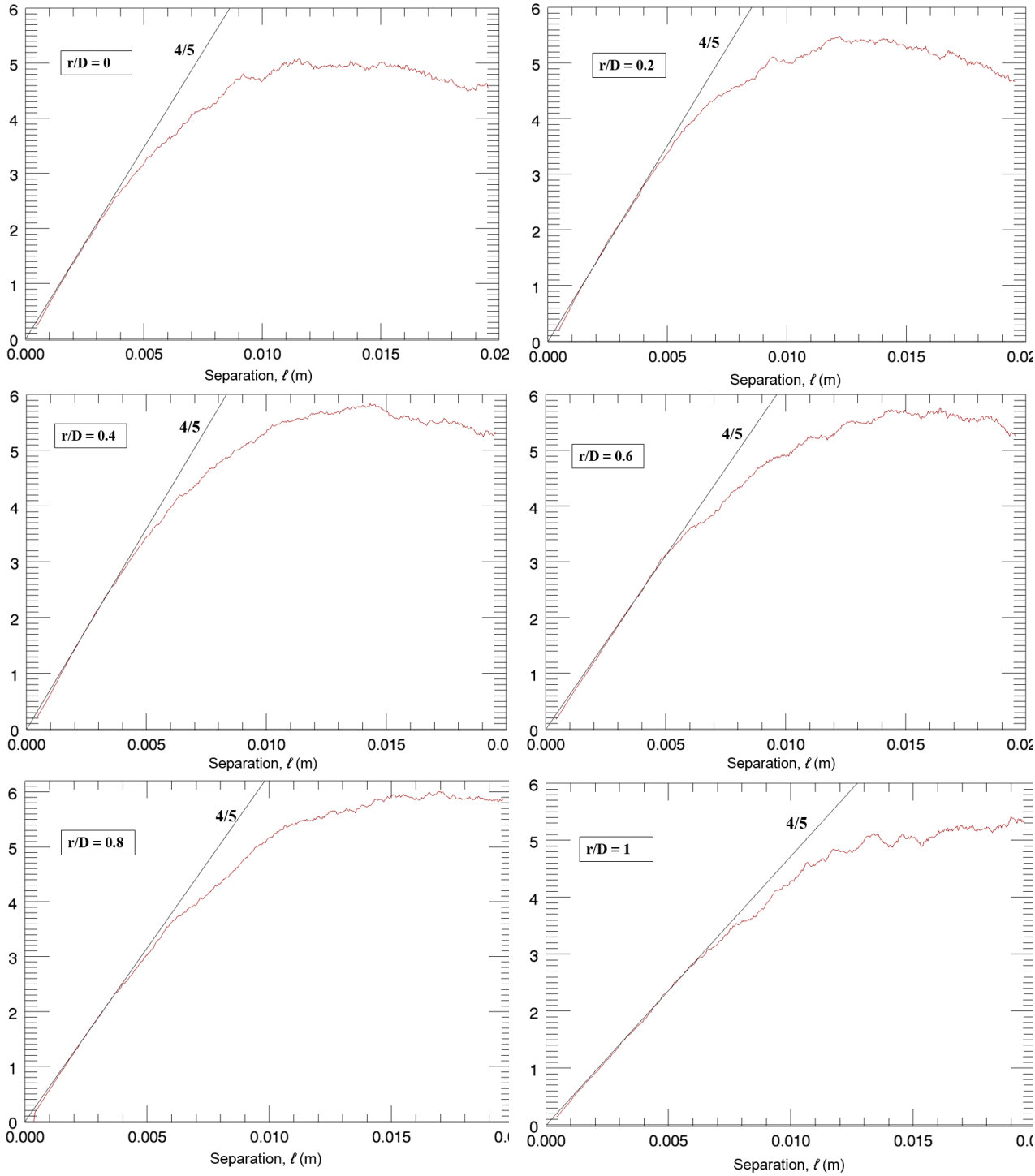

Figure 3-27 Spatial third order structure functions variations with radial distance at *x/D*=20, retrieved from Paper VI. Due to high variations in the plots beyond *r/D*=1, only functions up this position are presented. Separate plots are made to clearly show the coincidence between each function and the 4/5 slope.

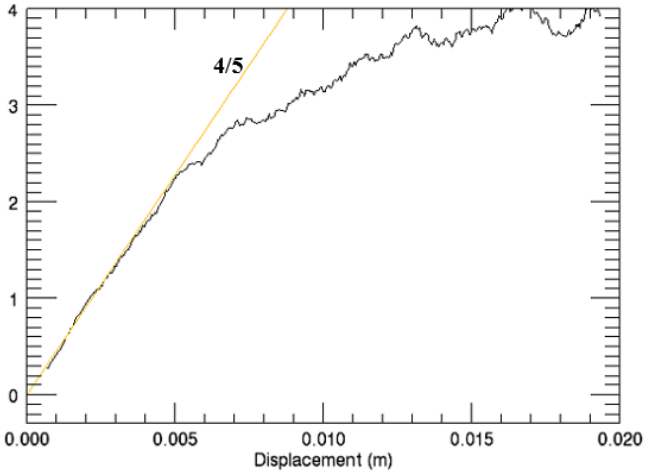

Figure 3-28 Spatial third-order structure function at *x/D*=28 (centerline), retrieved from Paper V. Figures of the same kind for the other downstream positions can be found in Appendix I of the same paper.

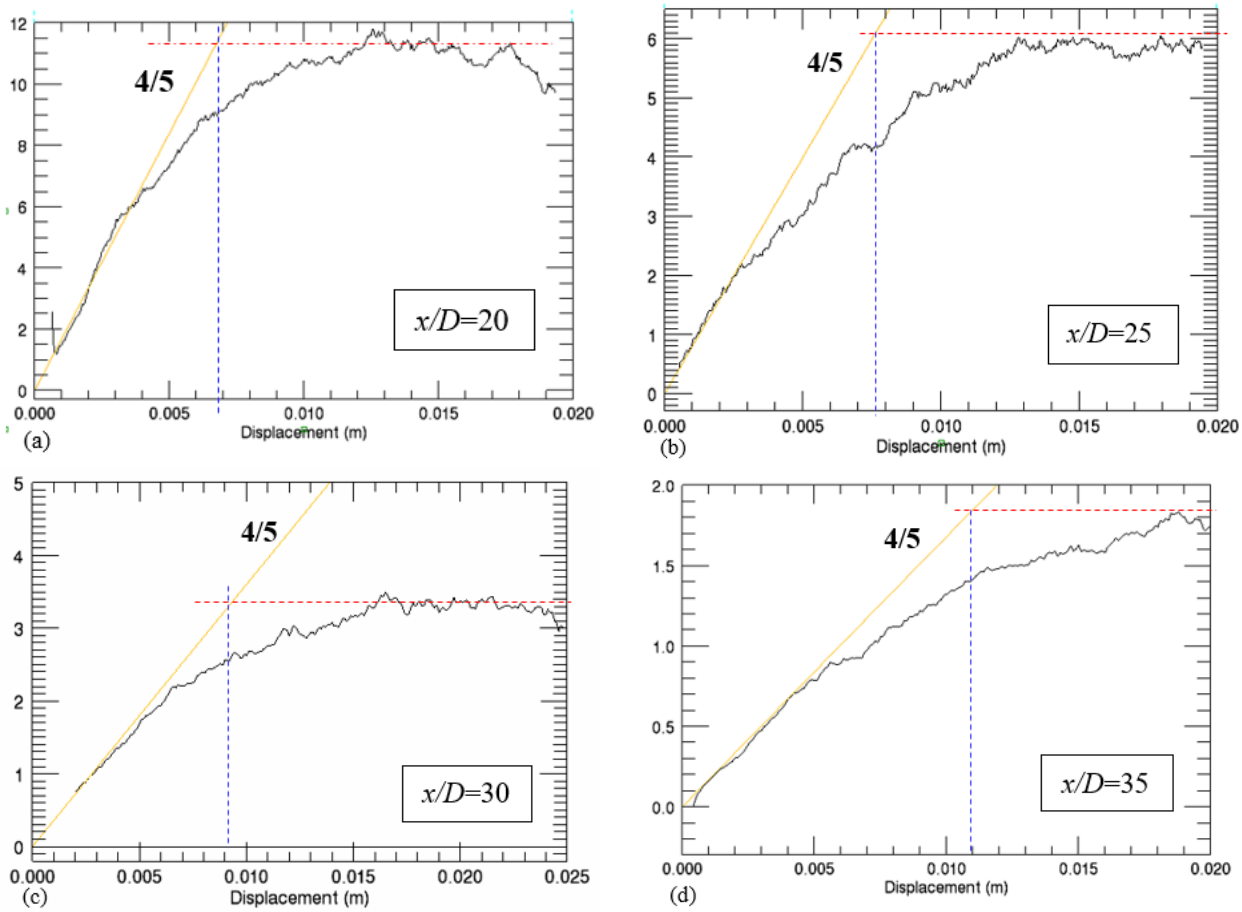

Figure 3-29 Spatial third order structure functions at centerline for selected downstream positions: (a) *x/D*=20, (b) *x/D*=25, (c) *x/D*=30, (d) *x/D*=35. The *yellow* and *red* lines represent the 4/5 slope and horizontal tangent line to each structure function curves, respectively, which intersection indicating the break point of the curve. The break occurs at approximately 6.9 mm, 7.7 mm, 9.1 mm and 11 mm at *x/D*=20, *x/D*=25, *x/D*=30 and *x/D*=35, respectively.

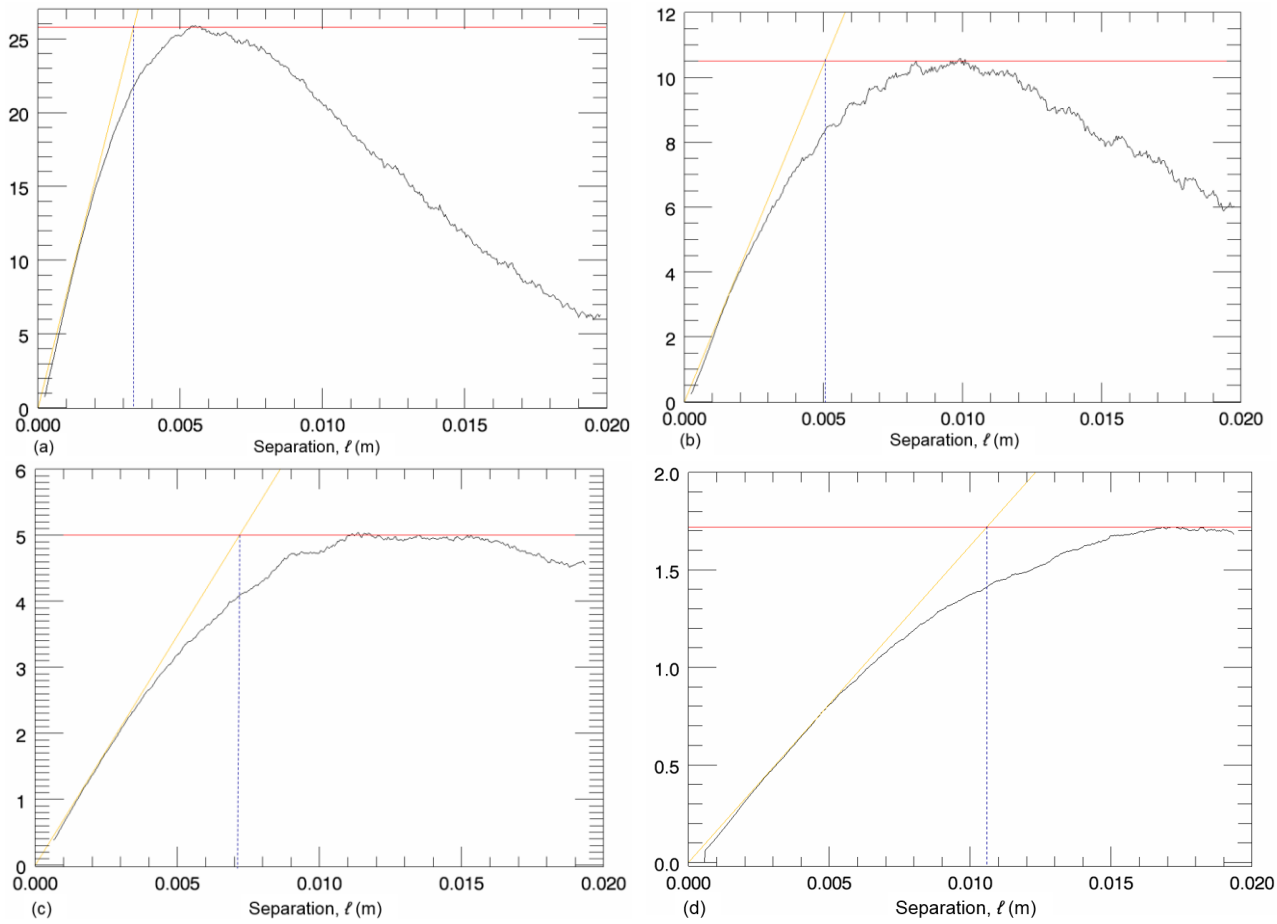

Figure 3-30 Spatial third order structure functions at centerline for: (a) *x/D*=10, (b) *x/D*=15 (c) *x/D*=20, (d) *x/D*=30. The *yellow* and *red* lines represent the 4/5 slope and horizontal line tangent to each structure function curves, respectively, which intersection indicating the break point of the curve. The break occurs at approximately 3.354 mm, 5.041 mm, 7.16 mm and 10.6 mm at *x/D*=10, *x/D*=15, *x/D*=20 and *x/D*=30, respectively.

3.7 Dissipation

Plotting the S_3 function is one of the ways to estimate the mean energy dissipation rate per unit mass, according to the assumptions of Kolmogorov (Kolmogorov 1941b). The fine-tuned value of ε in Equation (3.3), for which the 4/5 slope to best coincide at the small separations of an individual S_3 function, is saved as the dissipation at each measured position, ε_{45}. The radial and downstream profiles are plotted in Figure 3-31(a) and Figure 3-32(a), which are taken from Paper VI and V, respectively. Note that, in Paper VI or for Figure 3-31, Equation (3.3) is naively used to crudely estimate ε_{45} in the developing region.

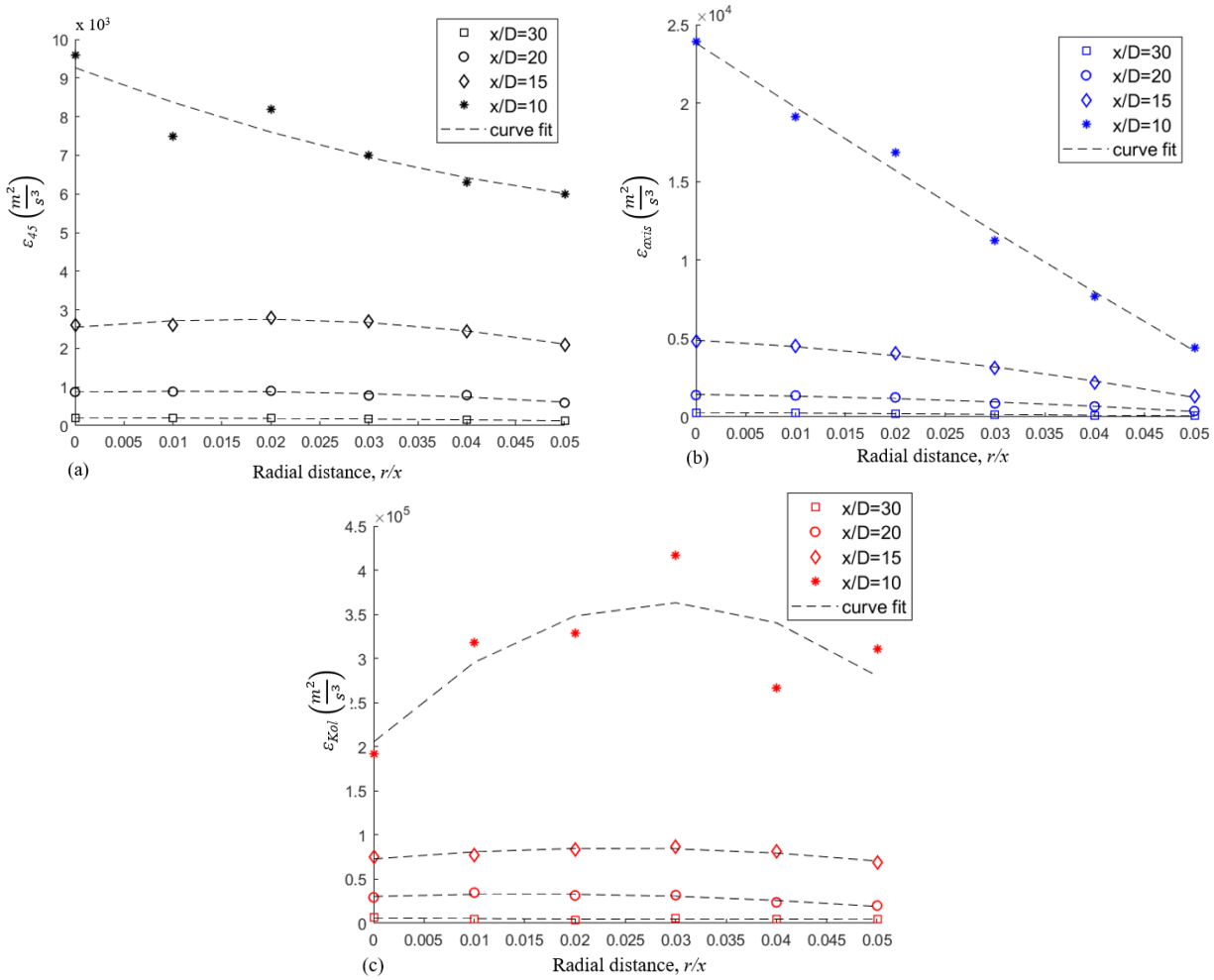

Figure 3-31 Radial evolutions of of (a) ε_{45}, (b) ε_{axis} and (c) ε_{Kol}, with second-order polynomial curve fit

In comparative to the overall plot of Figure 3-31(a), an almost consistent behavior is observed on the radial evolutions of ε_{45} in the fully developed region, e.g., at *x/D*=30 and *x/D*=20. The radial evolution at *x/D*=15 is surprisingly (relatively) consistent even though the previously stated assumptions do not really hold. Meanwhile, a sudden drop is observed along the radial direction of *x/D*=10, which certainly corresponds to the non-equilibrium region based on the energy spectra obtained in Figure 3-18 (d).

The dissipation based on the local axisymmetry, ε_{axis} and Kolmogorov estimation, ε_{Kol} are also computed and plotted in Figure 3-31(b) and (c), respectively. The former is determined by reading the value of $2\varepsilon_{axis}$ (x – x_0) / u3 ≈ 0.7 for the corresponding radial position $r/(x-x_0)$ of Figure 21 in (Hussein et al. 1994) while the latter is computed by $\overline{u^3}/L_u$, where L_u is the integral length scale. Both ε_{axis} and ε_{Kol} exhibit nearly similar trend with ε_{45} at *x/D*=15, 20 and 30. The trend is remarkably different *x/D*=10 (developing region) between ε_{45}, for which the assumptions for 4/5 law are not fulfilled, and ε_{Kol},, which are both central results from the same Kolmogorov theory. These two dissipation estimates should give (at least approximately) the same values AND consequently show similar trend if the theory and its underlying assumptions are correct and valid.

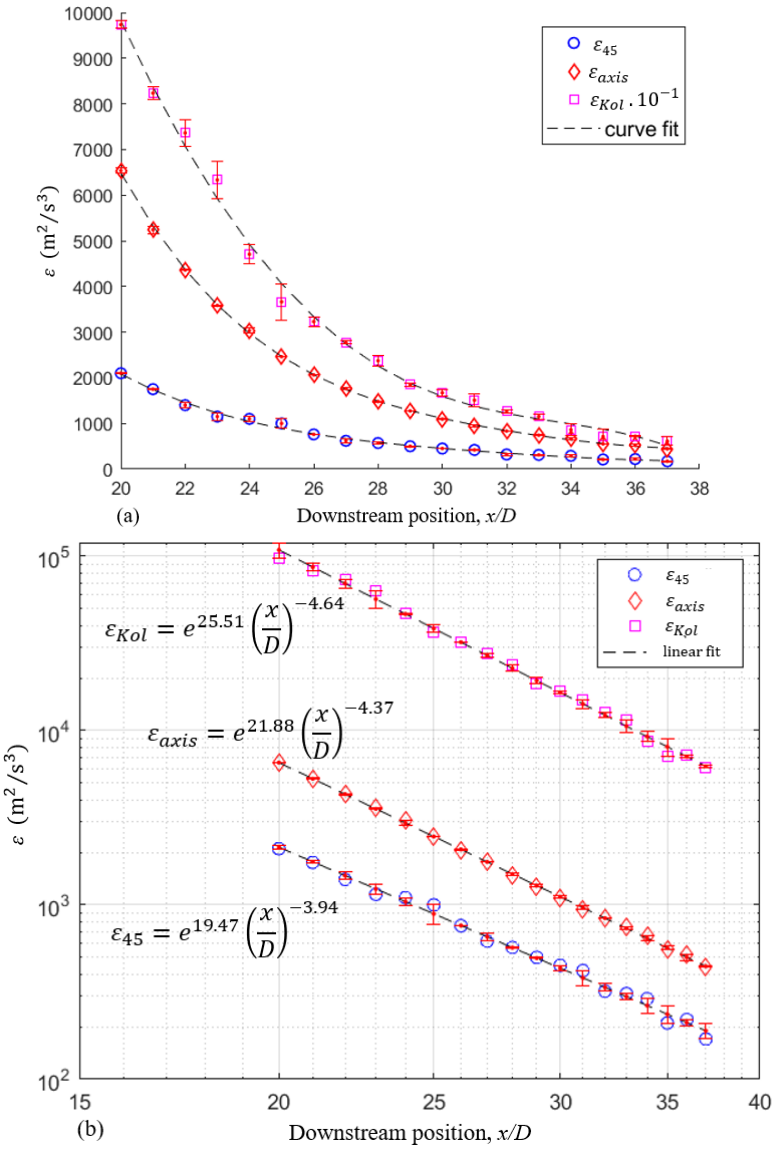

Figure 3-32 Downstream evolution of the mean energy dissipation rate per unit mass, ε_{45}, ε_{axis} and ε_{Kol} (a) in regular scales, with corresponding fourth-order polynomial curve fits. Note that ε_{Kol} is multiplied by 1/10 to compare for any similar trend. (b) in logarithmic scales, with linear fits.

From Figure 3-32(a), ε_{45} is observed to decay downstream with a higher rate at the beginning of the fully developed region. ε_{axis} and $\varepsilon_{Kol,}$ are also being overlaid in the same figure are. Though there is significant deviation between the three curves in the crudely assumed fully developed region ($x/D \geq 20$), each curve exhibits similar trends in both scales and seem to converge further downstream in the well-known fully developed region.

Similar plots are also constructed in logarithmic scale as in Figure 3-32(b). In this case, each dissipation estimate exhibits a linear trend downstream with different decay rates denoted by the exponent of x/D. It is also remarkable that the dissipation from the 4/5 law, $\varepsilon_{45,}$ (which assumptions are not fulfilled) does not agree with the dissipation estimate epsilon, ε_{Kol} that is another central result from the same Kolmogorov theory. If the theory were correct, the assumptions should be valid AND

the two dissipation estimates should give (at least approximately) the same values. The most credible estimate would be the axisymmetric one, ε_{axis}, since it has been empirically established in (George and Hussein 1991; Hussein et al. 1994).

3.8 Turbulence scales

The Kolmogorov time, τ_{Kol} and length scales, η_{Kol} are computed directly using Equation (3.4) and (3.5) respectively,

$$\tau_{Kol} = \left(\frac{\nu}{\varepsilon}\right)^{1/2} \tag{3.4}$$

$$\eta_{Kol} = \left(\frac{\nu^3}{\varepsilon}\right)^{1/4} \tag{3.5}$$

where ν is the kinematic viscosity and ε is the general notation for the mean energy dissipation rate per unit mass. In Paper VI, the radial evolutions at *x/D*=20 and *x/D*=30 are presented (see Figure 3-33), which show that both scales grow with a similar trend at each downstream position. The scales are also generally larger in the more downstream position. This similar observation can also be observed from the downstream evolutions presented in Paper V as depicted in Figure 3-34. The scales are also recomputed using the obtained values of ε_{axis} from the previous section and overlaid in Figure 3-33 and Figure 3-34. In both figures, a horizontal *blue* line representing the smallest resolvable length scale is also overlaid. The line is always below the polynomial curves of the Kolmogorov length scales, with an exception at *x/D*=20 of Figure 3-34, which value is just very slightly lower. This exception however can still be acceptable considering that the values of the MV and $\eta_{Kol,axis}$ are determined only based on estimations. Therefore, with the currently used spatial resolution, we should be able to resolve the Kolmogorov scale throughout this region, and perhaps in the upstream.

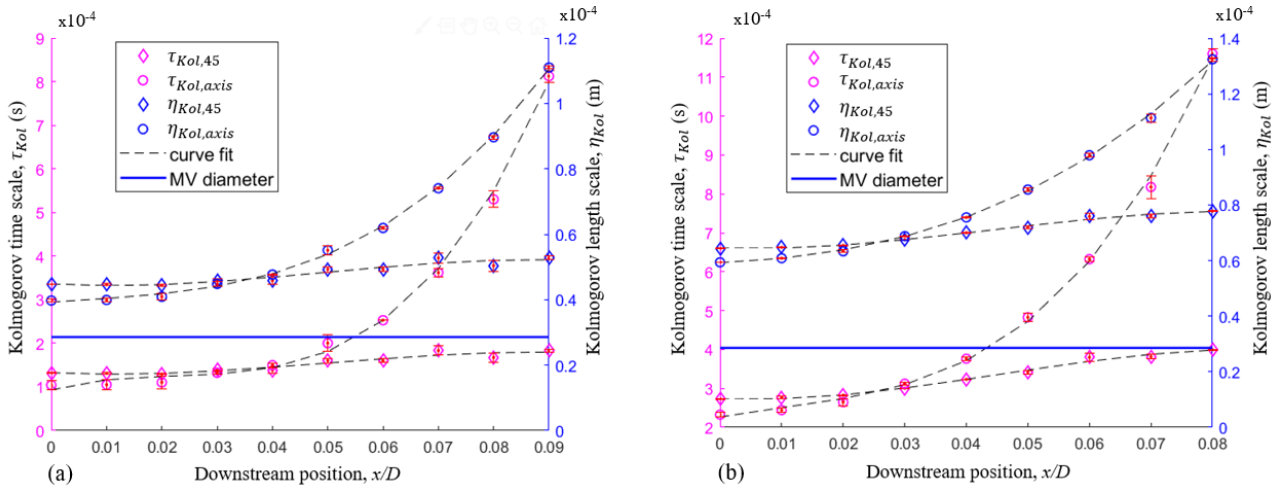

Figure 3-33 Radial evolution of the Kolmogorov scales at (a) *x/D*=20, (b) *x/D*=30, with third-order polynomial fit. The blue horizontal line represents the smallest resolvable scale of our instrument, i.e., 28.6 µm, which is always below the polynomial curve of the Kolmogorov length scales.

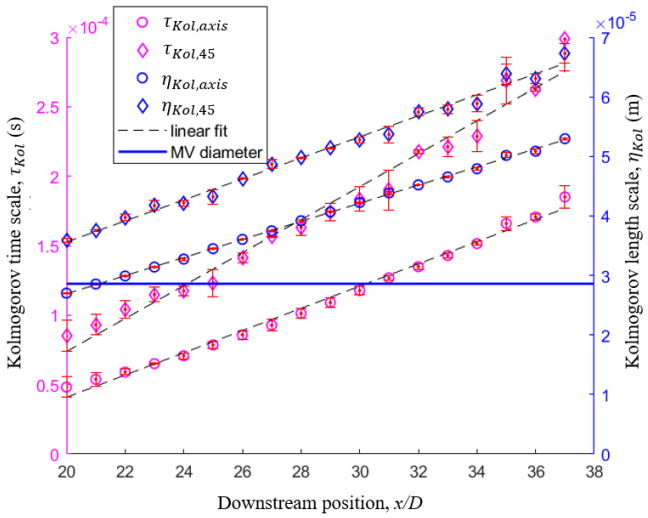

Figure 3-34 Downstream evolution of the Kolmogorov time and length scale, with corresponding linear fit. The horizontal *blue* line represents the smallest resolvable scale of our instrument, i.e., 28.6 µm

The integral time scale, T_u is computed from the integral under the covariance function:

$$T_u = \int_0^\infty \frac{\overline{u(t)u(t+\tau)}}{\overline{u^2}} d\tau \tag{3.6}$$

For the jet centreline measurements in Paper V, the spatial counterpart, L_u is estimated by multiplying T_u with the local mean velocity based on the Taylor's hypothesis. This hypothesis is assumed to be valid since measurements were performed along the jet centreline, where turbulence intensities are relatively low (Wyngaard and Clifford 1977). Meanwhile for the off-axis measurements in Paper VI, the multiplication is done with the convection velocity that is based on the convection record.

Similar to the Kolmogorov scales, the integral scales also grow and slow down downstream as what we can also observe Figure 3-35. Meanwhile, the radial evolution of the integral scales at various downstream positions are depicted in Figure 3-36, both in temporal and spatial domains. In general, the scales are larger downstream and develop different trend at different downstream positions. The development is almost consistent at *x/D*=10 and getting more unsteady as the measurements progress downstream. This may be due to the difficulty in obtaining sufficient statistics for proper spectral estimates in the outer parts of the jet, since the convection velocity (and hence also the measuring time required) changes dramatically when moving towards the outer parts of the jet. The results for large radial positions should therefore be interpreted with caution.

Apart from the Kolmogorov and integral scales, it was also our intention to estimate the corresponding values of the Taylor microscale, which definition is given by (Tennekes and Lumley 1972)

$$\lambda_L = \sqrt{\frac{\overline{u^2}}{\overline{\left(\frac{du}{dt}\right)^2}}} \tag{3.7}$$

However, difficulty arises as the measurements move away from the jet centerline since the flow becomes increasingly intermittent. The definition is clear for a fully turbulent flow, leaving us an ambiguity for computation in the intermittent counterpart and consequently demanding us more time to investigate on any other possible solutions rather than computing the Taylor scale directly from its definition. Besides, we also need to seriously take care of the issue regarding the random data filtering for computing the Taylor scales using SACF method. The filtering works for low-pass filter with a very low cut off frequency but the high frequency region is still dominated by high frequency noise, which consequently contaminates the Taylor scale computation.

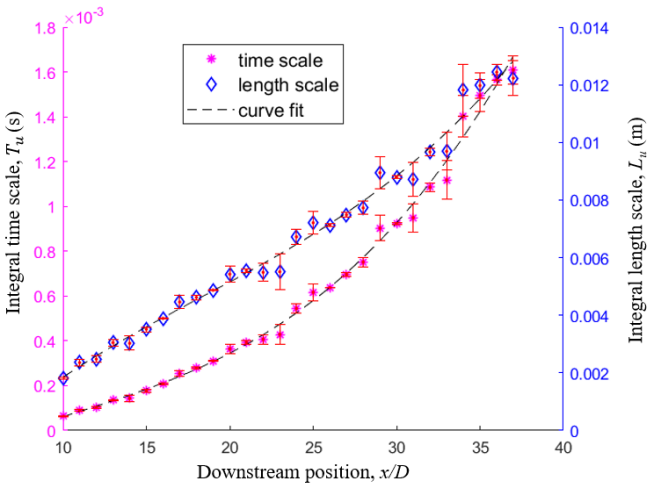

Figure 3-35 Downstream evolution of the integral time and length scale, with corresponding third-order fit

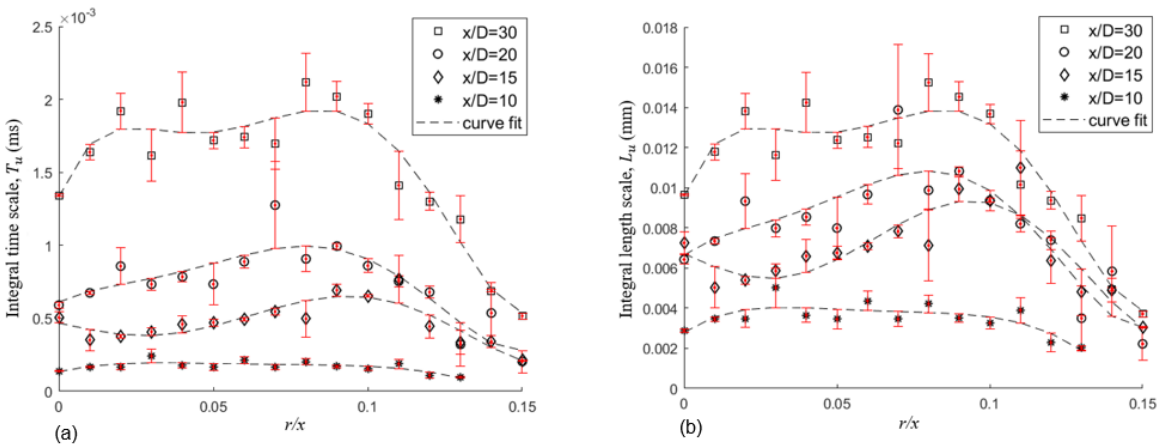

Figure 3-36 Radial evolution of the integral scales at various downstream positions in (a) time (b) space, with second-order polynomial fit.

Concluding Remarks

This thesis has presented continuous works in developing the state-of-the-art laser Doppler system optimized for the flow investigation in a turbulent round jet. The streamwise turbulence measurements have extensively covered different regions of the jet from e.g., the developing (including near the laminar region) to the fully developed region, and the centerline to the outermost region, which findings and conclusions are disclosed in a series of scientific papers.

Other than being transparent, our in-house LDA system has been successfully proven to provide accurate measurements with high dynamic range even in the challenging (high shear and intensity) regions of the jet. Results and diagnostics disclosed in Paper IV have shown that the system can successfully counter several of the limitations, which have been long suffered by the commercial counterpart.

The in-house LDA system has been proven to successfully produce experimental results that validate the Kolmogorov theory in the fully developed region and reveal some new and interesting non-equilibrium features in the developing part of the jet. The accumulation of results on the developing region from Paper I, V and VI has provided valuable insight into the limitations of Kolmogorov and its underlying theory.

Paper I has first shown preliminary experimental evidence on the invalidity of the local equilibrium assumption in the developing region of the jet. Paper VI has later shown in tethat interactions are not local in the hypothesized equilibrium range (inertial and dissipation ranges), based on the energy spectra and structure functions. This leads to a question whether the cornerstone assumption of local (and universal) equilibrium can really hold in general and the well-known Richardson's energy cascade is truly valid.

Paper V has demonstrated that the second-order statistics need longer time to fully developed than the first-order ones. It has also interestingly shown that the virtual origins from the linear fit of the mean velocity and variance are resulted at different downstream position, which can be of a great interest for investigation in the future.

Finally, it is our hope that this thesis may come out handy for ones who are about to operate the LDA system in the different scopes of investigations in the future. The measurements and their corresponding results provided herein, especially from Paper V and VI are hoped to be greatly useful for development and/or validation of turbulence models in a classical flow that at least on average displays the same physics as the Kolmogorov theory of turbulence, upon which the majority of current turbulence models are built.

Future Work

Although this project has been successfully executed as per plan, there are still rooms for future improvement in terms of the hardware and the software of the LDA system.

It would be remarkable to investigate the best method in reducing the processing time that will allow larger amount of data to be processed within the same amount of time. Converting the software, which has been written in IDL, to a more friendly user language/interface, i.e., Phyton or MATLAB is also something to think about, especially if there is a plan to make the software open to the public.

Dealing with enormously huge amount of data from the measurements does not only demand a much larger storage but also a more organized system for the data to be easily accessible whenever needed. This will come very handy if someone from outside the institution is interested to further analyze the measurements data.

In order to better utilize the functionality of the LDA system, the range of the traversing axis especially in the streamwise direction, could be expanded for capturing the data in much further downstream region. Especially when the current enclosure (tent) is actually providing more space than what has been used.

Finally, it will be another breakthrough for the current setup to be upgraded to a two-spot high performance LDA system for resolving much smaller scales in turbulence.

References

Abdel-Rahman, A. A., S. F. Al-Fahed, and W. Chakroun. 1996. "The Near-Field Characteristics of Circular Jets at Low Reynolds Numbers." *Mechanics Research Communications* 23(3):313–24.

Albrecht, H. E., M. Borys, N. Damaschke, and C. Tropea. 2003. *Laser Doppler and Phase Doppler Measurement Techniques*. Springer-Verlag.

Anselmet, F., R. A. Antonia, and L. Danaila. 2001. "Turbulent Flows and Intermittency in Laboratory Experiments." *Planetary and Space Science* 49:1177–91.

Ball, C. G., H. Fellouah, and A. Pollard. 2012. "The Flow Field in Turbulent Round Free Jets." *Progress in Aerospace Sciences* 50:1–26.

Barker, S. J. 1973. "Laser-Doppler Measurements on a Round Turbulent Jet in Dilute Polymer Solutions." *Journal of Fluid Mechanics* 60:721–31.

Bartlett, K. G. and C. Y. She. 1976. "Remote Measurement of Wind Speed Using a Dual Beam Backscatter Laser Doppler Velocimeter." *Appl. Opt.* 15(8):1980–83.

Batchelor, G. K. 1953. *The Theory of Homogeneous Turbulence*. Cambridge University Press.

Bell, James H. and Rabindra D. Mehta. 1988. "Contraction Design for Small Low-Speed Wind Tunnels."

Boratav, Oluş N. and Richard B. Pelz. 1997. "Structures and Structure Functions in the Inertial Range of Turbulence." *Physics of Fluids* 9(5):1400–1415.

Buchhave, P. 1979. "Errors and Correction Methods in Turbulence Measurements with the LDA." State University of New York.

Buchhave, P. 1984. "Three-Component LDA Measurements." *Disa Information* (29):3–9.

Buchhave, P., W. K. George, and J. L. Lumley. 1979. "The Measurement of Turbulence with the Laser-Doppler Anemometer." *Annual Review of Fluid Mechanics* 11:443–503.

Buchhave, P. and C. M. Velte. 2015. "Reduction of Noise and Bias in Randomly Sampled Power Spectra." *Experiments in Fluids* 56(4):1–17.

Buchhave, P. and C. M. Velte. 2017a. "Conversion of Measured Turbulence Spectra from Temporal to Spatial Domain." Pp. 343–62 in *Whither Turbulence and Big Data in the 21st Century?* Springer.

Buchhave, P. and C. M. Velte. 2017b. "Measurement of Turbulent Spatial Structure and Kinetic Energy Spectrum by Exact Temporal-to-Spatial Mapping." *Physics of Fluids* 29(8).

Buchhave, P., C. M. Velte, and W. K. George. 2014. "The Effect of Dead Time on Randomly Sampled Power Spectral Estimates." *Experiments in Fluids* 55(2):1–8.

Burattini, P. and R. A. Antonial Danaila. 2005. "Similarity in the Far Field of a Turbulent Round Jet." *Physics of Fluids* 17(025101).

Capp, S. P. 1983a. "Experimental Investigation of the Turbulent Axisymmetric Jet." State University of New York, Buffalo.

Capp, S. P. 1983b. “Experimental Investigation of the Turbulent Axisymmetric Jet.” State University of New York at Buffalo.

Champagne, H. 1978. “The Fine-Scale Structure of the Turbulent Velocity Field.” *Journal of Fluid Mechanics* 86(01):67–108.

Danaila, Ionut, Dušek Jan, and Fabien Anselmet. 1997. “Coherent Structures in a Round , Spatially Evolving , Unforced , Homogeneous Jet at Low Reynolds Numbers.” *Physics of Fluids* 9(3323).

Danaila, L., F. Anselmet, and R. A. Antonia. 2002. “An Overview of the Effect of Large-Scale Inhomogeneities on Small-Scale Turbulence.” *Physics of Fluids* 14(2475).

Davidson, P. 2004. *Turbulence: An Introduction for Scientist and Engineers*. Oxford University Press.

Durrani, Tariq S. 1972. “Noise Analysis for Laser Doppler Velocimeter Systems.” *IEEE TRANSACTIONS ON COMMUNICATIONS* 20(3):296–307.

Durrani, Tariq S. and Clive A. Greated. 1973. “Statistical Analysis and Computer Simulation of Laser Doppler Velocimeter Systems.” *IEEE Transactions on Instrumentation and Measurement* 22(1):23–34.

Falcone, Anthony M. and Joseph C. Cataldo. 2003. “Entrainment Velocity in an Axisymmetric Turbulent Jet.” *Journal of Fluids Engineering* 125(4):620.

Fellouah, H., C. G. Ball, and A. Pollard. 2009. “Reynolds Number Effects within the Development Region of a Turbulent Round Free Jet.” *International Journal of Heat and Mass Transfer* 52(17–18):3943–54.

Fellouah, H. and A. Pollard. 2009. “The Velocity Spectra and Turbulence Length Scale Distributions in the near to Intermediate Regions of a Round Free Turbulent Jet.” *Physics of Fluids* 21(11):011911PHF.

Ferdman, E., M. V. Otugen, and S. Kim. 2000. “Effect of Initial Velocity Profile on the Development of Round Jets.” *Journal of Propulsion and Power* 16(4):676–86.

Fingerson, L. M. 1982. “Laser Doppler Velocimeters.Pdf.” *Laser Focus* 18(8):53–56.

Fischer, A. 2017. “Imaging Flow Velocimetry with Laser Mie Scattering.” *Applied Sciences* 7(12):1298.

Frisch, By Uriel, Pierre-louis Sulem, and Mark Nelkin. 1978. “A Simple Dynamical Model of Intermittent Fully Developed Turbulence.” 87.

Frisch, U. 1995. *Turbulence: The Legacy of A.N. Kolmogorov*. Cambridge University Press.

George, W. K. 1988. “Quantitative Measurement with the Burst-Mode Laser Doppler Anemometer.” *Experimental Thermal and Fluid Science* 1(1):29–40.

George, W. K. and H. J. Hussein. 1991. “Locally Axisymmetric Turbulence.” *Journal of Fluid Mechanics* 233:1–23.

Gerosa, S. and G. P. Romano. 1994. “Effect of Noise in Laser Doppler Anemometry.” *Mechanical Systems and Signal Processing* 8(2):229–42.

Gibson, M. M. 1962. “Spectra of Turbulence at High Reynolds Number.” *Nature* 195:1281–83.

Gibson, M. M. 1963. “Spectra of Turbulence in a Round Jet.” *Journal of Fluid Mechanics* 15:161–73.

Grandchamp, X., A. Van Hirtum, and X. Pelorson. 2013. “Centreline Velocity Decay Characterisation in Low-Velocity Jets Downstream from an Extended Conical Diffuser.” *Meccanica* 48:567–83.

Gutmark, E. 1983. “Preferred Modes and the Spreading Rates of Jets.” *Physics of Fluids* 26(10):2932.

Hinze, J. O. 1975. *Turbulence*. 2nd ed. McGraw-Hill, the University of Michigan.

Hodzic, Azur. 2014. “PIV Measurements on a Turbulent Free Jet - Spatial Decomposition of a Turbulent Free Jet Using Proper Orthogonal Decomposition.” Technical University of Denmark.

Hodzic, Azur. 2019. “Experimental and Theoretical Investigations of Turbulent Axi-Symmetric Jets.” Technical University of Denmark.

Hsu, Cheng-hsing. 1989. “Laser Doppler Anemometry Measurements of a Confined Turbulent Water Jet with a Uniform Background Flow.” Virginia Polytechnic Institute and State University.

Hussein, H. J., S. P. Capp, and W. K. George. 1994. “Velocity Measurements in a High-Reynolds-Number, Momentum-Conserving, Axisymmetric, Turbulent Jet.” *Journal of Fluid Mechanics* 258:31–75.

Janssent, J. M. L., L. Ensingt, and J. B. Vaan Erp. 1959. “A Constant-Temperature-Operation Hot-Wire Anemometer *.” *Proceedings of the Institute of Radio Engineers* 47(4):555–67.

Jensen, K. D. 2004. “Flow Measurements.” *Journal of the Brazilian Society of Mechanical Sciences and Engineering* XXVI(4):400–419.

Johnson, D. A. 1988. *Laser Doppler Anemometry*. Moffett Field, California.

Johnson, Richard W. 2016. *Handbook of Fluid Dynamics*. Second Edi. CRC Press.

Jung, Daehan. 2001. “An Investigation of the Reynolds-Number Dependence of the Axisymmetric Jet Mixing Layer Using a 138 Hot-Wire Probe and the POD.” State University of New York.

Kassab, Sadek Z., Ayman E. Bakry, and Hassan A. Warda. 1996. “Laser Doppler Anemometry Measurements in an Axisymmetric Turbulent Jet.” *Review of Scientific Instruments* 67(5):1842–49.

Khashehchi, M., A. Ooi, J. Soria, and I. Marusic. 2013. “Evolution of the Turbulent/Non-Turbulent Interface of an Axisymmetric Turbulent Jet.” *Experiments in Fluids* 54(1):1449.

Kolmogorov, A. N. 1941a. “Decay of Isotropic Turbulence in Incompressible Viscous Fluids.” *Dok. Akad. Nauk. S. S. S. R* 31:538–41.

Kolmogorov, A. N. 1941b. “Dissipation of Energy in Local Isotropic Turbulence.” *Dokl. Akad. Nauk. SSSR* 32:15–17.

Kolmogorov, A. N. 1941c. “The Local Structure of Turbulence in Incompressible Viscous Fluid for

Very Large Reynolds Numbers." *C. R. Akad. Sci. SSSR* 30:9–13.

Kolmogorov, A. N. 1962. "A Refinement of Previous Hypothesis Concerning the Local Structure of Turbulence in a Viscous Incompressible Fluid at High Reynolds Number." *Journal of Fluid Mechanics* 13:82–85.

L'vov, V. and I. Procaccia. 2007. "Hydrodynamic Turbulence: A 19th Century Problem with a Challenge for the 21st Century." *Turbulence Modeling and Vortex Dynamics* 491:1–16.

Lading, Lars, Graham Wigley, and P. Buchhave. 1994. *Optical Diagnostics for Flow Processes*. Springer Science+Business Media New York.

Lin, C. C. 1953. "On Taylor'S Hypothesis and the Acceleration Terms in the Nawer-Stokes Equations." *Quarterly of Applied Mathematics* 10(4):295–306.

Liu, Chaoqun, Yonghua Yan, and Ping Lu. 2014. "Physics of Turbulence Generation and Sustenance in a Boundary Layer." *Computers and Fluids* 102:353–84.

Lumley, J. L. 1965. "Interpretation of Time Spectra Measured in High-Intensity Shear Flows." *Physics of Fluids* 8(6):1056–62.

Lumley, J. L., Y. Kobashi, and W. K. George. 1969. "The Influence of Doppler Ambiguity and Noise on the Measurement of Turbulent Spectra Using a Laser-Doppler Velocimeter." Pp. 3–9 in *Proc. Symp. Meas. Turb. in Liquids*.

McDonough, J. M. 2007. *Introductory Lectures on Turbulence: Physics, Mathematics and Modeling*. Departments of Mechanical Engineering and Mathematics University of Kentucky.

Melling, A. 1997. "Tracer Particles and Seeding for Particle Image Velocimetry." *Measurement Science and Technology* 8(12):1406–16.

Melling, A. and J. H. Whitelaw. 1973. "Seeding of Gas Flows for Laser Anemometry." *Danske Industri Syndikat A/s Information* (15):5–14.

Mi, J., G. J. Nathan, and D. S. Nobes. 2001. "Influence of Jet Exit Conditions on the Passive Scalar Field of an Axisymmetric Free Jet." *Journal of Fluids Engineering* 432:91–125.

Panchapakesan N. R. and J. L. Lumley. 1993. "Turbulence Measurements in Axisymmetric Jets of Air and Helium . Part 1 . Air Jet." *Journal of Fluid Mechanics* 246:197–223.

Peiponen, K. E., R. Myllylä, and A. V. Priezzhev. 2009. "Laser Velocimetry." Pp. 103–36 in *Springer Series in Optical Sciences*. Vol. 136. Springer Berlin Heidelberg.

Pope, S. B. 2000. *Turbulent Flows*. Cambridge: Cambridge University Press.

Pope, Stephen. 2000. *Turbulent Flows*. Cambridge University Press.

Reeks, Michael W. 2011. "PARTICLE TRANSPORT IN TURBULENT FLUIDS." *Thermopedia*.

Richardson, L. F. 1922. *Weather Prediction by Numerical Process*. UK: Cambridge Univ. Press.

Righini, Giancarlo C., Tajani Antonella, and Antonello Cutolo. 2009. *An Introduction to Optoelectronic Sensors*.

Roberts, J. B., J. Downie, and M. Gaster. 1980. "Spectral Analysis of Signals from a Laser Doppler Anemometer Operating in the Burst Mode." *Journal of Physics E: Scientific Instruments*

3(9):977–81.

Romano, G. P. and R. A. Antonia. 2001. “Longitudinal and Transverse Structure Functions in a Turbulent Round Jet: Effect of Initial Conditions and Reynolds Number.” *Journal of Fluid Mechanics* 436:231–48.

Ronald, D. Flack Jr. 1975. “The Application of a Laser Doppler Velocimeter (LDV) in Interpreting Turbulent Structure.” Purdue University.

Sato, Susumu. 1979. “Liquid-Crystal Lens-Cells with Variable Focal Length.” *Japanese Journal of Applied Physics* 18(9):1679–84.

Seoud, R. E. and J. C. Vassilicos. 2007. “Dissipation and Decay of Fractal-Generated Turbulence.” *Physics of Fluids* 19:105–8.

Stewart, R. W. 1959. “The Natural Occurrence of Turbulence.” *Journal of Geophysical Research* 64(12):2112–15.

Taylor, G. I. 1938. “The Spectrum of Turbulence.” *Proceedings of the Royal Society of London. Series A, Mathematical and Physical Sciences* 164(919):476–90.

Tennekes, H. and J. L. Lumley. 1972. *A First Course in Turbulence*. MIT Press.

Tsinober, Arkady. 2009. *An Informal Conceptual Introduction to Turbulence*. Springer Dordrecht Heidelberg London New York Library.

Velte, C. M. 2009. “Characterization of Vortex Generator Induced Flow.” Technical University of Denmark.

Velte, C. M., P. Buchhave, and W. K. George. 2014. “Dead Time Effects in Laser Doppler Anemometry Measurements.” *Experiments in Fluids* 55(11):1836.

Velte, C. M., P. Buchhave, and A. Hodzic. 2017. “Measurement of Turbulent Kinetic Energy Spectrum - Part 2 : Convection Record Measurements.” Pp. 171–76 in *iTi Conference on Turbulence VII*. Springer.

Velte, C. M., W. K. George, and P. Buchhave. 2014. “Estimation of Burst-Mode LDA Power Spectra.” *Experiments in Fluids* 55(3):1674.

Wänström, M., W. K. George, and K. E. Meyer. 2012. “Streamwise and Radial Decomposition of a Turbulent Axisymmetric Jet.” *Springer Proceedings in Physics* 141:147–50.

Van De Water, Willem and Janine A. Herweijer. 1999. “High-Order Structure Functions of Turbulence.” *Journal of Fluid Mechanics* 387:3–37.

Weisgraber, T. H. and D. Liepmann. 1998. “Turbulent Structure during Transition to Self-Similarity in a Round Jet.” *Experiments in Fluids* 24(3):210–24.

White, Frank M. 1991. *Viscous Fluid Flow*. McGraw-Hill.

Wyngaard, J. C. and S. F. Clifford. 1977. “Taylor’s Hypothesis and High-Frequency Turbulence Spectra.” *Journal of the Atmospheric Sciences* 34(6):922–29.

Xiong, Shen, Yu Hesheng, Chen Dianlan, and Xie Suhuan. 1984. “The Measurements of Axisymmetric Air Turbulent Jet Flow with an Individual Realization Laser Velocimeter System.” *Journal of Tsinghua University* 24(3):26–36.

Acknowledgements

First of foremost, all praise to the Almighty for his continuous blessings.

A never-ending gratitude to my family, especially to mum and dad for their undeniable love and affection, and for always having me in their prayers.

A sincere gratitude to my advisor, Clara Velte for her continuous and countless support, immense knowledge, motivation and patience throughout my PhD research. The deepest gratitude also goes to Preben Buchave for his close supervision and guidance, be it in the theoretical part or the experimental work. These two persons and the rest of the DTU Turbulence Research group have ironically made my PhD journey to be one of the best things that ever happened in my life.

A special mention to Knud Erik Meyer for hooking me up to this PhD project, Rasmus Schlander for precious collaboration in writing the papers, Morten Jørgensen and the rest of DTU Mechanical workshop for their technical support in fabricating and setting up the hardware, Benny Edelsten for his assitance in setting up the experiments, the FVM members for embracing hygge environment daily at work and all my friends around the world for their indirect support.

I am also very grateful to the Technical University of Malaysia Melaka (UTeM) and the Ministry of Education Malaysia for fully funding this PhD project. Not to forget, the Faculty of Electrical Engineering, UTeM for granting me a full paid study leave.

Paper I

Penerbit Akademia Baru

Journal of Advanced Research in Fluid Mechanics and Thermal Sciences

Journal homepage: www.akademiabaru.com/arfmts.html
ISSN: 2289-7879

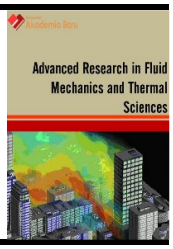

Experimental Evaluation of Kolmogorov's -5/3 and 2/3 Power Laws in the Developing Turbulent Round Jet

Open Access

Mohd Rusdy Yaacob[1,*], Rasmus Korslund Schlander[2], Preben Buchhave[3], Clara M.Velte[2]

[1] Faculty of Electrical Engineering, Universiti Teknikal Malaysia Melaka, Hang Tuah Jaya, 76100 Durian Tunggal, Melaka, Malaysia
[2] Department of Mechanical Engineering, Technical University of Denmark, 2800 Kgs. Lyngby, Denmark
[3] Intarsia Optics, Sønderskovvej 3, 3460 Birkerød, Denmark

ARTICLE INFO

Article history:
Received 28 February 2018
Received in revised form 22 March 2018
Accepted 5 May 2018
Available online 17 May 2018

Keywords:
Kolmogorov power law, turbulence, turbulent jet, laser Doppler anemometry

ABSTRACT

The current work investigates the validity of two cornerstone results of the Kolmogorov K41 theory of turbulence in terms of the typical power law representations viz. the -5/3 law for turbulence spectra and the 2/3 law for second order structure functions. The developing region of the jet has been chosen since it is an equilibrium flow once fully developed (but not necessarily in the development phase), it becomes fully developed over lengths that are practical on a laboratory scale and it is a high-intensity flow with accessibly resolvable scales in time and space. The developing region of the jet is thus the perfect testbed for these investigations, which can herein be accurately mapped using our in-house laser Doppler anemometry (LDA) system. The high turbulence intensity and high shear flow is challenging from a measurement technical perspective, which is perhaps why this flow is so underexplored. This software-driven LDA system was developed specifically to optimize measurement of high shear and high turbulence intensities accurately in challenging flows such as the turbulent round jet in air. The jet was investigated experimentally both in the developing (non-equilibrium) and in the developed regions (equilibrium). Velocity static moments at each point are first presented to show the time averaged flow behavior while the spatial energy spectra and second order structure functions are computed to evaluate the power laws postulated by Kolmogorov. Measurements from both the developed and from the developing parts of the jet are presented to show validity of the measurement technique and unveil the actual spectral shapes in the developing non-equilibrium region, respectively.

1. Introduction

Turbulence has for a long time been regarded as the last remaining unsolved problem of classical physics according to Richard Feynman. The postulation of Kolmogorov's universality assumptions which are also known as the K41 theory, resulted in two principal results viz. the 2/3 law for second

* *Corresponding author.*
E-mail address: rusdy@utem.edu.my (Mohd Rusdy Yaacob)

order structure functions and the -5/3 law for turbulence spectra [1]. Kolmogorov's 2/3 law states that "in a turbulent flow at very high Reynolds number, the mean-square velocity increments $< (\delta u(l))^2 >$ between two points separated by a distance ℓ behave approximately as the 2/3 power of the distance" [2]. It results from the derivation of the second-order structure function, based on Kolmogorov's classical assumption of turbulence dynamics [3-6]

$$S_2(l) = C\varepsilon^{2/3} l^{2/3} \tag{1}$$

where C is a universal constant (to be determined from experiments), ε is dissipation rate and ℓ is the length scale. Obukhov [2] later derived the turbulent kinetic energy spectrum from (1)

$$E(k) = C_k \varepsilon^{2/3} k^{-5/3} \tag{2}$$

where C_k is the Kolmogorov constant (to be determined from experiments) and k= $1/\ell$ is the wave number.

The theory stated by Kolmogorov [3-6] is formally based on three main hypotheses valid for sufficiently high Reynolds number flows; (1) local homogeneity/isotropy for $r<<L$, (2) where the scales for which $r<<L$ are uniquely determined by viscosity, ν, and dissipation, ε, (3) in addition to a range, $L>>r>>\eta$, that is uniquely characterized by ε, but not ν. L is the length scale characterizing the large scale turbulent structures. *Implicit* to all of these hypotheses is the "local equilibrium" hypothesis [7], which is based on the analogy of small scale turbulence to molecules in a thermodynamic system, wherein the molecules are decoupled from the macroscopic state and at a state of equilibrium. This is also by Kolmogorov assumed to be valid for the (significantly larger) small scales of turbulence.

The stationary round jet has been chosen for our investigations since it is known to be nearly at equilibrium, at least in the fully developed region, where it has also been proven to have good agreement with Kolmogorov's theory as the very first flow displaying the -5/3 slope of the energy spectrum [8-10]. However, we have specifically chosen to conduct our investigations in the developing region of the round turbulent jet, where the flow transitions from non-equilibrium (developing region) to an equilibrium state (developed region) in view of the great theoretical and practical interest in this flow regime.

This flow is challenging from a measurement technical perspective, due to high turbulence intensities and high shear, while at the same time developing (from non-equilibrium to equilibrium) over a relatively short distance that makes it practical and manageable to work with on a typical lab scale. This has typically not been the case with the classical decaying grid turbulence experiments, with the exception of the fractal grid wake experiments of Vassilicos *et al.* (see [11] for a comprehensive summary of their work).

The Laser Doppler Anemometer (LDA) has been specifically chosen for our investigation due to its capability to resolve velocity measurement without disturbing the flow [12] and for its ability to accurately distinguish the spatial velocity components from each other, even at high turbulence intensities [13]. On top of that, our system is also driven by an in-house developed software, which has been validated against corresponding measurements using a commercial LDA system [14] and spatial structure functions based on data measured using a side scattering LDA configuration [15].

Having our own fully functional state-of-the-art LDA system in-house, we can accurately test these laws in challenging high shear and high intensity turbulent flows. This may provide extended information of the range of validity of the underlying assumptions that Kolmogorov stated (listed above) and specifically of the local equilibrium hypothesis.

2. Methodology

The jet, which is a replica of the one used by [16], consisted of a settling chamber with an inner and an outer nozzle designed to condition the flow to follow as closely as possible a laminar top-hat profile at the jet exit with diameter *D*=10 mm. A laser with a wavelength of 532 nm, was split into a pair of separate beams and directed through Bragg cells. The experimental setup, depicted in Fig. 1, was enclosed in a large tent of dimensions 2.5 x 3 x 10 m, with the jet positioned at the back of the enclosure to ensure a sufficient distance downstream for the measurement. The laser power was set to its maximum intensity, 1.29 W, with an amplifying current setting of 60 µA. The jet input pressure was set to 1 bar, corresponding to a jet exit velocity ≈ 43 m/s and *Re* ≈ 29000. The seeding pressure of 1.4 bar was chosen to obtain the optimum number of bursts in terms of maximized data rate. A frequency shift of 3 MHz was set on the Bragg cell and a total number of 400 records was taken at each measurement point. All the above-mentioned parameters were used throughout the whole measurement sequence, but with varying sampling rate (MHz) and record length (s) according to the varying conditions across the jet flow. The total number of samples of the burst signal were kept the same though i.e. 25 MS. Measurements of the axial component of velocities were acquired at several radial points along three downstream positions, *x/D*=10, *x/D*=15 and *x/D*=30 as illustrated in Fig. 2.

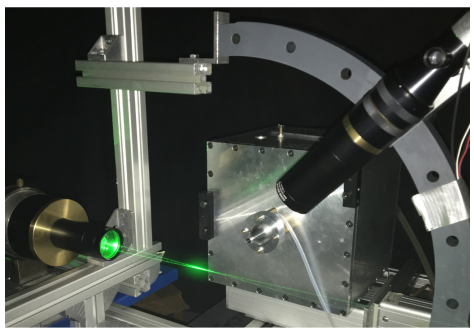

Fig. 1. Experiment setup showing jet exit, with the detector (lens focal length, *f*=200mm) positioned in 45° forward scattering

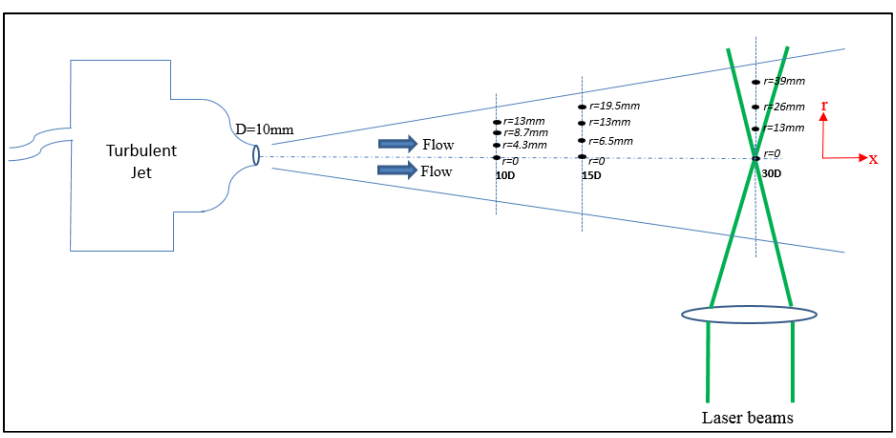

Fig. 2. Top view of the setup showing the measurement point distribution in the downstream *x*-direction and in the radial, *r*-direction

3. Results and Discussions

3.1 Velocity static moments

The raw signals obtained from the measurements were processed using our in-house software which provides the arrival time, residence time and velocities of each particle. The mean and variance of the velocity were calculated using residence time-weighting [16] to provide non-biased statistics of the LDA burst signal. Figures 3 and 4 show the radial profiles of mean velocity and variance at different downstream positions. As expected from theory and also some experimental work, e.g. [13,15], the highest velocity is spotted at the centreline for each mean velocity profile and the profiles seem to follow the expected nearly Gaussian shape, spread out and tapered in the downstream direction.

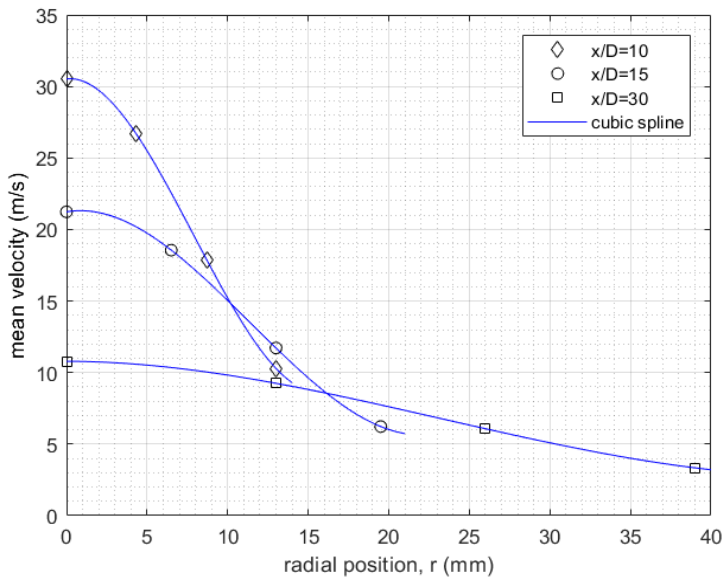

Fig. 3. Radial profiles of mean velocity at *x/D* = 10, 15 and 30 with cubic spline data interpolation

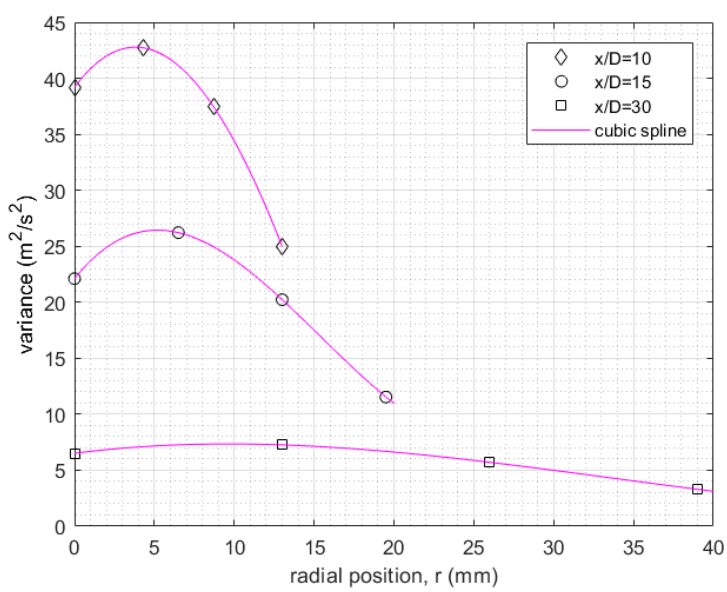

Fig. 4. Radial profiles of variance at *x/D* = 10, 15 and 30 with cubic spline data interpolation

3.2 Spatial turbulence kinetic energy spectra

Figures 5 to 7 show turbulent kinetic energy spectra as a function of wavenumber for different off-axis positions in the wave number (spatial) domain. The mapping from the temporal to the spatial domain was done using the instantaneous velocity magnitude (instead of the mean streamwise velocity as proposed by Taylor), which has been shown to yield a correct mapping between space and time using the so-called convection record [15]. Note that each spectrum was deliberately normalized to 1 in the low frequency asymptote for a clearer comparison in terms of its shape and slope with respect to Kolmogorov's -5/3 law. In the fully developed region at 30D, all spectra show a convincing collapse indicating that the turbulent kinetic energy is distributed nearly equally across the scales, independently of radial position from the jet centreline. It shows that the second order moments of turbulence in this fully developed region have finally reached a state of self-similarity. The clear -5/3 slope across a significant range, also observed in [14, 17-19], indicates the possibility of local turbulence equilibrium in the inertial subrange at this position in the flow, in accordance with the central, yet implicit assumption of Kolmogorov's local equilibrium of the small scales [7].

Meanwhile, the shape of the spectra varies with radial position in the developing region viz. at 10D and 15D, showing that the spatial structure of the velocity varies with different radial positions in the developing region of the jet. Higher energy is observed at lower wave numbers and spectra are shifted to lower wavenumbers, which explains that the smallest scales are growing away from the jet exit. The tendency to follow a -5/3 slope at higher wave number is the lowest at 10D, indicating that the local equilibrium assumption is not valid in this developing region of the jet.

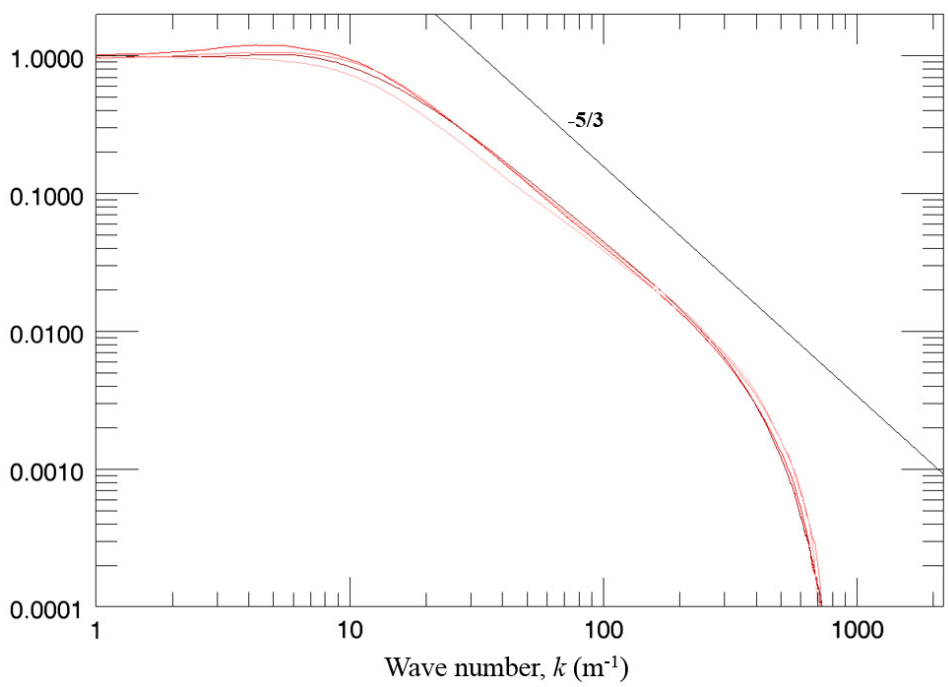

Fig. 5. Spatial turbulence kinetic energy spectra at 30D downstream. From *heavy red to light red*: off-axis position 0, 13, 26, 39 mm

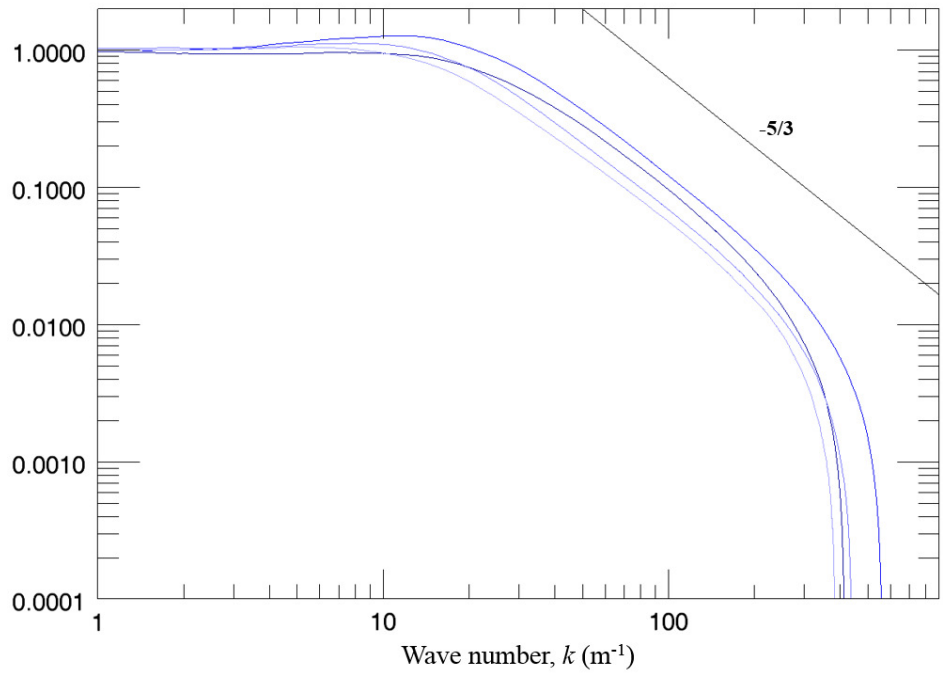

Fig. 6. Spatial turbulence kinetic energy spectra at 15D downstream. From *heavy blue to light blue*: off-axis position 0, 6.5, 13, 19.5 mm

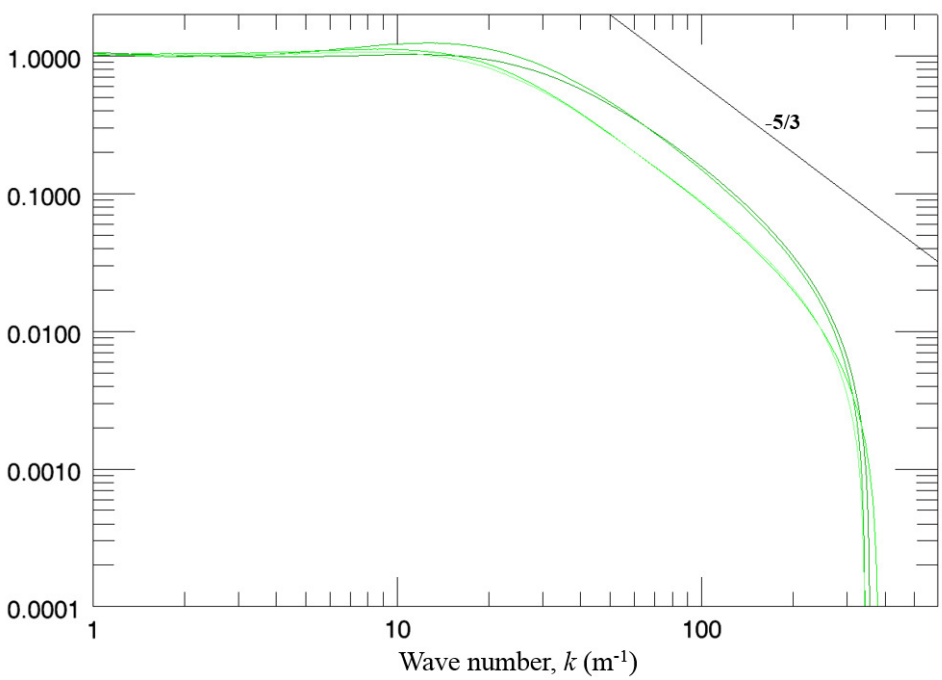

Fig. 7. Spatial turbulence kinetic energy spectra at 10D downstream. From *heavy green to light green*: off-axis position 0, 4.3, 8.7, 13 mm

3.3 Spatial second order structure function

Figure 8 shows the spatial second order structure functions across the range of measuring points. Also here, the temporal-to-spatial mapping has been done based on the convection record principle

where the instantaneous velocity magnitude has been employed [15], rather than the average streamwise velocity as proposed by Taylor. Each curve demonstrates that the large scales contain the most energy. The large scales are seen to grow as they move downstream. More large-scale activity is also relatively noticed in the outer part of the jet compared to in the centreline. The curves in the equilibrium region (30D) have a greater tendency to follow the expected 2/3 slope. Meanwhile, in the non-equilibrium region, the curves show slopes deviating from the 2/3 expected from the theory of Kolmogorov. This is another indication of the development of the turbulent scales in this region. The lower slope at 10D and 15D show that the large velocity increments have not yet been produced by the cascade process.

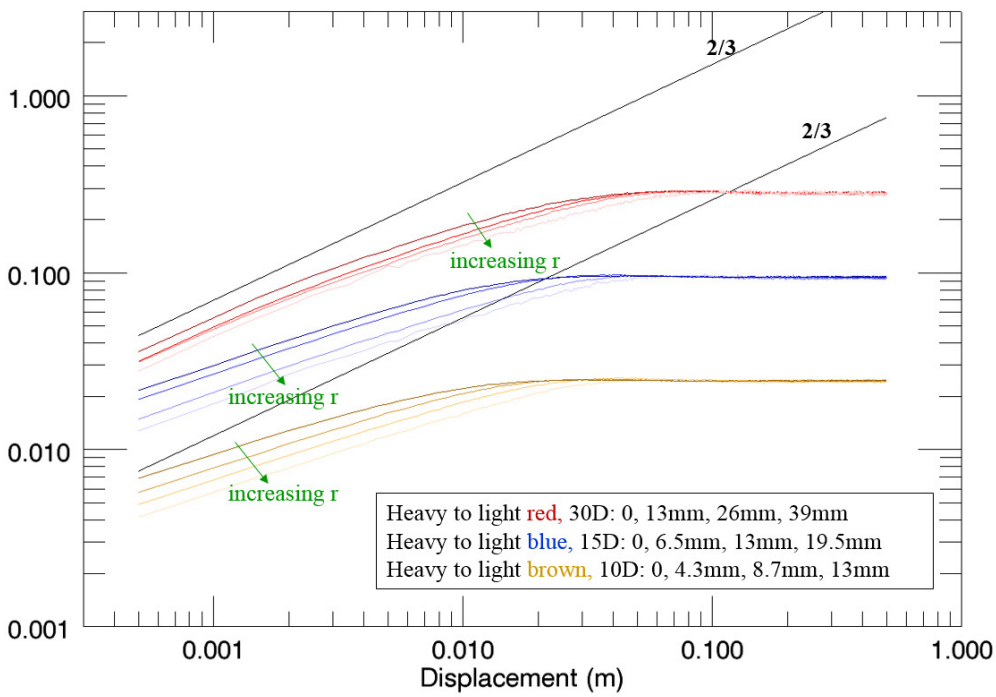

Fig. 8. Second order spatial structure functions. Curves of the same downstream position were shifted vertically for a clear comparison

4. Conclusions

The in-house LDA system was proven to successfully produce experimental results validating the Kolmogorov -5/3 and 2/3 laws in the fully developed region, while revealing interesting non-equilibrium features in the developing part of the jet flow. A more detailed mapping of the developing (non-equilibrium) region could provide further valuable insight into the limitations of the Kolmogorov -5/3 and 2/3 power laws and the underlying theory. This may not only help evaluate in which situations the restrictive assumptions suggested by Kolmogorov need to be relaxed but could also provide direct knowledge of the time scales required for the cascade process to develop into an equilibrium state.

Acknowledgement
The authors wish to acknowledge the support of Ministry of Higher Education Malaysia, Reinholdt W. Jorck og Hustrus Fond (grant journal no. 13-J9-0026), Fabriksejer, Civilingeniør Louis Dreyer

Myhrwold og hustru Janne Myhrwolds Fond (grant journal no. 13-M7-0039, 15-M7-0031 and 17-M7-0035) and Siemens A/S Fond grant no. 41.

References

[1] McDonough, James M. "Introductory lectures on turbulence: physics, mathematics and modeling." (2007).
[2] Frisch, Uriel. *Turbulence: the legacy of AN Kolmogorov*. Cambridge university press, 1995.
[3] Kolmogorov, Andrey Nikolaevich. "The local structure of turbulence in incompressible viscous fluid for very large Reynolds numbers." In *Dokl. Akad. Nauk SSSR*, vol. 30, no. 4, pp. 299-303. 1941.
[4] A. N. Kolmogorov, "Decay of isotropic turbulence in incompressible viscous fluids," *Dok. Akad. Nauk. S. S. S. R*, vol. 31, pp. 538–541, 1941.
[5] A. N. Kolmogorov, "Dissipation of energy in the locally isotropic turbulence," *Dok. Akad. Nauk. S. S. S. R*, vol. 32, pp. 19–21, 1941.
[6] Kolmogorov, Andrey Nikolaevich. "A refinement of previous hypotheses concerning the local structure of turbulence in a viscous incompressible fluid at high Reynolds number." *Journal of Fluid Mechanics* 13, no. 1 (1962): 82-85.
[7] G. K. Batchelor, *The theory of homogeneous turbulence*. Cambridge University Press, 1953.
[8] M. M. Gibson, "Spectra of Turbulence at High Reynolds Number," *Nature* 195 (1962): 1281–1283.
[9] Panchapakesan, N. R., and J. L. Lumley. "Turbulence measurements in axisymmetric jets of air and helium. Part 1. Air jet." *Journal of Fluid Mechanics* 246 (1993): 197-223.
[10] Wänström, Maja, William K. George, and K. E. Meyer. "Streamwise and radial decomposition of a turbulent axisymmetric jet." In *Progress in Turbulence and Wind Energy IV*, pp. 147-150. Springer, Berlin, Heidelberg, 2012.
[11] Vassilicos, J. Christos. "Dissipation in turbulent flows." *Annual Review of Fluid Mechanics* 47 (2015): 95-114.
[12] Buchhave, Preben, William K. George Jr, and John L. Lumley. "The measurement of turbulence with the laser-Doppler anemometer." *Annual Review of Fluid Mechanics* 11, no. 1 (1979): 443-503.
[13] Hussein, Hussein J., Steven P. Capp, and William K. George. "Velocity measurements in a high-Reynolds-number, momentum-conserving, axisymmetric, turbulent jet." *Journal of Fluid Mechanics* 258 (1994): 31-75.
[14] Buchhave, Preben, and Clara M. Velte. "Conversion of measured turbulence spectra from temporal to spatial domain." In *Whither Turbulence and Big Data in the 21st Century?*, pp. 343-362. Springer, Cham, 2017.
[15] Buchhave, Preben, and Clara M. Velte. "Measurement of turbulent spatial structure and kinetic energy spectrum by exact temporal-to-spatial mapping." *Physics of Fluids* 29, no. 8 (2017): 085109.
[16] Velte, Clara Marika, William K. George, and Preben Buchhave. "Estimation of burst-mode LDA power spectra." *Experiments in fluids* 55, no. 3 (2014): 1674.
[17] Velte, Clara M., Preben Buchhave, and William K. George. "Dead time effects in laser Doppler anemometry measurements." *Experiments in fluids* 55, no. 11 (2014): 1836.
[18] Buchhave, Preben, and Clara M. Velte. "Reduction of noise and bias in randomly sampled power spectra." *Experiments in Fluids* 56, no. 4 (2015): 79.
[19] C. M. Velte, P. Buchhave, and A. Hodzic, "Measurement of turbulent kinetic energy spectrum - Part 2 : Convection record measurements," *iTi Conference on Turbulence VII*, 2017, pp. 171–176.

Paper II

MJFAS MALAYSIAN JOURNAL OF FUNDAMENTAL AND APPLIED SCIENCES
PRINT ISSN: 2289-5981 | ONLINE ISSN: 2289-599X

RESEARCH ARTICLE

Mapping of the turbulent round jet developing region using a constant temperature anemometer (CTA)

Mohd Rusdy Yaacob [a,*], Rasmus Korslund Schlander [b], Preben Buchhave [c], Clara Marika Velte [b]

[a] Faculty of Electrical Engineering, Universiti Teknikal Malaysia Melaka, Durian Tunggal, Malaysia
[b] Department of Mechanical Engineering, Technical University of Denmark, Lyngby, Denmark
[c] Intarsia Optics, Sønderskovvej 3, Birkerød, Denmark

* Corresponding author: rusdy@utem.edu.my

Article history
Received 3 May 2018
Revised 25 August 2018
Accepted 11 September 2018
Published Online 25 October 2018

Graphical abstract

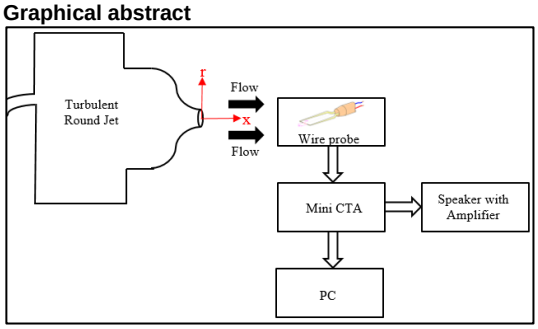

Abstract

The fully developed round turbulent jet has been extensively studied, whereas the developing region is much less understood. The high shear and turbulence intensities in the most interesting parts of the developing region make them inaccessible to common measurement techniques such as Constant Temperature Anemometry (CTA) due to the high demands on the measurement techniques for accuracy of the measurements. Turbulence measurements are therefore planned using our in-house laser Doppler anemometer (LDA) system based on its capability to provide accurate measurements and with its inherent ability to properly distinguish velocity components. A rigorous measurement with the intended LDA system however demands impractical processing time, so knowing the critical points at which measurement are to be taken will save valuable time. This information is herein acquired significantly faster and more practically, however less accurately, with single-wire CTA. A high-resolution measurement was done using a computer-controlled single-wire CTA with the wire probe mounted perpendicular to the incoming flow from the jet orifice. The measurements covered several points in the radial (*r*-direction) along *x/D*=10, *x/D*=15, *x/D*=20 and *x/D*=30 downstream (where *D* is the jet exit diameter), with spatial resolutions ranging from 1 to 3 mm between the points, depending on how far the measurement was from the jet centerline. A proper alignment was also conducted prior to measurement so that the same points can be reached again for LDA measurement on the same jet afterwards. The radial profiles of mean velocity and turbulence intensity at each downstream position are presented to show the statistics of the air flow inside and outside the jet. As expected from theory, the mean profiles display a nearly Gaussian shape, spread out and tapered with the downstream direction. The highest velocities are located at the centerline.

***Keywords*:** Hot wire; turbulent round jet, turbulence

INTRODUCTION

The flow field of a turbulent round jet is not only divided into the delevoping and fully developed regions in the streamwise direction (Mossa & Serio, 2016), but also in the variations along the radial direction which comprises three different layers viz. centreline layer, shear layer region and outer region (Ball *et al.*, 2012). These regions and layers are clearly illustrated in Fig. 1 and Fig. 2. The turbulent round jet is a classical turbulent flow of special interest for fundamental investigations (Hinze, 1975), where the fully developed region has been extensively studied, see e.g. (Hussein *et al.*, 1994). Due to the difficulties in measuring accurately high shear and high turbulence intensity flows, the developing region of the jet has remained substantially underexplored. This developing region is particularly interesting, however, since it allows for studying the downstream (or temporal) development of the turbulence cascade from non-equilibrium to an equilibrium state (in the fully developed jet). Accurate measurements in this region may thus provide highly valuable and novel information that can challenge the established theory of turbulence (Vassilicos, 2015).

LDA is capable of acquiring velocity measurements non-intrusively (i.e. without disturbing the flow) (Buchhave *et al.*, 1979) and are also able to accurately distinguish the spatial velocity components, even at high turbulence intensities (Hussein *et al.*, 1994). However, our improved in-house LDA system (Velte *et al.*, 2017; Buchhave & Velte, 2017; M. R. Yaacob *et al.*, 2018) demands much longer computational time compared to computer-controlled CTA, which is faster and easier to use especially with automated calibration (Jørgensen, 1996). Having to obtain the mean velocity and turbulence intensity profiles quickly from CTA measurement in our under-investigation turbulent round jet, will be time-efficient and the results will be useful for the upcoming high-resolution LDA measurement in mapping the developing region of the same jet using the same flow conditions. The results are aimed to help us in finding the boundary between the jet and the surrounding air, and also the shear layer for different downstream positions.

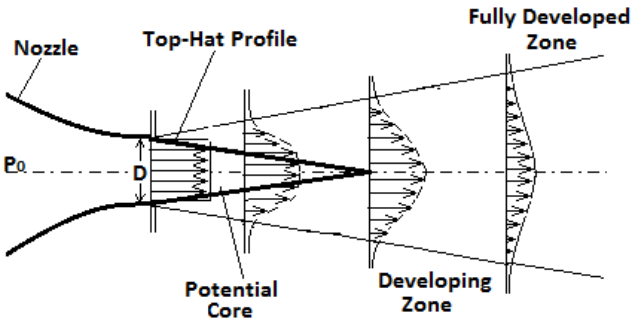

Fig. 1 Streamwise development and the various regions of a turbulent round jet (Kaushik *et al.*, 2015).

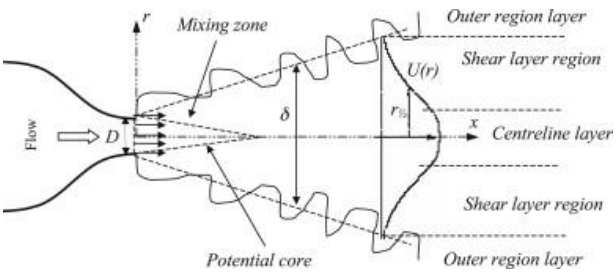

Fig. 2 Different layers of turbulent round jet in radial direction (Fellouah *et al.*, 2009).

EXPERIMENTAL METHOD

CTA provides velocity time-history information in one measurement position. Based on the convective heat transfer principle (Jørgensen, 2002), the passing air will cause temperature change on the heated wire placed within the flow. The anemometer is keeping the wire at a constant temperature by adjusting the voltage passing through the wire as depicted in Fig. 3.

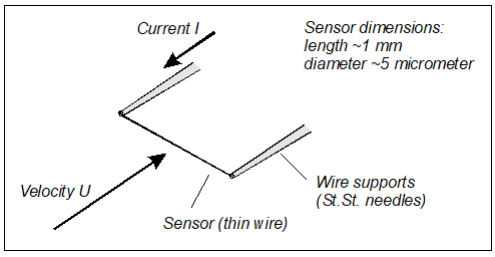

Fig. 3 Close-up of support and wire-sensor with a velocity, *U*, and current, *I* in the wire (F. Gökhan Ergin, 2016).

The jet box used for these investigations was made of aluminum with dimensions 58 x 58.5 x 59 cm and fitted with an outer nozzle which was designed to condition the flow to follow as closely as possible a laminar top-hat profile at the jet exit with diameter D =10 mm. The turbulent round jet itself was a replica of the one used by (Velte *et al.*, 2014), from which further details can be found. The jet input pressure was set to 1 bar, corresponding to a jet exit velocity ≈ 30 m/s and Reynolds number, $Re \approx 20{,}000$.

Prior to the measurements, the system was first calibrated using an automatic calibration system from Dantec Dynamics. This was separately done by increasing the air flow in accordance with pressure difference inside a well conditioned wind tunnel and then fitting a 4th-order polynomial to a relation between output voltage and velocity. The experimental settings listed in Table 1 were considered during the calibration.

Table 1 Experiment setting.

Sampling frequency	10 kHz
Sampling time	10s
Number of samples	100 kS
Temperature	≈ 21.5°C
Atmospheric pressure	≈ 1015hPa

The measurements were conducted using a uni-directional single sensor probe where the thin wire was placed perpendicular to the incoming flow from the jet orifice. The probe was mounted on a support (see Fig. 4) and connected to the CTA anemometer and computer installed with Dantec Dynamics MiniCTA software (see Fig. 5), from which a single time series data was reduced to a series of fluctuating velocity of the streamwise component, leading to the calculation of mean and rms velocity for each measurement point.

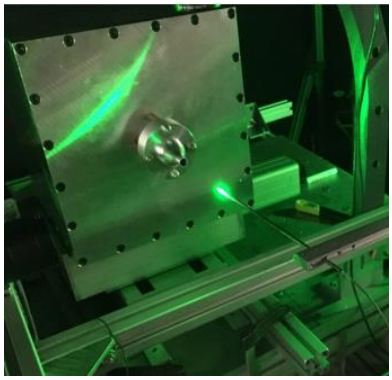

Fig. 4 CTA experiment showing jet orifice and the support mounted wire probe.

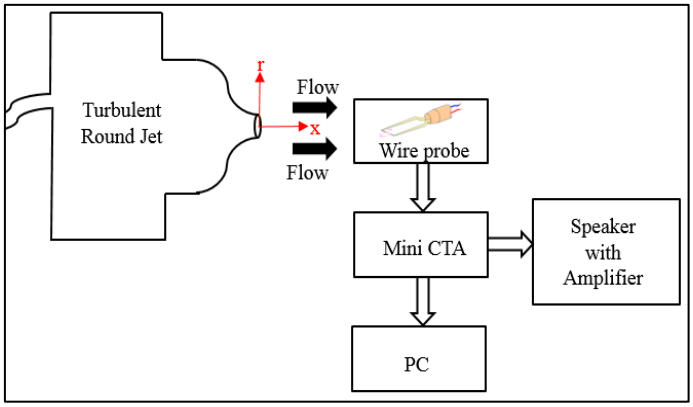

Fig. 5 Overall experimental setup. A speaker with amplifier was also installed at the CTA output to produce noise from the turbulence to help locating regions of various turbulence intensity such as the highest shear layer.

The measurement covered several points in the radial (r-direction) along x/D=10, x/D=15, x/D=20 and x/D=30 downstream, with resolution ranging from 1 to 3 mm between the points, depending on how far the measurements were from the jet centreline. The jet box was mounted on a 3-axis traversing system so that it can be easily manoeuvred to the desired points correspondingly when performing the LDA measurement.

Having in mind that the results will map the points or region of interest for the incoming LDA measurement, the probe was first carefully aligned (see Fig. 6) so that the thin wire was placed at the pinhole of a photodetector (M.R. Yaacob *et al.*, 2018), at which the jet centreline and measurement volume of LDA has been identified to overlap beforehand, without moving or changing the position of the photodetector. This location of the probe was fixed while traversing only the jet throughout the CTA measurement. The same points can therefore consequently be reached again for LDA measurement.

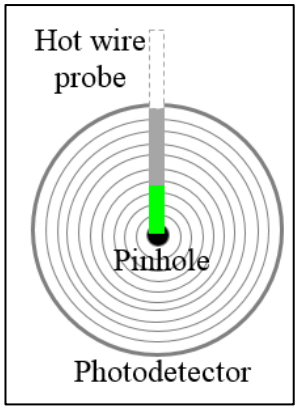

Fig. 6 View through a photodetector showing probe alignment with the pinhole.

RESULTS AND DISCUSSION

In the figures presented herein, the data have not been normalized or fitted to any order of polynomial, in order to display the direct flow results. Fig. 7 shows the radial profiles of mean velocity at various downstream positions throughout the developing region, namely *x/D* = 10, 15, 20 & 30. As expected from theory, the profiles seem to follow a nearly Gaussian shape, spread out and tapered with the downstream position. The highest average velocities are spotted at the centreline, while the points where average velocity is very close to zero indicate that the measurement was somewhere near the boundary between the jet and the surrounding air, which should be noted when conducting the LDA measurement.

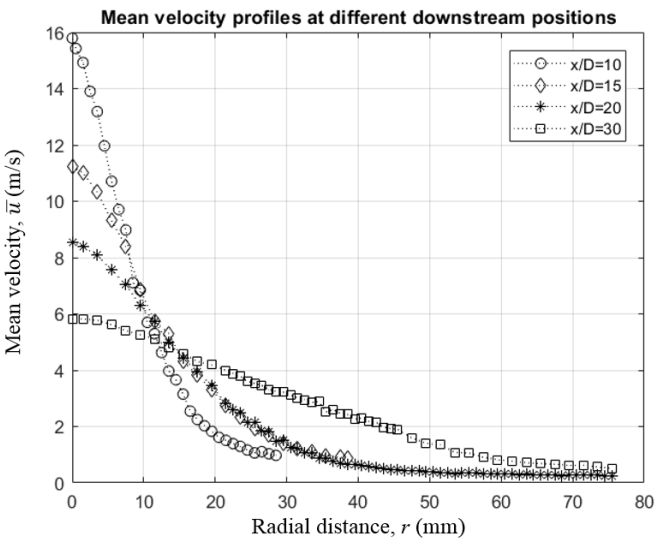

Fig. 7 Radial profiles of mean velocity at different downstream positions *x/D* = 10, 15, 20 & 30 where *D* is the jet exit diameter.

Fig. 8 shows radial profiles of the turbulence intensity, *I*, at different downstream positions:

$$I = \sqrt{\frac{\overline{u'^2}}{\bar{u}^2}} \quad (1)$$

where $\bar{u}$ is the mean velocity and u' is the rms velocity.

When the measurements progress away from the centerline, the turbulence intensity increases in the region where the shear layer is located. In these regions, the high levels of fluctuations will require an appropriate frequency shift to measure accurately with the LDA system (Buchhave, 1984). Again, keep in mind that the profiles obtained are just an approximation (and intended only to map the measurement points for the latter LDA measurement) and does not accurately describe turbulence especially in the region where fluctuations are large compared to the streamwise convection. More accurate counterparts measured using LDA, showing a rapid growth of turbulence intensity with radial distance from the centerline, can be found in (Buchhave & Velte, 2017). However the approximation is still more acceptable when turbulence intensities are low as the streamwise convection dominates over the fluctuations.

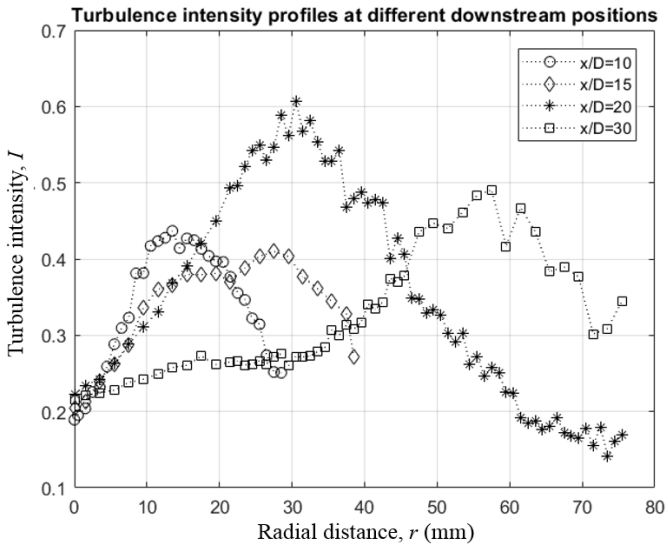

Fig. 8 Radial profiles of streamwise turbulence intensity at different downstream positions *x/D* = 10, 15, 20 & 30 where *D* is the jet exit diameter. With more accurate LDA measurements, the turbulence intensity can be seen to monotonically increase rapidly with radial distance (Buchhave & Velte, 2017).

CONCLUSION

A CTA measurement was successfully performed to provide a measurement scheme and to identify the spatial extent of regions of interest for future, more rigorous LDA turbulence measurement. The outcome of the planned LDA measurements will be published in a separate scientific article.

ACKNOWLEDGEMENT

The authors wish to acknowledge the support of Ministry of Higher Education Malaysia, Reinholdt W. Jorck og Hustrus Fond (grant journal no. 13-J9-0026) and Fabriksejer, Civilingeniør Louis Dreyer Myhrwold og hustru Janne Myhrwolds Fond (grant journal no. 13-M7-0039 and 15-M7-0031). Also we are grateful to Benny Edelsten (Laboratory Engineer) for helping out during the measurement.

REFERENCES

Ball, C. G., Fellouah, H. & Pollard, A., 2012. The flow field in turbulent round free jets. *Progress in Aerospace Sciences*, 50, pp. 1–26.

Buchhave, P., 1984. Three-component LDA measurements. *Disa Information*, (29), pp. 3–9.

Buchhave, P., George, W. K. & Lumley, J. L., 1979. The measurement of turbulence with the laser-Doppler anemometer. *Annual Review of Fluid Mechanics*, 11, pp. 443–503.

Buchhave, P. & Velte, C. M., 2017. Measurement of turbulent spatial structure and kinetic energy spectrum by exact temporal-to-spatial mapping. *Physics of Fluids*, 29(8), 085109.

F. Gökhan Ergin, 2016. *Constant Temperature Anemometry - A Theoretical Introduction*. Dantec Dynamics.

Fellouah, H., Ball, C. G. & Pollard, A., 2009. Reynolds number effects within the development region of a turbulent round free jet. *International Journal of Heat and Mass Transfer*, 52(17–18), pp. 3943–3954.

Hinze, J. O., 1975. *Turbulence* 2nd ed., Michigan: McGraw-Hill.

Hussein, H. J., Capp, S. P. & George, W. K., 1994. Velocity measurements in a high-Reynolds-number, momentum-conserving, axisymmetric, turbulent jet. *Journal of Fluid Mechanics*, 258, pp. 31–75.

Jørgensen, F. E., 2002. *How to measure turbulence with hot-wire anemometers - A practical guide*. Dantec Dynamics.

Jørgensen, F. E., 1996. The computer-controlled Aspects of set-up, probe calibration, data acquisition and data conversion. *Measurement Science and Technology*, 7(10), pp.1378–1387.

Kaushik, M., Kumar, R. & Humrutha, G., 2015. Review of computational fluid dynamics studies on jets. *American Journal of Fluid Dynamics*, 5(3A), pp.1–11.

Mossa, M. & Serio, F. De, 2016. *Rethinking the process of detrainment : Jets in obstructed natural flows*. Bari: Nature Publishing Group.

Vassilicos, J. C., 2015. Dissipation in turbulent flows. *Annual Review of Fluid Mechanics*, 47, pp. 95–114.

Velte, C. M., Buchhave, P. & Hodzic, A., 2017. Measurement of turbulent kinetic energy spectrum - Part 2 : Convection record measurements. In *iTi Conference on Turbulence VII*. Springer, pp. 171–176.

Velte, C. M., George, W. K. & Buchhave, P., 2014. Estimation of burst-mode LDA power spectra. *Experiments in Fluids*, 55(1674), p. 1-20.

Yaacob, M. R., Schlander, R. K., Velte, C. M., & Buchhave, P., 2018. Validation of improved laser Doppler anemometer (LDA) based on the fully developed turbulent round jet. *Symposium of Electrical, Mechatronics and Applied Science*. November 2018. Melaka. [Manuscript accepted for publication].

Yaacob, M. R., Schlander, R. K., Velte, C. M., & Buchhave, P., 2018. Experimental evaluation of kolmogorov's -5/3 and 2/3 power laws in the developing turbulent round jet. *Journal of Advanced Research in Fluid Mechanics and Thermal Sciences*, 45(2), pp. 14–21.

Paper III

Proceedings of Symposium on Electrical, Mechatronics and Applied Science 2018 (SEMA'18), pp. 89-90, 8 November 2018

Validation of improved laser Doppler anemometer (LDA) based on the fully developed turbulent round jet

Mohd Rusdy Yaacob[1*], Rasmus Korslund Schlander[2], Preben Buchhave[3], Clara Marika Velte[2]

[1)] Faculty of Electrical Engineering, Universiti Teknikal Malaysia Melaka,
Hang Tuah Jaya, 76100 Durian Tunggal, Melaka, Malaysia
[2)] Department of Mechanical Engineering, Technical University of Denmark, 2800 Kgs. Lyngby, Denmark
[3)] Intarsia Optics, Sønderskovvej 3, 3460 Birkerød, Denmark

[*]Corresponding e-mail: rusdy@utem.edu.my

Keywords: laser Doppler anemometer; turbulent flow; energy spectrum

ABSTRACT – Accurate turbulence measurements are practically challenging even with common measurement techniques. The existing commercial LDA processors come with practical limitations affecting the measurement accuracy. A novel LDA has therefore been developed with utilization of recent technologies and state-of-the-art hardware and software, which enhance the capability of turbulence flow measurements. The software embedded offers an unlimited functionality for signal processing and data interpretation. Measurements were performed in the fully developed (equilibrium) region of a round jet at which the spatial turbulent kinetic energy spectra were found to perfectly match the expected Kolmogorov's -5/3 power law in the equilibrium region.

1. INTRODUCTION

Turbulence has long been a study which is yet to be completely defined and discovered especially in the developing (non-equilibrium) region [1]. Accumulating evidence point to that accurate investigations of flows in changing circumstances may very well lead to serious questioning of the established theory [2]. In order to realize this, it is of great interest to develop a novel, well-functioning Laser Doppler anemometry system that can measure turbulence under notoriously difficult conditions such as those at large radial distances from the centerline in a round turbulent jet (high turbulence intensities and high shear). LDA has earlier proven its significance as the primary choice, accurate and non-intrusive technique for turbulent flow measurements [3]. However, the current commercial LDA systems suffer from practical limitations, e.g., data buffering limitations and additional dead time due to data transfer [4]. By conducting the measurements using our self-developed LDA system in the fully developed jet, which has been thoroughly investigated and understood [5], the functionality of the system can be substantially validated upon comparison with the existing turbulence theory. From here, more rigorous measurements can later be performed in the non-equilibrium and high shear regions, which will present various degrees of difficulty for the LDA processor, with an ultimate aim, i.e., to test the important outstanding questions of turbulence, e.g., the universal equilibrium assumption.

2. METHODOLOGY

An axisymmetric turbulent round jet has been chosen as the test bed for the LDA measurement since it was proven to produce spectral results that are in good agreement with the Kolmogorov theory of turbulence in the fully developed region [6]. The jet is a replica from the one used by [7], with an exit diameter, *D* and contraction ratio of 10 mm and 3.2:1, respectively. The LDA was operated in burst-mode and 90º side-scattering detection configuration as in Figure 1. It consists of a continuous wave laser emitting a single beam with wavelength, λ = 532 nm, which is split into two coherent beams and passed through dual Bragg cells with 2 MHz effective frequency shift. This value is chosen based on the maximum Doppler frequency or velocity to be acquired from the measurement. The beams are then directed through a converging lens (focal point = 200 mm) and focused to intersect and create a measurement volume (MV), based on the dual-beam principle. Glycerin particles (1 to 5 µm) are seeded into the flow to pass through the MV. With the known fringe spacing, *df*, velocity can be determined using Equation (1):

$$\mathbf{u} = \frac{\lambda \mathbf{d_f}}{2\sin\left(\theta/_2\right)} \qquad (1)$$

where θ is the angle between the two beams.

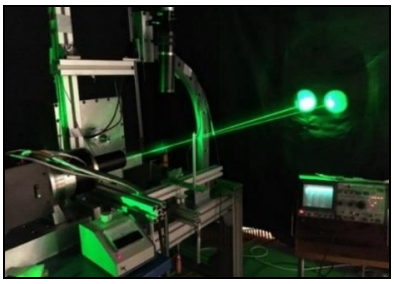

Figure 1 LDA system enclosed in a large tent

The block diagram for data acquisition of the LDA system is shown in Figure 2. The light scattered by each particle is received by a detector coupled to a photomultiplier which amplifies the photocurrent before passing through a low pass filter circuit. An electronic signal modulated by the frequency is then delivered to the oscilloscope and computer.

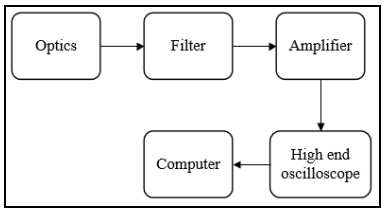

Figure 2 Data acquisition of the LDA system

Measurements were carried out along the radial, *r* direction at *x/D*=30 across the shear region as illustrated in Figure 3. The jet input pressure was set to 1 bar with an exit velocity around 40 m/s and the particles were fed into the flow at 1.2 bar. The laser was set nearly to its maximum intensity (1.29 W), with an amplifying current of 70 μA. A total of 400 records were taken at each measurement point with 2 s or 5 s record length, which corresponded to 25 MHz or 10 MHz sampling rate, respectively, optimized to the flow conditions at each measurement point. The output measured was transferred to a computer and processed using our self-developed software to obtain the spatial turbulent kinetic energy spectra employing the convection record method [8].

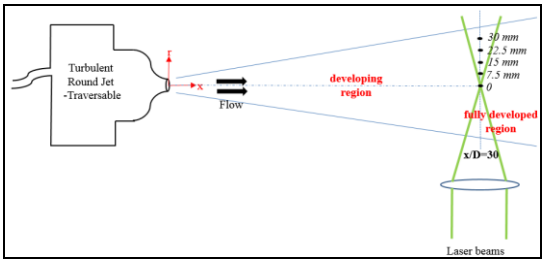

Figure 3 Distribution of the measurement points

3. RESULTS AND DISCUSSIONS

The shape of the kinetic energy spectrum is investigated in the fully developed region, i.e., at *x/D*=30 as in Figure 4.

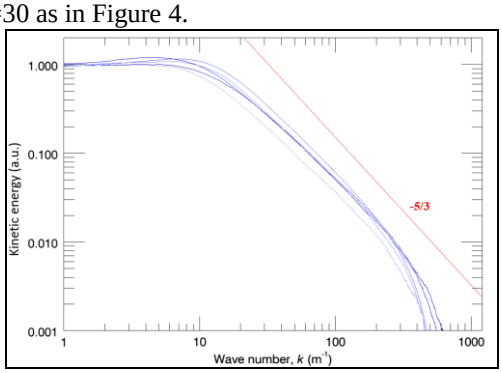

Figure 4 Radial development of spatial turbulent kinetic energy spectra at *x/D* = 30. From *heavy to light blue*: off-axis position 0, 7.5, 15, 22.5, 30 mm

The clear -5/3 slope across a significant range shows a good agreement with the -5/3 law for an (assumed) inertial subrange and the local equilibrium hypothesis postulated by Kolmogorov [9].

This behavior has also been previously supported experimentally using other measurement methods such as hot-wire anemometry [10] and stereoscopic Particle Image Velocimetry [11], which is clearly consistent with our results even at large radial distances from the centerline.

4. CONCLUSIONS

A high flexibility and accuracy novel LDA system has successfully been developed which provides the state-of-the-art tools; hardware in acquiring the data from measurement and software for data processing. The results obtained opens doors for further investigation to test the widely applied local equilibrium hypothesis for the structure of small scale turbulence.

ACKNOWLEDGEMENT

This work was supported by the Ministry of Education Malaysia, Reinholdt W. Jorck og Hustrus Fond (grant journal no. 13-J9-0026), Fabriksejer, Civilingeniør Louis Dreyer Myhrwold og hustru Janne Myhrwolds Fond (grant journal no. 13-M7-0039, 15-M7-0031 and 17-M7-0035) and Siemens A/S Fond grant no. 41.

REFERENCES

[1] Kolmogorov, A. N. (1941). The local structure of turbulence in incompressible viscous fluid for very large Reynolds numbers. *C. R. Akad. Sci. SSSR 30*, 301.

[2] Vassilicos, J. C. (2015). Dissipation in Turbulent Flows. *Annu. Rev. Fluid Mech. 47*, 95–114.

[3] Buchhave, P., George, W. K. and Lumley, J. L. (1979). The measurement of turbulence with the laser-Doppler anemometer. *Annu. Rev. Fluid Mech. 11*, 443–503.

[4] Buchhave, P., Velte, C. M. and George, W. K. (2014). The effect of dead time on randomly sampled power spectral estimates. *Exp. Fluids 55(2)*, 1–8.

[5] Buchhave, P. and Velte, C. M. (2017). Conversion of Measured Turbulence Spectra from Temporal to Spatial Domain. In *Whither Turbulence and Big Data in the 21st Century?*, Springer, 343–362.

[6] Panchapakesan, N.R. and Lumley, J. L. (1993). Turbulence measurements in axisymmetric jets of air and helium . Part 1 . Air jet. *J. Fluid Mech. 246*, 197–223.

[7] Velte, C. M., George, W. K. and Buchhave, P. (2014). Estimation of burst-mode LDA power spectra. *Exp. Fluids 55(3)*, 1674.

[8] Buchhave, P. and Velte, C. M. (2017). Measurement of turbulent spatial structure and kinetic energy spectrum by exact temporal-to-spatial mapping. *Phys. Fluids 29(8)*.

[9] Batchelor, G. K. (1953). *The theory of homogeneous turbulence*. Cambridge University Press.

[10] Gibson, M. M. (1962). Spectra of turbulence in a round jet. *J. Fluid Mech. 15*, 161–173.

[11] Velte, C. M., Buchhave, P. and Hodzic, A. (2017). Measurement of turbulent kinetic energy spectrum - Part 2 : Convection record measurements. *iTi Conference on Turbulence VII*, , 171–176.

Paper IV

A novel laser Doppler anemometer (LDA) for high-accuracy turbulence measurements

Mohd Rusdy Yaacob[1, ID]. Rasmus Korslund Schlander[2] . Preben Buchhave[3] . Clara Marika Velte[4, ID]

Abstract

High accuracy and dynamic range have been some of the most prominent challenges when it comes to fine-scale turbulence measurements. The current commercial LDA processors, which perform the signal processing of Doppler bursts directly using hardware components, are essentially black boxes and in particular are renown for suffering from practical limitations that reduce the measurement reliability and accuracy. A transparently functioning novel LDA, utilizing advanced technologies and up-to-date hardware and software has therefore been developed to enhance the measurement quality and the dynamic range. In addition, the self-developed software comes with a highly flexible functionality for the signal processing and data interpretation. The LDA setup and the combined forward/side scattering optical alignment (to minimize the effective measuring volume) are described first, followed by a description of the signal processing aspects. The round turbulent jet has been used as the test bed since it presents a wide range of degree of difficulty for the LDA processor (accuracy, dynamic range etc.) across the different radial distances and downstream development. The data are diagnosed for dynamic range in residence and interarrival times, and compared to a typical hardware driven processor. The radial profiles of measured mean streamwise velocity and variance agree well with previous studies of the round jet. The spatial turbulent kinetic energy spectra in the fully developed region perfectly match the expected (and in this region well established) -5/3 power law even for the largest measured distances from the centerline (where shear and turbulence intensity are significant).

Graphical Abstract

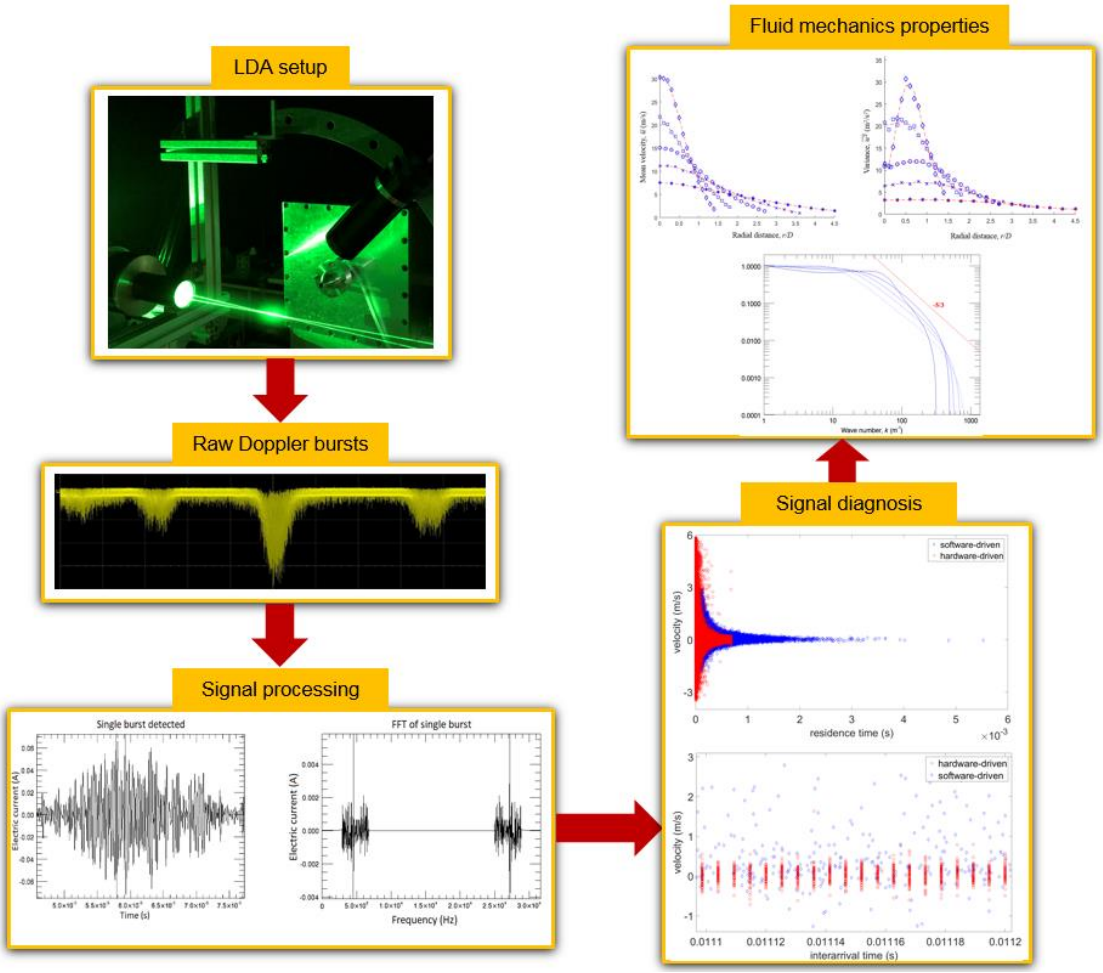

1 Introduction

Despite its omnipresence in various applications, e.g., combustion engines and weather forecast, turbulence has long been an area of classical physics which is yet to be completely defined and discovered (Davidson 2004; L'vov and Procaccia 2007). While the equilibrium aspects of stationary turbulence has been thoroughly investigated and understood (Batchelor 1953; Kolmogorov 1941c, 1962), the non-equilibrium counterparts are still largely underexplored. Vassilicos and his team (Goto and Vassilicos 2015; Mazellier and Vassilicos 2010; Valente and Vassilicos 2012; Vassilicos 2015) have raised serious questions to the established theory based on accumulated evidence from both experimental and simulation-based investigations.

One of the main reasons for the lack of our understanding of these non-equilibrium flows is that they are notoriously difficult to measure accurately since they are typically shear flows of high turbulence intensity and of great variations in dynamic range. If implemented and analyzed correctly, the laser Doppler anemometer (LDA in the following) is the most accurate existing instrument to measure these difficult flows, since it has inherently a wide dynamic range, unlike e.g., correlation based Particle Image Velocimetry, and it has the ability to, without ambiguity, distinguish between and discern the velocity components, unlike e.g., hotwires. Furthermore, a major challenge subsequently arises in measuring the kinetic energy spectrum, which is a powerful tool that can map the energy across all turbulence scales and provides valuable information about turbulence generation and its assumed cascade development more precisely (Frost 1977). Similar challenges arise when measuring the physical space counterparts, such as correlations (e.g., covariances) and structure functions (which are central to the nowadays debated Kolmogorov equilibrium description(s) of turbulence) (Kolmogorov 1941b, 1941a, 1941c, 1962).

LDA is one of the most preferred measurements techniques in these challenging turbulent flow measurement since it has been significantly recognized for its unique favorable properties in various experimental investigations (Barker 1973; Buchhave, George, and Lumley 1979; Peiponen, Myllylä, and Priezzhev 2009). It can truly distinguish the spatial velocity components of a flow from each other (Hussein, Capp, and George 1994) and therefore produce reliable data. However, existing commercial LDA systems have been restricted with some practical limitations, e.g., for turbulence measurements that require high dynamic range and signal-to-noise ratio (Buchhave, Velte, and George 2014; Velte, Buchhave, and George 2014). A more detailed discussion of the practical limitations can be found in (Velte, George, and Buchhave 2014).

It is therefore of great interest to develop a novel, well-functioning, LDA system that is able to measure turbulence more accurately. With a more well-functioning LDA processor, it is possible to credibly measure turbulence in experimentally challenging regions, e.g., non-equilibrium, high intensity and high shear regions, to test the debatable universal equilibrium theory of Kolmogorov (Batchelor 1953; Kolmogorov 1941b, 1941a, 1941c, 1962; Monin and Yaglom 1972).

2 Methodology

2.1 Flow generation facility

The axisymmetric turbulent round jet has been a popular research subject for turbulent flow investigations since many years (Abdel-Rahman, Chakroun, and AI-Fahed 1997). Moreover, in the fully developed region, it was proven to produce results that are in good agreement with the classical Kolmogorov theory of turbulence (Gibson 1962; Panchapakesan N. R. and Lumley 1993; Wänström, George, and Meyer 2012). At the same time, this flow presents a wide variation of degree of shear and turbulence intensities across the downstream and radial directions, which is why it has been chosen as the test bed for validation of turbulence measurement with our LDA system.

The axisymmetric turbulent round jet used for this measurement is a replica of the one used by Velte, George and Buchhave (2014). It is fitted with an outer nozzle at the end, having an exit diameter D = 10 mm and contraction ratio of 3.2:1. Pressurized air is injected through the jet together with the glycerin particles (~1-5 μm) at regulated pressure values. The particles have been proven to be sufficiently small to faithfully track the flow to a sufficient degree, while also scattering light sufficiently well to be well detectable by the LDA system (Capp 1983). The jet is mounted on a two-axis traversing system which is driven by, for each axis, a hybrid two-phase stepper motor and computerized by a motion control software, *RemoteWin* for maneuvering the jet along streamwise (x) and radial (r) directions. With this, the jet centreline can be easily traversed to different coordinates within the flow for turbulence measurement at high spatial resolution. The choice of traversing the jet instead of the LDA optics is based on the sensitivity in alignment of the LDA optics, since this is a combined forward/side scattering system (as will be described below).

2.2 Laser Doppler anemometer

The LDA is operated in the burst-mode (Roberts, Downie, and Gaster 1980) and consists of a continuous wave laser beam with wavelength, λ = 532 nm split into two coherent beams. The two beams are directed through a dual Bragg cell (BC in the following) in order to distinguish the moving direction of the particles along the measured component axis (Buchhave 1984; Diop, Piponniau, and Dupont 2019). This issue was remarked to be critical, in particular within the flow region where fluctuations and turbulence intensities are high (Yaacob et al. 2018), since the velocity variations are more likely to exist in both directions. The frequency of one of the beams is shifted by 40 MHz, which value is known from the BC module used, while the frequency of the other beam is shifted by 37 MHz. The two beams consequently experience 3 MHz of effective frequency shift, f_s which creates movement of the interference fringes in the direction opposite to the main flow direction. This value is sufficient for acquiring the maximum Doppler

frequency or velocity from our measurement (Peiponen, Myllylä, and Priezzhev 2009).

The parallel beams are then passed through a converging lens and focused to intersect at a focal point of 200 mm based on the dual-beam principle (Bartlett and She 1976; Grant and Orloff 1973; Sommerfeld and Tropea 1999). The volume where the frequency shifted beams intersect, commonly referred to as the measurement volume (MV in the following), is where the local velocity of the flow is measured (Albrecht et al. 2003).

The working block diagram for acquiring the data from LDA is depicted in Fig. 1. The photodetector receives the light scattered by each seeding particle and converts the photons into photocurrent. The detector is also coupled to a photomultiplier (Hamamatsu H10425) that amplifies the photocurrent internally before passing through the load resistor in the filter circuit. A first-order low pass filter (load resistor, R=270 Ω) is connected between the photomultiplier which has capacitance value of 22 pF, and the amplifier, giving a resulting cut-off frequency of around 26 MHz. The analog frequency modulated signal is then delivered to and visualized through a high end oscilloscope. An A/D converter is also embedded in the scope yielding a 13 bits resolution. In order to utilize this resolution, the amplitude on the oscilloscope must be set such that most of the bursts can be seen in their full size. Some of the largest burst are allowed to be clipped in order to get most of the bursts digitized with the full resolution, which is critical in computing the energy spectra. The clipping was shown not to cause any biasing of the Doppler frequency.

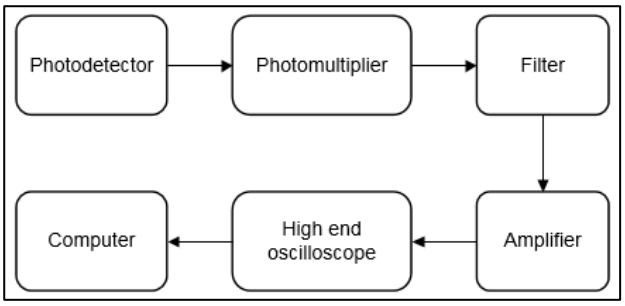

Fig. 1 Block diagram for data acquisition of the LDA system

The experimental setup (see Fig. 2) is enclosed in a large tent of dimensions 3 x 5.8 x 3.1 m^3, made out of black canvas to minimize light pollution and to create an undisturbed environment for the jet to freely develop. With the jet positioned at the back of the enclosure, the jet flow generated in the facility should be expected to correspond well to a free jet up until x/D = 70, which is sufficient for the purpose of our current experiments and future investigations (Hussein, Capp, and George 1994; Wänström, George, and Meyer 2012). The LDA system is operated in a forward-scattering detection mode by mounting the detector at 45° from the MV in order to minimize the light extinction from the Mie scattering and improve the signal-to-noise ratio (Fischer 2017). Such configuration will also result in a smaller and nearly spherical MV (since the optical cross-section of the detector dictates the effective MV) to obtain unbiased measurement especially in a highly turbulent flow and achieve the highest possible spatial resolution (Buchhave and Velte 2017b). A schematic side view of the setup is also shown in Fig. 3.

2.3 Optical alignment

Operating the system in a combined a forward/side scattering mode demanded thorough and rigid adjustment on the optical parts in order to assure good quality of the Doppler signals from the measurement. It is difficult to see by naked eye whether the two beams do in fact overlap to produce an MV. Therefore, a microscope objective is used to produce magnified beam spots on the wall of the tent (see Fig. 4). The beams are aligned accordingly to make them overlap to a good approximation. Precedent to this alignment, the MV was first assured to be at the distance equal to the focal length of the focusing lens, i.e., 200 mm. Apart from that, the working distance between the detector and the MV should also be determined by the focal length of the focusing lens (Tropea, Yarin, and Foss 2007), i.e., 200 mm, or at 1:1 ratio to the focal length.

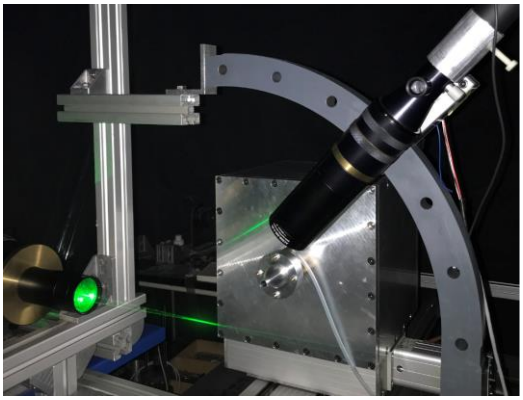

Fig. 2 LDA system in a large tent (3 x 5.8 x 3.1 m^3)

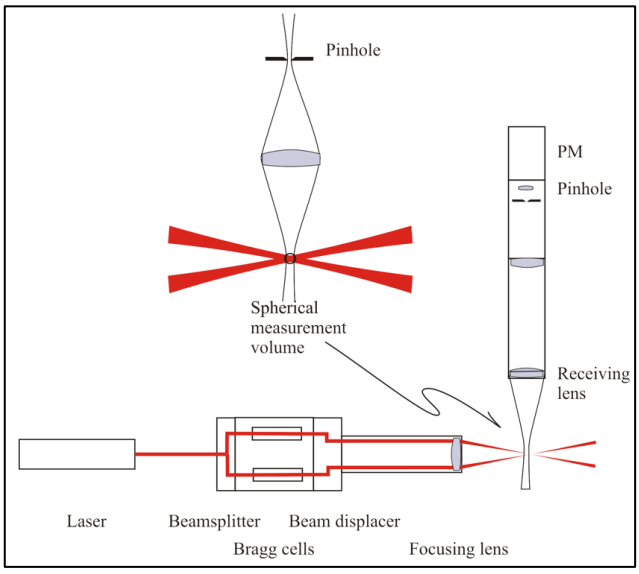

Fig. 3 Schematic drawing (side view) of the LDA setup, displaying a 90° (side scattering) configuration. However, the detector is mounted at 45° from the MV during the measurements.

In addition, the photodetector must be well aligned with the MV. By looking through the photodetector, there is a black pinhole located in the middle of a circular area. The photodetector, which is mounted to a holder, needs to be adjusted so that the pinhole resides at the center of the beam intersection as in Fig. 5. However, a more reliable test of signal quality is to simply observe the burst signal from an analog scope which is temporarily channeled from the output of the amplifier. The pinhole's position at which the highest burst S/N ratio is observed on the scope should be chosen for the measurement. The amplifier is also set to an optimum value in a way that the high value of current setting should not cut the burst off too much.

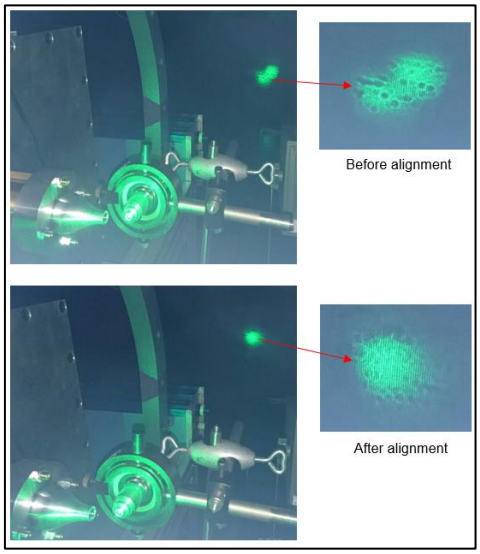

Fig. 4 Alignment of the beams' overlapping

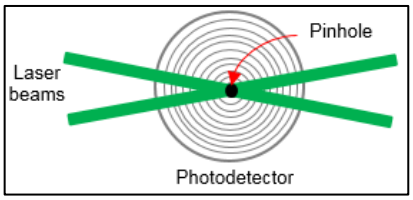

Fig. 5 Pinhole alignment with MV through the photodetector

2.4 LDA measurement

A series of measurements spanning from *x/D*=5 up to *x/D*=30 downstream from the jet exit were carried out with the LDA system. For each downstream position, measurements were acquired at several points in the radial direction across the shear region, as depicted in Fig.6.

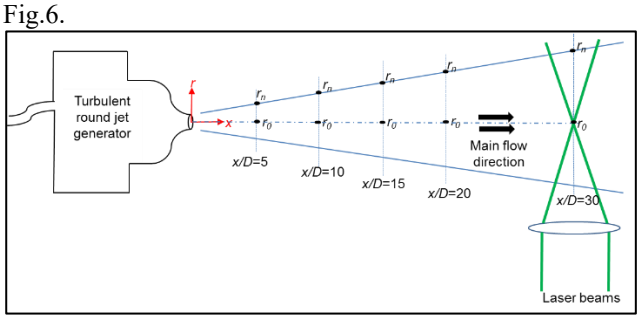

Fig. 6 Schematic of the measurement points (MP), which are listed in detail in Appendix I.

The jet input pressure was set to give an exit velocity, U_0 of 32 m/s (*Re*=25000). Seeding particles were fed into the flow at a pressure of 1.2 bar which resulted in an optimum number of Doppler bursts (spatial seeding density resolving the relevant scales without significant burst-overlap) as seen from the scope (see Fig. 7). The seeding was allowed to distribute uniformly throughout the ambient air to improve the homogeneity of the seeding. The laser was adjusted to nearly reach its maximum intensity (1.29 W), along with 70 μA amplifying current on the photomultiplier.

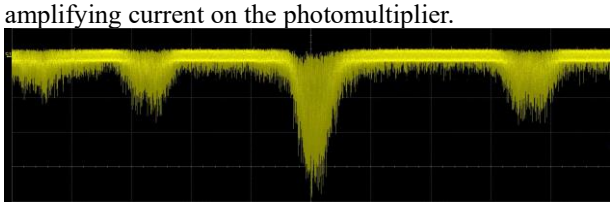

Fig. 7 Doppler bursts acquired from the scope

All the abovementioned parameters were consistently used throughout the whole measurement except for the sampling rate of the raw burst-signal and the record length, which were optimized to accommodate to the flow variations. The sampling rate of the raw burst signal was chosen to fulfill the Nyquist sampling rate in relation to the Doppler frequency. The maximum frequency was determined from the built-in spectrum analyzer of the scope as in Fig. 8, prior to data recording at every measurement point. A sampling rate of either 12.5 MHz or 25 MHz was chosen for all measurement points, accommodating to the variations in flow conditions at each measurement point. The resulting record lengths were 2 s and 1 s, respectively, which are long enough to obtain sufficient statistics from the flow. A total of 400 records were taken at each measurement point.

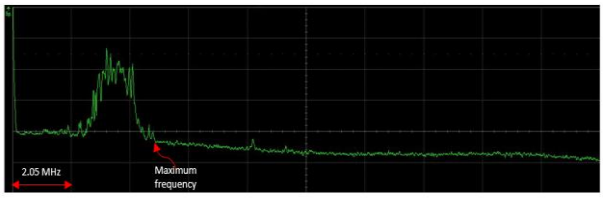

Fig. 8 Range of Doppler frequency at one particular measurement point

2.5 Signal processing

The output measured at each measurement point is an equidistantly sampled digital record of electrical current and the acquired signal is in the form of an array of discrete points. Beside all the measured Doppler bursts, the signal also contains various sources of noise, e.g., quantum noise from the photomultiplier, thermal noise from the detector's circuit or optical noise from the surroundings (Buchhave, George, and Lumley 1979). This noise needs to be minimized to clearly reveal (to the processor) the desired burst. By transforming the signal to frequency space, most of the frequencies are clustered around a range (see Fig. 9) with frequencies corresponding to the measured velocities. Anything outside this range is considered as unwanted noise and therefore not to be processed. By using the calibration

factor, d (from $d = u/f_D$, where u is the local instantaneous flow velocity and f_D is the Doppler frequency), and since the approximate velocity is known, it is possible to remove potentially unphysical velocities/Doppler frequencies. In this case, the frequencies in the center correspond to velocities between -40 to 40 m/s, and anything outside of this range is deemed unrealistic.

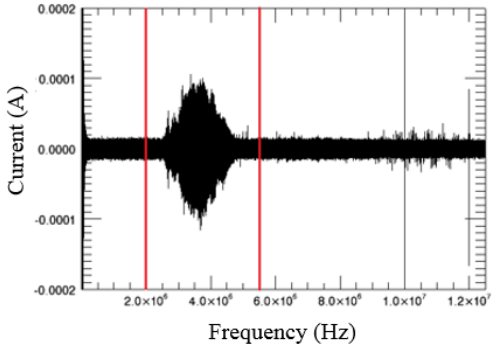

Fig. 9 Simple band pass filter (band within the red lines) to isolate Doppler bursts

In order to detect the individual Doppler bursts, it is necessary to find their envelope. This is done by using the Hilbert transform (Schneider et al. 2007), which shifts the function by $\frac{\pi}{2}$. A sum signal is created, which is the original signal squared added to the Hilbert transformed signal squared. This yields an envelope of the signal, which is shown in Fig. 10. However, the signal is still too noisy to detect the individual bursts properly. Therefore, the envelope signal is filtered by a running convolution that is adjusted to remove noise at frequencies above the minimum burst length. The frequency is chosen to avoid bias, which could otherwise reduce the number of high velocity bursts. The result of the convolution is shown in Fig. 11, which also illustrates two horizontal lines known as trigger lines that are used to detect every burst having an amplitude higher than the upper trigger line. The burst is recorded until the amplitude gets below the lower trigger line. This method, commonly known as Schmidt triggering, is used to reduce the probability for detection of a noise spike. After detection, each burst is analyzed using the fast Fourier transform (FFT) in order to find the Doppler frequency. The challenge is now to extract a single frequency in finding the corresponding particle velocity**.** A single burst is shown in Fig. 12. Even though the Doppler burst is fairly visible, there are still many frequencies present throughout its extent.

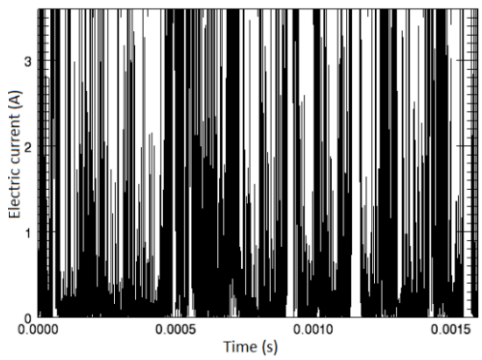

Fig. 10 The sum signal

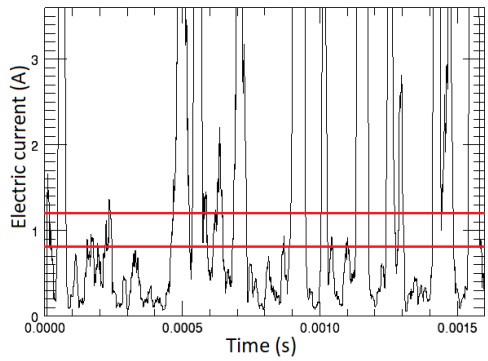

Fig. 11 Convoluted sum signal now used to detect Doppler bursts using a Schmidt trigger system (illustrated by the two horizontal red lines)

In order to find the corresponding velocity from each Doppler burst, the FFT is applied to each burst as shown in Fig. 13. Only one of the obtained frequencies should correspond to the velocity for the particle moving through the MV. The situation is further complicated by the fact that, in addition to frequencies due to the noise, the Doppler frequency itself can change across the burst as the seeding particles may have a varying velocity when transiting through the finite sized MV. This is natural, since the spatial velocity gradients in turbulence are expected to become larger for smaller flow scales. A Gaussian function is therefore fitted across the Doppler peak and its maximum value is used as the frequency of the Doppler shift (see Fig. 14). This method is effective since the Doppler burst has the shape of a Gaussian function, and transforming such a function to Fourier space, will result in a Gaussian function as well.

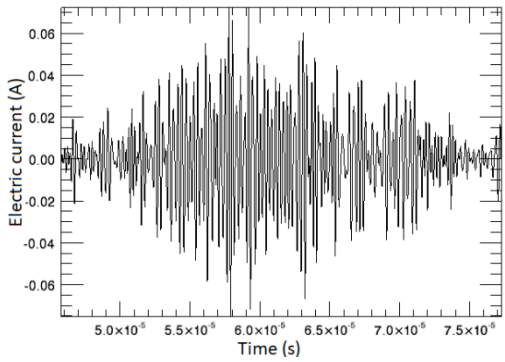

Fig. 12 An example of a filtered Doppler burst with several frequencies contained

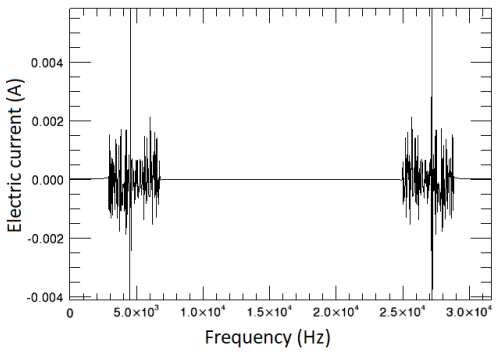

Fig. 13 FFT of a single (band pass filtered) burst

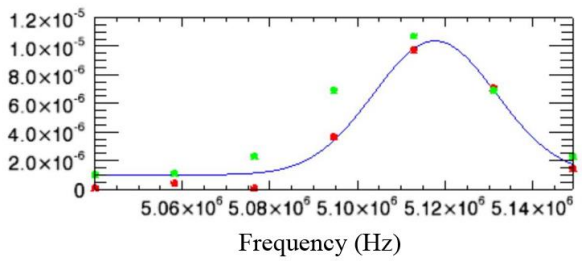

Fig. 14 Gaussian fit across the Doppler peak. *Red square* ■ : measured points. *Green square* ■ : suggested function for the fit. *Blue curve*: best fit to the measured points.

2.6 Diagnosis of processed signal

Since our software driven LDA processor was initially developed to overcome the practical limitations of the hardware based ones (Velte, George, and Buchhave 2014), the processed signals from both types of processors will be simultaneously diagnosed. For this purpose, the data acquired from the commercial LDA system by Velte, George, and Buchhave (2014) are taken into consideration.

A central problem with the commercial hardware driven systems that the authors have experienced with is that both the long and short residence times are not well-represented in the data set due to the hardware limitations in the burst sampling. An accurate representation of these residence times is necessary for measuring unbiased statistics, in particular for high intensity and high shear flows, as has been shown from first principles (Velte, George, and Buchhave 2014). This misrepresentation of the residence times should not be problematic using this software driven system, which is highly flexible in this regard.

This can be illustrated with a simple diagnostics tool for LDA data quality, namely by scatter plotting the instantaneous velocities against their respective residence/transit times. For large positive convection velocities and relatively low turbulence intensities, the scatter plot should take on the familiar 'banana' shape, where high velocities are represented by small residence times and low velocities by long residence times (Capp 1983). For average convection velocities close to zero, the data should be distributed evenly around the residence time axis and reach high values. The traditional processors are clearly limited in this respect, as was seen in (Velte, George, and Buchhave 2014).

This is illustrated in Fig. 15, where the novel software driven processor is compared to a commercial counterpart in a turbulent round jet at 30 jet exit diameters downstream and two different radial distances; r=26 mm and 52 mm. The slight differences in global scatter distribution appear due to different validation of measured data between the processors as well as slightly different flows as similar, but different, jet generators have been used. This is, however, not critical to the current comparison.

Much longer residence times can be captured at the lowest (near zero) velocities by our novel processor compared to that of the commercial one, which maximum value is abruptly limited at the outermost off-axis positions (52 mm). The length of the longest measurable bursts as defined in the commercial hardware has effectively limited the maximum burst length and consequently the quality of low mean velocity (high intensity) result. One may optimize the hardware driven LDA measurements with improved settings, but the inherent problem with long residence time clipping is in principle better countered using the flexible software driven processor.

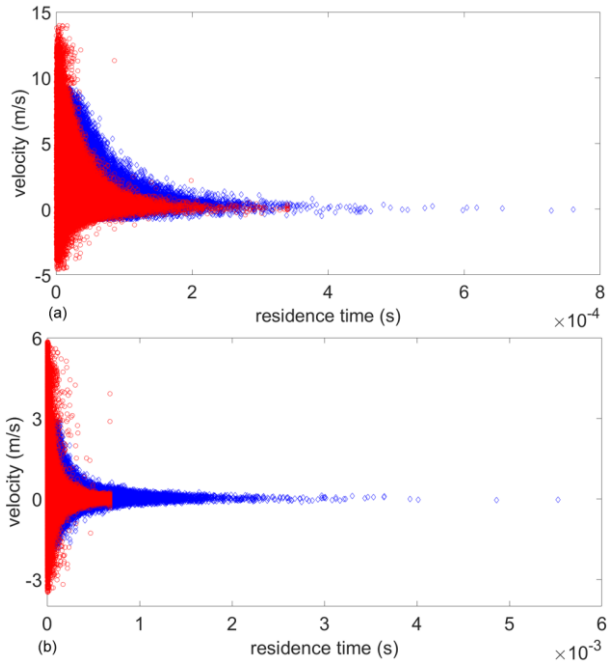

Fig. 15 Velocity vs. residence time scatter plots for **a** r = 26 and 27 mm, **b** r = 52 and 51 mm. *Red circle* ○ : hardware driven LDA processor, *Blue diamond* ◇: software driven LDA processor

Another critical effect due to digitization could be found in the interarrival times (Buchhave, Velte, and George 2014; Velte, Buchhave, and George 2014). A closer examination showed that the processor had a finite data transfer time for each measured burst, which effectively limited the minimum attainable time between measurements. This can be illustrated, e.g., by a zoomed-in scatter plot of the individual velocities against the difference in arrival time between neighboring bursts (see Fig. 16). The vertical lines and the separations between them show the digitization and dead time effect, respectively. In power spectra computed using the residence time weighted discrete Fourier transform (DFT), this dead time was shown to produce oscillations in the high frequency end of the spectrum (Velte, George, and Buchhave 2014), originating from the Fourier transform of the dead time window. These regular interarrival time intervals appear to originate from data transfer times, during which new measurements cannot be acquired.

This dead time introduced has consequently been reported to have been removed in newer generations of the LDA processors for some of the commercial producers (private communication). However, the dead time effect of the finite measuring volume (no more than

one particle allowed in the MV at any time when operating in burst-mode), which is a conceptual limitation of the optics, apparently must remain also in the current processor. The reduced effective MV size from operating the LDA in the combined forward/side scattering configuration does however aid in reducing this problem.

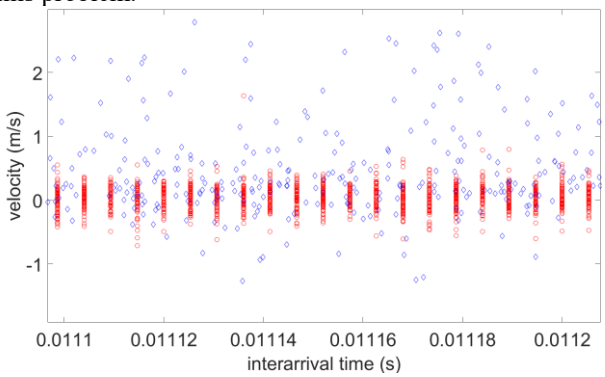

Fig. 16 A zoomed-in of the velocity and the difference in arrival time between neighboring points. *Red circle* ○ : hardware driven LDA processor at r = 52 mm, *Blue diamond* ◇ : software driven LDA processor at r = 51 mm

2.7 Analysis

The output of all previous steps results in a temporal record of randomly sampled velocities, $u_i(t)$, since the seeding particles enter the MV randomly (the random arrivals of the particles in the MV effectively dictate the sampling) (Lading, Wigley, and Buchhave 1994). With optimal seeding density (data rate), one can maximize the highest frequency (smallest scale) resolvable, while keeping the amount of overlapping bursts (more than one particle in the MV simultaneously) to a minimum. This is important in getting a higher dynamic range of the power spectrum (Buchhave and Velte 2015). The random sampling prevents the use of the FFT, which requires equidistant samples. Instead, the discrete Fourier transform (DFT) must be used, which computes the transform at the actual (random) sampling times. This manner of computing the Fourier transform is usually slower than the FFT. However, we have developed a fast array processing algorithm for the DFT which makes it comparable in computational speed to the FFT (Buchhave and Velte 2015; Velte, George, and Buchhave 2014). The velocity power spectrum can now be computed using Equation (1):

$$S_i(f) = \frac{1}{T}\hat{u}_i(f)\hat{u}_i(f)^* \qquad (1)$$

where T is the length of the time record and $\hat{u}_i(f)$ is the Fourier transform of $u_i(t)$. For randomly sampled data, computing the Fourier transform of the velocities (or any statistics for that matter) requires special care and, as has been shown from first principles, should be carried out using residence time weighting to obtain unbiased statistics (Buchhave 1979; Buchhave, George, and Lumley 1979; Buchhave and Velte 2015; Buchhave, Velte, and George 2014; Velte, Buchhave, and George 2014; Velte, George, and Buchhave 2014). The spectra display the kinetic energy distributed across the measured bandwidth of frequencies.

To avoid scrambling of energy due to the fluctuating convection velocity and similar effects (Buchhave 1979; Lumley 1965), the energy spectra presented in the Results part are plotted in the wavenumber, k, domain:

$$S_i(k) = \frac{1}{L}\hat{u}_i(k)\hat{u}_i(k)^* \qquad (2)$$

where L is the length of the spatial record and $\hat{u}_i(k)$ is the Fourier transform of $u_i(s)$. The spatial record has been computed based on the convection record method (Buchhave and Velte 2017a) which does in an exact manner what Taylor's hypothesis only approximates (Buchhave and Velte 2017b). Thereby, the spectral scrambling and other adverse effects of the time spectra are effectively avoided.

3 Results and Discussions

Previous studies have shown that the mean velocity profile of a typical fully developed turbulent round jet flow should follow the well-known Gaussian distribution (Ball, Fellouah, and Pollard 2012; Mossa and Serio 2016). This behavior is also observed in the results obtained from our measurement (see Fig. 17) which covered only one half of the jet (up to a maximum of ~45 mm in the radial direction), since we assumed symmetry. Note that, the radial distance is normalized by the exit diameter of the jet. For each profile, the mean velocity is the highest at the jet centerline and approaching zero at large distances away from the centerline, as expected. The shape is also tapering off in the upstream direction. Meanwhile, as also expected, the streamwise velocity variance profiles (see Fig. 18) indicate the positions of maximum shear at each highest value, from which they also spread and taper with the downstream development.

As a quantitative test of the accuracy of the LDA velocity measurements, it is illustrative to test momentum conservation of the round turbulent jet. Momentum is conserved for a jet in an infinite environment, which is well approximated here for a jet exit diameter D=10 mm and an enclosure of 3 x 5.8 m^2. The velocity moment profiles can be tested using the momentum integral approximated to second order in (Hussein, Capp, and George 1994), which is valid in the fully developed jet region. We find that the ratio between the momentum flux per unit mass at x/D=30 to that at the jet exit is M/M_0 =0.99. More details on the calculations can be found in Appendix II. This shows that the profiles of the velocity moments obtained at x/D=30 from Fig. 17 and 18 satisfy momentum conservation, as expected. These convincing results also support that our LDA system is well suited for this kind of highly challenging measurement especially in the outer jet where velocity fluctuations are large, which demands a high dynamic range to accurately measure the small velocity changes (Jensen 2004).

The shape of the kinetic energy spectrum was also previously investigated in the fully developed (equilibrium) region (Fellouah, Ball, and Pollard 2009;

Gibson 1962), which for the current nozzle corresponds to approximately *x/D*=30 or beyond, where turbulence has become fully developed. For a clear comparison, each spectrum has been normalized with their respective mean square velocity value in Fig. 19. The results show good agreement with the expected -5/3 power law for an (assumed) inertial range (Batchelor 1953; Gibson 1962). Previous experimental investigations have been done by Velte, Buchhave and Hodzic (2017) using stereoscopic Particle Image Velocimetry, which results are clearly consistent with the present ones. The range within which each spectrum follows the -5/3 slope is also significant from our results, even for large radial distances from the centerline, strongly supporting that our novel LDA system is highly reliable even for high intensity and shear turbulence measurement.

Spectra at the centerline for every downstream position are also shown in Fig. 20, which demonstrates significant deviations from the power law as the position of measurement moved away from the equilibrium region.

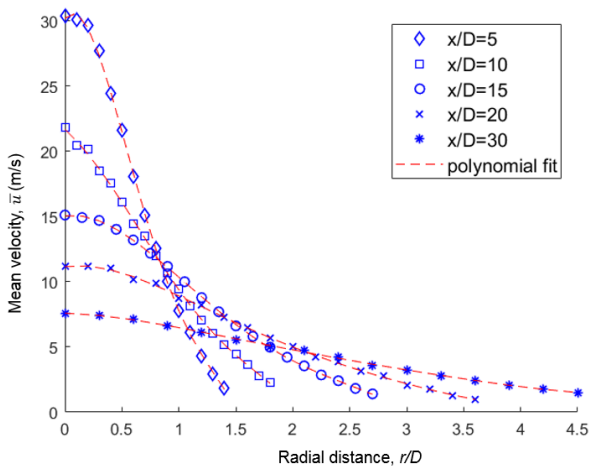

Fig. 17 Radial profiles of the mean streamwise velocity at *x/D* = 5, 10, 15, 20 and 30 with fifth-order polynomial curve fits

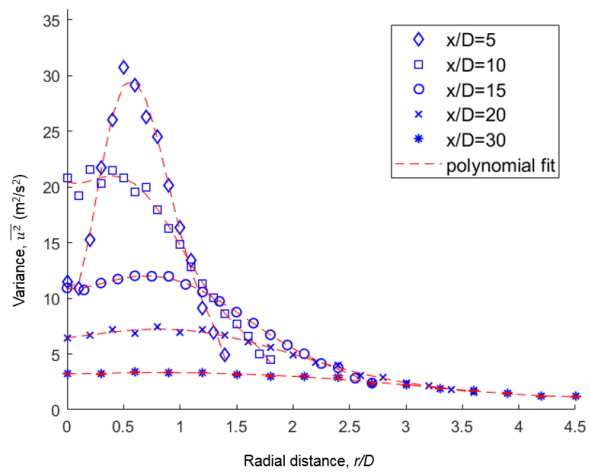

Fig. 18 Radial profiles of the local streamwise velocity variance at *x/D* = 5, 10, 15, 20 and 30 with fifth-order polynomial curve fits

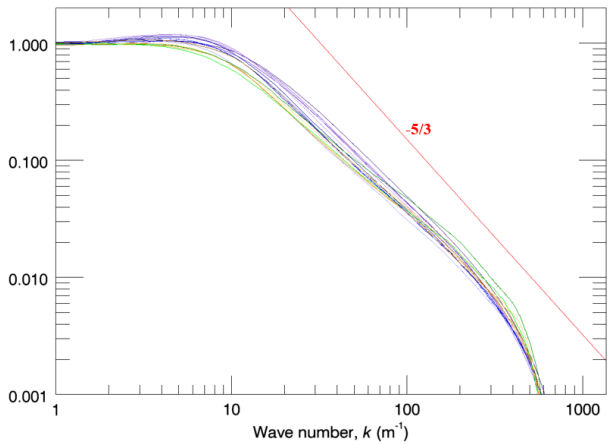

Fig. 19 Radial development of spatial turbulent kinetic energy spectra (based on the streamwise velocity component) at *x/D* = 30. From *heavy to light purple*: off-axis position 0, 3, 6, 9, 12 mm. From *heavy to light blue*: 15, 18, 21, 24, 27 mm. From *heavy to light brown*: 30, 33, 36, 39 mm. From *heavy to light green*: 42, 45 mm

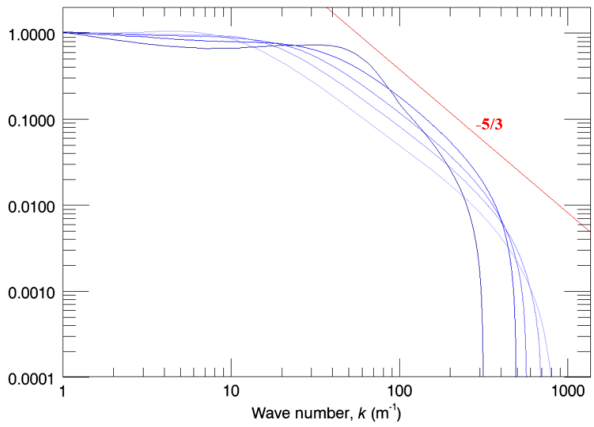

Fig. 20 Downstream development of spatial turbulent kinetic energy spectra (based on the streamwise velocity component) along the centerline (*r* = 0). *From heavy to light blue*: *x/D* = 5, 10, 15, 20, 30

4 Conclusions

A high dynamic range, transparent and accurate novel LDA system has successfully been developed. Measurement results have been compared to a typical classical hardware driven processor. Detailed diagnostics of the measurements shows that the novel software driven processor can successfully counter several of the limitations of the hardware driven counterpart, including quantization and clipping of the data. Both hardware and software have also been tested and validated for data acquisition and processing, respectively, which provides results that are in a good agreement with previous studies on turbulent round jets, even for challenging large off-axis distances. This proven functionality opens up an opportunity to further investigate the dynamics of significantly more challenging high intensity and high shear flows (in particular potentially non-equilibrium flows) to properly test the well-known local equilibrium hypothesis for the structure of the small scale turbulence.

Acknowledgements The authors wish to acknowledge the support of Ministry of Education Malaysia, DTU Mechanical Engineering, Reinholdt W. Jorck og Hustrus Fond (grant journal no. 13-J9-0026), Fabriksejer, Civilingeniør Louis Dreyer Myhrwold og hustru Janne Myhrwolds Fond (grant journal no. 13-M7-0039, 15-M7-0031 and 17-M7-0035) and Siemens A/S Fond grant no. 41. Credits should be also given to Pierre Margotteau, who helped to develop the first generation of the processor.

Appendix I

List of measurement points for Fig. 6

	Radial distance [mm]				
MP	***x/D*=5**	***x/D*=10**	***x/D*=15**	***x/D*=20**	***x/D*=30**
r_0	0	0	0	0	0
r_1	1	1	1.5	2	3
r_2	2	2	3	4	6
r_3	3	3	4.5	6	9
r_4	4	4	6	8	12
r_5	5	5	7.5	10	15
r_6	6	6	9	12	18
r_7	7	7	10.5	14	21
r_8	8	8	12	16	24
r_9	9	9	13.5	18	27
r_{10}	10	10	15	20	30
r_{11}	11	11	16.5	22	33
r_{12}	12	12	18	24	36
r_{13}	13	13	19.5	26	39
r_{14}	14	14	21	28	42
r_{15}	N/A	15	22.5	30	45
r_{16}	N/A	16	24	32	N/A
r_{17}	N/A	17	25.5	34	N/A
r_{18}	N/A	18	27	36	N/A

Appendix II

Detailed steps to estimate the momentum integral, *M* at *x/D*=30

The momentum flux per unit mass at the jet exit is calculated by

$$M_0 = \pi \left(\frac{D}{2}\right)^2 \bar{u}^2 = 0.0962\ m^4/s^2$$

At 30 jet exit diameters downstream of the jet nozzle, the momentum across the jet should be the same since the momentum is conserved for a free turbulent jet. The momentum integral to second order can be expressed as

$$M = 2\pi \int_0^\infty \left[\bar{u}^2 + \overline{u^2} - \frac{1}{2}\left(\overline{v^2} + \overline{w^2}\right)\right] r\, dr \qquad (3)$$

as shown in (Hussein, Capp, and George 1994).

This integral requires knowledge about the second order moments of the two additional components of velocity, namely *v*-variance, $\overline{v^2}$ and *w*-variance, $\overline{w^2}$. It has previously been established that the static statistical moments in a turbulent round jet obey axisymmetry (George and Hussein 1991). Furthermore, (Hussein, Capp, and George 1994) provides usable quantitative data on the relation between the variances of the velocity components. The Reynolds stress profiles of Figure 9-11 in (Hussein, Capp, and George 1994) are digitized and replotted all together in Fig. 21.

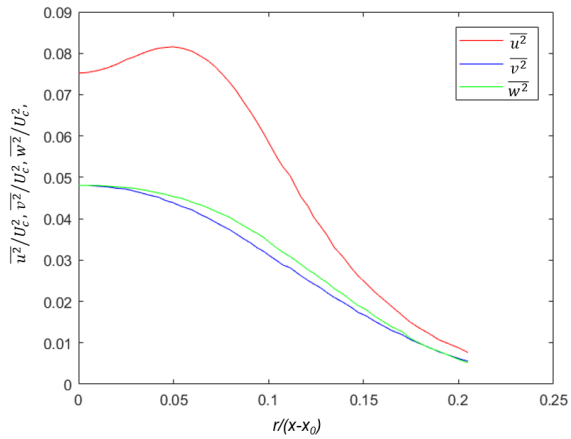

Fig. 21 Streamwise, radial and azimuthal components of turbulence kinetic energy (normalized by the square of the centreline velocity) at *x/D*=30

The ratio between each pair of profiles has been plotted in Fig. 22. The average ratio between each pair of variance profiles has also been computed accordingly:

$$\overline{v^2}/\overline{w^2} \approx 0.95 \qquad (4)$$

$$\overline{v^2}/\overline{u^2} \approx 0.60 \qquad (5)$$

$$\overline{w^2}/\overline{u^2} \approx 0.63 \qquad (6)$$

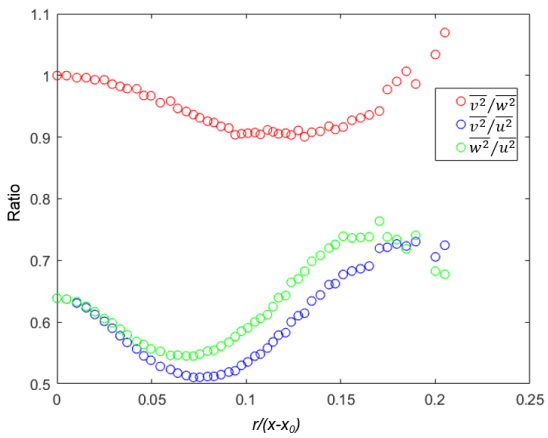

Fig. 22 Ratio between two different components

Substituting Equation (5) and (6) into Equation (3) resulted in:

$$M = 2\pi\left[\int_0^{r_{max}} \bar{u}^2 r\, dr - 0.39 \int_0^{r_{max}} \overline{u^2} r\, dr\right] \qquad (7)$$

where r_{max} = 45 mm. The mean streamwise velocity and variance profiles (particularly for *x/D*=30) in the integral are based on the fifth-order polynomial obtained by replotting the profiles over the non-normalized radial distance, *r*, which is given by

$$\bar{u}(r) = (8.53 \times 10^7)\, r^5 - (1.13 \times 10^7)\, r^4 + (5.88 \times 10^5)\, r^3 - (1.4 \times 10^4) r^2$$

$$\overline{u^2}(r) = 2.35\, r^5 - 0.084\, r^4 - 0.001 r^3 - 0.0002\, r^2$$

References

Abdel-Rahman, A. A., W. Chakroun, and S. F. AI-Fahed. 1997. "LDA Measurements in the Turbulent Round Jet." *Mechanics Research Communications,* 24(3): 277–88.

Albrecht, H. E., M. Borys, N. Damaschke, and C. Tropea. 2003. *Laser Doppler and Phase Doppler Measurement Techniques*. Springer-Verlag.

Ball, C. G., H. Fellouah, and A. Pollard. 2012. "The Flow Field in Turbulent Round Free Jets." *Progress in Aerospace Sciences* 50: 1–26.

Barker, S. J. 1973. "Laser-Doppler Measurements on a Round Turbulent Jet in Dilute Polymer Solutions." *Journal of Fluid Mechanics* 60: 721–31.

Bartlett, K. G., and C. Y. She. 1976. "Remote Measurement of Wind Speed Using a Dual Beam Backscatter Laser Doppler Velocimeter." *Appl. Opt.* 15(8): 1980–83.

Batchelor, G. K. 1953. *The Theory of Homogeneous Turbulence*. Cambridge University Press.

Buchhave, P. 1979. "Errors and Correction Methods in Turbulence Measurements with the LDA." State University of New York.

Buchhave, P. 1984. "Three-Component LDA Measurements." *Disa Information* (29): 3–9.

Buchhave, P., W. K. George, and J. L. Lumley. 1979. "The Measurement of Turbulence with the Laser-Doppler Anemometer." *Annual Review of Fluid Mechanics* 11: 443–503.

Buchhave, P., and C. M. Velte. 2015. "Reduction of Noise and Bias in Randomly Sampled Power Spectra." *Experiments in Fluids* 56(4): 1–17.

Buchhave, P., and C. M. Velte. 2017a. "Conversion of Measured Turbulence Spectra from Temporal to Spatial Domain." In *Whither Turbulence and Big Data in the 21st Century?*, Springer, 343–62.

Buchhave, P., and C. M. Velte. 2017b. "Measurement of Turbulent Spatial Structure and Kinetic Energy Spectrum by Exact Temporal-to-Spatial Mapping." *Physics of Fluids* 29(8).

Buchhave, P., C. M. Velte, and W. K. George. 2014. "The Effect of Dead Time on Randomly Sampled Power Spectral Estimates." *Experiments in Fluids* 55(2): 1–8.

Capp, S. P. 1983. "Experimental Investigation of the Turbulent Axisymmetric Jet." State University of New York, Buffalo.

Davidson, P. 2004. *Turbulence: An Introduction for Scientist and Engineers*. Oxford University Press.

Diop, Moussa, Sébastien Piponniau, and Pierre Dupont. 2019. "High Resolution LDA Measurements in Transitional Oblique Shock Wave Boundary Layer Interaction." *Experiments in Fluids* 60(4): 57.

Fellouah, H., C. G. Ball, and A. Pollard. 2009. "Reynolds Number Effects within the Development Region of a Turbulent Round Free Jet." *International Journal of Heat and Mass Transfer* 52(17–18): 3943–54.

Fischer, A. 2017. "Imaging Flow Velocimetry with Laser Mie Scattering." *Applied Sciences* 7(12): 1298.

Frost, W. 1977. "Spectral Theory of Turbulence." In *Handbook of Turbulence: Volume 1 Fundamentals and Applications*, Springer US, 85–125.

George, William K., and H. J. Hussein. 1991. "Locally Axisymmetric Turbulence." *Journal of Fluid Mechanics* 233: 1–23.

Gibson, M. M. 1962. "Spectra of Turbulence at High Reynolds Number." *Nature* 195: 1281–83.

Goto, S., and J. C. Vassilicos. 2015. "Energy Dissipation and Flux Laws for Unsteady Turbulence." *Physics Letters A* 379(16–17): 1144–48.

Grant, G. R., and K. L. Orloff. 1973. "Two-Color Dual-Beam Backscatter Laser Doppler Velocimeter." *Applied optics* 12(12): 2913–16.

Hussein, H. J., S. P. Capp, and W. K. George. 1994. "Velocity Measurements in a High-Reynolds-Number, Momentum-Conserving, Axisymmetric, Turbulent Jet." *Journal of Fluid Mechanics* 258: 31–75.

Jensen, K. D. 2004. "Flow Measurements." *Journal of the Brazilian Society of Mechanical Sciences and Engineering* XXVI(4): 400–419.

Kolmogorov, A. N. 1941a. "Decay of Isotropic Turbulence in Incompressible Viscous Fluids." *Dok. Akad. Nauk. S. S. S. R* 31: 538–41.

Kolmogorov, A. N. 1941b. "Dissipation of Energy in Local Isotropic Turbulence." *Dokl. Akad. Nauk. SSSR* 32: 15–17.

Kolmogorov, A. N. 1941c. "The Local Structure of Turbulence in Incompressible Viscous Fluid for Very Large Reynolds Numbers." *C. R. Akad. Sci. SSSR* 30: 9–13.

Kolmogorov, A. N. 1962. "A Refinement of Previous Hypothesis Concerning the Local Structure of Turbulence in a Viscous Incompressible Fluid at High Reynolds Number." *Journal of Fluid Mechanics* 13: 82–85.

L'vov, V., and I. Procaccia. 2007. "Hydrodynamic Turbulence: A 19th Century Problem with a Challenge for the 21st Century." *Turbulence Modeling and Vortex Dynamics* 491: 1–16.

Lading, Lars, Graham Wigley, and Preben Buchhave. 1994. *Optical Diagnostics for Flow Processes*. Springer Science+Business Media New York.

Lumley, J. L. 1965. "Interpretation of Time Spectra Measured in High-Intensity Shear Flows." *Physics of Fluids* 8(6): 1056–62.

Mazellier, N., and J. C. Vassilicos. 2010. "Turbulence without Richardson-Kolmogorov Cascade." *Physics of Fluids* 22(7): 1–25.

Monin, A., and A. Yaglom. 1972. 2 *Statistical Fluid Mechanics*. Cambridge: MA: MIT Press.

Mossa, M., and F. D. Serio. 2016. Nature Publishing Group *Rethinking the Process of Detrainment : Jets in Obstructed Natural Flows*. Nature Publishing Group.

Panchapakesan N. R., and J. L. Lumley. 1993. "Turbulence Measurements in Axisymmetric Jets of Air and Helium . Part 1 . Air Jet." *Journal of Fluid Mechanics* 246: 197–223.

Peiponen, K. E., R. Myllylä, and A. V. Priezzhev. 2009. "Laser Velocimetry." In *Springer Series in Optical Sciences*, Springer Berlin Heidelberg, 103–36.

Roberts, J. B., J. Downie, and M. Gaster. 1980. "Spectral Analysis of Signals from a Laser Doppler Anemometer Operating in the Burst Mode."

Journal of Physics E: Scientific Instruments 3(9): 977–81.

Schneider, Kai et al. 2007. "Review of Some Fundamentals of Data Processing." In *Springer Handbook of Experimental Fluid Mechanics*, , 1337–98.

Sommerfeld, Martin, and Cameron Tropea. 1999. "Single-Point Laser Measurement." In *Instrumentation for Fluid Particle Flow*, 252–317.

Tropea, C., A. L. Yarin, and J. F. Foss. 2007. *Springer Handbook of Experimental Fluid Mechanics*. Springer.

Valente, P. C., and J. C. Vassilicos. 2012. "Universal Dissipation Scaling for Non-Equilibrium Turbulence." *Physical Review Letters* 108(21): 214503.

Vassilicos, J. C. 2015. "Dissipation in Turbulent Flows." *Annual Review of Fluid Mechanics* 47: 95–114.

Velte, C. M., P. Buchhave, and W. K. George. 2014. "Dead Time Effects in Laser Doppler Anemometry Measurements." *Experiments in Fluids* 55(11): 1836.

Velte, C. M., P. Buchhave, and A. Hodzic. 2017. "Measurement of Turbulent Kinetic Energy Spectrum - Part 2 : Convection Record Measurements." In *ITi Conference on Turbulence VII*, Springer, 171–76.

Velte, C. M., W. K. George, and P. Buchhave. 2014. "Estimation of Burst-Mode LDA Power Spectra." *Experiments in Fluids* 55(3): 1674.

Wänström, M., W. K. George, and K. E. Meyer. 2012. "Streamwise and Radial Decomposition of a Turbulent Axisymmetric Jet." *Springer Proceedings in Physics* 141: 147–50.

Yaacob, M. R., R. K. Schlander, P. Buchhave, and C. M. Velte. 2018. "Mapping Of Turbulent Round Jet Developing Region Using a Constant Temperature Anemometer (CTA)." *Malaysian Journal of Fundamental and Applied Sciences* (Special Issue on Natural Sciences and Mathematics (ESCon 2018)): 443–46.

Affiliations

Mohd Rusdy Yaacob[1, ID]. Rasmus Korslund Schlander[2]. Preben Buchhave[3]. Clara Marika Velte[4, ID]

Mohd Rusdy Yaacob
rusdy@utem.edu.my

Rasmus Korslund Schlander
r.schlander19@imperial.ac.uk

Preben Buchhave
buchhavepreben@gmail.com

Clara Marika Velte
cmve@dtu.dk

[1] Faculty of Electrical Engineering, Universiti Teknikal Malaysia Melaka, Hang Tuah Jaya, 76100 Durian Tunggal, Melaka, Malaysia

[2] Department of Aeronautics, Imperial College London, London SW7 2AZ, United Kingdom

[3] Intarsia Optics, Sønderskovvej 3, 3460 Birkerød, Denmark

[4] Department of Mechanical Engineering, Technical University of Denmark, 2800 Kgs. Lyngby, Denmark

Paper V

Penerbit Akademia Baru

Journal of Advanced Research in Fluid Mechanics and Thermal Sciences

Journal homepage: www.akademiabaru.com/arfmts.html
ISSN: 2289-7879

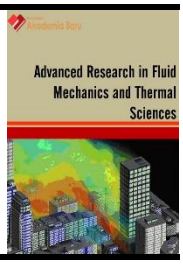

Statistical Description of the Turbulent Round Jet Developing Region Along Its Centerline

Open Access

Mohd Rusdy Yaacob[1,*], Preben Buchhave[2], Clara Marika Velte[3]

[1] Faculty of Electrical Engineering, Universiti Teknikal Malaysia Melaka, Hang Tuah Jaya, 76100 Durian Tunggal, Melaka, Malaysia
[2] Intarsia Optics, Sønderskovvej 3, 3460 Birkerød, Denmark
[3] Department of Mechanical Engineering, Technical University of Denmark, 2800 Kgs. Lyngby, Denmark

ARTICLE INFO

Article history:
Received 29 October 2016
Received in revised form 1 December 2017
Accepted 9 December 2017
Available online 10 December 2017

ABSTRACT

Turbulent round jet is mapped in terms of statistical moments along the centerline throughout and beyond the developing region. The measurements are carried out using laser Doppler anemometry, which accurately measures high turbulence intensity flows with high spatial and temporal resolution and dynamic range. The static moments, including mean velocity and variance, follow the expected trends. About 25-30 jet exit diameters downstream, turbulence begins to approach the fully developed state where the mean velocity and variance develop in parallel in a seeming equilibrium. Turbulence intensity is consequently observed to initially increase before levelling out when approaching the fully developed state. The downstream development of the measured spatial energy spectra and second-order structure functions further support these observations in that they begin to develop the Kolmogorov characteristic -5/3 and 2/3 slopes in the inertial subrange within the downstream distance of 25-30 jet exit diameters. The validated convection record method is implemented to obtain the spatial dynamic statistics. The dissipation can be to a reasonable approximation extracted from the third-order structure functions from about 20 jet exit diameters and further downstream. The results, acquired with an improved high-accuracy laser Doppler anemometer, should be useful for development of analytic and numerical turbulence models.

Keywords:
Turbulent round jet; Centerline measurements; Laser Doppler anemometer;

1. Introduction

The axisymmetric turbulent round jet is a classical turbulent flow that exhibits a wide range of dynamical variations [1]. While the fully developed jet has been extensively studied in the past [2]–[8], the developing region has often been omitted from the analysis since the transitional development and high intensity and shear in this region present additional measurement technical difficulties and since equilibrium and similarity in a general sense (defined as similar development of

* *Corresponding author.*
rusdy@utem.edu.my (Mohd Rusdy Yaacob)

the first and second-order statistics) have been assumed not to be valid. At the same time, a deeper understanding of the developing region is vital for understanding how the state in the fully developed region is reached (e.g., if there exists a dependency upon initial conditions)[9]–[11] and, not least, how to accurately model it in computer simulations. Of particular interest is testing the (range of) validity of the Kolmogorov hypotheses within this region and providing data for validation of analytical and computational models.

In terms of accuracy of measurements, the centerline region is considered less challenging compared to the shear region, where the velocity fluctuations and turbulence intensity are much larger [12], [13]. However, measurements along the jet centerline can be of significant interest in mapping the energy cascade in the centerline region. In general, a mapping of the static and dynamic statistics of the velocity field in the developing jet region using high accuracy measurements can be of significant interest in synthesizing analytical and numerical models for developing flows. It is therefore of interest to perform these centerline measurements in the developing jet region using a novel and sophisticated laser Doppler anemometry system [14], which has been proven to function robustly even in the more difficult high shear and intensity regions of the jet [15], [16].

Herein, we present laser Doppler anemometry measurements of the cascade development along the jet centerline, including the static moments, spatial kinetic energy spectra as well as spatial second- and third-order structure functions. From the latter, the dissipation time and length scales have been extracted along the lines of Kolmogorov [17]–[20] as a function of downstream distance, where applicable. The corresponding temporal/spatial Kolmogorov and integral scales obtained from the measurements are also presented.

2. Instrumentation and Measurements

2.1 Traversable Turbulent Round Jet

The design and interior of the jet generator box, which was fabricated in the DTU workshop, replicates the one used by [12], [21]. Inside the box, baffles with foam coating have been inserted to even out large disturbances, followed by screens to remove remaining fluctuations in the stream. The nozzles following consist firstly of a trumpet nozzle (Fig. 1(a)), which is tooled to transition to a pipe connecting it to an outer nozzle (Fig. 1(b)). The outer nozzle has an inner diameter of 32 mm, an exit diameter, D=10 mm and a fifth-order polynomial contraction that allows a uniform flow [22] resulting in a well-approximated top-hat velocity profile [23].

The jet generator box is mounted on two linear traversing units (stacked to each other) for maneuvering the measurement volume to the desired measurements points throughout the ensuing jet in the streamwise and transverse directions. Each unit is equipped with limit switches and a stepper motor from ISEL Automation. An iMC-S8 stepper motor controller is permanently connected to a computer to drive the motors in micro stepping mode. A *RemoteWIN* software is installed in the computer to operate the traversing units in a semi-auto mode. In order to match the distance traversed on the hardware and the software parts, the number of steps per revolution and spindle elevation needs to be set according to the datasheets.

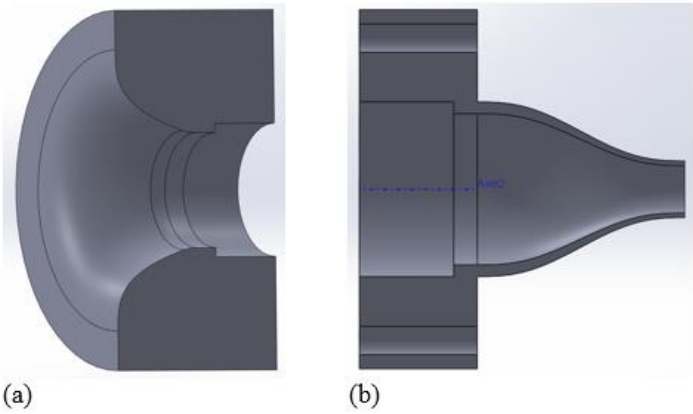

Fig. 1. (a) Trumpet nozzle (b) Outer nozzle with fifth-order polynomial contraction. The two nozzles are connected by a geometrically smoothly transitioning pipe that penetrates the jet generator box wall

2.2 Laser Doppler System

Laser Doppler anemometry (LDA) is a non-intrusive method for measuring the velocity of a flow. By seeding the working fluid with seeding particles with an optimal size in terms of faithfulness in tracing the flow and light scattering properties [24], the velocity of each particle can be acquired and assumed to represent the flow velocity to an acceptable approximation [25], [26]. The measuring volume is created when a coherent laser beam is split into two and focused into a common point using a converging lens (see Fig. 2**Error! Reference source not found.**). Where they intersect, a fringe pattern is formed from the two coherent beams and the Doppler frequency of the seeding particles can be measured [27]–[29]. Before the beams intersect, each beam passes through a Bragg cell with an effective frequency shift difference between the beams, f_s=3 MHz to resolve any negative component of the velocity in the measured flow [30], [31]. After compensating for the differential frequency shift, the velocity can be calculated by

$$u = \frac{\lambda f_D}{2sin\left(\theta/_2\right)} = f_D d_f \tag{1}$$

where λ is the wavelength of the laser (532 nm), ϑ is the beam angle and f_D is the Doppler frequency of the moving particle. d_f is the fringe spacing in the measuring volume.

$$d_f = \frac{\lambda}{2\sin(\theta/_2)} \tag{2}$$

In order to obtain a sufficiently high spatial resolution to convincingly resolve the Kolmogorov length scale throughout the measurement domain, a converging lens with a focal length of 200 mm was used. This resulted in a measuring volume of the order of 90 μm and a sufficiently dense fringe spacing that produced good quality bursts for Doppler frequency detection compared to the seeding particle size. Based on this measuring volume, the smallest resolvable length scale can therefore be computed. From

$$k\eta_{Kol} = \frac{2\pi}{\lambda}\eta_{Kol} = 1 \tag{3}$$

at which the dissipation is approximately 99% resolved, the smallest resolvable Kolmogorov length scale using our instrument can be calculated by

$$\eta'_{Kol} = \frac{\lambda}{2}\frac{1}{\pi} \tag{4}$$

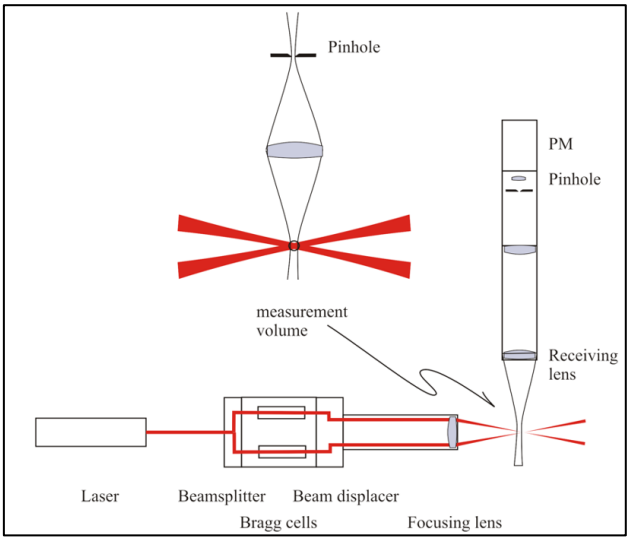

Fig. 2. Schematic drawing (side view) of the LDA setup

Since the laser Doppler anemometer is operating in burst-mode, the processor cannot process more than one seeding particle in the measuring volume at a time, since this would result in overlapping bursts with in general different phases and faulty residence times. A smaller measuring volume thus enables a higher spatial seeding density, since for a smaller volume the probability of having more than one particle in the measuring volume is lowered. This consequently enables a higher spatial seeding density (thereby a higher data rate), and thus a wider spectral turbulent kinetic energy content with a higher signal-to-noise ratio [32].

For the same purpose, the photodetector is mounted at a 45° forward scattering angle (see Fig. 3) from the transmitting optics axis to allow an optimum between sufficient amount of light scattered by each particle and an effective reduction of the detected region of the measuring volume [33]. Thereby, the effective (detectable) measuring volume is reduced from an ellipsoid to a nearly spherical shape. This configuration has led us to attach both traversing units to the jet box instead of traversing the optical head, which sensitivity to misalignment may otherwise cause erroneous or complete dropout of measurements as observed by the photodetector.

To obtain quality measurements, it is thus vital that the transmitting and receiving optics of the laser Doppler anemometer is carefully aligned. The optics inside the transmitting optics must be tilted accordingly in a way that the two beams perfectly overlap at the desired focal point. Furthermore, the photodetector needs to be carefully aligned with respect to the MV until a high-quality burst is observed. This is in practice best achieved by observing the voltage signal from the photomultiplier (detector) live on an oscilloscope. The LDA optics and processing are described in great detail in [14][16][34].

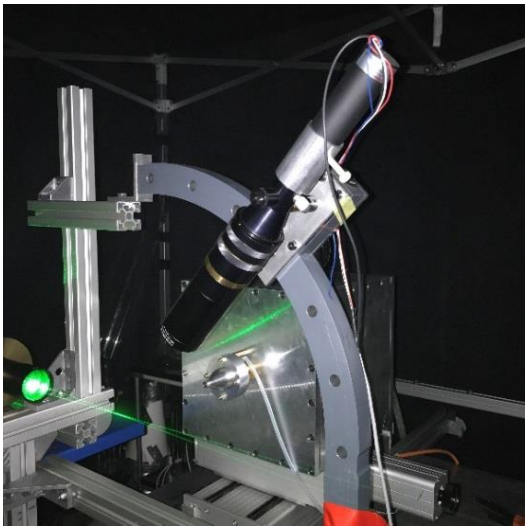

Fig. 3. LDA system in a large tent (3 x 5.8 x 3.1 m^3)

3. Computation of Turbulence Statistics

Upon data processing, the software outputs the value of the residence (transit) time, arrival time and instantaneous streamwise velocity of each detected burst. The mean streamwise velocity, $\bar{u}_i$ and the velocity variance, $\overline{u_i^2}$ at each measurement point are determined based on residence time-weighting [12], [35]–[37].

$$\bar{u} = \frac{\sum_{n=0}^{N-1} u_i(t_n)\Delta t_n}{\sum_{n=0}^{N-1} \Delta t_n} \tag{5}$$

$$\overline{u^2} = \frac{\sum_{n=0}^{N-1} [u_i(t_n) - \bar{u}_i]^2 \Delta t_n}{\sum_{n=0}^{N-1} \Delta t_n} \tag{6}$$

where Δt_n is the residence time for the nth realization. It has been shown from first principles to produce non-biased statistics of the LDA burst signal and experimental validation supports the theoretical deductions [12], [15].

The time records acquired from the measurements are mapped to spatial records based on the convection record principle in order to devotedly represent the energy content of the spatial structures [15].

$$s(t) = \int_0^t |\bar{u}(x_0, t')| dt' \tag{7}$$

where s is the scalar length of accumulated convection elements for fluid passing through the measuring volume, x_0 is the location of the fixed measuring volume and $\bar{u}$ is the instantaneous velocity vector at a time, t'. This method provides an exact mapping of what Taylor's hypothesis only approximates, where the instantaneous velocity magnitude is used instead of the averaged streamwise velocity component. One can consequently measure kinetic energy spectra in the wave number (spatial) domain that display the true distribution of spatial scales instead of the one

displayed in the frequency (temporal) domain. The latter is unreliable towards the unsteady convection of the large scales [38], among other factors.

The spatial kinetic energy spectra are computed by

$$S_i(k) = \frac{1}{L}\hat{u}_i(k)\hat{u}_i(k)^* \tag{8}$$

where $\hat{u}_k(k)$ is the Fourier transform of $u_i(s)$ and *L* is the length of the spatial record. Note that also the Fourier transform must be computed using residence time weighting for laser Doppler measurements [12], [35]–[37]. The spatial second-order and third-order structure functions are also computed based on the (residence time averaged) convection record, which are expressed respectively by

$$S_2(\ell_s) = \langle(\bar{u}(s+\ell_s) - \bar{u}(s))^2\rangle \tag{9}$$

$$S_3(\ell_s) = \langle(\bar{u}(s+\ell_s) - \bar{u}(s))^3\rangle \tag{10}$$

where ℓ_s is the spatial separation along the *s*-record and the < >-brackets denote ensemble averaging.

In his seminal papers, Kolmogorov assumed local (i.e. small and intermediate scale) homogeneity and isotropy as well as equilibrium and universality [17]–[20]. These assumptions make the structure function equation reduce into the famous 2/3 and 4/5 laws for the second- and third-order, respectively [39]. The latter is only valid for local homogeneity, isotropy and equilibrium, which supports discarding the measurement points for *x/D*<20 in the following (Results and Discussions) section to meet the last of those conditions. The 4/5 law proposes that the third-order structure functions of velocity increments scale linearly with separation distance ℓ_s [40] as given by

$$S_3(\ell_s) = -\frac{4}{5}\varepsilon\ell_s \tag{11}$$

where ε is the mean energy dissipation rate per unit mass and ℓ_s in this case, is also the abscissa on the third-order structure function plot in the following section. As a consequence, if the theory and associated assumptions are valid, the dissipation should be attainable directly from the third-order structure function.

The Kolmogorov time, τ_{Kol} and length scales, η_{Kol} are computed directly from the classic definitions:

$$\tau_{Kol} = \left(\frac{\nu}{\varepsilon}\right)^{1/2} \tag{12}$$

$$\eta_{Kol} = \left(\frac{\nu^3}{\varepsilon}\right)^{1/4} \tag{13}$$

where ε is the mean energy dissipation rate per unit mass and ν is kinematic viscosity of the air.

The integral time scale, T_u is computed from the integral under the covariance function:

$$T_u = \int_0^\infty \frac{\overline{u(t)u(t+\tau)}}{\overline{u^2}} d\tau \tag{14}$$

By using Taylor's hypothesis, the spatial counterpart, L_u is estimated by multiplying T_u with the local mean velocity. This hypothesis is assumed to be valid since measurements were performed along the jet centreline, where turbulence intensities are relatively low [41].

4. Results and Discussions

The downstream profiles along the centerline ($10 \leq x/D \leq 37$) of the local mean streamwise velocity and the velocity variance are presented in Fig. 4. In general, the velocity decays downstream, as expected [42], where a faster decay occurs in the intermediate field (developing region) compared to the fully developed region, as also being observed in [23], [43]. The velocity variance has a similar close to inversely proportional development with downstream distance.

To simplify the comparison, the normalized inverse of the local mean streamwise velocity and the velocity variance within the range of $10 \leq x/D \leq 37$ are shown in Fig. 5. It is immediately observed, that the inverse mean velocity displays a close to linear behavior even in the developing region $10 \leq x/D \leq 30$, whereas the velocity variance clearly is not fully developed until approximately 24 jet exit diameters downstream of the jet exit. Linear curve fits are displayed within the ranges that crudely represent the linear self-preserving regions, e.g., $x/D \geq 20$ and $x/D \geq 24$ for the mean velocity and variance, respectively. The profile demonstrates proportionality between the scaled inverse centerline mean velocity and x/D as suggested by [42] in describing the far field evolution in the jet.

From the linear fit of the inverse mean velocity, the virtual origin is determined to x_0=2.3D and the decay constant to B_u=6.6, based on the calculation at x/D=30. These results are compared to the ones obtained in the previous studies of turbulent round jets of different Reynold numbers, downstream range and using different measurement techniques (see Table 1). Slight deviations compared to our results are most likely due to the different nozzle geometries (and other initial conditions variations) and the different measurement techniques used. The Reynolds number is known not to affect the spreading rate or the decay constant of turbulent round jets [44]. It is particularly interesting to note, that the inverse variance seems to originate from a different point (x/D=15.6) than the inverse average centerline velocity. The normalized inverse of the RMS velocity is also plotted, which linear self-preserving region is similar to that of the local mean streamwise velocity, i.e., $x/D \geq 20$ (see Fig. 6). In this case, the origin of the inverse RMS velocity is found to be approximately at x/D=1.27.

The streamwise turbulence intensity profile along the centerline is plotted in Fig. 7, in terms of the ratio between the velocity fluctuations, u' and the mean velocity. The turbulence intensity builds up in the intermediate field (developing region) due to an increasingly higher influence of the large scale Kelvin-Helmholtz instability development in the shear layer [23], [43]. The turbulence intensity increases gradually and asymptotes to a nominal value of around 0.23 in the fully developed region, similarly to [5]. This behavior and the asymptotic value are also found to be in close agreement with most of the previous findings accumulated by [45]. Based on the known similarity scalings for the

fully developed turbulent round jet [46], this asymptotic behavior is assumed to be well sustained farther downstream [47].

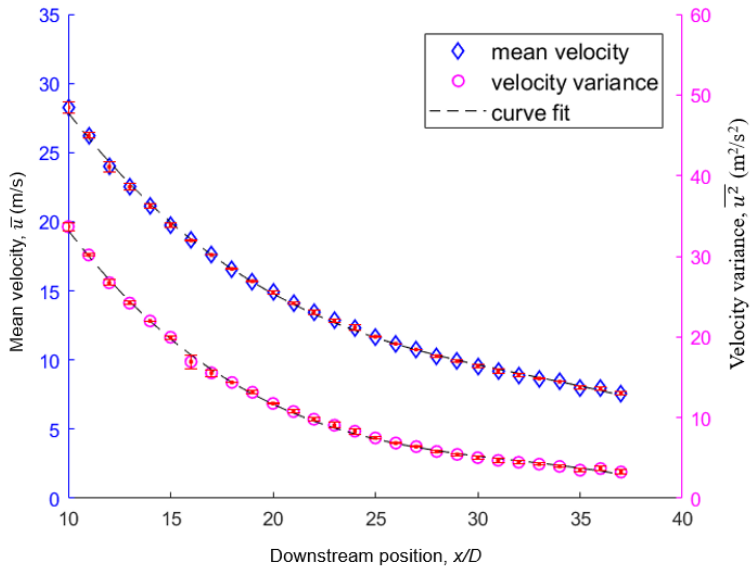

Fig. 4. The downstream profiles (with error bars) of local mean streamwise velocity and streamwise velocity variance with corresponding fourth-order polynomial curve fits. Coefficient values for the profiles (also for the profiles in the following figures) are listed in Appendix B.

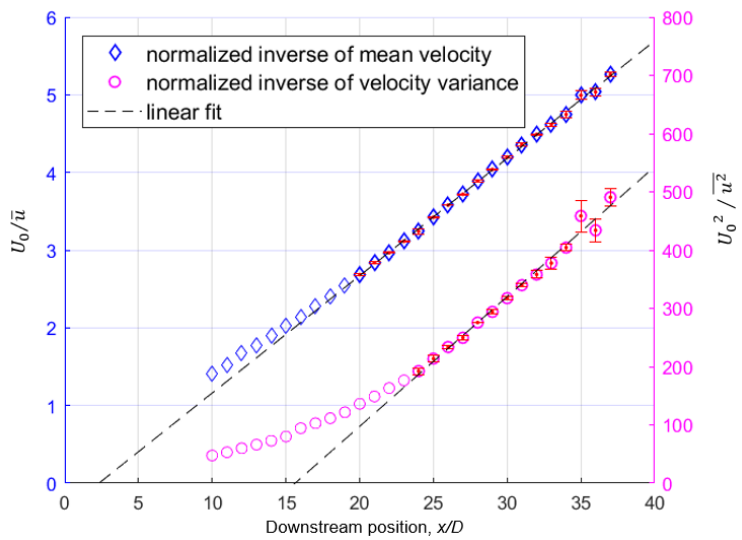

Fig. 5. The normalized inverse of the local mean streamwise velocity and velocity variance, with linear fits and corresponding error bars, covering the points within the estimated linear regions. U_0 is the jet exit velocity ≈ 40 m/s. The linear fit line is extrapolated until it intercepts the x-axis.

Table 1 The values of Reynolds number and velocity

Authors	***Re***	***x_0/D***	***B_u***	***x/D***	**Technique**
Present study	25000	2.3	6.6	20-37	LDA
[2]	16000	-	6.6	17-27	PIV
[48]	24000	2.5	6.7	15-80	Hot-wire
[5]	100000	4	5.8	15-100	LDA
[49]	20000	3.1	5.9	30-105	PIV
[6]	11000	-	6.06	30-160	Hot-wire

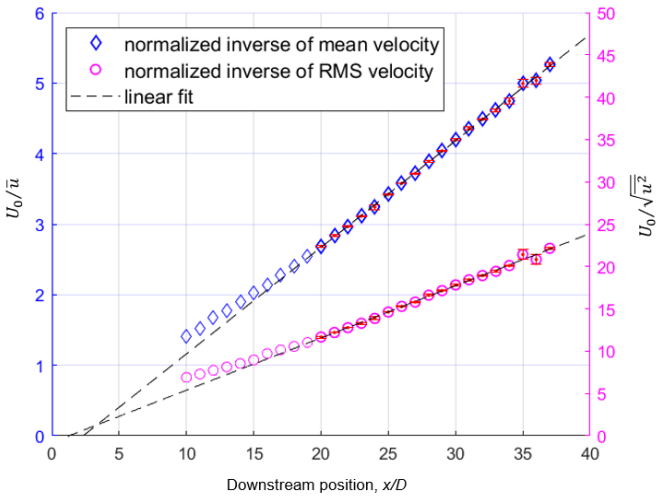

Fig. 6. The normalized inverse of the local mean streamwise velocity and velocity variance, with linear fits and corresponding error bars, covering the points within the estimated linear regions. U_0 is the jet exit velocity ≈ 40 m/s. The linear fit line is extrapolated until it intercepts the x-axis.

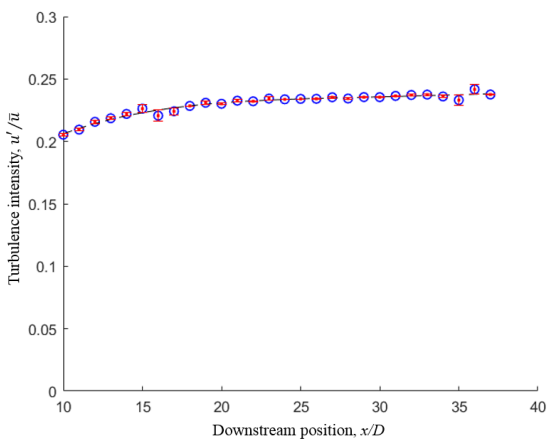

Fig. 7. The downstream development of the streamwise turbulence intensity, $u'/\overline{u}$.

Fig. 8 presents the downstream development of the spatial kinetic energy spectra along the jet centerline. Each spectrum is deliberately normalized in the low wave number asymptote to visualize a clearer comparison in term of its shape and slope with respect to the Kolmogorov's -5/3 law. As expected, a wider (assumed existent) inertial subrange is observed in the fully developed region [50]. There is a rapid development from a significant steep deviation in the developing region (intermediate field) to a remarkable resemblance to the -5/3 slope across a wider range in the fully developed counterpart [51]. This observation has also been previously accumulated by [14]–[16], [52], [53] that indicates the possibility of local equilibrium of the small scales in the inertial subrange, at least in this averaged representation, which has been implicitly assumed by Kolmogorov in the fully developed region [50]. Again, one can observe that the spectra have already developed a significant -5/3 range in the assumed inertial subrange at $x/D \approx 25$-30.

The spatial second-order structure functions based on the convection record method are shown in Fig. 9. With downstream position, the width of the variations in the small scales grows, corresponding to the development in the spectra in Fig. 8. This clearly demonstrates the downstream development of the turbulence scales. The large scales contain the highest energy in each curve and grow gradually downstream, as denoted by the arrow in the figure. As expected from Kolmogorov's 2/3 law [39] and what has also been obtained by [54], [55], a greater tendency for the curves to follow the 2/3 slope is observed in the fully developed region, compared to those measured in the developing region where a smaller slope is observed. This indicates that, in the developing region, the cascade process is yet to produce the large velocity increments [16].

According to the Kolmogorov theory, as described above, the dissipation should be directly obtainable from the third-order structure function assuming local homogeneity, isotropy and equilibrium. Although these assumptions are known not to be fulfilled in the jet, and in particular not in the developing region [5], we nevertheless apply the theory herein and compare with other obtained dissipation estimates. The downstream profile of the mean energy dissipation rate per unit mass as obtained from the third order structure functions, ε_{45} is plotted in Fig. 10. Measurements upstream of $x/D<20$ are discarded due to the strong deviations from the underlying assumptions in that region. The individual value of ε_{45} is obtained by best-fitting a 4/5 slope with the corresponding third-order structure function at the small separations, as demonstrated by Equation (9) and illustrated in Fig. 11, specifically at $x/D=28$ as an example. Figures of the same kind for the other downstream positions are shown in Appendix A.

In general, ε_{45} decreases downstream with a higher decay rate at the beginning of the fully developed region. This has been compared to the dissipation measured in (Hussein, Capp and George 1994), which present measurement of the dissipation based on the assumption of local axisymmetry of the small scale turbulence (which has been empirically shown to be the best representation in the round turbulent jet). From Figure 21 in [5], the dissipation along the centerline in the fully developed jet can be empirically scaled as $2\ \varepsilon_{axis}\ (x - x_0) / \bar{u}^3 \approx 0.7$ and has been overlaid in Fig. 10 for comparison. Since this estimate is only assumed to be valid in the fully developed jet region, the plot only includes the measurements for $x/D \geq 25$. Though there is significant deviation between the two curves in the crudely assumed fully developed region, the two curves have similar trends and seem to converge further downstream in the thoroughly explored fully developed region.

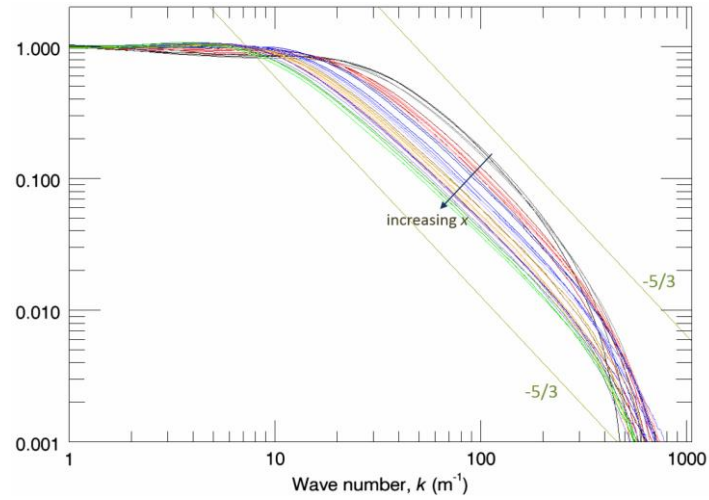

Fig. 8. Downstream development of spatial turbulent kinetic energy (convection record) spectra along the jet centerline. From *heavy to light black*: *x/D*=10, 11, 12, 13. From *heavy to light red*: *x/D* =14, 15, 16, 17, 18, 19. From *heavy to light blue*: *x/D* =20, 21, 22, 23, 24, 25. From *heavy to light brown*: *x/D* =26, 27, 28, 29, 30. From *heavy to light purple*: *x/D* =31, 32, 33, 34. From *heavy to light green*: *x/D* =35, 36, 37. Each spectrum is normalized in the low wave number asymptote to better compare their shapes and slopes with respect to Kolmogorov's -5/3 law.

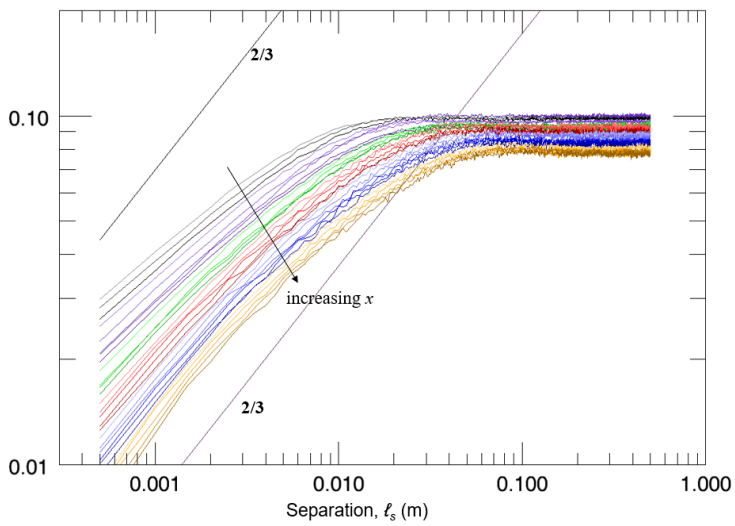

Fig. 9. Spatial second-order structure functions for different downstream positions. From *heavy to light brown*: *x/D*=37, 36, 35, 34, 33. From *heavy to light blue*: *x/D*=32, 31, 30, 29, 28, 27. From *heavy to light red*: *x/D*=26, 25, 24, 23, 22. From *heavy to light green*: *x/D*=21, 20, 19, 18. From *heavy to light purple*: x/D=17, 16, 15, 14, 13. From *heavy to light black*: *x/D*=12, 11, 10. Each curve is shifted vertically for a clear comparison of the scales development

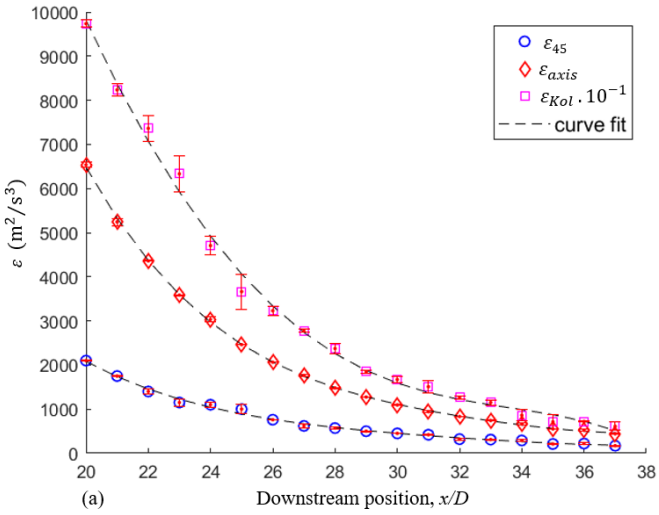

Fig. 10. Downstream evolution of the mean energy dissipation rate per unit mass, ε, with corresponding fourth-order polynomial curve fits. Note that ε_{Kol} is multiplied by 1/10 to compare for any similar trend.

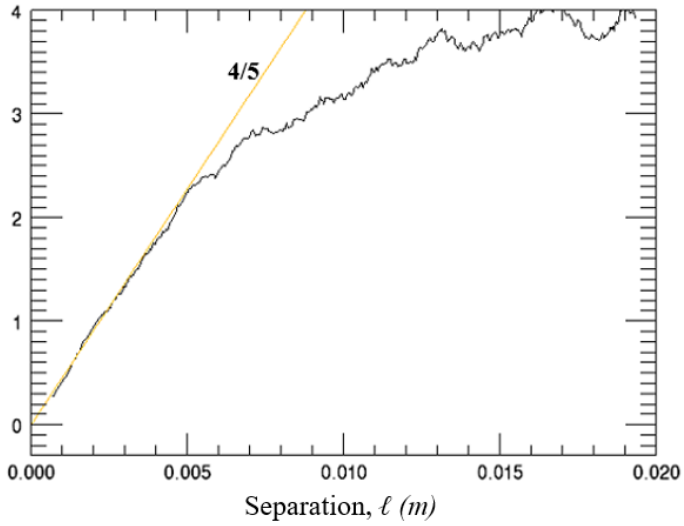

Fig. 11. Spatial third-order structure function at *x/D*=28 (centerline). (Figures of the same kind for the other downstream positions can be found in Appendix A)

The values of dissipation, ε_{45} extracted from the third-order structure function are first used to compute the Kolmogorov scales (both temporal and spatial) as shown in Fig. 12. The scales are growing downstream almost linearly, as expected from its inverse proportionality with the dissipation based on Equation (12) and (13). Similar behavior has also been presented in [56]. The smallest resolvable length scale is also computed based Equation (4) to be around $\lambda/2 \cdot 1/\pi$ = 28.6 µm. This value is represented by a horizontal *blue* line in Fig. 12, which is always way below the linear curve of the Kolmogorov length scales in the measured region. It shows that, with the current spatial resolution of our measurement setup, we should be able to resolve the Kolmogorov scale throughout our measured domain.

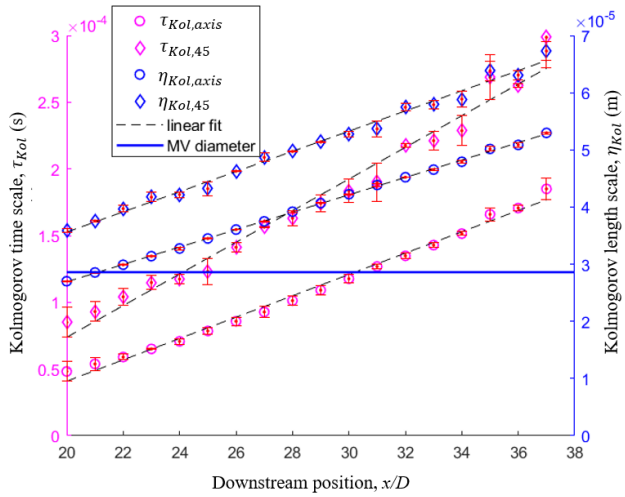

Fig. 12. Downstream evolution of the Kolmogorov time and length scale, with corresponding linear fit. The blue horizontal line represents the smallest resolvable scale of our instrument, i.e., 14.3 µm, which is always below the linear curve of the Kolmogorov length scales.

An attempt to estimate the corresponding value of the Taylor microscales has also been done based on its given definition [57]

$$\lambda_L = \sqrt{\frac{\overline{u^2}}{\left(\frac{du}{dt}\right)^2}} \tag{15}$$

However, this definition is only clear for a fully turbulent flow that leads to an ambiguity for computations in the intermittent flow. This limitation demands us more time to investigate on any other possible solutions rather than computing the Taylor scale directly from its definition. Another issue with the high frequency domination in the high frequency region also needs to be seriously taken into account since these high frequencies may contaminate the computation of the Taylor scales. Nevertheless, in general, the spatial scales are expected to grow and slow down downstream as what we can observe from the downstream profiles of the Kolmogorov and integral scales in as Fig. 12 and Fig. 13, respectively.

From the values of the integral length scale, L_u obtained, the Kolmogorov dissipation estimate, ε_{Kol} is also computed by $\overline{u^3}/L_u$, which values have been overlaid together with ε_{45} and ε_{axis} in Fig. 10. Though there is significant deviation between the three curves in the crudely assumed fully developed region ($x/D \geq 20$), each curve exhibits similar trends in both scales and seem to converge further downstream in the well-known fully developed region. Similar plots are also constructed in logarithmic scale as in Fig. 14. In this case, each dissipation estimate exhibits a linear trend downstream with different decay rates denoted by the exponent of x/D. It is also remarkable that the dissipation from the 4/5 law, ε_{45}, (which assumptions are not fulfilled) does not agree with the dissipation estimate epsilon, ε_{Kol}, which are both central results from the same Kolmogorov theory. If the theory was correct, the assumptions should be valid AND the two dissipation estimates should give (at least approximately) the same values.

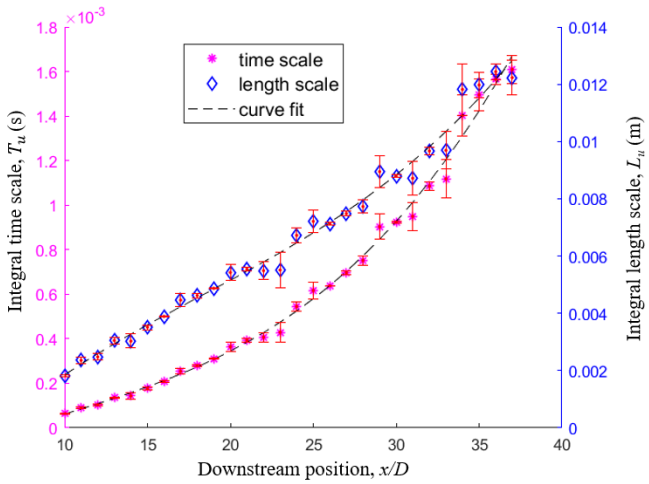

Fig. 13. Downstream evolution of the integral time and length scale, with corresponding third-order polynomial fit.

The most credible estimate would be the axisymmetric one, ε_{axis}, since it has been empirically established in [5], [58]. The values of this estimate are therefore used to recalculate the Kolmogorov length scales, $\eta_{Kol,axis}$ and time scales, $\tau_{Kol,axis}$ that have been overlaid in Fig. 12. In this case, the values of $\eta_{Kol,axis}$ measured are still beyond and equal to the smallest resolvable length scale (horizontal *blue* line) except for the only one at x/D=20, which value is just very slightly smaller. This exception however can still be acceptable considering that the values of the MV and $\eta_{Kol,axis}$ are determined only based on estimations.

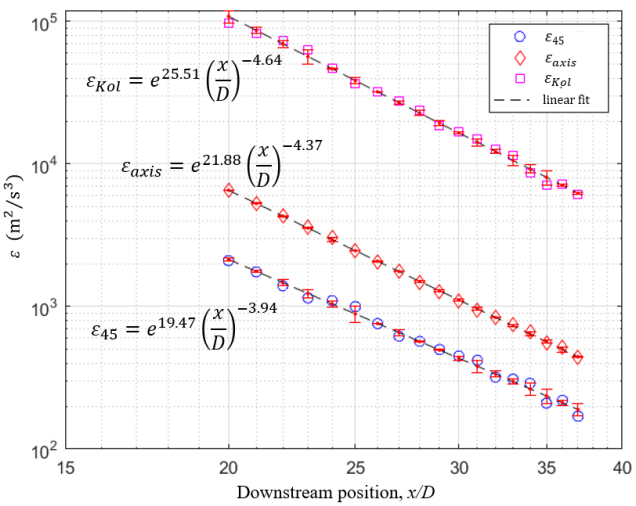

Fig. 14. Downstream evolution of the mean energy dissipation rate per unit mass, ε, in logarithmic scales with corresponding linear fits.

5. Conclusions

In the current work, we have presented the centerline development of the main static and dynamic statistical quantities obtainable using a single component (streamwise oriented) laser Doppler anemometer throughout the developing and part of the developed region of a round turbulent jet.

The employed laser Doppler anemometer has been built in-house and optimized for accurate measurements of fine-scale turbulence [14][34].

The statistics clearly show that the current jet becomes fully developed in both the first and second central statistical moments beyond approximately 25 jet exit diameters downstream of the jet exit. The second-order statistics take longer to develop fully than the first-order ones. The dynamic statistics show correspondingly that the spectra and second-order structure functions develop gradually until 30 jet exit diameters downstream of the jet exit has been reached. Beyond this limit, the jet displays (on average) a wide -5/3 range for the spectra and 2/3 region for the second-order structure functions. The measurements provide the time and length scales for the downstream development of the jet from the initial laminar uniform profile at the jet exit. These results can consequently be used for development and/or validation of turbulence models in a classical flow that at least on average displays the same physics as the Kolmogorov theory of turbulence, upon which the majority of current turbulence models are built.

It is also interesting that the linear fits of the mean velocity and the velocity variance appear to originate in different downstream positions, which will be further investigated in future publications.

Acknowledgement
The authors wish to acknowledge the support of Ministry of Education Malaysia, Universiti Teknial Malaysia Melaka (UTeM), DTU Mechanical Engineering, Reinholdt W. Jorck og Hustrus Fond (grant journal no. 13-J9-0026), Fabriksejer, Civilingeniør Louis Dreyer Myhrwold og hustru Janne Myhrwolds Fond (grant journal no. 13-M7-0039, 15-M7-0031 and 17-M7-0035) and Siemens A/S Fond grant no. 41.

References

[1] S. P. Capp, “Experimental investigation of the turbulent axisymmetric jet,” State University of New York, Buffalo, 1983.
[2] T. H. Weisgraber and D. Liepmann, “Turbulent structure during transition to self-similarity in a round jet,” *Exp. Fluids*, vol. 24, no. 3, pp. 210–224, 1998.
[3] Wyganski I. and H. Fielder, “Some measurements in the self-preserving jet,” *J. Fluid Mech.*, vol. 38, no. 3, pp. 577–612, 1969.
[4] G. A. Zarruk and E. A. Cowen, “Simultaneous velocity and passive scalar concentration measurements in low Reynolds number neutrally buoyant turbulent round jets,” *Exp. Fluids*, vol. 44, pp. 865–872, 2008.
[5] H. J. Hussein, S. P. Capp, and W. K. George, “Velocity measurements in a high-Reynolds-number, momentum-conserving, axisymmetric, turbulent jet,” *J. Fluid Mech.*, vol. 258, pp. 31–75, 1994.
[6] Panchapakesan N. R. and J. L. Lumley, “Turbulence measurements in axisymmetric jets of air and helium . Part 1 . Air jet,” *J. Fluid Mech.*, vol. 246, pp. 197–223, 1993.
[7] C. D. Richards and W. M. Pitts, “Global density effects on the self-preservation behaviour of turbulent free jets,” *J. Fluid Mech*, vol. 254, no. 1, pp. 417–435, 1993.
[8] D. R. Dowling and P. E. Dimotakis, “Similarity of the concentration field of gas-phase turbulent jets,” *J. Fluid Mech.*, vol. 218, no. 1, pp. 109–141, 1990.
[9] W. K. George and M. M. Gibson, “The self-preservation of homogeneous shear flow turbulence,” *Exp. Fluids*, vol. 13, no. 4, pp. 229–238, 1992.
[10] W. K. George, “The decay of homogeneous anisotropic turbulence,” *Phys. Fluids A Fluid Dyn.*, vol. 4, no. 7, pp. 1492–1509, 1992.
[11] W. K. George, “Asymptotic Effect of Initial and Upstream Conditions on Turbulence,” *J. Fluids Eng.*, vol. 134, no. 6, p. 061203, 2012.
[12] C. M. Velte, W. K. George, and P. Buchhave, “Estimation of burst-mode LDA power spectra,” *Exp. Fluids*, vol. 55, no. 3, p. 1674, 2014.
[13] M. R. Yaacob, R. K. Schlander, P. Buchhave, and C. M. Velte, “Mapping Of Turbulent Round Jet Developing

Region Using a Constant Temperature Anemometer (CTA)," *Malaysian J. Fundam. Appl. Sci.*, no. Special Issue on Natural Sciences and Mathematics (ESCon 2018), pp. 443–446, 2018.

[14] M. R. Yaacob, R. K. Schlander, P. Buchhave, and C. M. Velte, "Validation of improved laser Doppler anemometer (LDA) based on the fully developed turbulent round jet," in *Symposium of Electrical, Mechatronics and Applied Science*, 2018, pp. 89–90.

[15] P. Buchhave and C. M. Velte, "Measurement of turbulent spatial structure and kinetic energy spectrum by exact temporal-to-spatial mapping," *Phys. Fluids*, vol. 29, no. 8, 2017.

[16] M. R. Yaacob, R. Schlander, P. Buchhave, and C. M. Velte, "Experimental Evaluation of Kolmogorov's -5/3 and 2/3 Power Laws in the Developing Turbulent Round Jet," *J. Adv. Res. Fluid Mech. Therm. Sci.*, vol. 45, no. 2, pp. 14–21, 2018.

[17] A. N. Kolmogorov, "Decay of isotropic turbulence in incompressible viscous fluids," *Dok. Akad. Nauk. S. S. S. R*, vol. 31, pp. 538–541, 1941.

[18] A. N. Kolmogorov, "Dissipation of energy in local isotropic turbulence," *Dokl. Akad. Nauk. SSSR*, vol. 32, pp. 15–17, 1941.

[19] A. N. Kolmogorov, "The local structure of turbulence in incompressible viscous fluid for very large Reynolds numbers," *C. R. Akad. Sci. SSSR*, vol. 30, pp. 9–13, 1941.

[20] A. N. Kolmogorov, "A Refinement of Previous Hypothesis Concerning the Local Structure of Turbulence in a Viscous Incompressible Fluid at High Reynolds Number," *J. Fluid Mech.*, vol. 13, pp. 82–85, 1962.

[21] D. Jung, "An investigation of the Reynolds-number dependence of the axisymmetric jet mixing layer using a 138 hot-wire probe and the POD," State University of New York, 2001.

[22] J. H. Bell and R. D. Mehta, "Contraction design for small low-speed wind tunnels," 1988.

[23] H. Fellouah, C. G. Ball, and A. Pollard, "Reynolds number effects within the development region of a turbulent round free jet," *Int. J. Heat Mass Transf.*, vol. 52, no. 17–18, pp. 3943–3954, 2009.

[24] A. Melling and J. H. Whitelaw, "Seeding of gas flows for laser anemometry," *Danske Ind. Syndikat A/s Inf.*, no. 15, pp. 5–14, 1973.

[25] H. E. Albrecht, M. Borys, N. Damaschke, and C. Tropea, *Laser Doppler and Phase Doppler Measurement Techniques*. Springer-Verlag, 2003.

[26] C. Tropea, A. L. Yarin, and J. F. Foss, *Springer Handbook of Experimental Fluid Mechanics*. Springer, 2007.

[27] K. G. Bartlett and C. Y. She, "Remote measurement of wind speed using a dual beam backscatter laser Doppler velocimeter," *Appl. Opt.*, vol. 15, no. 8, pp. 1980–1983, 1976.

[28] G. R. Grant and K. L. Orloff, "Two-color dual-beam backscatter laser Doppler velocimeter.," *Appl. Opt.*, vol. 12, no. 12, pp. 2913–2916, 1973.

[29] M. Sommerfeld and C. Tropea, "Single-Point Laser Measurement," in *Instrumentation for Fluid Particle Flow*, 1999, pp. 252–317.

[30] M. Diop, S. Piponniau, and P. Dupont, "High resolution LDA measurements in transitional oblique shock wave boundary layer interaction," *Exp. Fluids*, vol. 60, no. 4, p. 57, 2019.

[31] P. Buchhave, "Three-component LDA measurements," *Disa Inf.*, no. 29, pp. 3–9, 1984.

[32] P. Buchhave and C. M. Velte, "Reduction of noise and bias in randomly sampled power spectra," *Exp. Fluids*, vol. 56, no. 4, pp. 1–17, 2015.

[33] A. Fischer, "Imaging Flow Velocimetry with Laser Mie Scattering," *Appl. Sci.*, vol. 7, no. 12, p. 1298, 2017.

[34] M. R. Yaacob, R. K. Schlander, P. Buchhave, and C. M. Velte, "A novel laser Doppler anemometer (LDA) for high-accuracy turbulence measurements," *ArXiv ID 1905.08066*.

[35] P. Buchhave, "Errors and Correction Methods in Turbulence Measurements with the LDA," State University of New York, 1979.

[36] P. Buchhave, W. K. George, and J. L. Lumley, "The measurement of turbulence with the laser-Doppler anemometer," *Annu. Rev. Fluid Mech.*, vol. 11, pp. 443–503, 1979.

[37] C. M. Velte, "Characterization of vortex generator induced flow," Technical University of Denmark, 2009.

[38] J. L. Lumley, "Interpretation of time spectra measured in high-intensity shear flows," *Phys. Fluids*, vol. 8, no. 6, pp. 1056–1062, 1965.

[39] U. Frisch, *Turbulence: The Legacy of A.N. Kolmogorov*. Cambridge University Press, 1995.

[40] J. M. McDonough, *Introductory Lectures on turbulence: Physics, Mathematics and Modeling*. Departments of Mechanical Engineering and Mathematics University of Kentucky, 2007.

[41] J. C. Wyngaard and S. F. Clifford, "Taylor's hypothesis and high-frequency turbulence spectra," *J. Atmos. Sci.*, vol. 34, no. 6, pp. 922–9, 1977.

[42] X. Grandchamp, A. Van Hirtum, and X. Pelorson, "Centreline velocity decay characterisation in low-velocity jets downstream from an extended conical diffuser," *Meccanica*, vol. 48, pp. 567–583, 2013.

[43] C. G. Ball, H. Fellouah, and A. Pollard, "The flow field in turbulent round free jets," *Prog. Aerosp. Sci.*, vol. 50, pp.

1–26, 2012.
[44] S. Pope, *Turbulent Flows*. Cambridge University Press, 2000.
[45] J. Mi, G. J. Nathan, and D. S. Nobes, "Influence of jet exit conditions on the passive scalar field of an axisymmetric free jet," *J. Fluids Eng.*, vol. 432, pp. 91–125, 2001.
[46] A. Hodzic, "Experimental and theoretical investigations of turbulent axi-symmetric jets," Technical University of Denmark, 2019.
[47] S. Z. Kassab, A. E. Bakry, and H. A. Warda, "Laser Doppler anemometry measurements in an axisymmetric turbulent jet," *Rev. Sci. Instrum.*, vol. 67, no. 5, pp. 1842–1849, 1996.
[48] E. Ferdman, M. V. Otugen, and S. Kim, "Effect of initial velocity profile on the development of round jets," *J. Propuls. Power*, vol. 16, no. 4, pp. 676–686, 2000.
[49] A. Hodzic, "PIV Measurements on a Turbulent Free Jet - Spatial Decomposition of a Turbulent Free Jet using Proper Orthogonal Decomposition," Technical University of Denmark, 2014.
[50] G. K. Batchelor, *The theory of homogeneous turbulence*. Cambridge University Press, 1953.
[51] M. M. Gibson, "Spectra of Turbulence at High Reynolds Number," *Nature*, vol. 195, pp. 1281–1283, 1962.
[52] P. Buchhave and C. M. Velte, "Conversion of Measured Turbulence Spectra from Temporal to Spatial Domain," in *Whither Turbulence and Big Data in the 21st Century?*, Springer, 2017, pp. 343–362.
[53] C. M. Velte, P. Buchhave, and A. Hodzic, "Measurement of turbulent kinetic energy spectrum - Part 2 : Convection record measurements," in *iTi Conference on Turbulence VII*, 2017, pp. 171–176.
[54] L. Danaila, F. Anselmet, and R. A. Antonia, "An overview of the effect of large-scale inhomogeneities on small-scale turbulence," *Phys. Fluids*, vol. 14, no. 2475, 2002.
[55] G. P. Romano and R. A. Antonia, "Longitudinal and transverse structure functions in a turbulent round jet: effect of initial conditions and Reynolds number," *J. Fluid Mech.*, vol. 436, pp. 231–248, 2001.
[56] H. Fellouah and A. Pollard, "The velocity spectra and turbulence length scale distributions in the near to intermediate regions of a round free turbulent jet," *Phys. Fluids*, vol. 21, no. 11, p. 011911PHF, 2009.
[57] H. Tennekes and J. L. Lumley, *A First Course in Turbulence*. MIT Press, 1972.
[58] W. K. George and H. J. Hussein, "Locally Axisymmetric Turbulence," *J. Fluid Mech.*, vol. 233, pp. 1–23, 1991.

Appendix A

Spatial third-order structure function plots along the jet centreline for 20≤*x/D*≤37

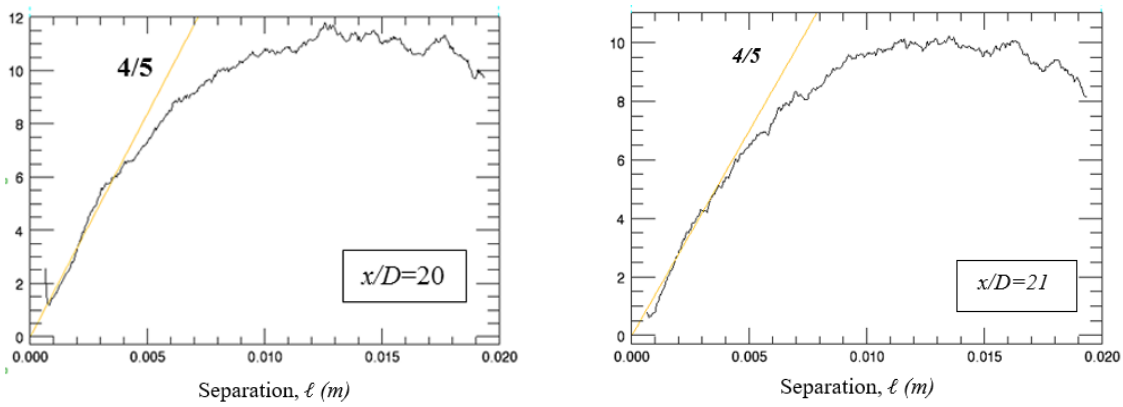

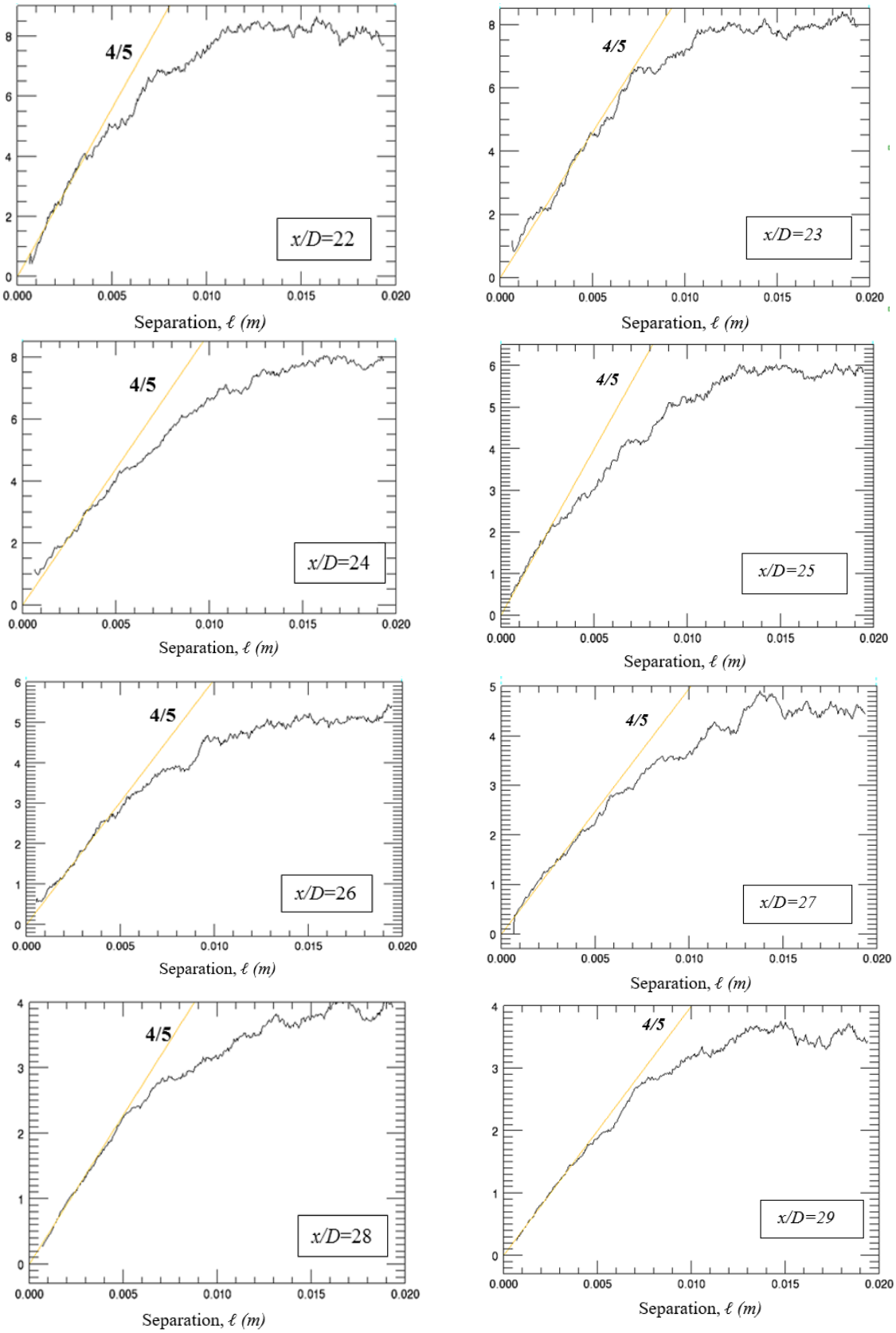
4/5
x/D=22
x/D=23
x/D=24
x/D=25
x/D=26
x/D=27
x/D=28
x/D=29
Separation, ℓ (m)

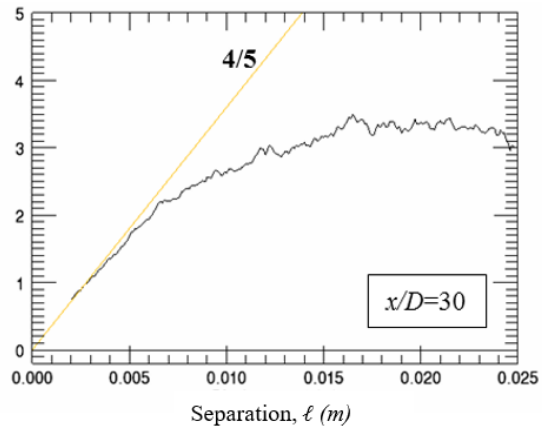
4/5
x/D=30
Separation, ℓ (m)

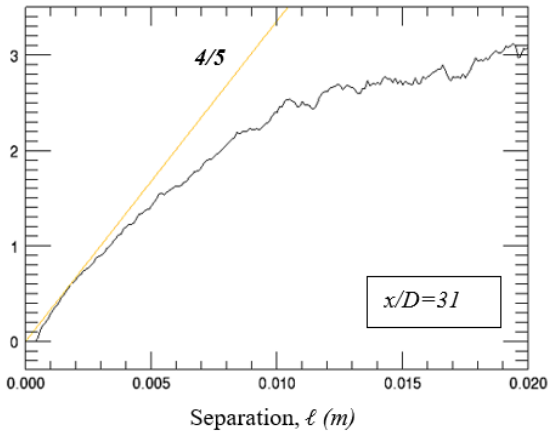
4/5
x/D=31
Separation, ℓ (m)

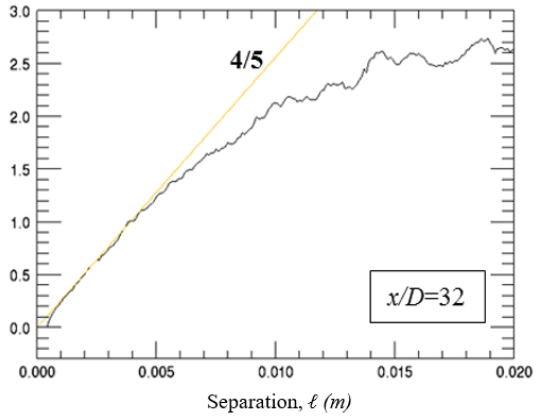
4/5
x/D=32
Separation, ℓ (m)

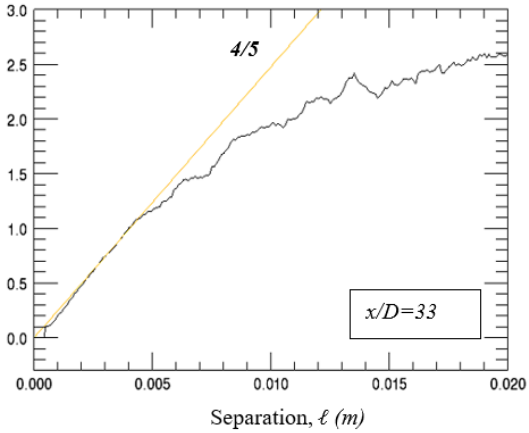
4/5
x/D=33
Separation, ℓ (m)

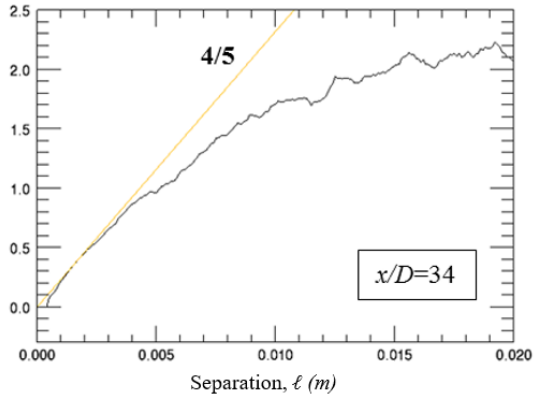
4/5
x/D=34
Separation, ℓ (m)

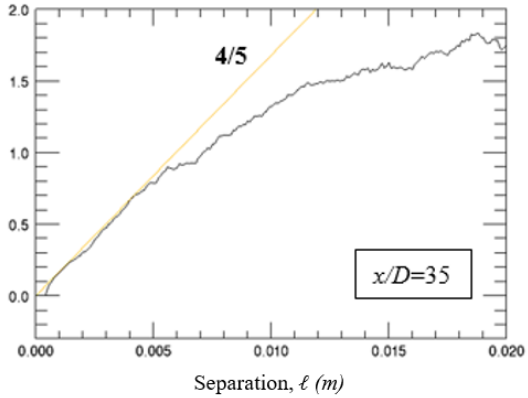
4/5
x/D=35
Separation, ℓ (m)

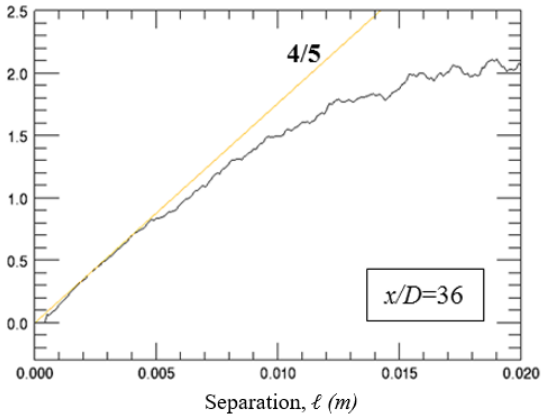
4/5
x/D=36
Separation, ℓ (m)

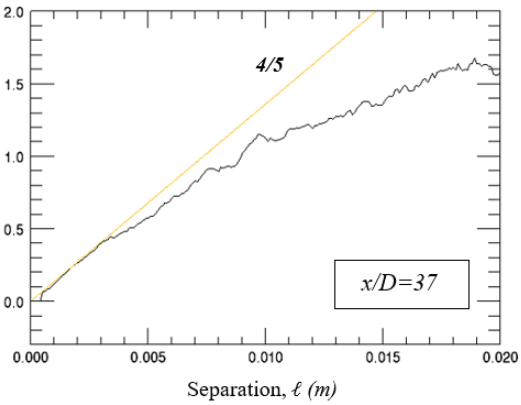
4/5
x/D=37
Separation, ℓ (m)

Appendix B

Coefficient values for polynomial profiles, e.g., $P(x)= C_4x^4 + C_3x^3 + C_2x^2 + C_1x + C_0$

Figure No.	Profiles	C_4	C_3	C_2	C_1	C_0
4	$\bar{u}$	N/A	-0.001	0.1021	-3.6430	55.1326
	$\overline{u^2}$	N/A	-0.0021	0.2017	-6.7328	82.4643
5	$U_0/\bar{u}$	N/A	N/A	N/A	0.1511	-0.3513
	${U_0}^2/\overline{u^2}$	N/A	N/A	N/A	22.2738	-347.9181
6	U_0/RMS	N/A	N/A	N/A	0.6169	-0.7816
7	$u'/\bar{u}$	N/A	N/A	-6.0338E-05	0.0038	0.1781
10	ε_{45}	0.0374	-4.8296	236.2882	-5.2287E3	4.48E4
	ε_{axis}	0.1098	-14.5552	730.5065	-1.6544E4	1.4404E5
	ε_{Kol}	-0.0775	6.4832	-128.0662	-1.7017E3	5.5609E4
12	$\tau_{Kol,45}$	N/A	N/A	N/A	1.1865E-5	-1.6355E-4
	$\tau_{Kol,axis}$	N/A	N/A	N/A	8.0018E-6	-1.1921E-4
	$\eta_{Kol,45}$	N/A	N/A	N/A	1.7652E-6	3.1288E-7
	$\eta_{Kol,axis}$	N/A	N/A	N/A	1.5219E-6	-3.5285E-6
13	T_u	N/A	4.9693E-8	-1.4861E-6	3.8096E-5	-2.2047E-4
	L_u	N/A	3.7542E-7	-2.0678E-5	6.8835E-4	-0.003342

Paper VI

Mapping of the Energy Cascade in the Developing Region of a Turbulent Round Jet

Mohd Rusdy Yaacob[1, a)], Preben Buchhave[3, b)], Clara Marika Velte[2, b)]

[1)] *Faculty of Electrical Engineering, Universiti Teknikal Malaysia Melaka, Hang Tuah Jaya, 76100 Durian Tunggal, Melaka, Malaysia*

[2)] *Department of Mechanical Engineering, Technical University of Denmark, Nils Koppels Alle, Building 403, 2800 Kgs. Lyngby, Denmark*

[3)] *Intarsia Optics, Sønderskovvej 3, 3460 Birkerød, Denmark*

Developing turbulence has been underexplored due to practical limitations for conducting measurements in the most interesting, yet measurement technically difficult, high shear and high intensity regions. One classical example is the developing and outermost regions of a jet, where high shear and turbulence intensities are generally expected. This has impaired the ability to properly test the critical assumptions of the existing theory by Richardson and Kolmogorov and their consequences, such as decoupling between large and small scales, and universality and equilibrium of the small and intermediate scales. Substantial challenges to this theory by previous researchers and the development of a novel, in-house laser Doppler system have driven us to conduct an experimental study in mapping the developing region of a turbulent round jet and obtaining high-quality measurement data, which have the potential to help fill the knowledge gap. This paper is a major extension from our previous investigations (M. R. Yaacob, R. Schlander, et al. 2018) and fairly describing experimental works for acquiring the velocity data points as well as the application of previously developed novel techniques (Buchhave and Velte 2017b) to determine higher order moments of velocities, which may reveal interesting non-equilibrium features of the flow. Spatial kinetic energy spectra and second-order structure functions illustrate the distribution of energy across the scales and the development of the turbulence scales, respectively, in the developing region. Meanwhile, third-order structure functions allow us to determine the mean energy dissipation across the flow, but only in the case of the fully developed region. The measurements presented herein provides a uniquely accurate measurement database of a canonical high shear and high intensity turbulent flow that can serve as a baseline for further theoretical and modelling developments.

Keywords: Turbulent round jet, developing region, spatial energy spectra, structure functions, dissipation

I. INTRODUCTION

The central assumptions of the Kolmogorov theory of turbulence is that of the universal equilibrium of the intermediate and smallest scales (Batchelor 1953; George 2014; Kolmogorov 1941c). Many studies

[a)] Electronic mail: rusdy@utem.edu.my
[b)] Electronic mail: buchhavepreben@gmail.com and cmve@dtu.dk

have been conducted since the 1940's, predominantly paying only limited attention to what happens when turbulence is still developing. Of particular interest are the mechanisms that determine how energy is cascaded from large to small scales and, consequently, the mechanisms setting the level of dissipation, which is central to turbulence theory and modelling (Stewart 1959). According to Richardson's energy cascade, turbulent kinetic energy is transferred primarily by interaction between adjacent scales (so-called local interactions) (Richardson 1922). Recent evidence, however, suggests that the interactions are likely to be more complex. (Tsinober 2001) has challenged the misconception that large scales and small scales are decoupled and non-interacting. Furthermore, (Anselmet, Antonia, and Danaila 2001) have introduced the non-universality of small scale properties due to stream-wise inhomogeneity, by considering the small-scale intermittency of energy transfer, which contradicts the Richardson-Kolmogorov theory (L'vov and Procaccia 2007). In fact, (Kolmogorov 1962) and (Frisch, Sulem, and Nelkin 1978) have even suggested corrections to the K41 law for intermittency in the inertial subrange.

Significant challenges to this theory have continued to emerge: For example, studies conducted by (Danaila, Anselmet, and Antonia 2002) investigating spectrally the discrepancy between the asymptotic predictions of Kolmogorov's -5/3 power law and actual measured phenomena in the case of decaying grid turbulence flow. They also found non-negligible inhomogeneity in the same flow, which suggested a future experiment to be done with a turbulent round jet. (Seoud and Vassilicos 2007) have further conducted numerous experiments to investigate the dissipation anomaly during the stream-wise development of turbulence in decaying grid-generated flows in wind tunnels. Few years later, (Valente and Vassilicos 2012) have recorded energy spectra having tendency to the power law symptom even in the non-equilibrium region. In the recent years, Vassilicos and his team have been actively accumulating both experimental and computational evidence related to the existence of non-equilibrium (developing) regions in turbulent flows (Goto and Vassilicos 2015, 2016; Laizet, Nedić, and Vassilicos 2015; Valente and Vassilicos 2015; Vassilicos 2015). These works have motivated us to further investigate for the non-equilibrium anomaly of a free turbulent shear flow, e.g., the stationary turbulent round jet, which has been proven to display good agreement with Kolmogorov's theory on average in the fully developed (equilibrium) region (Gibson 1962, 1963; Panchapakesan N. R. and Lumley 1993; Wänström, George, and Meyer 2012).

The complex conditions in the developing region of a jet, such as high turbulence intensities, significant shear and inhomogeneity, considerably limit the choice of usable (accurate) measurement techniques and analysis applicable methods. The laser Doppler anemometer (LDA) is the only known instrument that can accurately measure within this region with sufficient dynamic range, without disturbing the flow (Buchhave, George, and Lumley 1979) and successfully distinguishing the spatial velocity components from each other, even at high turbulence intensities (Hussein, Capp, and George 1994). Unfortunately, commercial systems have turned out to produce unreliable outputs necessary for producing unbiased statistics (Velte, George, and Buchhave 2014). That is why we have developed a novel and state-of-the-art LDA system to overcome the known limitations of commercially available systems (Velte et al. 2014). This software-driven system has also been validated through series of measurements using both side scattering (Buchhave and Velte 2017b) and forward scattering configurations (M. R. Yaacob, R. Schlander, et al. 2018). Results from both have shown good agreement with Kolmogorov's local equilibrium assumption in the equilibrium region of the jet, while revealing promising new features in the non-equilibrium counterpart, which will be emphasized further in this paper. This system was therefore used to map the developing region (downstream and radial traverses) of the round turbulent jet up to the point where the second-order moments of the velocities are known to be fully developed.

The following section briefly explains the LDA experimental set-up and how the static moments were computed. In Section 3, the development of mean velocities, variance, turbulence intensities, spatial energy spectra, structure functions and mean energy dissipation profiles are reported and discussed.

II. METHODOLOGY

A. Experimental setup

The same setup as in (M. R. Yaacob, R. Schlander, et al. 2018) was used, which is a jet generator box fabricated in the DTU workshop and replicates the one used by (Jung 2001)(Velte et al. 2014). The jet box is fitted with an outer nozzle of 10 mm-diameter and contraction ratio of 3.2:1 and supplied with pressurized air and seeding particles (glycerine). It was mounted on a two-axis traverse and placed in a large tent (3 x 5.8 x 3.1 m^3) to minimize light pollution, external flow disturbances and particles leakage to surroundings. The jet pressure was set to provide a jet exit velocity ≈ 35 m/s and corresponding $Re \approx$ 22000, while the seeding pressure was adjusted to be around 1.4 bar to give an optimum data rate. The diameter of the (approximately spherical) measurement volume is around 90 µm and the average data rate was approximately 25000 s^{-1} at x/D=30, centreline. Suitable sampling rates were chosen based on the Nyquist condition (Seoud and Vassilicos 2007) in order to avoid erroneous frequency measurement by the scope; either 25 MHz or 12.5 MHz, which resulted in a total number of samples of 25 million. To increase the signal-to-noise ratio, the photodetector was mounted in 45° forward scattering (see FIG. 1), which naturally puts high demands on accurate and robust optical alignment.

Measurements of the axial (streamwise) component of velocities spanning from downstream positions x/D=5 up to x/D=30 were acquired at different radial points as illustrated in FIG. 2. This measurement scheme was determined from the mapping obtained during the preliminary experiment (M.R. Yaacob, R. Schlander, et al. 2018), which was performed earlier to capture the regions where the turbulence development was most marked. The high level of fluctuations observed from that experiment has also highlighted the need to use a suitable optical frequency shift in order to obtain unbiased velocity measurement especially in the shear layers and the outer region of the jet. To do this, the beams were directed through a dual Bragg cell, which shifted one of the beams by a known frequency i.e. 40MHz while the other shifted the frequency of the other beam by 37MHz, which resulted in an effective shift of 3MHz.

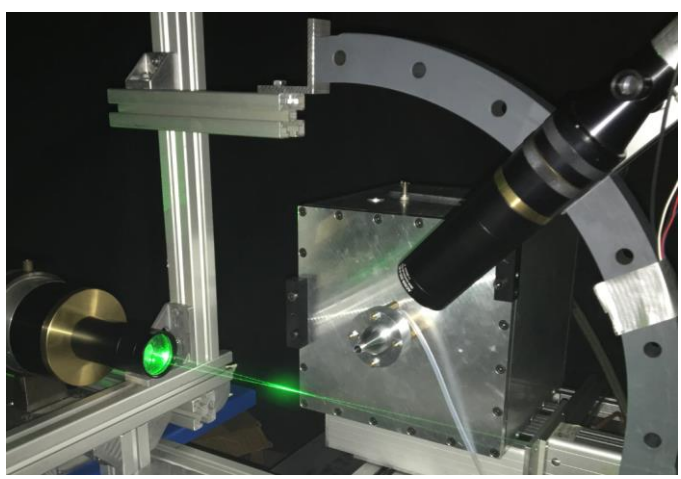

FIG. 1. In-house LDA system showing jet exit with the detector (lens focal length, f=200mm) positioned in 45° forward scattering

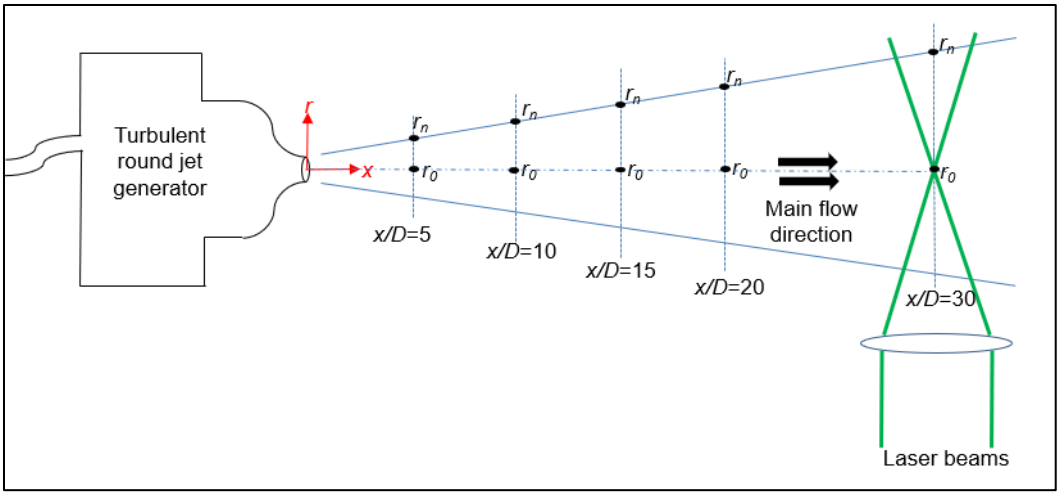

FIG. 2. Top view sketch of the setup showing the measurement point distribution in the downstream *x*-direction and in the radial, *r*-direction

B. Velocity static moments

Signals obtained from the measurements were digitized, saved and processed using our own, recently developed, in-house software (M. R. Yaacob, R. K. Schlander, et al. 2018; Yaacob, Schlander, et al. *under preparation*), which provides the arrival time, residence time and instantaneous streamwise velocity of each particle. The mean velocity, $\bar{u}$ and variance, $\overline{u^2}$ are calculated using Equation (1) and Equation (2), respectively, which employed residence time-weighting for unbiased statistics, as proposed by (Buchhave 1979; Buchhave et al. 1979; Velte 2009; Velte et al. 2014):

$$\bar{u} = \frac{\sum_{n=0}^{N-1} u_i(t_n)\Delta t_n}{\sum_{n=0}^{N-1} \Delta t_n} \tag{1}$$

$$\overline{u^2} = \frac{\sum_{n=0}^{N-1} [u_i(t_n) - \bar{u}_i]^2 \Delta t_n}{\sum_{n=0}^{N-1} \Delta t_n} \tag{2}$$

where Δt_n is the residence time for the nth realization. This scheme has been shown analytically, from first principles (Buchhave et al. 1979; Velte 2009), as well as experimentally (Buchhave and Velte 2017b), to provide non-biased statistics of the LDA burst signal.

C. Temporal-to-spatial mapping

Though the measurements were acquired as time records, energy spectra were herein computed and are presented in the wave number domain. This is to avoid the unwished effect of temporal energy spectra to display incorrect distribution of spatial scales e.g., due to the convection effect from velocity fluctuations of the large scale (Lumley 1965). Furthermore, the -5/3 power law shapes are well predicted in the spatial energy spectra instead of in the temporal ones (Pope 2000). To obtain a faithful representation of the energy content of the spatial structures, the mapping from temporal to spatial records was performed based on the convection record principle (Buchhave and Velte 2017b), where the instantaneous velocity magnitude has been employed rather than the average streamwise velocity as proposed by (Taylor 1938). Turbulent flow measurement records were thereby converted from temporal to spatial domain, bypassing the adverse fluctuating convection velocity effect. This transformation is given by Equation (3):

$$s(t) = \int_0^t |\bar{u}(x_0, t')| dt' \quad (3)$$

where s is the scalar length of accumulated convection elements for fluid passing through the spatial record volume , $\bar{u}$ is the instantaneous velocity vector at an instantaneous time, t' and x_0 is the location of the fixed MV. Note that this method requires the flow to be stationary at the measurement point in order to acquire a homogeneous spatial record, which can be used to compute sensible static statistical quantities. Having the energy spectra plotted in the wave number domain allows us to study the spatial turbulence structure, which is of great interest in turbulence theory since the classical turbulence theory (Batchelor 1953; Kolmogorov 1941c, 1941a, 1941b, 1962) is indeed formulated in space rather than in time.

D. Computation of spatial structure functions

The classical second- and third-order spatial structure functions, respectively, are defined as:

$$S_2(\ell_x) = \langle \left(\bar{u}_x(x + \ell_x, t) - \bar{u}_x(x, t)\right)^2 \rangle \quad (4)$$

$$S_3(\ell_x) = \langle \left(\bar{u}_x(x + \ell_x, t) - \bar{u}_x(x, t)\right)^3 \rangle \quad (5)$$

where $\bar{u}_x$ is the streamwise velocity and ℓ_x is the spatial separation along the x-axis. Since the convection record (as described earlier in section 2.3) is employed herein, in a stationary random velocity signal in a measurement point, the second- and third-order structure functions, respectively, can be expressed as:

$$S_2(\ell_s) = \langle \left(\bar{u}_x(s + \ell_s) - \bar{u}_x(s)\right)^2 \rangle \quad (6)$$

$$S_3(\ell_s) = \langle \left(\bar{u}_x(s + \ell_s) - \bar{u}_x(s)\right)^3 \rangle \quad (7)$$

where ℓ_s is the spatial separation along the s-record. Note that the < > brackets denote ensemble averaging. Both second- and third-order structure functions are also related to each other for locally isotropic turbulence (small and intermediate range scales are isotropic), as given by (Kolmogorov 1941b):

$$\left(\frac{d}{d\ell_s} + \frac{4}{\ell_s}\right)\left(6\nu \frac{dS_2}{d\ell_s} - S_3\right) = 4\varepsilon \quad (8)$$

where ν is the kinematic viscosity and ε is the mean energy dissipation rate per unit mass. Based on the second hypothesis of similarity for large ℓ_s(Kolmogorov 1941c), the second-order structure function from equation (6) can be reduced to:

$$S_2(\ell_s) \sim C\varepsilon^{2/3}{\ell_s}^{2/3} \quad (9)$$

Meanwhile with the conditions where $\frac{dS_2(0)}{d\ell_s} = S_3(0) = 0$ and for small ℓ_s (Frisch 1995), the third-order structure functions from equation (7) can be reduced to:

$$S_3(\ell_s) \sim -\frac{4}{5}\varepsilon\ell_s \quad (10)$$

The size of the measurement volume was firstly estimated prior to the conversion process by equating the spatial record obtained from the convection record method with the one obtained by Taylor's frozen

turbulence hypothesis (Buchhave and Velte 2017a). The actual size of the measurement volume could be found if the spatial records obtained from both methods were equal to each other, as long as the gain used throughout the measurement is constant. This comparison was made for the record at the jet centreline for each downstream position, where turbulence intensities are at the lowest and where Taylor's hypothesis is known to be valid to a good approximation (Buchhave and Velte 2017b).

E. Computation of turbulence time and length scales

The Kolmogorov time, τ_{Kol} and length scales, η_{Kol} are computed directly using Equation (11) and (12) respectively:

$$\tau_{Kol} = \left(\frac{\nu}{\varepsilon}\right)^{1/2} \tag{11}$$

$$\eta_{Kol} = \left(\frac{\nu^3}{\varepsilon}\right)^{1/4} \tag{12}$$

where ε is the mean energy dissipation rate per unit mass and ν is the kinematic viscosity of the working fluid.

The integral time scale, T_u is computed from the integral under the temporal covariance function as in Equation (13).

$$T_u = \int_0^\infty \frac{\overline{u(t)u(t+\tau)}}{\overline{u^2}} d\tau \tag{13}$$

By using the convection record, the spatial counterpart, L_u is estimated by multiplying T_u with the convection velocity.

Meanwhile, the Taylor length scale, λ_L can be computed based on the its definition (Tennekes and Lumley 1972)

$$\lambda_L = \sqrt{\frac{\overline{u^2}}{\overline{\left(\frac{du}{dt}\right)^2}}} \tag{14}$$

However, this definition is only clear for a fully turbulent flow that leads to an ambiguity for computations in the intermittent flow. This limitation demands us more time to investigate on any other possible solutions rather than computing the Taylor scale directly from its definition. There is also another issue with the high frequency domination in the high frequency region that needs serious attention since these high frequencies may contaminate the computation of the Taylor scales. The results of the Taylor scales are therefore not to be included in this paper.

III. RESULTS

A. Velocity static moments

FIG. 3 shows the radial profiles of measured mean velocity, variance and turbulence intensity, respectively, at each measured downstream position throughout the developing region. As expected from the spreading of the jet, the mean velocity profiles spread out and taper with increasing downstream position. Meanwhile, the variance peaks in the production intensive shear layer, as expected, and spreads and tapers with downstream development. Due to the early turbulence developments of the laminar jet core, the turbulence intensities are significantly lower at *x/D*=5 compared to the other downstream positions along the jet centreline. These measurements are by nature very challenging to be done especially in the outer part of the jet due to limitation in dynamic range with common measurement techniques. For instance, hot wire anemometry (HWA) may offer a high dynamic range but it cannot accurately represent high turbulence intensities while particle image velocimetry (PIV) could not measure small velocity changes accurately since due to its low dynamic range (Jensen 2004). The promising results shown in the following figures indicate that our software-driven and improved LDA system is uniquely suited for this kind of measurements and validate the advantages of LDA as discussed in Section I.

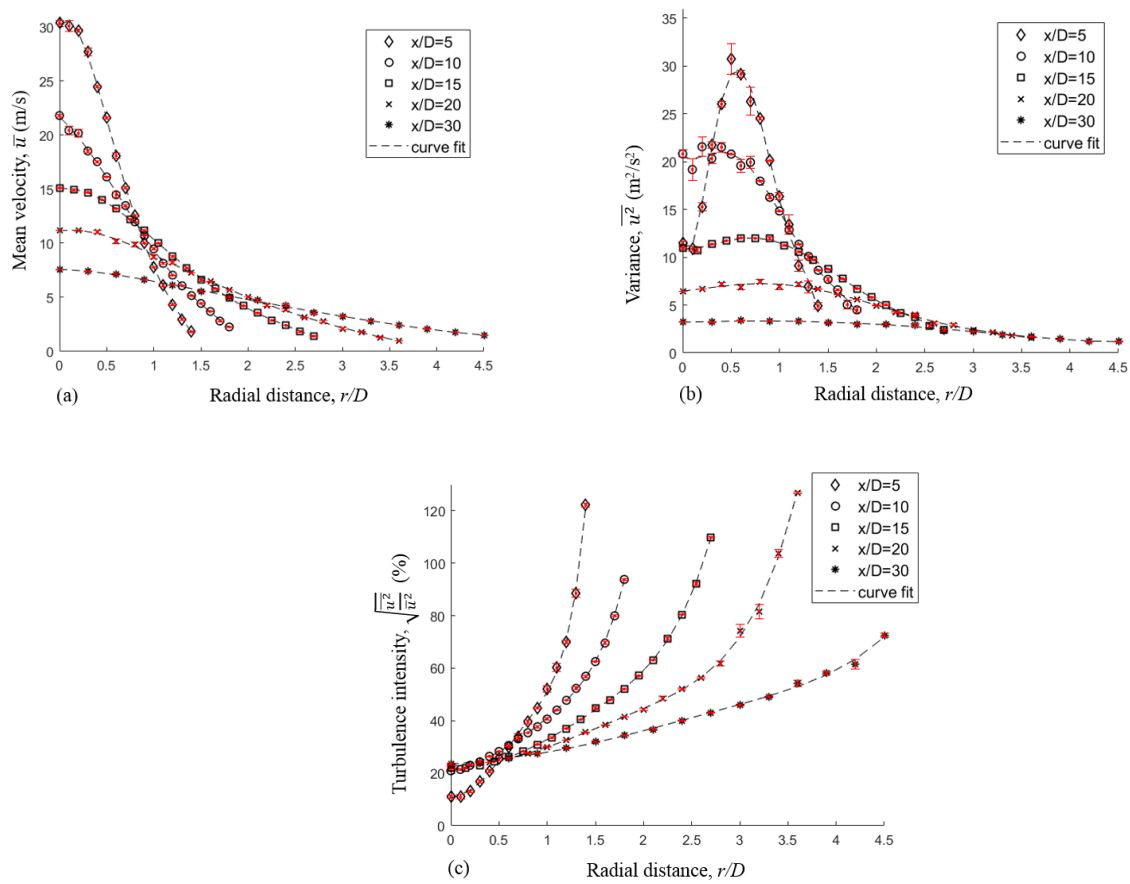

FIG. 3. Radial profiles of (a) mean velocity, (b) variance, (c) turbulence intensity at *x/D* = 5, 10, 15, 20 and 30 with 5th order polynomial curve fits and error bars (in *red*). Coefficients for the polynomials are listed in Appendix I (also for the following figures).

The radial profiles of turbulence intensity (except for *x/D*=5) were also replotted in the search of potential collapses by normalizing the radial distance, *r* with the downstream distance, *x* as depicted in FIG. 4(a). In general, higher turbulence intensities are observed in the shear layer compared to the centreline due to the highly energetic large turbulent structures generated by the mixing layer (Fellouah, Ball, and Pollard 2009). The profiles for the more downstream positions (*x/D*=15, 20 and 30) are observed to collapse, which agrees with the established finding obtained by (Panchapakesan N. R. and Lumley 1993; Wänström et al. 2012), established in the *fully developed* region. In our case, it is also surprising to observe that even the profile for *x/D*=10 nearly collapses with the more downstream positions throughout the developing region. This behaviour should therefore be predicted on the radial profiles of mean velocity and variance too since turbulence intensity is comprised of these two parameters. The prediction agrees with the results plotted in FIG.4(b) and nearly in FIG. 4(c), where the data at each measurement point were normalized by the centreline mean velocity, U_C, as previously implemented by (Abdel-Rahman, Chakroun, and AI-Fahed 1997; Ball, Fellouah, and Pollard 2012), and the centreline variance, $\overline{u^2}_C$, respectively. Except for *x/D*=10, the radial profiles of the normalized mean velocity collapse convincingly, which is in a good agreement with the results obtained by (Khashehchi et al. 2013) where the collapse occurred at *x/D*= 15, 18 and 20. Radial profiles of the normalized velocity variance at *x/D*=10 is also the most unlikely to collapse while for the rest, the collapse is more dominant at larger radial positions.

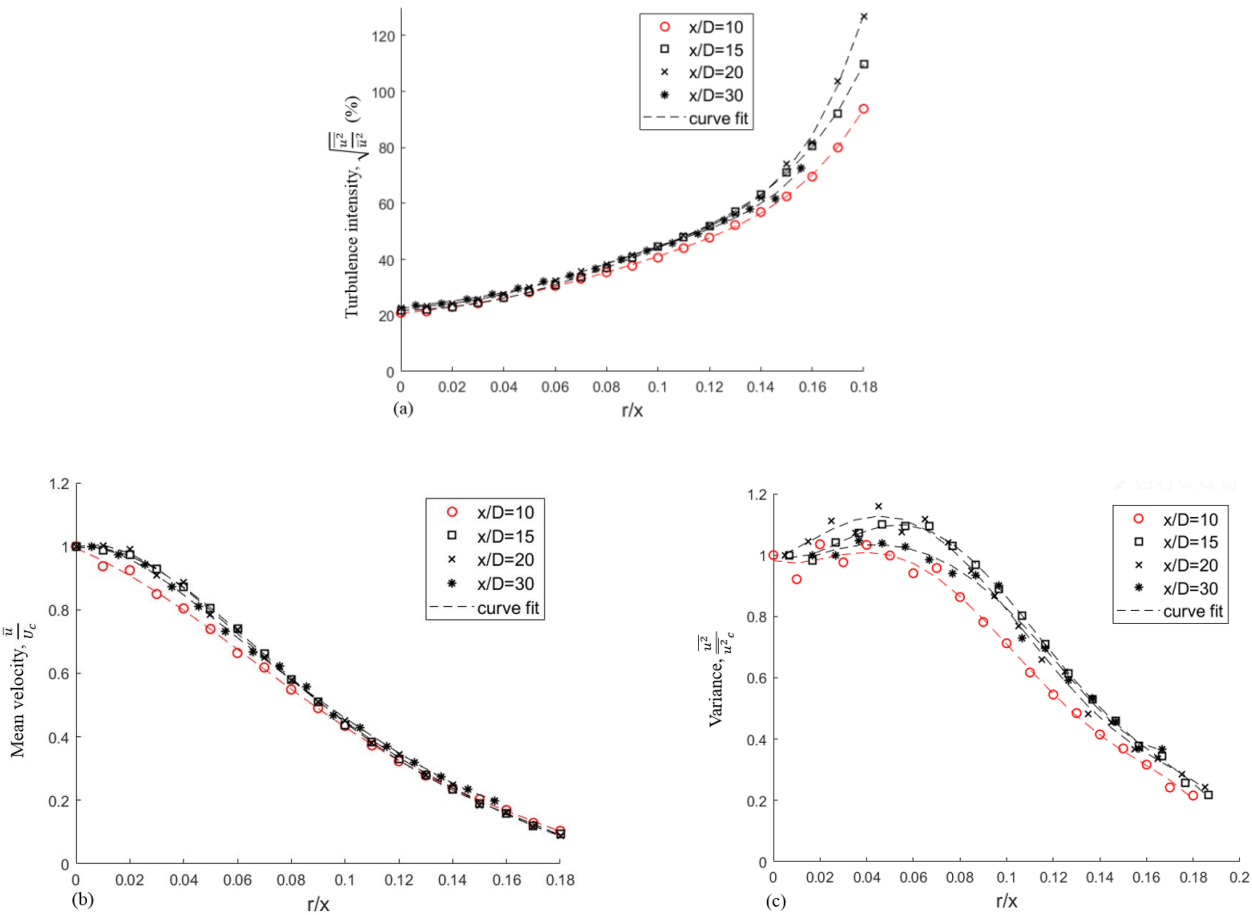

FIG. 4. Radial profiles of normalized (a) turbulence intensity (b) mean velocity, (c) variance at *x/D* = 10, 15, 20 and 30 with 5th order polynomial curve fits

B. Spatial kinetic energy spectra

Resulting spatial spectra for each measured centreline position downstream are shown in FIG. 5. Each spectrum is normalized to 1 (also for the following figures) in the low wave number asymptote so that a fair comparison can be made in terms of the spectrum's shape and slope with respect to Kolmogorov's -5/3 law. The (assumed) inertial subrange is wider in the fully developed part of the jet, as should be expected, and larger energy is in general observed at lower wave numbers. With downstream distance, the turbulence is seen to rapidly develop from a clear steep deviation from the -5/3 slope to a state approaching -5/3 in the fully developed region with an increasingly (spectrally) wider -5/3 slope region. At the most upstream positions, the -5/3 slope is, at best, locally tangent to any of the measured spectra.

The spectrum for the position closest to the jet exit, i.e. x/D=5, displays a 'bump', which is suspected to result from vortex rings emerging due to the Kelvin Helmholtz shear layer instability (Danaila, Jan, and Anselmet 1997). The vortex rings then merge and become unstable as they are convected downstream, explaining the gradual disappearance of the bump on the spectra for the positions away from the jet exit and also from the jet centreline as demonstrated in FIG. 6. It shows that the effect of the Kelvin Helmholtz instability does not remain dominating in the spectrum for a very long time and is not only local in the downstream direction, but in radial direction as well. From the temporal energy spectrum plotted in the frequency domain for x/D=5, centreline, the peak of the bump was found to be at around 800 Hz, which corresponded to a Strouhal number of 0.25. This value is in good agreement with the range of the preferred mode when operating an axisymmetric turbulent jet according to (Gutmark 1983), i.e., from 0.24 to 0.64.

Meanwhile, spectra for all measured radial distances from the jet centreline, along the remaining measured downstream positions are shown in FIG. 7(a) – (d). A clear shift from high to lower wave numbers with increasing radial distance can be observed in the developing region, so the smallest scales are larger away from the jet exit. The shape of the spectra also varies with radial position, in particular in the more upstream measurement positions, showing that the distribution of spatial velocity structures varies with radial distance from the centreline and also with downstream direction. In the fully developed region, i.e., at x/D=30, the spectra convincingly collapse (to within measurement error), indicating that energy is distributed nearly equally across all the scales independent of radial position from the centre-line (Buchhave and Velte 2017b). This indicates that the second-order moments of turbulence have finally reached a state of self-similarity in the far field of the jet (Burattini and Danaila 2005). Also, in the most downstream measured position, i.e., x/D=30, a clear -5/3 slope across a significant range is finally displayed. It is only when we have a clear -5/3 slope that we can argue for the existence of an inertial subrange with a constant spectral flux, which makes the local equilibrium model of Kolmogorov and Batchelor valid. On a separate note, the tendency for the spectra to follow -5/3 can already be observed at x/D=20 but just across a smaller range since it is not fully developed yet, compared to at x/D=30 where turbulence has finally reached the solution displaying local equilibrium like behaviour.

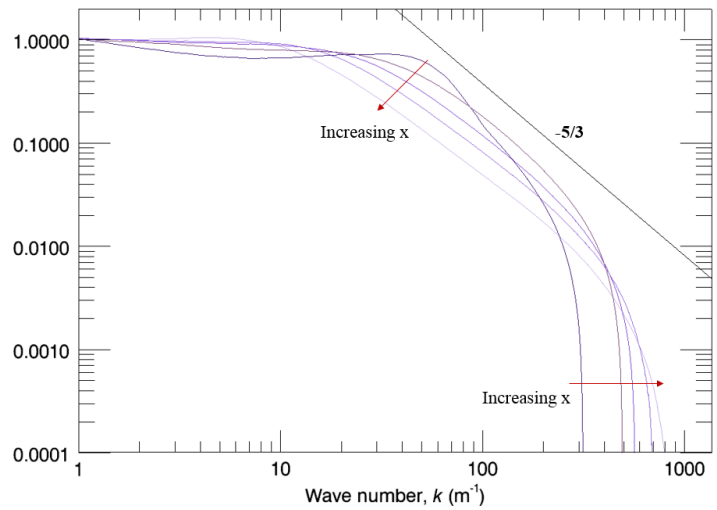

FIG. 5. Downstream development of spatial turbulent kinetic energy (convection record) spectra along the jet centreline ($r = 0$). Each spectrum is normalized to 1 in the low wave number asymptote for a more clear comparison in terms of its shape and slope with respect to Kolmogorov's -5/3 law. From *heavy to light purple*: x/D = 5, 10, 15, 20, 30.

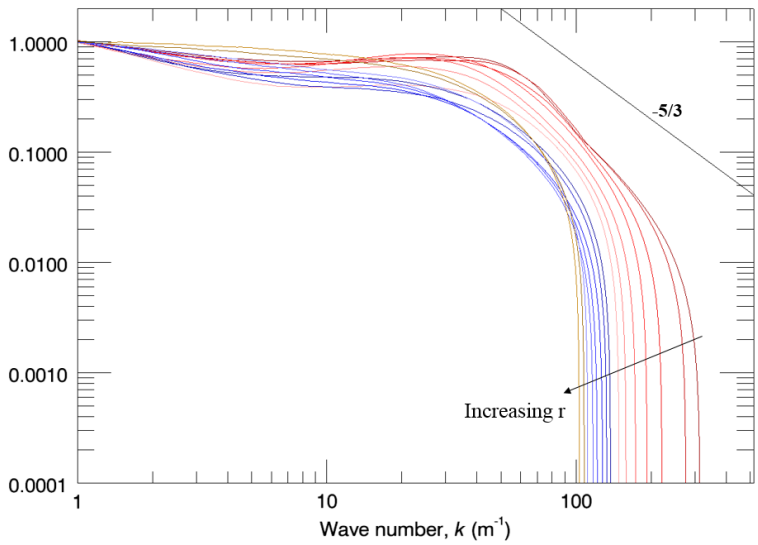

FIG. 6. Radial development of spatial turbulent kinetic energy (convection record) spectra at x/D=5. Each spectrum is normalized to 1 in the low wave number asymptote for a more clear comparison in terms of its shape and slope with respect to Kolmogorov's -5/3 law. From *heavy to light red*: r/D = 0, 0.1, 0.2, 0.3, 0.4, 0.5, 0.6. From *heavy to light blue*: r/D = 0.7, 0.8, 0.9, 1, 1.1, 1.2. From *heavy to light brown*: r/D = 1.3, 1.4.

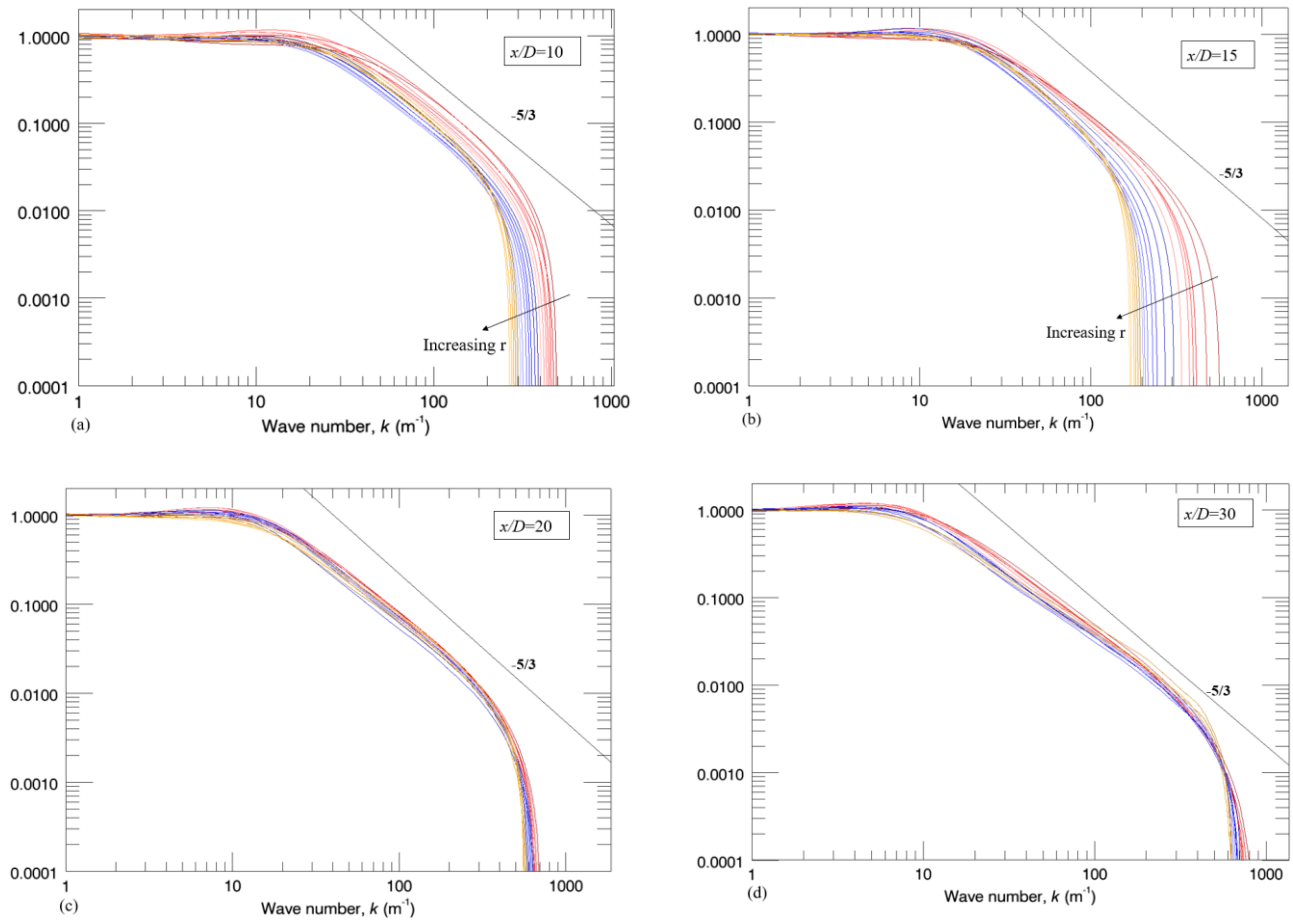

FIG. 7. Radial development of spatial turbulent kinetic energy (convection record) spectra at: **(a)** ***x/D*=10**. From *heavy to light red*: *r/D* = 0, 0.1, 0.2, 0.3, 0.4, 0.5, 0.6. From *heavy to light blue*: *r/D* = 0.7, 0.8, 0.9, 1, 1.1, 1.2, 1.3. From *heavy to light brown*: *r/D* = 1.4, 1.5, 1.6, 1.7, 1.8. **(b)** ***x/D*=15**. From *heavy to light red*: *r/D* = 0, 0.15, 0.3, 0.45, 0.6, 0.75. From *heavy to light blue*: *r/D* = 0.9, 1.05, 1.2, 1.35, 1.5, 1.65, 1.8. From *heavy to light brown*: *r/D* = 1.95, 2.1, 2.25, 2.4, 2.55, 2.7. **(c)** ***x/D*=20.** From *heavy to light red*: *r/D* = 0, 0.2, 0.4, 0.6, 0.8, 1. From *heavy to light blue*: *r/D* = 1.2, 1.4, 1.6, 1.8, 2, 2.2, 2.4. From *heavy to light brown*: *r/D* = 2.6, 2.8, 3, 3.2, 3.4, 3.6**.** **(d)** ***x/D*=30.** From *heavy to light red*: *r/D* = 0, 0.3, 0.6, 0.9, 1.2, 1.5. From *heavy to light blue*: *r/D* = 1.8, 2.1, 2.4, 2.7, 3, 3.3, 3.6. From *heavy to light brown*: *r/D* = 3.9, 4.2, 4.5**.** Each spectrum is normalized to 1 in the low wave number asymptote for a more clear comparison in terms of its shape and slope with respect to Kolmogorov's -5/3 law.

C. Spatial second-order structure function

FIG. 8 shows the spatial (convection record based) second-order structure functions along the centerline for the various measured downstream positions. Each curve is shifted in the vertical direction (also for the following figures) at the small separation region to clearly differentiate the shape of the scales development. The range within which each curve well approximates the 2/3 slope is observed to become larger in the downstream direction. The greatest tendency to follow the 2/3 slope is at *x/D*=30 (equilibrium), as expected and also obtained in (Danaila et al. 2002; Romano and Antonia 2001), while a significant deviation, gradually changing with the downstream development, can be observed in the non-equilibrium counterpart. This indicates the ongoing development of turbulent scales in the non-equilibrium region as the lower slopes at *x/D*=5 and *x/D*=10 show that the large velocity increments have not yet been produced by the cascade process.

Furthermore, the second-order structure functions have significant spread at small separations closer to the jet exit and approach the same curve in the more downstream direction, which is consistent with the behavior of the spectra in the preceding section. Meanwhile FIG. 9(a) – (e) show the spatial second-order structure functions along all measured radial positions, displaying one figure per measured downstream position. A similar bump is also noticed at the most upstream position as what has been seen in the corresponding spectra earlier. Most of the turbulent kinetic energy is dominated by the large scales in this position, as expected. Increasing large-scale activity is noticed in the outer part of the jet compared to on the centreline and just like what is well known in the developing region, the large scales are seen to grow as they move downstream.

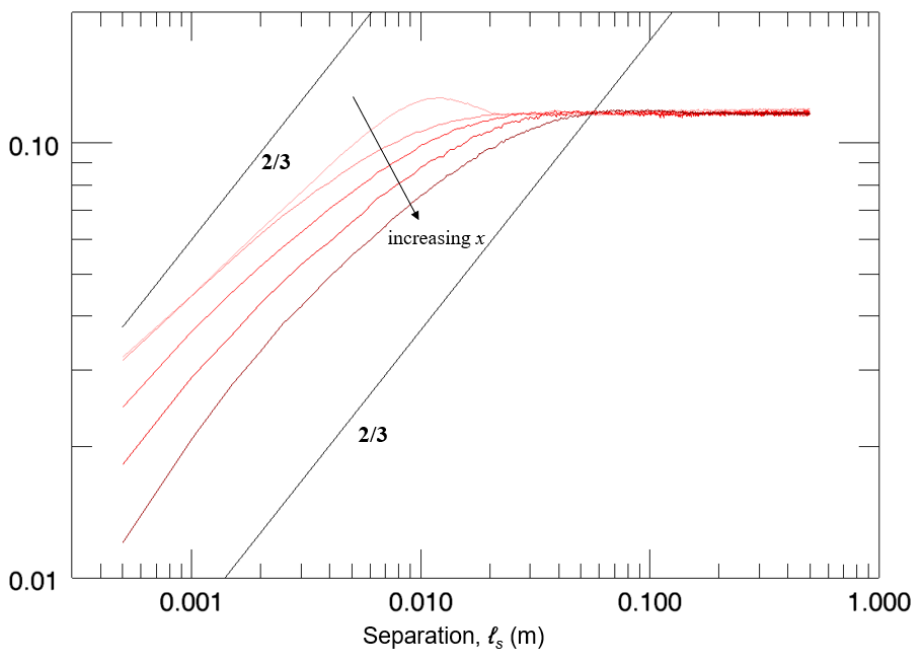

FIG.8. Downstream development of second-order spatial structure functions along the jet centreline (r = 0). Each curve was shifted vertically for a clear comparison of the scales development. From *heavy to light red*: *x/D* = 30, 20, 15, 10, 5

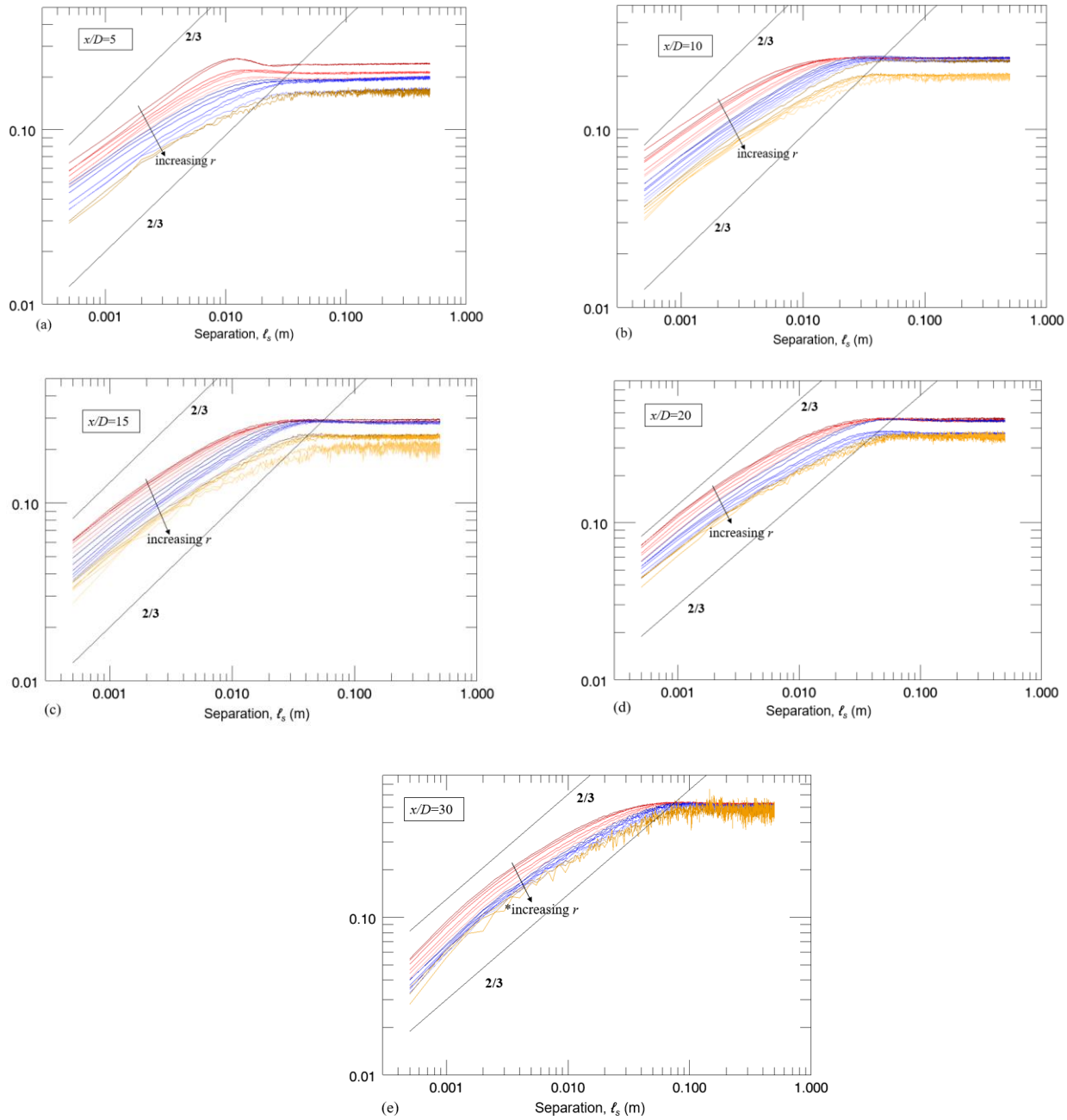

FIG. 9. Second-order spatial structure functions variations with radial distance at: **(a)** ***x/D*=5**. From *heavy to light red*: *r/D* = 0, 0.1, 0.2, 0.3, 0.4, 0.5, 0.6. From *heavy to light blue*: *r/D* = 0.7, 0.8, 0.9, 1, 1.1, 1.2. From *heavy to light brown*: *r/D* = 1.3, 1.4. **(b)** ***x/D*=10**. From *heavy to light red*: *r/D* = 0, 0.1, 0.2, 0.3, 0.4, 0.5, 0.6. From *heavy to light blue*: *r/D* = 0.7, 0.8, 0.9, 1, 1.1, 1.2, 1.3. From *heavy to light brown*: *r/D* = 1.4, 1.5, 1.6, 1.7, 1.8. **(c)** ***x/D*=15**. From *heavy to light red*: *r/D* = 0, 0.15, 0.3, 0.45, 0.6, 0.75. From *heavy to light blue*: *r/D* = 0.9, 1.05, 1.2, 1.35, 1.5, 1.65, 1.8. From *heavy to light brown*: *r/D* = 1.95, 2.1, 2.25, 2.4, 2.55, 2.7. **(d)** ***x/D*=20**. From *heavy to light red*: *r/D* = 0, 0.2, 0.4, 0.6, 0.8, 1. From *heavy to light blue*: *r/D* = 1.2, 1.4, 1.6, 1.8, 2, 2.2, 2.4. From *heavy to light brown*: *r/D* = 2.6, 2.8, 3, 3.2. **(e)** ***x/D*=30**. From *heavy to light red*: *r/D* = 0, 0.3, 0.6, 0.9, 1.2, 1.5. From *heavy to light blue*: *r/D* = 1.8, 2.1, 2.4, 2.7, 3, 3.3, 3.6. From *heavy to light brown*: *r/D* = 3.9, 4.2, 4.5. *Note that the arrow indicating the increment of radial distance, *r,* is not applicable for the two outermost points due to high variation in the plots. Each curve was shifted vertically for a clear comparison of the scales development.

D. Spatial third-order structure function

The third-order structure function is expected to follow Kolmogorov's 4/5 law only under these three assumptions, viz., the flow is locally in equilibrium, locally homogeneous and isotropic (McDonough 2007). We thereby present the third-order structure function as a function of spatial separation, ℓ at x/D=30 (see FIG. 10) where turbulence is evidenced to be fully developed based on the energy spectra presented earlier and also in (Buchhave and Velte 2017b; Velte, Buchhave, and Hodzic 2017; M. R. Yaacob, R. Schlander, et al. 2018). The results presented in our paper only cover up to the first six radial points including at the centerline due to due to high noise level towards the outermost region. For clear comparison to the Kolmogorov 4/5 law, a straight line constructed from Equation (10) is also included in each plot, having the 4/5 slope. Note that the slope in this case is positive since the negative sign has been cancelled out by the negative value of the mean energy dissipation rate, ε. The structure function plots are observed to follow the 4/5 slope at the lower separation region, as expected. This finding also supports the simulation work done by (Boratav and Pelz 1997) where the 4/5 power law has been approximately indicated from an unforced turbulent flow. The third-order structure functions at x/D=20 are also shown in FIG. 11 after we observed the positive tendency to follow the -5/3 slope to a certain extent of the wavenumber range based on the spectra in FIG. 7(c) previously. In fact, (Van De Water and Herweijer 1999) has shown a clear approximation to the 4/5 law for the third-order structure function measured at x/D=22 in a turbulent round jet, based on Taylor's hypothesis. (Wyganski I. and Fielder 1969) has also discovered the possibility that the jet is already fully developed at x/D≈20.

The main advantage of plotting the spatial third-order structure function according to the assumptions of Kolmogorov (Kolmogorov 1941b), is to be able to estimate the mean energy dissipation rate per unit mass, ε_{45}. The parameter ε from Equation (10) was fine-tuned in the program for the 4/5 slope to best coincide at the small separations of the third-order structure function. This fit gave us the value of ε_{45} at each measured position in the flow. The absolute values are then plotted in FIG. 12, which reveals that ε_{45} drops substantially at x/D=20 but slowly at x/D=30. There is also a rapid drop along the centreline from x/D=20 to x/D=30, which further detailed investigation can be found in another concurrently written manuscript by the same authors (Yaacob, Buchhave, & Velte, *under preparation*)

Though the Kolmogorov 4/5 law is only valid for locally homogeneous flow, Equation (10) has been naively employed to crudely estimate ε_{45} in the non-equilibrium region. Repeating naively the same approach as implemented before, radial variation of ε_{45} for x/D=10 and x/D=15 were determined and plotted in FIG. 13(a) together with those previously obtained for x/D=30 and x/D=20. We could observe that in comparison to the overall plot, the ε_{45} evolutions for x/D=30 and x/D=20, which were claimed to be in the equilibrium region, behave almost consistently in this case. Surprisingly, the radial variation of ε_{45} is also (relatively) consistent even at x/D=15 where the assumptions stated earlier clearly do not hold. Meanwhile, a sudden drop is observed along the radial direction of x/D=10, which certainly corresponds to the non-equilibrium region based on the spectra obtained in FIG. 8. Although these could not be credible regarding dissipation estimation, the third-order structure functions for x/D=15 and x/D=10 are nevertheless attached in Appendix II and III, respectively.

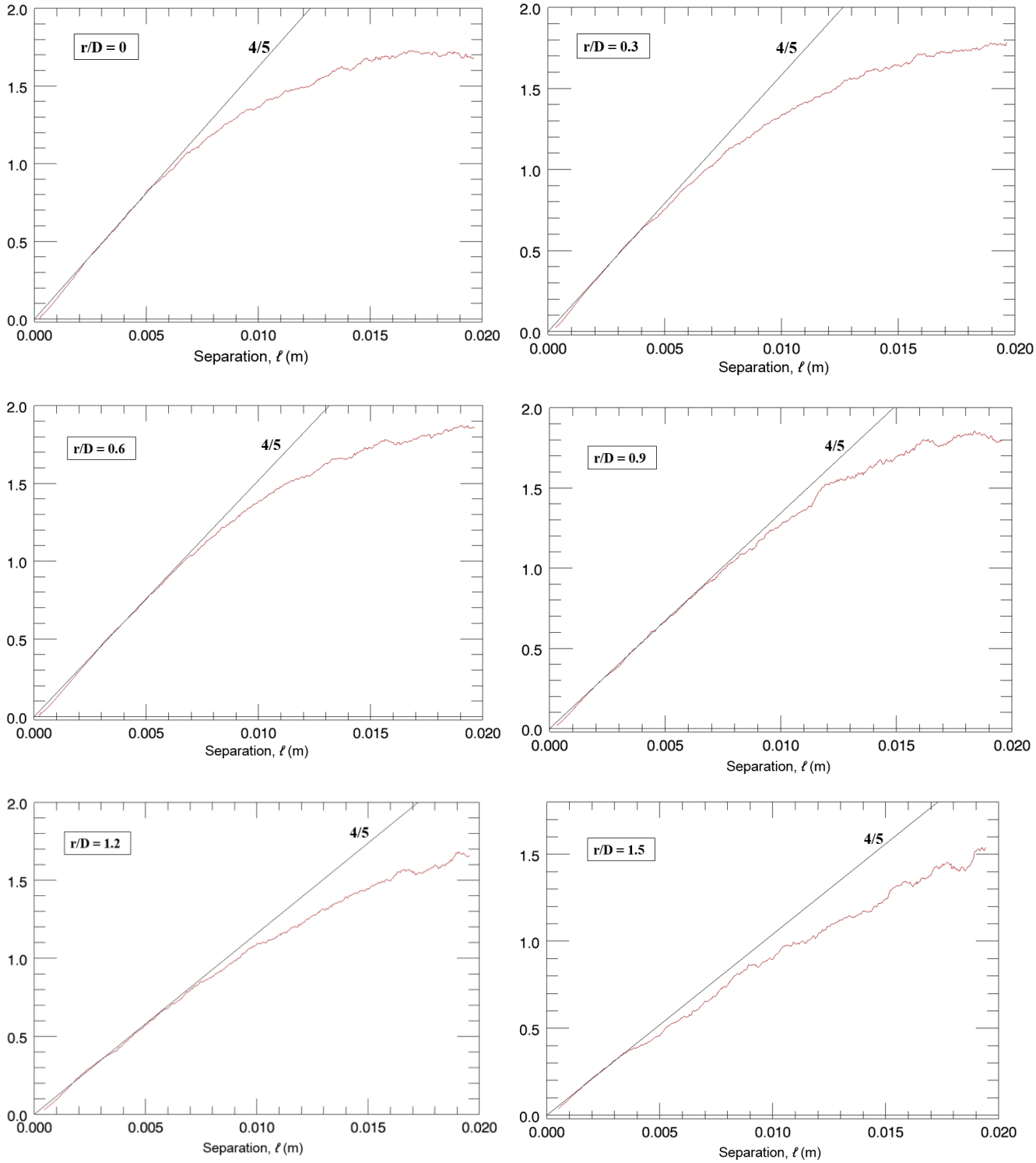

FIG. 10. Spatial third-order structure functions variations with radial distance at *x/D*=30. Due to high variations in the plots beyond *r/D* =1.5, only functions up this position are presented. Separate plots are made to clearly show the coincidence between each function and the 4/5 slope.

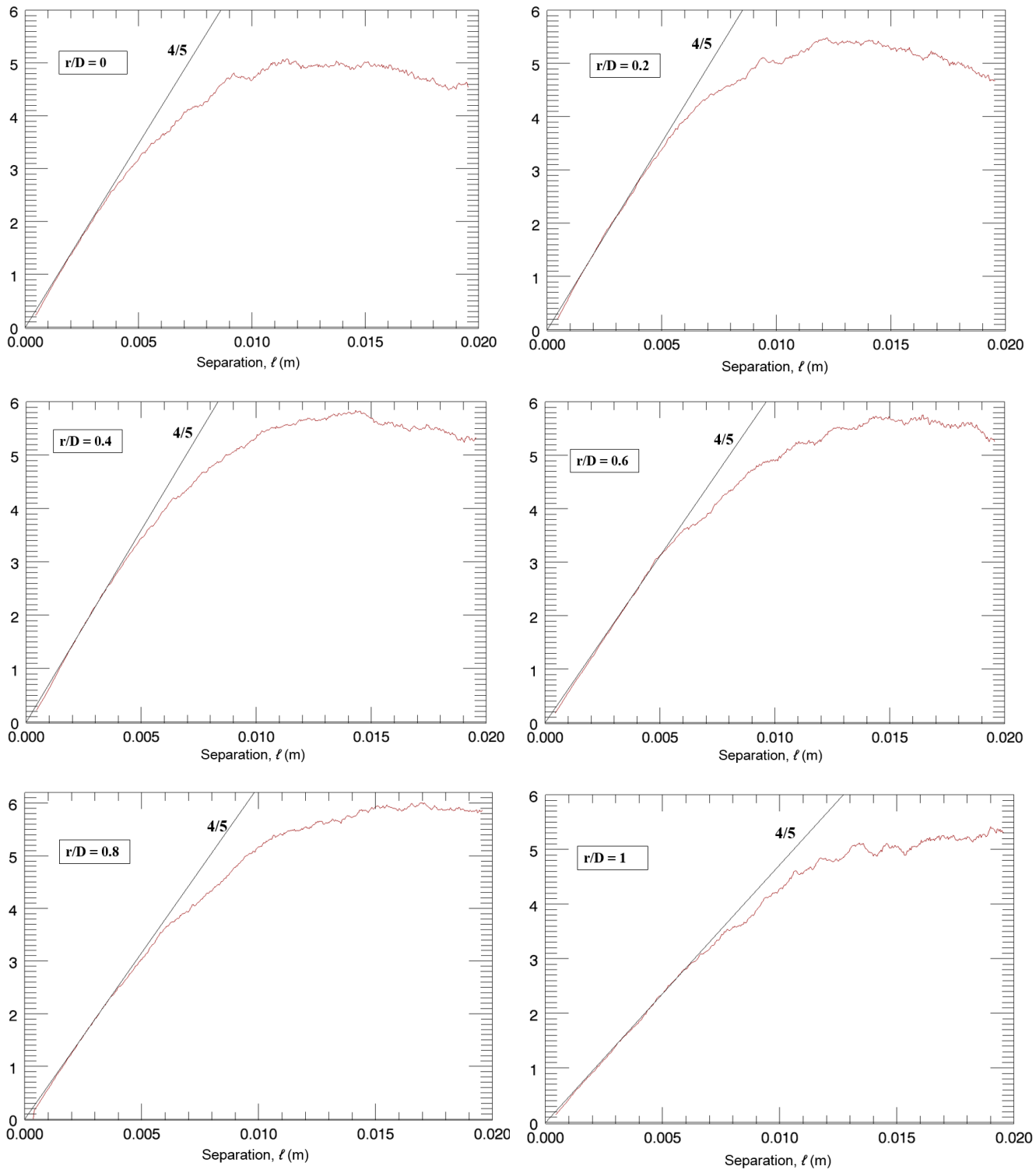

FIG. 11. Spatial third-order structure functions variations with radial distance at *x/D*=20. Due to high variations in the plots beyond *r/D* =1, only functions up this position are presented. Separate plots are made to clearly show the coincidence between each function and the 4/5 slope.

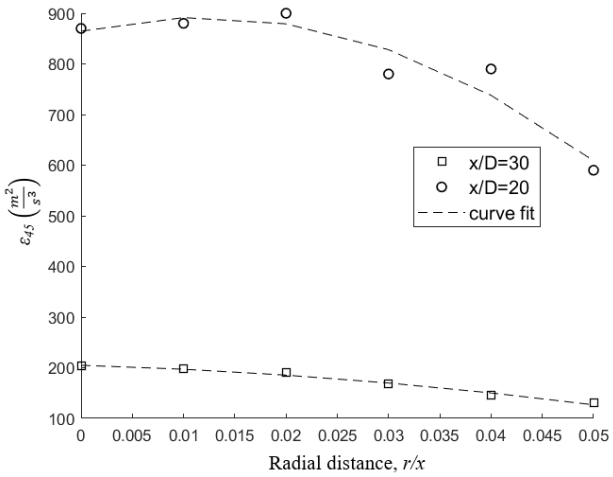

FIG. 12. Radial evolutions of ε_{45} at x/D=30 and x/D=20, with second-order polynomial curve fits

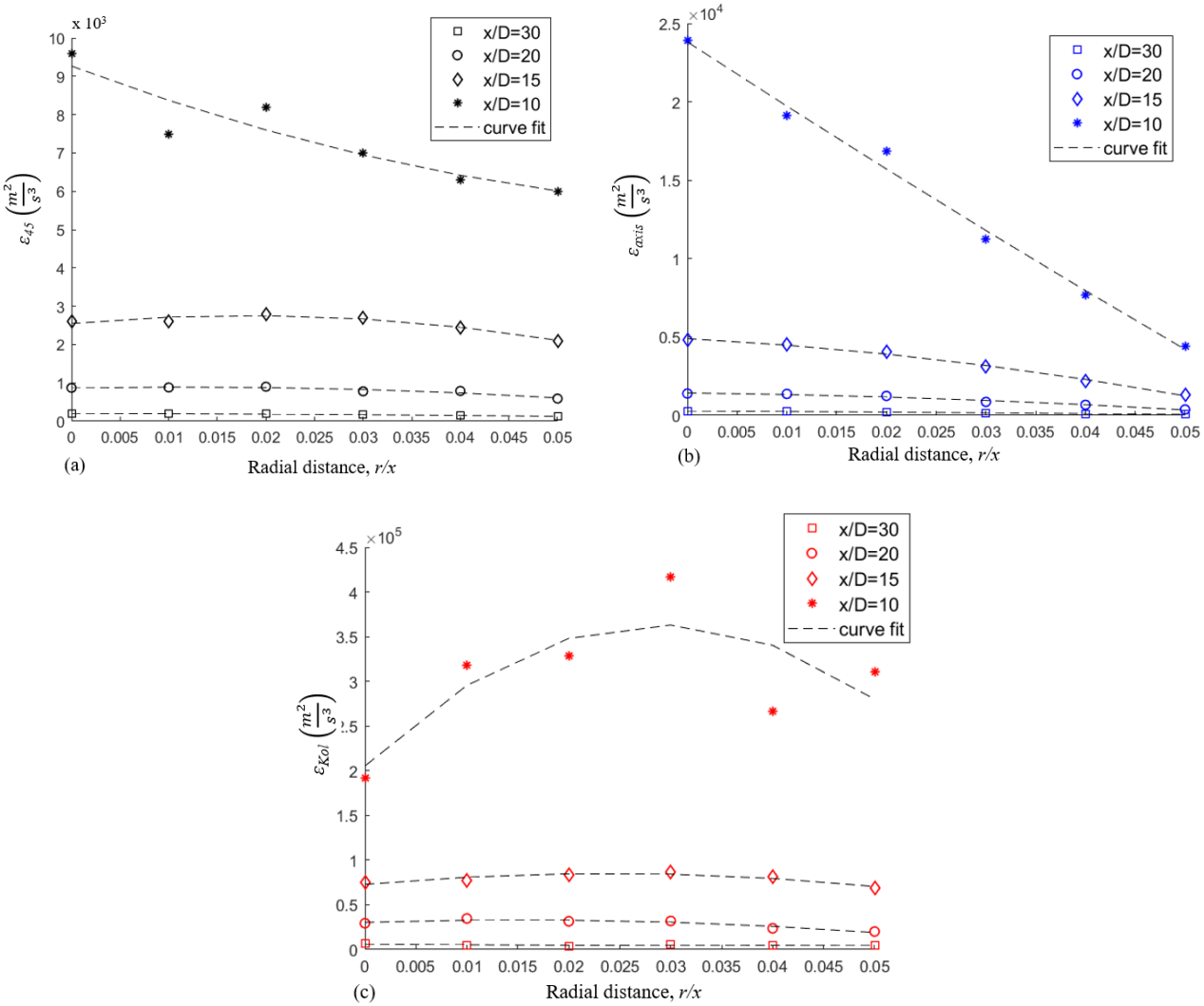

FIG. 13 Radial evolutions of (a) ε_{45}, (b) $\varepsilon_{\text{axis}}$ and (c) ε_{Kol}, with second-order polynomial curve fit

Besides ε_{45}, the dissipation based on the local axisymmetry, ε_{axis} and Kolmogorov estimation, ε_{Kol} are also computed and plotted in FIG. 13(b) and (c), respectively. The former is determined by reading the value of $2\varepsilon_{axis}\,(x - x_0) / u^3 \approx 0.7$ for the corresponding radial position $r/(x-x_0)$ of Figure 21 in (Hussein et al. 1994) while the latter is computed by $\overline{u^3}/L_u$, where L_u is the integral length scale. The value of x_0 is taken from another measurement along the jet centerline (Yaacob, Buchhave, & Velte, *under preparation*). The dissipation radially evolves much more consistently in the fully developed region compared to the more upstream counterpart. A remarkably different trends are shown at x/D=10 (developing region) between ε_{45}, for which the assumptions for 4/5 law are not fulfilled, and $\varepsilon_{Kol,}$, which are both central results from the same Kolmogorov theory. These two dissipation estimates should give (at least approximately) the same values AND consequently show similar trend if the theory and its underlying assumptions are correct and valid.

The spatial third-order structure functions for the other centreline positions i.e. at x/D=15 and x/D=10 are shown in FIG. 14(a) and (b), respectively. By looking at the functions across different downstream distances, for instance at r/D=0, the tendency for the functions to follow the 4/5 slope is getting lower in the upstream direction. The break in the curves is observed also to occur at smaller ℓ as the measurement gets closer to the jet exit, which indicates that there are fewer large structures in the upstream region. The plot for x/D=5 is not shown, since we observe that the flow is still laminar in this position and therefore not possible to fit the 4/5 slope.

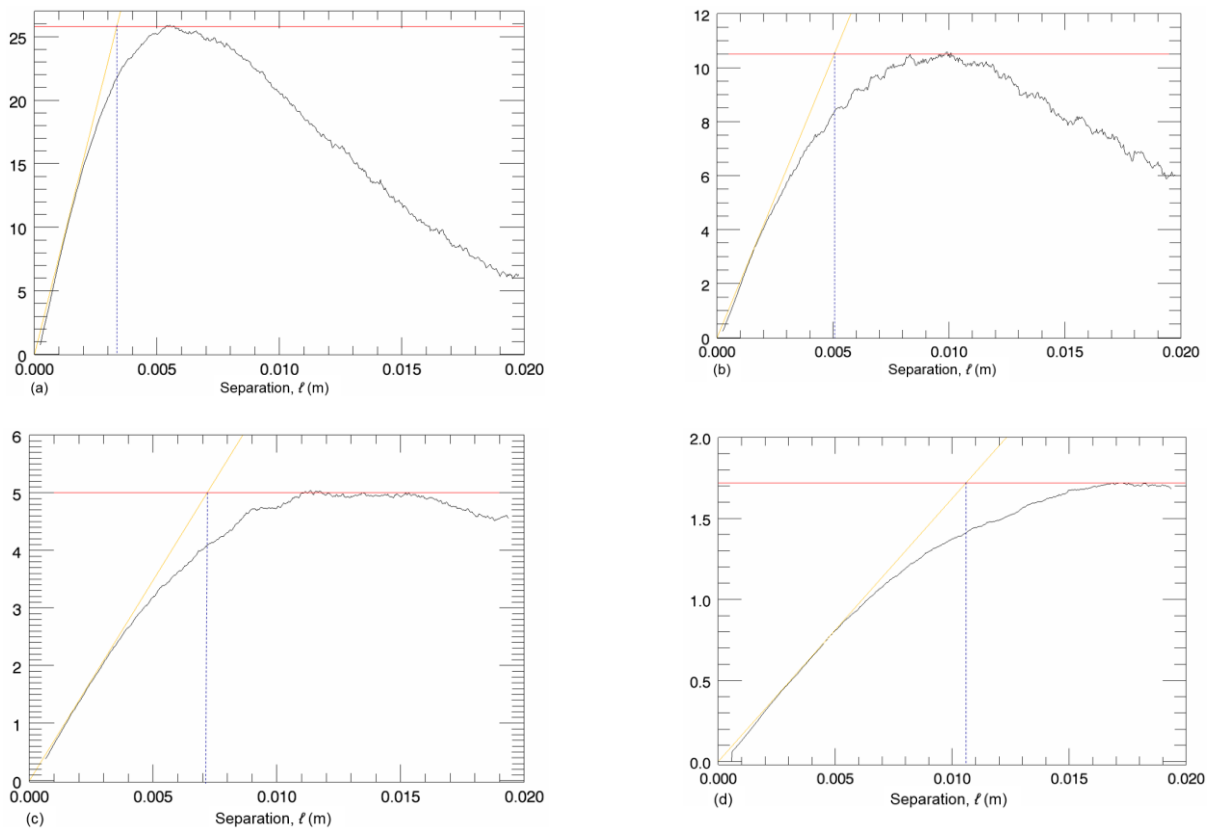

FIG. 14 Spatial third-order structure function at centreline for: a) x/D=10, b) x/D=15 c) x/D=20, d) x/D=30. The yellow and red lines represent the 4/5 slope and horizontal tangent line to each structure function curves, respectively, which intersection indicating the break point of the curve. The break occurs at approximately 3.354 mm, 5.041 mm, 7.16 mm and 10.6 mm at x/D=10, x/D=15, x/D=20 and x/D=30, respectively.

E. Turbulent scales

The values of dissipation extracted from the third-order structure function, ε_{45}, are used to determine the Kolmogorov time and length scales at *x/D*=20 and 30, which are plotted in FIG. 15. Both scales grow with a similar trend at each downstream position. The scales at *x/D*=30 are also larger than those at *x/D*=20. The Kolmogorov scales are also computed based on the axisymmetric dissipation, ε_{axis}, which values are overalaid also in FIG. 15. This dissipation estimate is taken into account since it has been empirically established in (George and Hussein 1991; Hussein et al. 1994) and therefore considered as the most credible one.

The smallest resolvable length scale is also computed based on the size of measuring volume used in the measurements. From

$$k\eta_{Kol} = 1 \tag{15}$$

at which the dissipation is approximately 99% resolved, the smallest resolvable scale using our instrument is calculated to be around $\lambda/2 \cdot 1/\pi = 28.6$ µm. This value is represented by a horizontal *blue* line in FIG. 15, which is always way below the polynomial curve of the Kolmogorov length scales. It shows that, with the current spatial resolution used in our measurement setup, we should be able to resolve the Kolmogorov scale throughout this region, and perhaps in the upstream region since the *blue* line falls much lower than the estimated length scales.

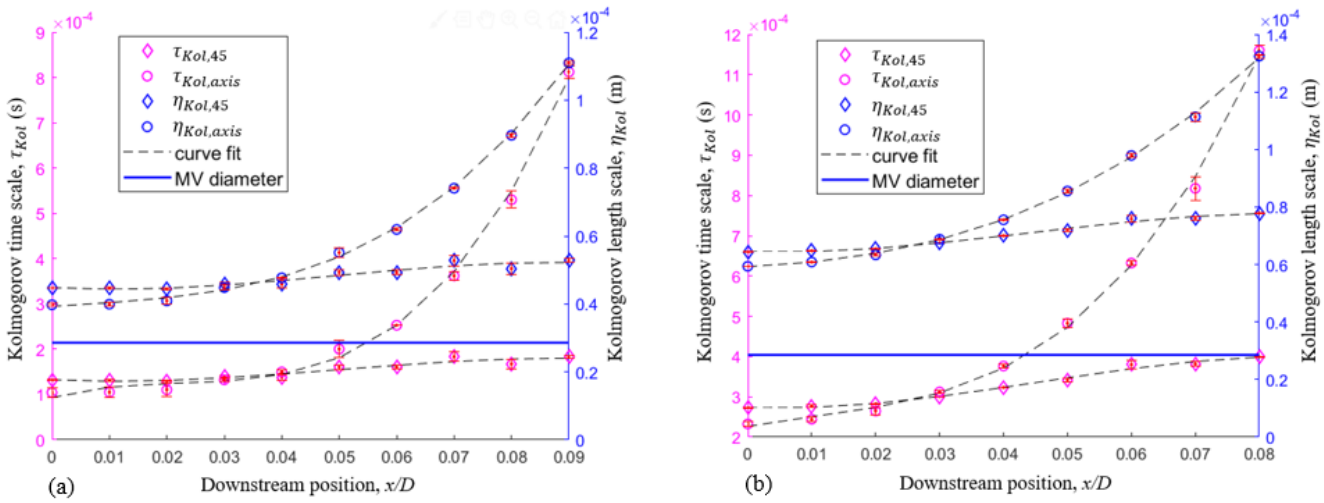

FIG. 15 Radial evolution of the Kolmogorov scales at (a) *x/D*=20, (b) *x/D*=30, with third-order polynomial fit. The *blue* horizontal line represents the smallest resolvable scale of our instrument, i.e., 28.6 µm, which is always below the polynomial curve of the Kolmogorov length scales.

The radial evolution of the integral scales at various downstream positions are depicted in FIG. 16, both in temporal and spatial domains. In general, the scales are larger downstream and develop different trend at different downstream positions. The development is almost consistent at *x/D*=10 and getting more unsteady as the measurements progress downstream. This may be due to the difficulty in obtaining sufficient statistics for proper spectral estimates in the outer parts of the jet, since the convection velocity (and hence also the measuring time required) changes dramatically when moving towards the outer parts of the jet. The results for large radial positions should therefore be interpreted with caution.

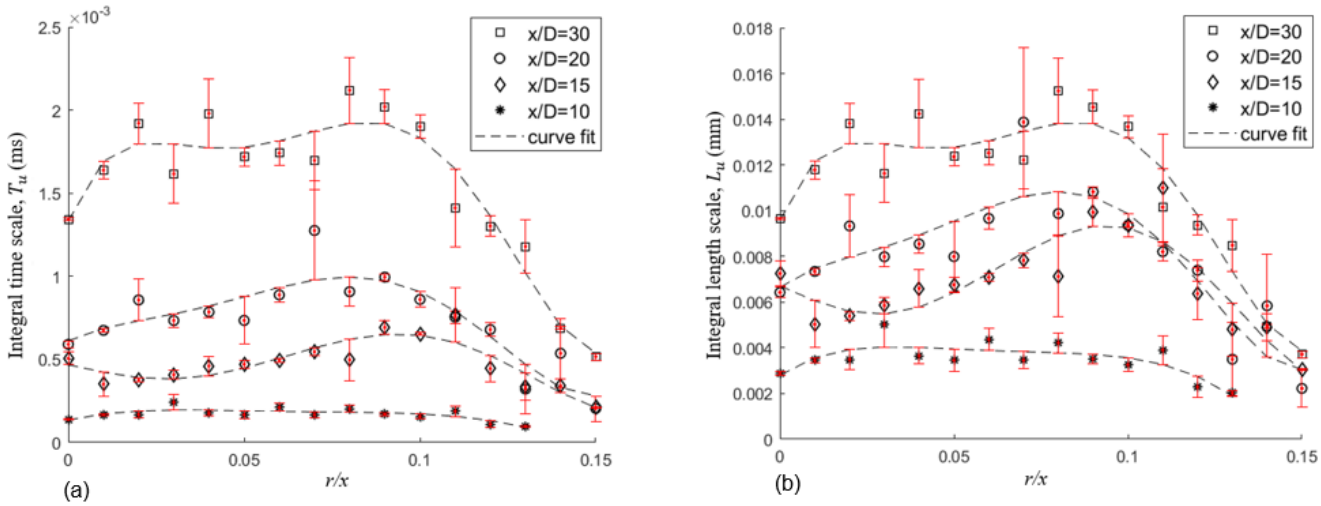

FIG. 16 Radial evolution of the integral scales at various downstream positions in (a) time (b) space, with second-order polynomial fit.

CONCLUSIONS

Both the static and dynamic first and second-order statistics of the streamwise velocity across the developing region of the round jet have been presented in spatial domain. These statistics have been measured with an improved laser Doppler anemometry system (as compared to the limited commercially available systems). Due to the high dynamic range and ability to unambiguously distinguishing the velocity components, laser Doppler anemometry is the most suitable method to measure these high shear and intensity flows.

It is observed that the first and second-order static moments can be collapsed across radial scans even down to approximately 15-20 jet exit diameters from the jet exit. Dynamic statistics mapping of the developing region, including across the radial dimension, has been presented in terms of spatial spectra as well as second- and third-order structure functions. The gradual development towards the Kolmogorov power laws (-5/3, 2/3 and 4/5, from the spatial spectra and second- and third-order structure functions, respectively) as one approaches the fully developed region is explicitly mapped. The - 5/3 law in the spectra and the 2/3 law in the second-order structure functions are approximated as early as 20 jet exit diameters downstream of the jet exit.

Although we only present statistics herein, these (averaged) spectra and structure functions clearly witness that interactions are not local in the hypothesized equilibrium range (inertial and dissipation ranges). Under such conditions, the expected -5/3 spectral and 2/3 second order structure function power laws do not appear and the cornerstone assumption of local (and universal) equilibrium cannot hold in general. The direct transfer of energy from large to incrementally smaller scales therefore becomes questionable and leads to violation against the well-known Richardson's energy cascade (Richardson 1922).

The measuring volume has been shown to be sufficiently small to capture scales of the order of the Kolmogorov length scale. Dissipation has been estimated using the 4/5 law based on the third-order structure functions, as well as based on the axisymmetric dissipation scaling of (Hussein et al. 1994). The corresponding Kolmogorov length and time scales have been mapped, displaying similar trends but with somewhat different values of the scales.

Finally, all the important findings provided from these measurements should be of direct relevance to turbulence theoreticians and modelers alike, concerning the cascade development in a turbulent round jet developing region.

ACKNOWLEDGMENT

The support of Ministry of Education Malaysia is gratefully acknowledged. The authors also wish to acknowledge the generous support of Fabriksejer, Civilingeniør Louis Dreyer Myhrwold og hustru Janne Myhrwolds Fond (grant journal no. 13-M7-0039 and 15-M7-0031) and Reinholdt W. Jorck og Hustrus Fond (grant journal no. 13-J9-0026).

REFERENCES

Abdel-Rahman, A. A., W. Chakroun, and S. F. AI-Fahed. 1997. "LDA Measurements in the Turbulent Round Jet." *Mechanics Research Communications,* 24(3):277–88.

Anselmet, F., R. A. Antonia, and L. Danaila. 2001. "Turbulent Flows and Intermittency in Laboratory Experiments." *Planetary and Space Science* 49:1177–91.

Ball, C. G., H. Fellouah, and A. Pollard. 2012. "The Flow Field in Turbulent Round Free Jets." *Progress in Aerospace Sciences* 50:1–26.

Batchelor, G. K. 1953. *The Theory of Homogeneous Turbulence*. Cambridge University Press.

Boratav, Oluş N. and Richard B. Pelz. 1997. "Structures and Structure Functions in the Inertial Range of Turbulence." *Physics of Fluids* 9(5):1400–1415.

Buchhave, P. 1979. "Errors and Correction Methods in Turbulence Measurements with the LDA." State University of New York.

Buchhave, P., W. K. George, and J. L. Lumley. 1979. "The Measurement of Turbulence with the Laser-Doppler Anemometer." *Annual Review of Fluid Mechanics* 11:443–503.

Buchhave, P. and C. M. Velte. 2017a. "Conversion of Measured Turbulence Spectra from Temporal to Spatial Domain." Pp. 343–62 in *Whither Turbulence and Big Data in the 21st Century?* Springer.

Buchhave, P. and C. M. Velte. 2017b. "Measurement of Turbulent Spatial Structure and Kinetic Energy Spectrum by Exact Temporal-to-Spatial Mapping." *Physics of Fluids* 29(8).

Burattini, P. and R. A. Antonial Danaila. 2005. "Similarity in the Far Field of a Turbulent Round Jet." *Physics of Fluids* 17(025101).

Danaila, Ionut, Dušek Jan, and Fabien Anselmet. 1997. "Coherent Structures in a Round , Spatially Evolving , Unforced , Homogeneous Jet at Low Reynolds Numbers." *Physics of Fluids* 9(3323).

Danaila, L., F. Anselmet, and R. A. Antonia. 2002. "An Overview of the Effect of Large-Scale Inhomogeneities on Small-Scale Turbulence." *Physics of Fluids* 14(2475).

Fellouah, H., C. G. Ball, and A. Pollard. 2009. "Reynolds Number Effects within the Development Region of a Turbulent Round Free Jet." *International Journal of Heat and Mass Transfer* 52(17–18):3943–54.

Frisch, U. 1995. *Turbulence: The Legacy of A.N. Kolmogorov*. Cambridge University Press.

Frisch, Uriel, Pierre-louis Sulem, and Mark Nelkin. 1978. "A Simple Dynamical Model of Intermittent

Fully Developed Turbulence." *Journal of Fluid Mechanics* 87:719–36.

George, W. K. 2014. "Reconsidering the ' Local Equilibrium ' Hypothesis for Small Scale Turbulence" edited by M. Farge, H. K. Moffatt, and K. Schneider. *EDP Sciences* 1–27.

George, W. K. and H. J. Hussein. 1991. "Locally Axisymmetric Turbulence." *Journal of Fluid Mechanics* 233:1–23.

Gibson, M. M. 1962. "Spectra of Turbulence at High Reynolds Number." *Nature* 195:1281–83.

Gibson, M. M. 1963. "Spectra of Turbulence in a Round Jet." *Journal of Fluid Mechanics* 15:161–73.

Goto, S. and J. C. Vassilicos. 2015. "Energy Dissipation and Flux Laws for Unsteady Turbulence." *Physics Letters A* 379(16–17):1144–48.

Goto, Susumu and J. C. Vassilicos. 2016. "Unsteady Turbulence Cascades." *Physical Review E - Statistical, Nonlinear, and Soft Matter Physics* 94(5):053108.

Gutmark, E. 1983. "Preferred Modes and the Spreading Rates of Jets." *Physics of Fluids* 26(10):2932.

Hussein, H. J., S. P. Capp, and W. K. George. 1994. "Velocity Measurements in a High-Reynolds-Number, Momentum-Conserving, Axisymmetric, Turbulent Jet." *Journal of Fluid Mechanics* 258:31–75.

Jensen, K. D. 2004. "Flow Measurements." *Journal of the Brazilian Society of Mechanical Sciences and Engineering* XXVI(4):400–419.

Jung, Daehan. 2001. "An Investigation of the Reynolds-Number Dependence of the Axisymmetric Jet Mixing Layer Using a 138 Hot-Wire Probe and the POD." State University of New York.

Khashehchi, M., A. Ooi, J. Soria, and I. Marusic. 2013. "Evolution of the Turbulent/Non-Turbulent Interface of an Axisymmetric Turbulent Jet." *Experiments in Fluids* 54(1):1449.

Kolmogorov, A. N. 1941a. "Decay of Isotropic Turbulence in Incompressible Viscous Fluids." *Dok. Akad. Nauk. S. S. S. R* 31:538–41.

Kolmogorov, A. N. 1941b. "Dissipation of Energy in Local Isotropic Turbulence." *Dokl. Akad. Nauk. SSSR* 32:15–17.

Kolmogorov, A. N. 1941c. "The Local Structure of Turbulence in Incompressible Viscous Fluid for Very Large Reynolds Numbers." *C. R. Akad. Sci. SSSR* 30:9–13.

Kolmogorov, A. N. 1962. "A Refinement of Previous Hypothesis Concerning the Local Structure of Turbulence in a Viscous Incompressible Fluid at High Reynolds Number." *Journal of Fluid Mechanics* 13:82–85.

L'vov, V. and I. Procaccia. 2007. "Hydrodynamic Turbulence: A 19th Century Problem with a Challenge for the 21st Century." *Turbulence Modeling and Vortex Dynamics* 491:1–16.

Laizet, S., J. Nedić, and J. C. Vassilicos. 2015. "The Spatial Origin of -5/3 Spectra in Grid-Generated Turbulence." *Physics of Fluids* 27(6):065115.

Lumley, J. L. 1965. "Interpretation of Time Spectra Measured in High-Intensity Shear Flows." *Physics of Fluids* 8(6):1056–62.

McDonough, J. M. 2007. *Introductory Lectures on Turbulence: Physics, Mathematics and Modeling*. Departments of Mechanical Engineering and Mathematics University of Kentucky.

Panchapakesan N. R. and J. L. Lumley. 1993. "Turbulence Measurements in Axisymmetric Jets of Air and Helium . Part 1 . Air Jet." *Journal of Fluid Mechanics* 246:197–223.

Pope, S. B. 2000. *Turbulent Flows*. Cambridge: Cambridge University Press.

Richardson, L. F. 1922. *Weather Prediction by Numerical Process*. UK: Cambridge Univ. Press.

Romano, G. P. and R. A. Antonia. 2001. "Longitudinal and Transverse Structure Functions in a Turbulent

Round Jet: Effect of Initial Conditions and Reynolds Number." *Journal of Fluid Mechanics* 436:231–48.

Seoud, R. E. and J. C. Vassilicos. 2007. "Dissipation and Decay of Fractal-Generated Turbulence." *Physics of Fluids* 19:105–8.

Stewart, R. W. 1959. "The Natural Occurrence of Turbulence." *Journal of Geophysical Research* 64(12):2112–15.

Taylor, G. I. 1938. "The Spectrum of Turbulence." *Proceedings of the Royal Society of London. Series A, Mathematical and Physical Sciences* 164(919):476–90.

Tennekes, H. and J. L. Lumley. 1972. *A First Course in Turbulence*. MIT Press.

Tsinober, Arkady. 2001. *An Informal Introduction to Turbulence*. Kluwer Academic Publishers.

Valente, P. C. and J. C. Vassilicos. 2012. "Universal Dissipation Scaling for Non-Equilibrium Turbulence." *Physical Review Letters* 108(21):214503.

Valente, P. C. and J. C. Vassilicos. 2015. "The Energy Cascade in Grid-Generated Non-Equilibrium Decaying Turbulence." *Physics of Fluids* 27(4):045103.

Vassilicos, J. C. 2015. "Dissipation in Turbulent Flows." *Annual Review of Fluid Mechanics* 47:95–114.

Velte, C. M. 2009. "Characterization of Vortex Generator Induced Flow." Technical University of Denmark.

Velte, C. M., P. Buchhave, and A. Hodzic. 2017. "Measurement of Turbulent Kinetic Energy Spectrum - Part 2 : Convection Record Measurements." Pp. 171–76 in *iTi Conference on Turbulence VII*. Springer.

Velte, C. M., W. K. George, and P. Buchhave. 2014. "Estimation of Burst-Mode LDA Power Spectra." *Experiments in Fluids* 55(3):1674.

Wänström, M., W. K. George, and K. E. Meyer. 2012. "Streamwise and Radial Decomposition of a Turbulent Axisymmetric Jet." *Springer Proceedings in Physics* 141:147–50.

Van De Water, Willem and Janine A. Herweijer. 1999. "High-Order Structure Functions of Turbulence." *Journal of Fluid Mechanics* 387:3–37.

Wyganski I. and H. Fielder. 1969. "Some Measurements in the Self-Preserving Jet." *Journal of Fluid Mechanics* 38(3):577–612.

Yaacob, M. R., Preben Buchhave, and Clara M. Velte. "Statistical Description of the Round Turbulent Jet Developing Region along Its Centerline" *(Manuscript under preparation).*

Yaacob, M. R., R. Schlander, P. Buchhave, and C. M. Velte. 2018. "Experimental Evaluation of Kolmogorov's -5/3 and 2/3 Power Laws in the Developing Turbulent Round Jet." *Journal of Advanced Research in Fluid Mechanics and Thermal Sciences* 45(2):14–21.

Yaacob, M. R., R. K. Schlander, P. Buchhave, and C. M. Velte. 2018. "Validation of Improved Laser Doppler Anemometer (LDA) Based on the Fully Developed Turbulent Round Jet." Pp. 89–90 in *Symposium of Electrical, Mechatronics and Applied Science*.

Yaacob, M. R., R. K. Schlander, P. Buchhave, and C. M. Velte "A Novel Laser Doppler Anemometer (LDA) for High-Accuracy Turbulence Measurements." *(Manuscript under preparation).*

Yaacob, M.R., Rasmus Schlander, P. Buchhave, and C. M. Velte. 2018. "Mapping Of Turbulent Round Jet Developing Region Using a Constant Temperature Anemometer (CTA)." in *Emerging Scientists Conference*.

Appendix I

Coefficient values for polynomial profiles, e.g., $P(x)= C_5x^5 + C_4x^4 + C_3x^3 + C_2x^2 + C_1x + C_0$

FIG. 3

Profiles	x/D	C_5	C_4	C_3	C_2	C_1	C_0
$\bar{u}$	5	2.7043	-31.5232	92.7324	-99.05	12.6895	30.2185
	10	-0.9914	2.7245	1.8098	-7.8979	-7.946	21.6883
	15	-0.0344	-0.4016	3.9716	-9.4386	1.195	15.0599
	20	0.0459	-0.5736	2.7533	-5.7668	1.294	11.1633
	30	0.0085	-0.1127	0.5881	-1.3992	-0.1950	7.5924
$\overline{u^2}$	5	-164.4077	657.5424	-909.1178	459.1237	-38.3987	11.2505
	10	-12.1741	57.5851	-89.7139	43.7588	-5.1223	20.4405
	15	-0.9391	6.7945	-16.1307	11.5517	-0.5859	10.8377
	20	-0.1019	0.9497	-2.72	1.5749	1.0260	6.4602
	30	0.0023	-0.0084	-0.0097	-0.1677	0.3021	3.2004
$\sqrt{\frac{\overline{u^2}}{\bar{u}^2}}$	5	139.3703	-341.2986	261.6864	-33.0136	13.5632	10.6128
	10	13.14	-40.0016	41.8063	-6.4274	11.9347	20.6575
	15	2.1464	-9.3531	12.445	3.4893	2.4062	21.7319
	20	0.8674	-4.8501	8.2393	-0.0668	3.1112	22.6348
	30	0.1292	-1.1715	3.5103	-2.4894	4.6474	23.3794

FIG. 4

Profiles	x/D	C_5	C_4	C_3	C_2	C_1	C_0
$\sqrt{\frac{\overline{u^2}}{\overline{u}^2}}$ (normalized)	10	1.314E6	-4E5	4.1806E4	-642.7418	119.3467	20.6575
	15	1.63E6	-4.735E5	4.2002E4	785.0979	36.093	21.7319
	20	2.7756E6	-7.7601E5	6.5914E4	-26.7026	62.2235	22.6348
	30	3.1407E6	-1.0379E6	1.173E5	-4.0403E3	174.65	22.4991
$\frac{\bar{u}}{U_C}$	10	-4.5466E3	1.2494E3	82.9961	-36.2184	-3.6439	0.9946
	15	-1.7303E3	-1.3448E3	886.6266	-140.4744	1.1857	0.9962
	20	1.3163E4	-8.2202E3	1.973E3	-206.6252	2.3181	1
	30	2.7306E4	-1.2796E4	2.3731E3	-203.8171	1.32	1
$\frac{\overline{u^2}}{\overline{u^2}_C}$	10	-5.8475E4	2.7659E4	-4.3092E3	210.1828	-2.4604	0.9818
	15	-6.5205E4	3.3625E4	-5.8456E3	345.7944	-4.6739	1.0084
	20	-5.0687E4	2.4884E4	-3.867E3	152.2504	1.9446	0.9910
	30	1.7747E4	-3.5952E3	108.8738	-47.2045	4.3604	0.9353

FIG. 12

Profiles	x/D	C_5	C_4	C_3	C_2	C_1	C_0
ε_{45}	20	N/A	N/A	N/A	-1.9464E5	4.6179E3	864.6429
	30	N/A	N/A	N/A	-1.9643E4	-577.8571	204.7857

FIG. 13

Profiles	*x/D*	C_5	C_4	C_3	C_2	C_1	C_0
ε_{45}	10	N/A	N/A	N/A	6.0714E5	-9.55E4	9.2643E3
	15	N/A	N/A	N/A	-6.3393E5	2.2982E4	2.5482E3
	20	N/A	N/A	N/A	-1.9464E5	4.6179E3	864.6429
	30	N/A	N/A	N/A	-1.9643E4	-577.8571	204.7857
ε_{axis}	10	N/A	N/A	N/A	5.2797E6	-4.9709E6	2.8588E5
	15	N/A	N/A	N/A	-7.8928E5	-3.3403E4	4.8936E3
	20	N/A	N/A	N/A	-2.8703E5	-7.2421E3	1.4316E3
	30	N/A	N/A	N/A	-2.1889E4	-3.4142E3	285.1434
ε_{Kol}	10	N/A	N/A	N/A	-2.82E8	1.6342E7	3.0801E5
	15	N/A	N/A	N/A	-2.1393E7	1.024E6	7.2855E4
	20	N/A	N/A	N/A	-1.165E7	3.5573E5	3.0383E4
	30	N/A	N/A	N/A	1.4792E6	-9.439E4	6.0981E3

FIG. 15

x/D	Profiles	C_5	C_4	C_3	C_2	C_1	C_0
20	$\tau_{Kol,45}$	N/A	N/A	-0.2202	0.0329	-6.495E-4	1.3274E-4
	$\eta_{Kol,45}$	N/A	N/A	-0.03552	0.005231	-1.0113E-4	4.4833E-5
	$\tau_{Kol,axis}$	N/A	N/A	2.0677	-0.1375	0.003461	9.3416E-5
	$\eta_{Kol,axis}$	N/A	N/A	0.1001	-0.0015	1.1587E-4	3.9277E-5
30	$\tau_{Kol,45}$	N/A	N/A	-0.5103	0.0696	-7.5205E-4	2.7469E-4
	$\eta_{Kol,45}$	N/A	N/A	-0.0564	0.007477	-7.2468E-5	6.4493E-5
	$\tau_{Kol,axis}$	N/A	N/A	2.236	-0.07126	0.002889	2.2652E-4
	$\eta_{Kol,axis}$	N/A	N/A	0.0584	0.005458	9.6858E-5	5.9252E-5

FIG. 16

Profiles	x/D	C_5	C_4	C_3	C_2	C_1	C_0
T_u	10	13.6903	-9.4634	1.8048	-0.1456	0.004974	1.3484E-4
	15	160.7938	-53.233	4.7839	-0.04375	-0.004535	4.6798E-4
	20	262.2984	-86.1051	8.8756	-0.3633	0.01041	6.1142E-4
	30	820.8543	-311.4520	40.8385	-2.2913	0.05511	0.001333
L_u	10	284.1285	-196.4038	37.4568	-3.0214	0.1032	0.002798
	15	2305.0438	-763.1165	68.5785	-0.6272	-0.065	0.006709
	20	2854.0885	-936.9162	96.5765	-3.9534	0.1132	0.006653
	30	5905.4256	-2240.6618	293.8023	-16.4842	0.3965	0.009592

Appendix II

Spatial third order structure function plots at *x/D*=15

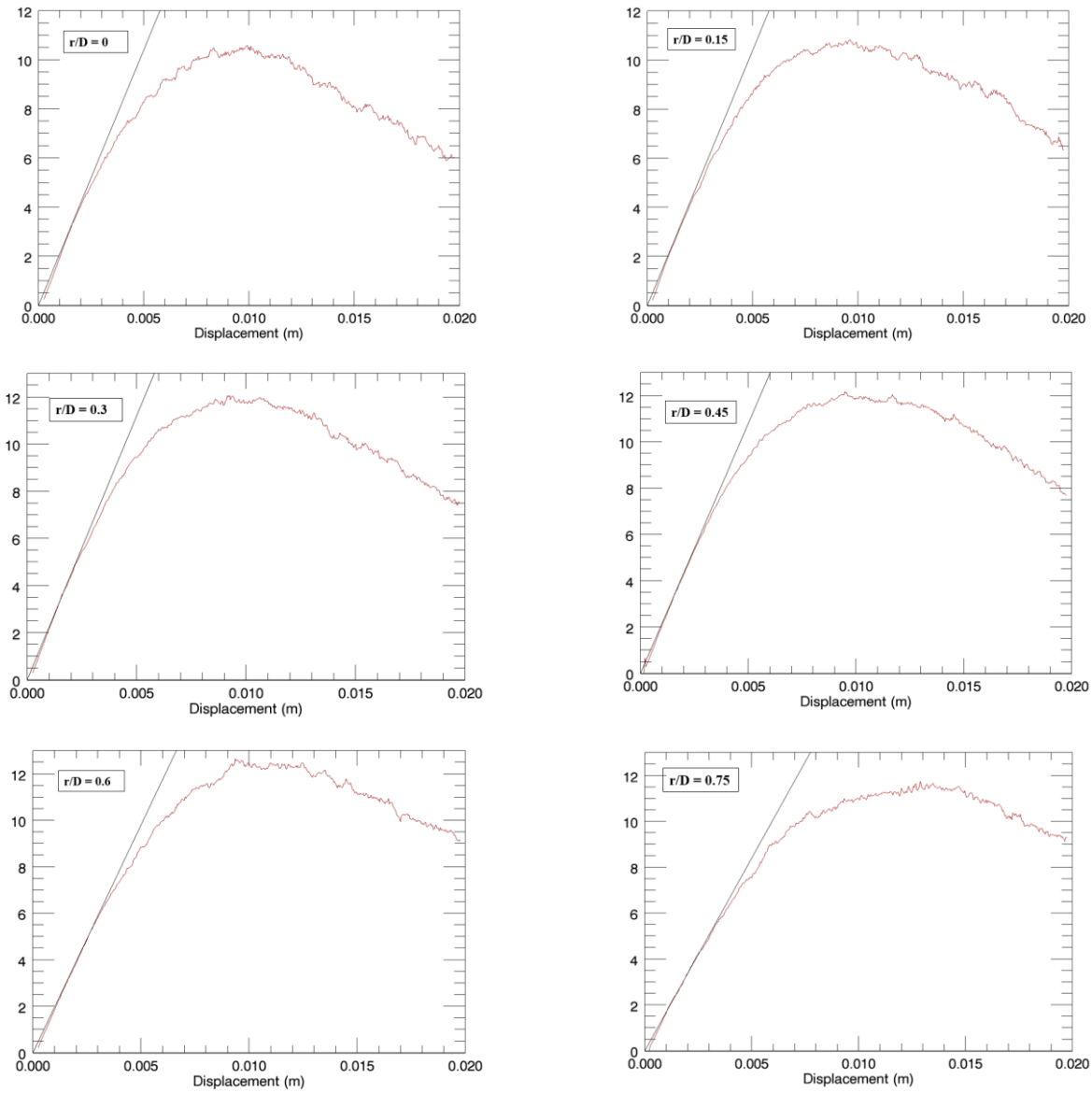

Appendix III

Spatial third order structure function plots at *x/D*=10

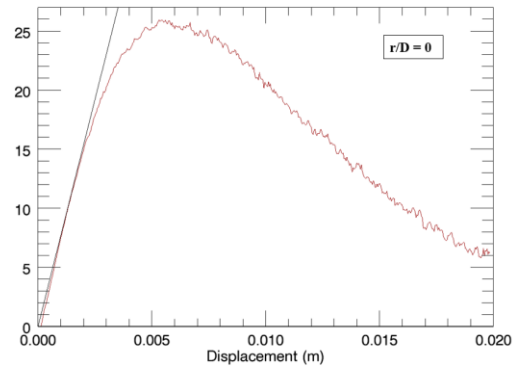

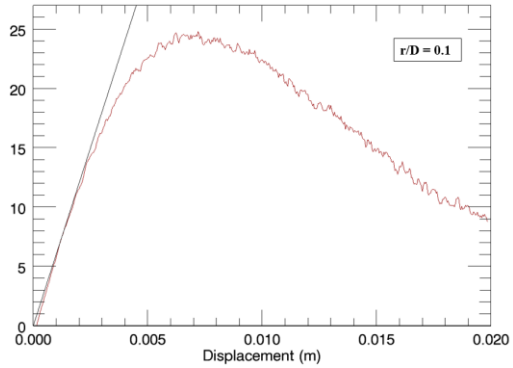

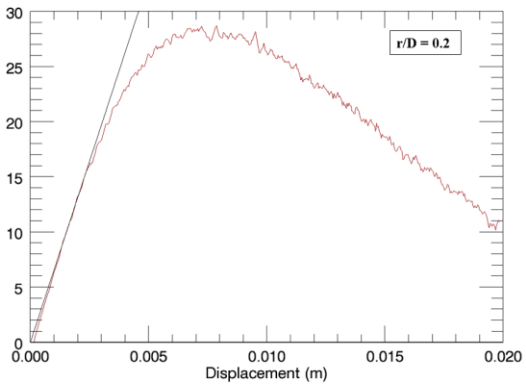

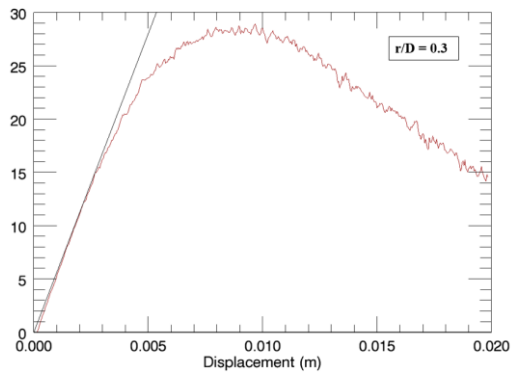

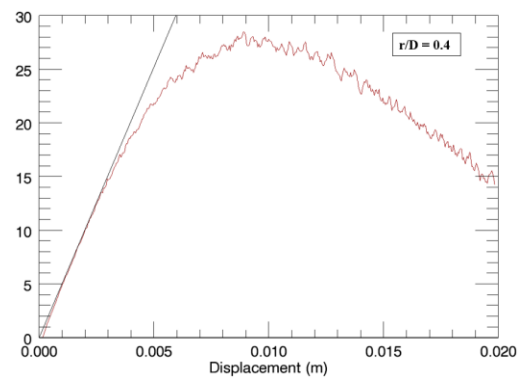

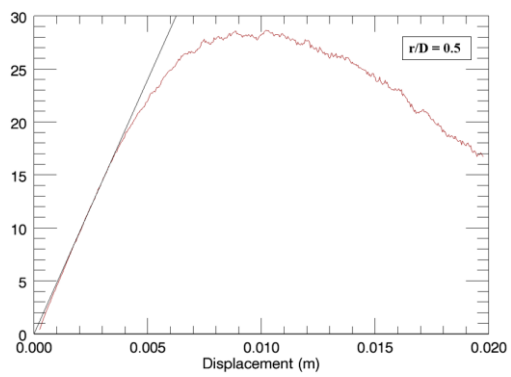

Appendix I

excel

532nm compact laser

- CW 532nm laser
- Highly efficient
- Power 1W - 2W

TECHNICAL DATA SHEET

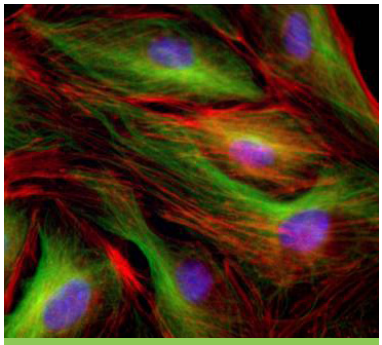

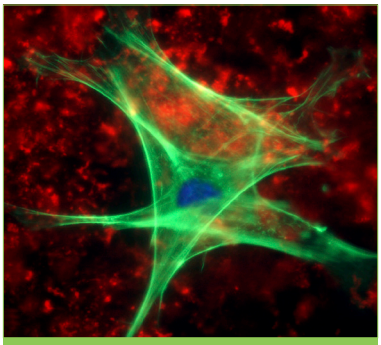

Laser Quantum

INNOVATIVE RELIABLE INTELLIGENT

excel

532nm compact laser

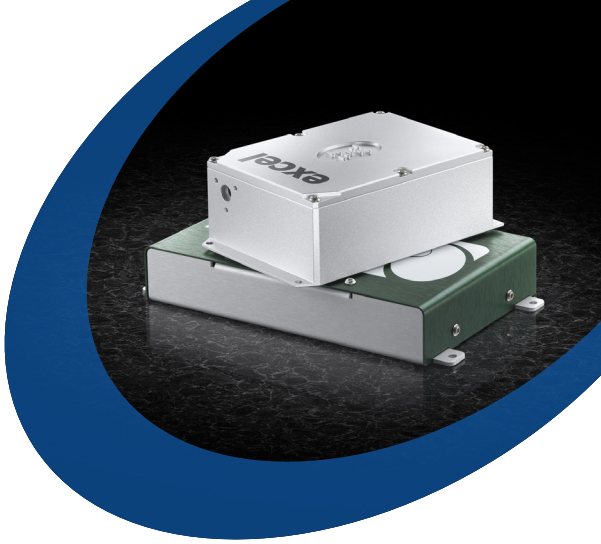

The high specification 532nm laser

Overview

The excel from Laser Quantum is a versatile laser. It has a unique stress-free cavity architecture, is small and robust in design and is capable of providing a high-power 532nm beam up to 2W. The excel can be used for numerous applications including PIV and biomedical research and was the first system to undergo ruggedisation for extreme vibration and temperature for military applications at Laser Quantum, making the excel a unique laser in its class.

Low Noise

Low noise results from the cavity architecture which restricts the number of oscillation modes and maintains tight control of the component temperature. What little heat is generated within the head is removed by conduction, therefore no water cooling is required. Only high quality optical components are used, resulting in a noise specification of <0.5% RMS (up to 6MHz) over a wide operating temperature range.

Stability

The smd12 power supply is a highly intelligent and functional control unit. It allows the laser to be operated in power or current mode using the RS232 control; in power mode the output power is stabilised to better than <0.4% using optical feedback to the laser head.

The temperature of all critical components is regulated by PID temperature controllers, solidly maintaining all temperature-sensitive parameters within the cavity at their optimum values. The stability is maintained over a wide operating temperature.

Construction

Laser Quantum builds all lasers to a high standard, and the excel is no exception.

To minimise the effect of shock impacts zero-stress mounts are used throughout the cavity. The laser's feet are engineered to deform under high stress, eliminating mechanical strain within the head.

The excel is capable of withstanding extreme vibrational shocks without diminishing its performance. Before shipment each excel is subjected to rigorous quality assurance, in line with our strict ISO9001 procedures. Every unit is nitrogen purged and hermetically sealed. This is followed by a rigorous burn-in procedure under user-realistic conditions.

Beam Quality

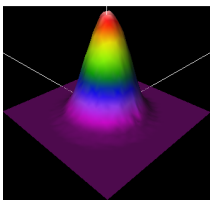

The excel has a pure spectral and spacial quality, consequently the typical M-squared value of the excel beam is <1.1 resulting in a near perfect and near diffraction-limited beam.

Features

Features include: diffraction limited beam, permanently aligned cavity, low noise, stable output, compact design, low M-squared, zero-stress cavity, hermetically sealed, single phase mains driven, diode >40,000 hrs MTTF and full RS232 control.

smd12 power supply

The smd12 is an integral part of the excel laser system and has become much more than a power supply. It is able to flip between power mode and user mode via the RS232 interface and also monitors component temperatures in the laser head, automatically maintains laser output power and provides diagnostic analysis.

Supply voltage: 100, 120, 240 AC, frequency: 47 - 63 Hz

Technical Specifications*

	EXCEL
Power	1W, 1.5W & 2W
Wavelength	532nm
Beam diameter[1]	1.5mm ± 0.1mm
Spatial Mode	TEM_{00}
Ellipticity	< 1:1.15
Bandwidth	30 - 40GHz
Divergence	≤ 0.5 mrad
M-squared	< 1.1
Power stability[2]	< 0.4% RMS
Beam pointing stability	< 2 µrad/°C
RMS noise[3]	< 0.5%
Polarisation ratio	> 100:1
Polarisation direction	horizontal
Coherence length	1cm
Beam angle[4]	1 mrad
Operating temperature	10 - 40°C
Head weight	0.9kg
Umbilical length	1.5m
Warm-up time	10 minutes

* Subject to change without notice.
[1] Beam diameter defined as the average of major and minor $1/e^2$ beam size measured at 25cm from exit port, at specified power.
[2] Test duration >100 hrs at constant temerature.
[3] Measured up to 6MHz.
[4] Tolerance relative to head orientation.

excel

532nm compact laser

Dimensions

Front view

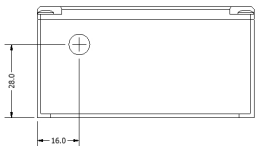

Back view

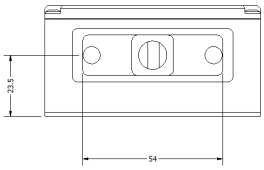

Side view

Top view

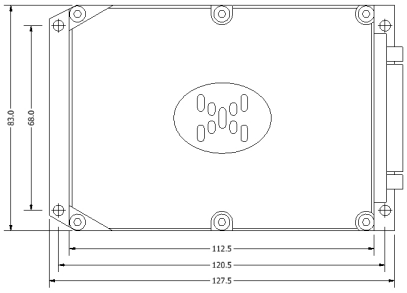

Bottom view

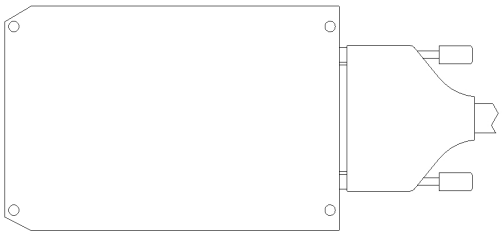

smd 12 - front view

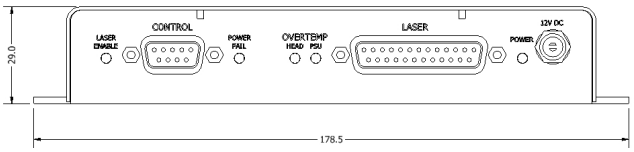

smd 12 - back view

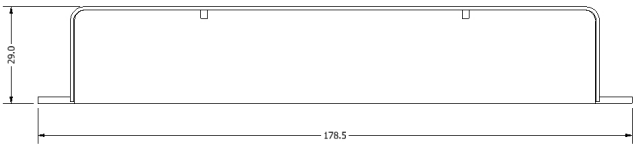

smd 12 - top view

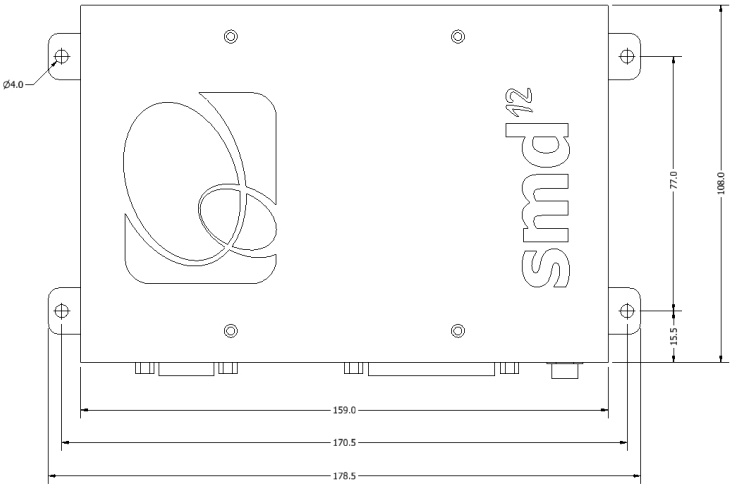

Typical Applications

PIV

Opthalmology

PSU options

smd 12

mpc 6000

Drawings are for illustrative purposes only, please contact Laser Quantum for complete engineer's drawings, including mpc 6000.

• INNOVATIVE • RELIABLE • INTELLIGENT

LASER QUANTUM LTD
tel: +44 (0) 161 975 5300
fax: +44 (0) 161 975 5309
email: info@laserquantum.com
web: www.laserquantum.com

LASER QUANTUM INC
tel: +1 408-467-3885
fax: +1 408-467-3886
email: info@laserquantum.com
web: www.laserquantum.com

LASER QUANTUM GmbH
tel: +49 7531 368371
fax: +49 7531 368372
email: info@laserquantum.com
web: www.laserquantum.com

Laser Quantum
INNOVATIVE RELIABLE INTELLIGENT

Appendix II

HAMAMATSU

PHOTOSENSOR MODULES
H10425/H10426

OVER VIEW

The H10425 is a photosensor module that integrates a 25-mm (1") diameter head-on photomultiplier tube with a high-voltage power supply circuit. The H10425 has a large effective photocathode area of 22 mm diameter and features fast time response.
The H10426 is a photosensor module that integrates a 28-mm (1-1/8") diameter head-on photomultiplier tube with a high-voltage power supply circuit. The H10426 has a large effective photocathode area of 25 mm diameter.

Left: H10425 Right: H10426

SPECIFICATIONS

Parameter			H10425	H10426	Unit
Spectral Response			300 to 650		nm
Input Voltage			+11.5 to +15.5		V
Max. Input Voltage			+18		V
Max. Input Current *1			3.0		mA
Max. Output Signal Current			100		µA
Max. Control Voltage *2			+1.2 (Input impedance 1 MΩ)	+1.5 (Input impedance 1 MΩ)	V
Recommended Control Voltage Adjustment Range			0.5 to 1.1	0.5 to 1.4	V
Effective Photocathode Area			ϕ22	ϕ25	mm
Sensitivity Adjustment Range			1: 1000		—
Peak Sensitivity Wavelength			420		nm
Cathode	Luminous Sensitivity	Min.	60	60	µA/lm
		Typ.	90	95	
	Blue Sensitivity Index (CS 5-58)	Typ.	10.5	11	—
	Radiant Sensitivity *3	Typ.	85	88	mA/W
Anode	Luminous Sensitivity *4	Min.	40	50	A/lm
		Typ.	180	200	
	Radiant Sensitivity *3 *4	Typ.	1.7×10^5	1.8×10^5	A/W
	Dark Current *1 *5	Typ.	3	2	nA
		Max.	20	10	
Rise Time *4		Typ.	1.5	4	ns
Ripple Noise *4 *6 (peak to peak)		Max.	0.5		mV
Settling Time *7		Max.	10		s
Operating Ambient Temperature *8			+5 to +50		°C
Storage Temperature *8			-20 to +50		°C
Weight			170	270	g

NOTE: *1: Input Voltage=+15.0 V, Control Voltage=+1.0 V, Output Current=Dark Current
*2: Availabel I^2C interface instead of the low voltage input cable. Please consult with our sales office before ordering.
*3: Measured at the peak sensitivity wavelength
*4: Control voltage=+1.0 V
*5: After 30 minutes storage in darkness
*6: Cable RG-174/U, Cable length 450 mm, Load resistance= 1 MΩ, Load capacitance=22 pF
*7: The time required for the output to reach a stable level following a change in the control voltage from +1.0 V to +0.5 V.
*8: No condensation

Figure 1: Sensitivity Adjustment Method

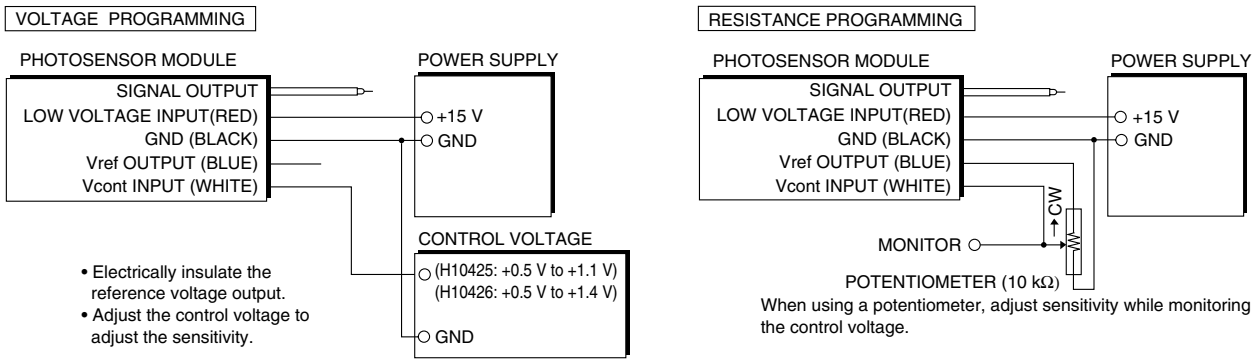

TPMOC0206EA

Figure 2: Dimensional Outlines (Unit: mm)

H10425

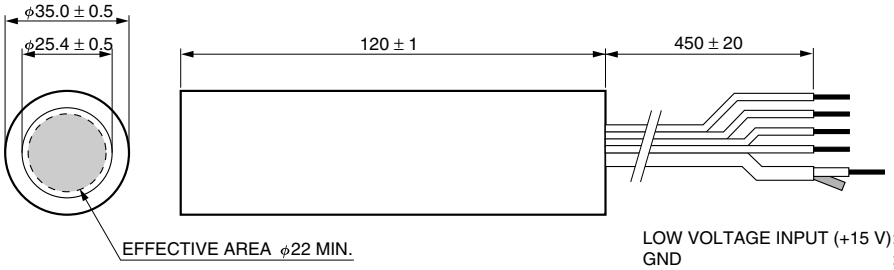

LOW VOLTAGE INPUT (+15 V): AWG26 (RED)
GND : AWG26 (BLACK)
Vref OUTPUT (+1.2 V) : AWG26 (BLUE)
Vcont INPUT (+0.5 V to +1.1 V) : AWG26 (WHITE)
SIGNAL OUTPUT : RG-174/U

TPMOA0046EA

H10426

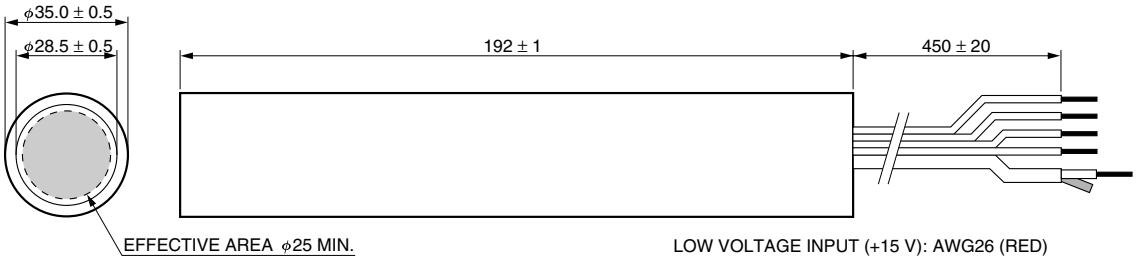

LOW VOLTAGE INPUT (+15 V): AWG26 (RED)
GND : AWG26 (BLACK)
Vref OUTPUT (+2.5 V) : AWG26 (BLUE)
Vcont INPUT (+0.5 V to +1.4 V) : AWG26 (WHITE)
SIGNAL OUTPUT : RG-174/U

TPMOA0047EA

HAMAMATSU WEB SITE www.hamamatsu.com
HAMAMATSU PHOTONICS K.K., Electron Tube Division
314-5, Shimokanzo, Iwata City, Shizuoka Pref., 438-0193, Japan, Telephone: (81)539/62-5248, Fax: (81)539/62-2205
U.S.A.: Hamamatsu Corporation: 360 Foothill Road, P. O. Box 6910, Bridgewater. N.J. 08807-0910, U.S.A., Telephone: (1)908-231-0960, Fax: (1)908-231-1218 E-mail: usa@hamamatsu.com
Germany: Hamamatsu Photonics Deutschland GmbH: Arzbergerstr. 10, D-82211 Herrsching am Ammersee, Germany, Telephone: (49)8152-375-0, Fax: (49)8152-2658 E-mail: info@hamamatsu.de
France: Hamamatsu Photonics France S.A.R.L.: 19, Rue du Saule Trapu, Parc du Moulin de Massy, 91882 Massy Cedex, France, Telephone: (33)1 69 53 71 00, Fax: (33)1 69 53 71 10 E-mail: infos@hamamatsu.fr
United Kingdom: Hamamatsu Photonics UK Limited: 2 Howard Court, 10 Tewin Road Welwyn Garden City Hertfordshire AL7 1BW, United Kingdom, Telephone: 44-(0)1707-294888, Fax: 44(0)1707-325777 E-mail: info@hamamatsu.co.uk
North Europe: Hamamatsu Photonics Norden AB: Smidesvägen 12, SE-171-41 SOLNA, Sweden, Telephone: (46)8-509-031-00, Fax: (46)8-509-031-01 E-mail: info@hamamatsu.se
Italy: Hamamatsu Photonics Italia: S.R.L.: Strada della Moia, 1/E, 20020 Arese, (Milano), Italy, Telephone: (39)02-935 81 733, Fax: (39)02-935 81 741 E-mail: info@hamamatsu.it

TPMO1038E01
FEB. 2008 IP

Appendix III

Appendix III - Cookbook in attending the LDA setup

This cookbook section is intended to provide a step-by-step procedure with few important tips and cautions in attending the LDA setup for a typical turbulence measurement.

1. Turn on the laser and BC module.

   Caution: At this stage, laser intensity should be set to a minimum level, just enough for us to see the beam spots.

2. Adjust the screw on each reflecting mirror (see Figure 2-6) until the beam is going through the optical head at the center of the entrance hole.

   Tips: Hold an optical or a white paper at the hole to better visualize the beam spot.

3. Dismount the focusing lens from the optical head and check whether the beams are passing through the center of the prisms as in Figure 1.

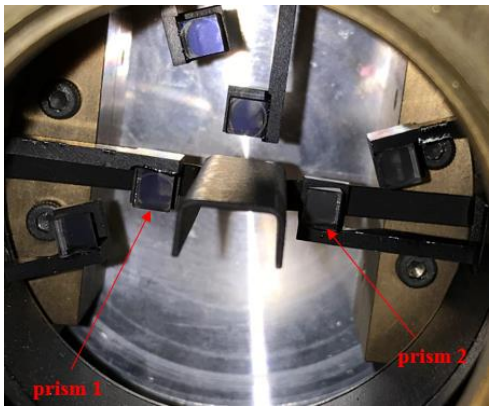

Figure 1 The outer prisms of the optical heads

4. Connect the BC panels (on the optical head) to the *Analog Input* on Channel 1 and 2 of the BC module (Figure 2) with a BNC cable. Set the frequency on Channel 2 according to your desired frequency shift. For example, setting it to 37 MHz will result in a resulting 3 MHz differential shift.

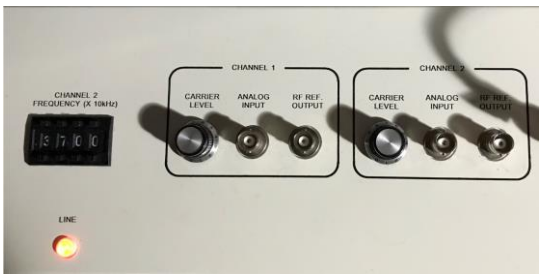

Figure 2 Front panel of the BC module

5. Take off the black plate of the BC panels (Figure 2-7) and adjust any of the screws as well as the *Carrier Level* on Channel 1 and 2 simultaneously until the frequency-shifted beam spots seen on the wall becomes stronger than the unshifted ones Figure 2-8(b).

   Tips: Turning down the *Carrier Level* on both channels to zero should project only the unshifted (original) beams on the wall. This help to differentiate between the frequency-shifted beams and original ones.
6. Mount back the focusing lens to the optical head and put back the black plate to cover the BC panels. Never touch or change the BC settings anymore from this stage ahead.
7. Mount the microscope objective (housed on a 3-axis mini traverse as in Figure 3) at a distance around 200 mm from the focusing lens. Traverse the scope thoroughly in all directions until frequency-shifted beams are passing through it and beam spots are seen on the wall.

   Caution: Make sure to look at the right (frequency-shifted) beam spots, instead of the original ones.

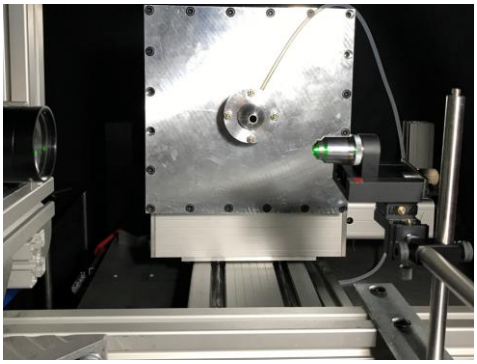

Figure 3 Microscope objective housed on a three-axis mini traverse

8. Adjust the screws next to the optical head to align the beams until the two beam spots collapse on top of each other (Figure 4). If the beam spots are found unequally strong, adjust the *Carrier Level* on the BC module until both spots look equally strong. Remove out the microscope objective from the setup.

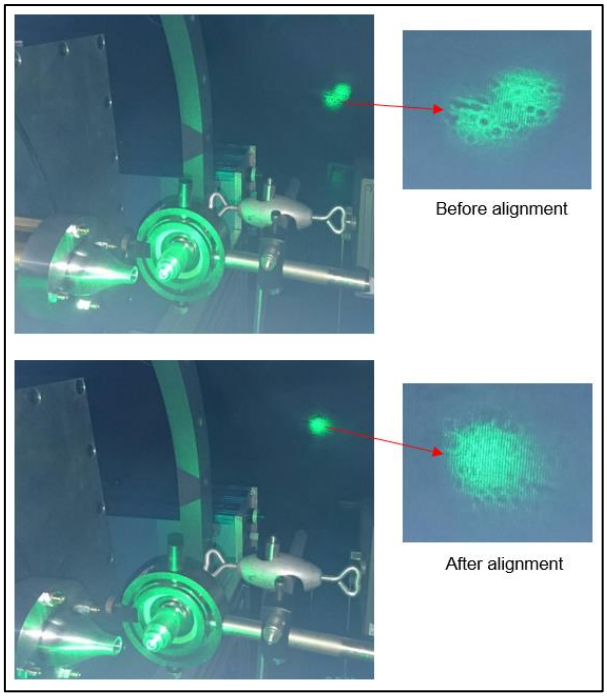

Figure 4 Beams overlapping alignment

9. Turn on the preamplifier and PMT power supply. Set the latter to a suitable level, e.g., around 70 µA and turn up the laser intensity to its maximum.

   Caution: The current setting on the preamplifier should not cut the burst off too much while working on *Step 13* later.

10. Activate the jet. Regulate the opening valve while using a pressure meter to measure the pressure difference that corresponds to the desired jet exit velocity given by Equation (2.11) (see Figure 2-30).

11. Activate seeding generator at a suitable pressure level, e.g., around 1.2 bar, to begin with. Traverse the jet box approximately to the center of the MV (Refer Appendix VIII for the operating manual of the traversing system).

12. Turn on the analog oscilloscope and channel it temporarily to the output of the preamplifier with a BNC cable.

13. Adjust the detector head position according to your desired scattering (angle) configuration, e.g., at 45° (see Figure 2-21).

    Caution: Regardless of any position chosen, the distance, L_2 between the receiving lens and the MV should be kept at around 200 mm (see Figure 2-12).

14. Align the detector until the pinhole is positioned on top of the center of the MV, as in Figure 5. Further guidance in adjusting the detector head is listed below:

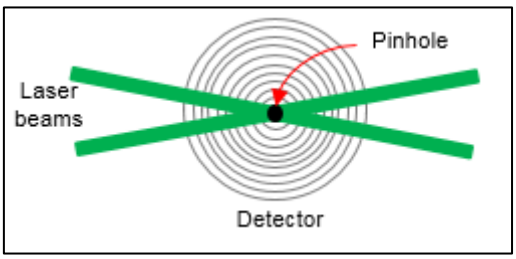

Figure 5 Pinhole alignment of the detector

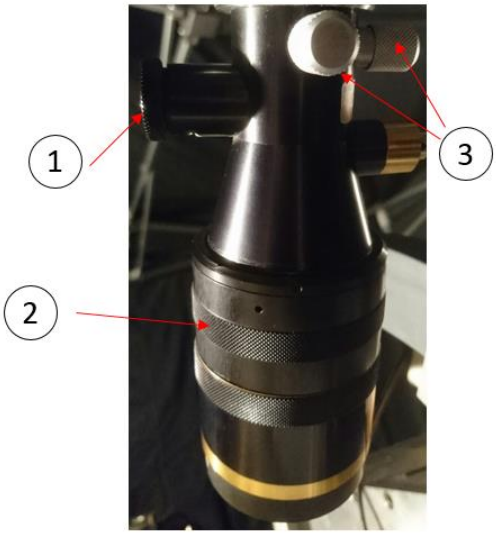

Figure 6 Adjustable knobs on the detector head

From Figure 6:

Knob 1 - To adjust the sharpness of the image seen by different eyes.

Knob 2 - To adjust the intersection so that the beams are intersecting at the narrowest region as depicted in Figure 7. This adjustment is crucial when detector head is mounted at certain angle from the MV.

Tips: At this stage, the position of pinhole may not be necessary at the center of the MV.

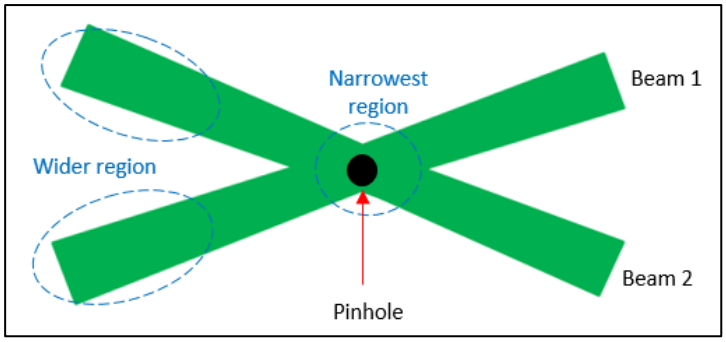

Figure 7 The necking seen through the detector if it is mounted at a certain to the MV

Knob 3 – To align the pinhole position to be at the center of the MV. While adjusting this knob, the analog oscilloscope can be observed. The pinhole position at which the highest burst S/N ratio is observed should be chosen for the measurement (see Figure 8).

Tips: It is highly recommended to check the pinhole position from time to time, especially during a big measurement.

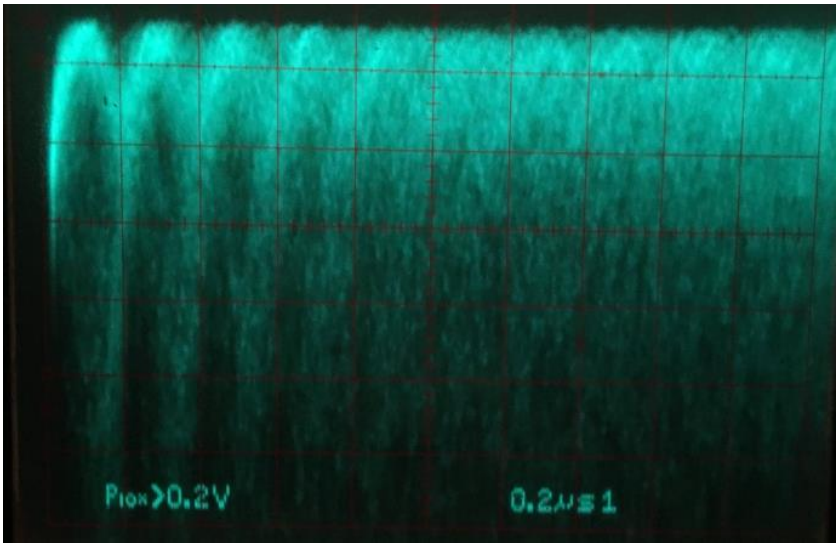

Figure 8 Example of good Doppler burst from the analog oscilloscope

15. Make double check for the BC setting. If the frequency is increased, for example, to 37.1 MHz and so on, the frequency observed on the scope should also become larger.
16. Disconnect the BNC cable from the analog oscilloscope and connect it to the digital oscilloscope for data visualization and recording. A sample of good Doppler burst is also shown in Figure 2-25.

17. Traverse the jet to a desired measurement point, fully close the inner curtain and the tent, and leave the setup for a while for the seeding particles to distribute uniformly throughout the ambient air.
18. Use the *Spectrum Analyzer* feature on the oscilloscope to estimate the Doppler frequency of the burst (see Figure 2-26), from which the sampling frequency should be determined and set on the oscilloscope, along with the desired record length.
19. Adjust the gain (in *mV*/*div*) on the oscilloscope such that you see most of the bursts in their full size.

    Tips: You may allow some of the largest burst to be clipped in order to get the most bursts digitized with the full resolution. It has been tested that a certain degree of clipping does not significantly influence the results.
20. Plug in an external drive and record the data in the binary format to suit with the compatibility of the processing software, i.e., *ldapro_17_02_19_sdtw*

Appendix IV

200 MHz High Input Impedance Voltage Amplifier

Features	• **Switchable Gain 20/40 dB (x10 / x100)** • **Bandwidth DC ... 200 MHz** • **High Input Impedance 1 MΩ** • **Switchable AC/DC Coupling**
Applications	• **Oscilloscope and Transient Recorder Preamplifier** • **Photomultiplier and Microchannel Plate Amplifier** • **Signal Booster for Optical Receivers and Current Amplifiers** • **Time-Resolved Pulse and Transient Measurements**

Specifications	Test Conditions	Vs = ± 15 V, Ta = 25°C
Gain	Gain	20/40 dB switchable
	Gain Accuracy	± 0.2 dB
Frequency Response	Lower Cut-Off Frequency (-3 dB)	DC/1 Hz switchable
	Upper Cut-Off Frequency (-3 dB)	200 MHz
	Rise/Fall Time (10% - 90%)	1.8 ns
Input	Input Impedance	1 MΩ II 15 pF
	Input Voltage Noise	4.5 nV/√Hz (@ 50 MHz, 40 dB gain) 5.5 nV/√Hz (@ 50 MHz, 20 dB gain)
	Intregrated Input Noise	450 µV peak-peak (@ 40 dB gain) 600 µV peak-peak (@ 20 dB gain)
	Input Bias Current	10 pA
	Input Offset Voltage	500 µV typ.
	Input Voltage Drift	5 µV/°C
Output	Output Impedance	50 Ω (terminate with 50 Ω load for best performance)
	Output Voltage	± 1 V (@ 50 Ω load, for linear amplification)
	Max. Output Current	60 mA
	Output Offset Trimmer Range	± 100 mV
	Slew Rate	600 V/µs (@ 20 dB, 50 Ω load) 1,100 V/µs (@ 40 dB, 50 Ω load)
Power Supply	Supply Voltage	± 15 V
	Supply Current	± 70 mA typ. (depends on operating conditions, recommended power supply capability min. ± 150 mA)
Case	Weight	200 g (0.5 lbs)
	Material	AlMg4.5Mn, nickel-plated

200 MHz High Input Impedance Voltage Amplifier

Specifications (continued)		
Temperature Range	Storage Temperature	- 40 ... + 100 °C
	Operating Temperature	0 ... + 60 °C
Absolute Maximum Ratings	Power Supply Voltage	± 20 V
	Input Voltage	± 5 V
	Transient Input Voltage	200 V (out of a 200 pF source)
Connectors	Input	BNC
	Output	BNC
	Power Supply	LEMO series 1S, 3-pin fixed socket Pin 1: + 15V Pin 2: - 15V Pin 3: GND

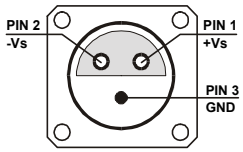

Dimensions

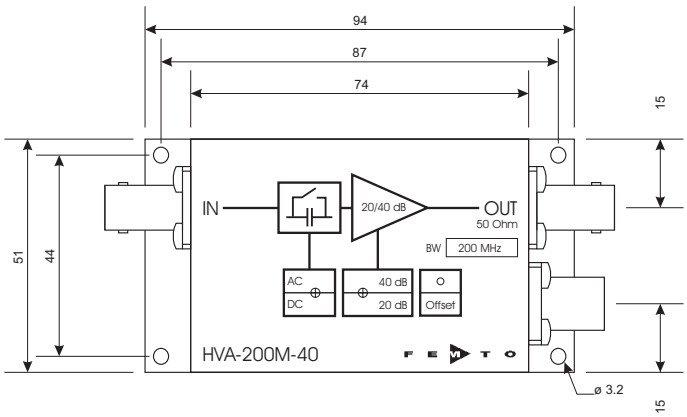

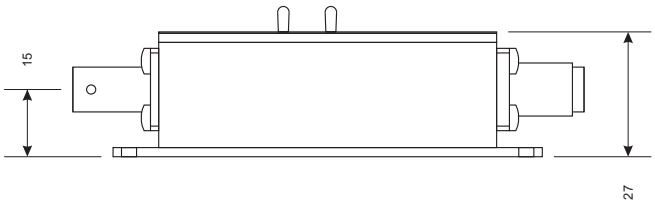

all measures in mm unless otherwise noted

DZ_HVA-200M-40_R2

FEMTO Messtechnik GmbH
Klosterstr. 64
10179 Berlin · Germany
Phone: +49 30 280 4711-0
Fax: +49 30 280 4711-11
Email: info@femto.de
www.femto.de

Appendix V

Appendix V

2D-drawing of the outer nozzle with dimensions

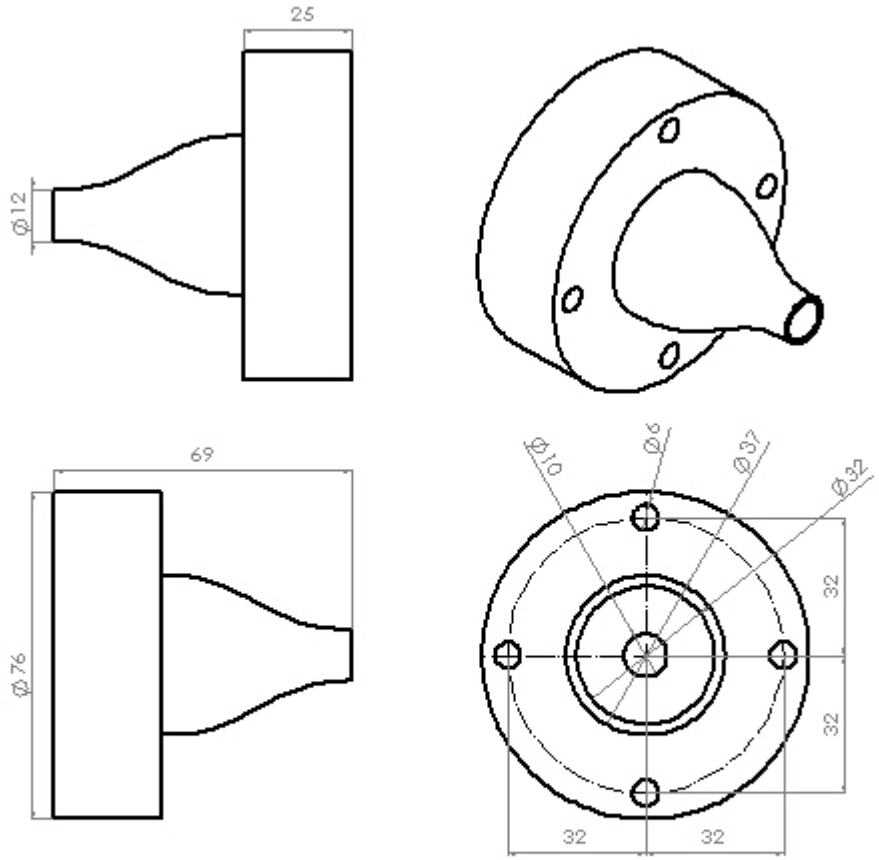

Title: Nozzle (all dimensions are in milimeters)
Tolerance: DIN ISO 2768-1
Quantity: 2
Material: Aluminum (or Brass)
Contact: Clara Velte, 3140 7620 (cell),cmve@dtu.dk (email)

2D-drawing of the trumpet nozzle with dimensions

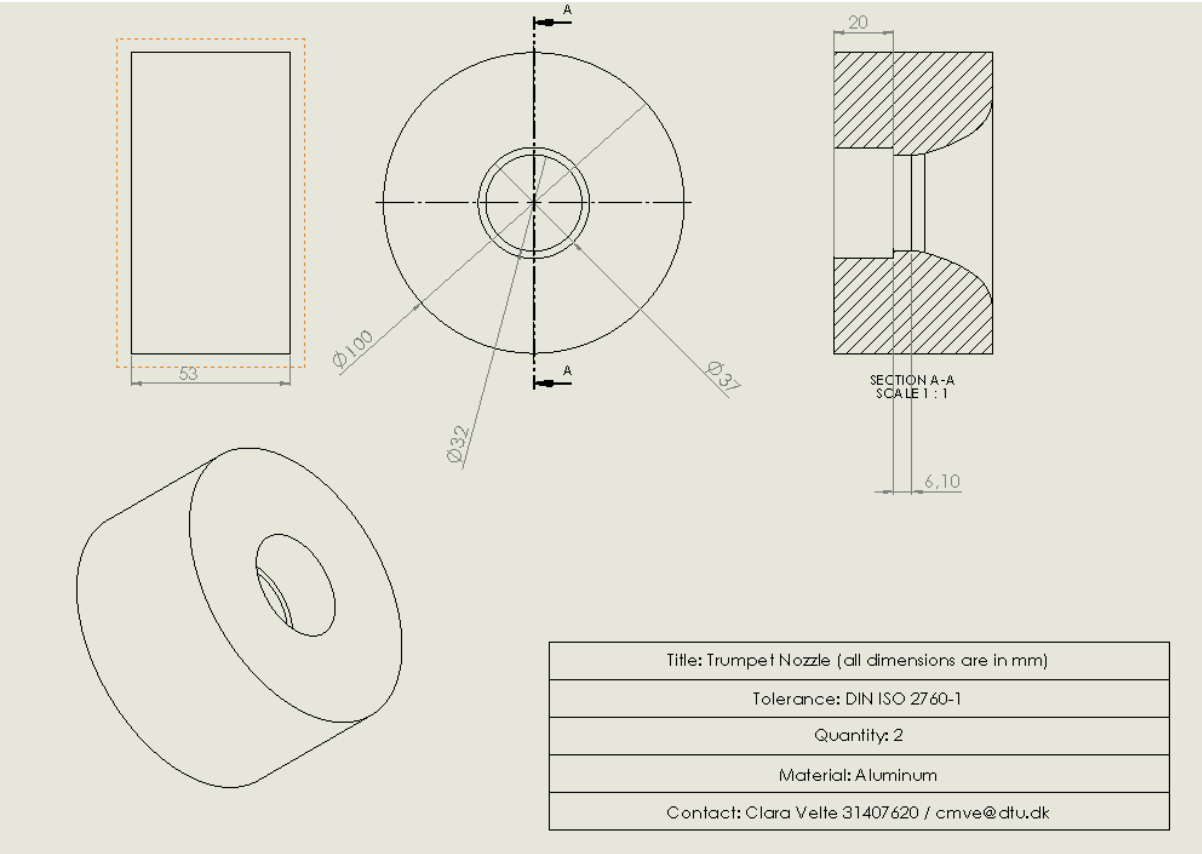

Appendix VI

isel® Hybrid Two-Phase Stepper Motor MS 110 Item-No. 473030
isel® Hybrid Two-Phase Stepper Motor MS 160 Item-No. 473041
isel® Hybrid Two-Phase Stepper Motor MS 160 W Item-No. 473043

English

Characteristics

- Hybrid stepper motors with energy density in various power classes
- Unipolar and bipolar modes thanks to 8-wire connection
- Speed control via step sequence frequency in the open control loop
- small step angle error, non cumulative
- Angle of rotation of the motor shaft is directly proportional to the number of input pulses
- Second shaft end for optional attachment of brake and encoder (Typ HEDS 55..., Fab.: HP)

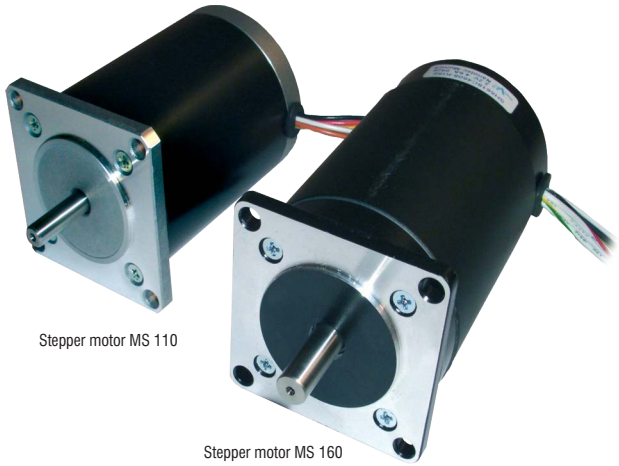

Stepper motor MS 110

Stepper motor MS 160

Technical Data

Description		MS 110	MS 160	MS 160W
Holding torque bipolar	**Nm**	1,1	1,84	1,84
Winding current per phase serial / parallel	**A**	2,0 / 4,0	2,0 / 4,0	3,25 / 6,5
Coil voltage per phase serial / parallel	**V**	5,6 / 2,8	4,82 / 2,41	3,12 / 1,56
Winding resistance per phase at 25°C serial / parallel	Ω	2,0 / 0,5 ± 15%	2,4 / 0,6 ± 15%	0,96 / 0,24 ± 15%
Winding inductivity per phase at 1 kHZ serial / parallel	**mH**	7,6 / 1,9 ± 20%	8,4 / 2,5 ± 20%	4,0 / 2,0 ± 20%
Rotor inertia	**kg-m²**	$3,5 \times 10^{-5}$	$3,5 \times 10^{-5}$	$3,5 \times 10^{-5}$
Step angle / angle error	**° / %**	1,8° / ±5%	1,8° / ±5%	1,8° / ±5%
Connection cables		8	8	8
Weight	**kg**	1,0	1,4	1,4
Item-No.		**473030**	**473041**	**473043**

Maximum permissible radial load: 90 N (at 10mm)
ISO-cass: B (130°)
Protection class: IP40
Ambient temperature: -10°C ... +50°C
Insulation resistance: 100 MΩ

www.isel.com

isel®

Technical specification subject to change !.

isel Germany AG ■ Buergermeister-Ebert-Str. 40 ■ D-36124 Eichenzell
Tel.: +49 (6659) 981-0 ▪ Fax: +49 (6659) 981-776 ▪ E-Mail: automation@isel.com ▪ www.iselautomation.de

isel® Hybrid Two-Phase Stepper Motor MS 110 Item-No. 473030
isel® Hybrid Two-Phase Stepper Motor MS 160 Item-No. 473041
isel® Hybrid Two-Phase Stepper Motor MS 160 W Item-No. 473043

English

Torque characteristics

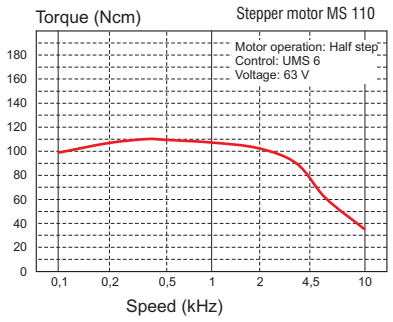

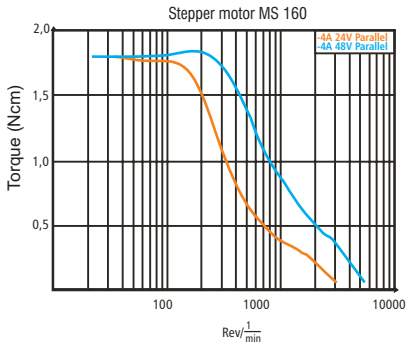

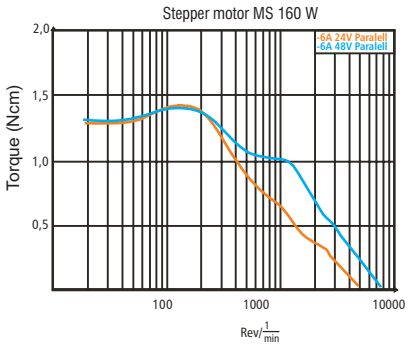

Scale drawings

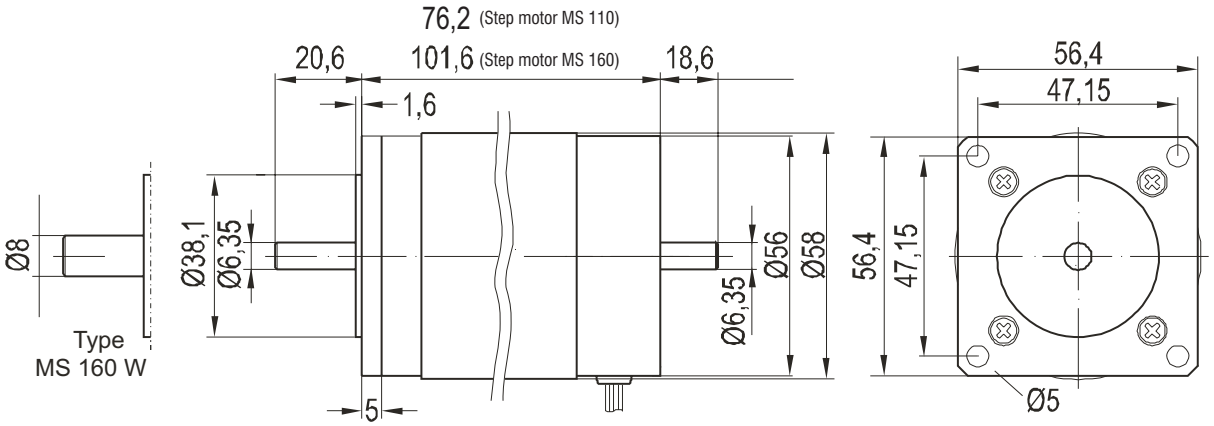

Type MS 160 W:strengthened shaft end at the output side,Ø 8 mm

Connection consignment

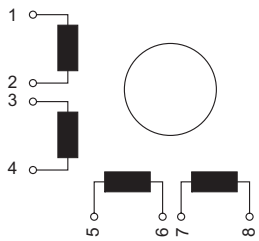

Type of connection (extern)				motor			
unipolar	bipolar				Leads MS110	Leads MS160	Winding
	1 Winding	serial	parallel				
A	A	A	A	1	black	red	A
COM				2	black / white	red / white	
A\		A\	A\	3	orange / white	black / white	A\
B	B	B	B	4	orange	black	B
COM				5	red	green	
B\		B\	B\	6	red / white	green / white	B\
				7	yellow / white	yellow / white	
				8	yellow	yellow	

STEP	A	B	A\	B\	CW	CCW
1	+	+	-	-		
2	-	+	+	-		
3	-	-	+	+		
4	+	-	-	+		

Technical specification subject to change !.

www.isel.com

isel Germany AG ■ Buergermeister-Ebert-Str. 40 ■ D-36124 Eichenzell
Tel.: +49 (6659) 981-0 ▪ Fax: +49 (6659) 981-776 ▪ E-Mail: automation@isel.com ▪ www.iselautomation.de

Appendix VII

Manual for Traversing System

I. Make sure the two stepper motors on each traversing axis are connected to the orange cables according to the right labels (*X* and *Y*).

II. Turn ON the stepper motor (***isel*** iMC-S8) controller by:
   i. Switching ON the button at the back
   ii. Switching ON the button on the front panel (just below Emergency Stop)
   iii. Press the green **POWER** button and wait until the red **FAULT** button is automatically off

III. Log on to the computer and launch ***Remote*** software from the Desktop.

IV. The message below will automatically pop up. Click **Yes** to allow reference run and the jet should be automatically traversed to its home position.

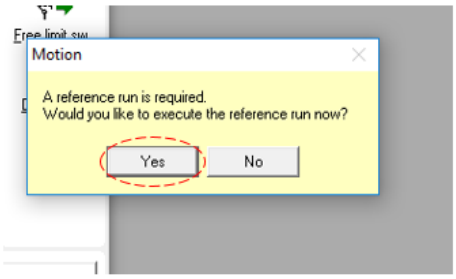

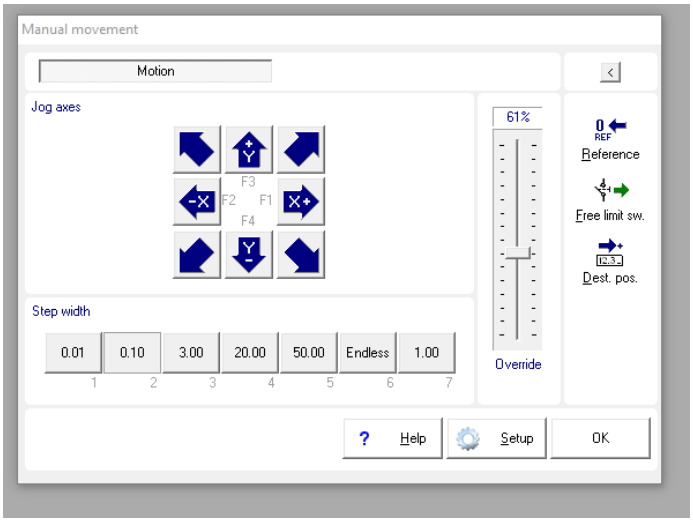

Manual movement window

V. If the manual movement window does not appear upon launching the software, click at the "*palm*" icon on the shortcut panel as below.

VI. Now the jet is ready to be maneuvered along *X*- and *Y*-direction by clicking the arrow **X+, X-, Y+** and **Y-** with your desired **step width**. Refer the attachment (pasted on the board) to distinguish between positive and negative directions of each axis.

Appendix VIII

Appendix VIII(a) –Measurement points (MP) and processing parameters for **Paper I**

x/D=10

MP, *r* (mm)	Vertical division LeCroy (mV/div)	fctr (MHz)	fmin (MHz)	fmax (MHz)	fwin (MHz)	Sampling rate (MHz)	Record length (s)	Gain	Percent validation (%)	Total data rate (Hz)	Average data rate (Hz)	Mean velocity (m/s)	RMS (m/s)
0	50	8.5	4.5	12	7	25	1	1d4	95.3	15460828	38652	30.523399	6.2622825
4.3		7.7	4	12	7.2	25	1	1d4	98.1	13420383	33551	26.725837	6.5363309
8.7		6	3.2	10.5	7	25	1	1d4	98.9	9961749	24904	17.885255	6.1216762
13		5.2	2	8.5	6	25	1	1d4	96.9	5402169	13505	10.290568	4.9969195

x/D=15

MP, *r* (mm)	Vertical division LeCroy (mV/div)	fctr (MHz)	fmin (MHz)	fmax (MHz)	fwin (MHz)	Sampling rate (MHz)	Record length (s)	Gain	Percent validation (%)	Total data rate (Hz)	Average data rate (Hz)	Mean velocity (m/s)	RMS (m/s)
0	50	7	4	10	5.3	25	1	2d4	97.7	10904152	27260	21.2348	4.7019234
6.5		6.5	3.5	10	6.2	25	1	2d4	97.7	11726814	29317	18.554484	5.1204037
13		5.5	2.5	8.5	5.5	25	1	2d4	96.1	5706816	14267	11.716972	4.4979611
19.5		4.3	2.3	6.5	4	25	1	2d4	95.9	1792192	4480	6.2283511	3.3972126

x/D=30

MP, *r* (mm)	Vertical division LeCroy (mV/div)	fctr (MHz)	fmin (MHz)	fmax (MHz)	fwin (MHz)	Sampling rate (MHz)	Record length (s)	Gain	Percent validation (%)	Total data rate (Hz)	Average data rate (Hz)	Mean velocity (m/s)	RMS (m/s)
0	20	5.1	3.5	6.5	3	25	1	2d4	98.3	4840477	12101	10.787637	2.5525803
13		4.8	3	6.5	3.2	25	1	2d4	97.8	4987392	12468	9.2492484	2.6951843
26		4	2.5	6	3	12.5	2	2d4	97.4	4798693	11997	6.076199	2.3894708
39		3.7	2.5	5	2	12.5	2	4d4	84.2	1571672	3929	3.3421673	1.8167427

Appendix VIII(b) – Measurement points (MP) and mini CTA data for **Paper II**

x/D=10		x/D=15		x/D=20		x/D=30	
MP, r (mm)	mean velocity (m/s)	MP, r (mm)	mean velocity (m/s)	MP, r (mm)	mean velocity (m/s)	MP, r (mm)	mean velocity (m/s)
0	15.794	0	11.2263	0	8.551	0	5.8172
0.5	15.4246	1.5	11.011	1.5	8.3923	1.5	5.8209
1.5	14.9253	3.5	10.3299	3.5	8.0788	3.5	5.7704
2.5	13.9023	5.5	9.3089	5.5	7.554	5.5	5.6134
3.5	13.1845	7.5	8.3919	7.5	7.0312	7.5	5.4023
4.5	11.9664	9.5	6.8575	9.5	6.311	9.5	5.26
5.5	10.7103	11.5	5.757	11.5	5.7352	11.5	5.1208
6.5	9.707	13.5	5.2921	13.5	4.9739	13.5	4.8086
7.5	8.9789	15.5	4.3161	15.5	4.4255	15.5	4.5953
8.5	7.1089	17.5	3.8217	17.5	3.9602	17.5	4.3089
9.5	6.8413	19.5	3.311	19.5	3.4454	19.5	4.1883
10.5	5.6973	21.5	2.7446	21.5	2.8111	21.5	3.9894
11.5	5.2977	23.5	2.3469	22.5	2.6125	22.5	3.8788
12.5	4.6248	25.5	1.9106	23.5	2.4827	23.5	3.7829
13.5	3.9728	27.5	1.6876	24.5	2.135	24.5	3.6057
14.5	3.6589	29.5	1.3988	25.5	2.1322	25.5	3.5294
15.5	3.1497	31.5	1.1999	26.5	1.8417	26.5	3.4605
16.5	2.5443	33.5	1.0943	27.5	1.7955	27.5	3.3085
17.5	2.2471	35.5	0.962	28.5	1.4952	28.5	3.2506
18.5	2.0227	37.5	0.8973	29.5	1.5274	29.5	3.2213
19.5	1.8304	38.5	0.8954	30.5	1.2553	30.5	3.1182
20.5	1.6163			31.5	1.2228	31.5	3.0184
21.5	1.5088			32.5	1.0686	32.5	2.9506
22.5	1.3913			33.5	1.0489	33.5	2.8547
23.5	1.2969			34.5	0.8877	34.5	2.8839
24.5	1.1646			35.5	0.8832	35.5	2.5122
25.5	1.0641			36.5	0.7678	36.5	2.6038
26.5	1.1071			37.5	0.6979	37.5	2.4667
27.5	1.0327			38.5	0.6674	38.5	2.4312
28.5	0.9751			39.5	0.6395	39.5	2.267
				40.5	0.6134	40.5	2.2971
				41.5	0.5643	41.5	2.1742
				42.5	0.5283	42.5	2.1487

		43.5	0.5169	43.5	1.9775
		44.5	0.4659	44.5	1.9275
		x/D=20		x/D=30	
		MP, r (mm)	mean velocity (m/s)	MP, r (mm)	mean velocity (m/s)
		45.5	0.4641	45.5	1.8954
		46.5	0.4356	47.5	1.5895
		47.5	0.4208	49.5	1.404
		48.5	0.4154	51.5	1.3464
		49.5	0.4035	53.5	1.081
		50.5	0.3892	55.5	1.0571
		51.5	0.3672	57.5	0.9102
		52.5	0.3695	59.5	0.8204
		53.5	0.3361	61.5	0.7707
		54.5	0.341	63.5	0.7148
		55.5	0.3406	65.5	0.6821
		56.5	0.3387	67.5	0.6615
		57.5	0.3099	69.5	0.62
		58.5	0.3273	71.5	0.627
		59.5	0.3046	73.5	0.5609
		60.5	0.3054	75.5	0.5124
		61.5	0.3173		
		62.5	0.2907		
		63.5	0.3018		
		64.5	0.2934		
		65.5	0.2883		
		66.5	0.2897		
		67.5	0.2963		
		68.5	0.2601		
		69.5	0.2779		
		70.5	0.2646		
		71.5	0.2645		
		72.5	0.2674		
		73.5	0.2918		
		74.5	0.2488		
		75.5	0.2431		

Appendix VIII(c) – Measurement points (MP) and processing parameters for **Paper III, IV** and **VI**

x/D=5

MP, *r* (mm)	Vertical division LeCroy (mV/div)	fctr (MHz)	fmin (MHz)	fmax (MHz)	fwin (MHz)	Sampling rate (MHz)	Record length (s)	Seeding pressure (bar)	Gain	Total data rate (Hz)	Average data rate (Hz)	Percent validation (%)	Mean velocity (m/s)	RMS (m/s)
0		9	5.5	10.5	5	25	1			15858547	39646	98	30.406463	3.3847665
1		9	5	11	6	25	1			14606017	36515	98	30.090263	3.3021649
2		9	5	10.5	5.5	25	1			16145240	40363	98	29.659999	3.9079855
3		8.3	4	10.5	6.5	25	1			14592558	36481	99	27.70994	4.6643743
4		8	3.5	10.5	7	25	1			11108973	27772	98.6	24.478518	5.1001989
5		7	3.5	10	6.5	25	1			12212285	30531	98.7	21.60784	5.5439506
6		6	3.5	9.5	6	25	1			8284583	20711	99	18.084322	5.4004964
7		5	2.5	9	6.5	25	1			7226602	18067	98.1	15.134531	5.1296538
8		5	2.5	8.5	6	25	1			8683292	21708	98.4	12.533872	4.9540584
9		4	2	8	6	25	1			6526185	16315	97.4	10.004549	4.4842486
10		4	2	7	5	25	1			4246131	10615	97.9	7.7656133	4.047225
11		3.5	2	7	5	25	1			3669594	9174	94.3	6.0976928	3.6681142
12		3	2	6	4	12.5	2	1.4		2831273	7078	93.1	4.3112048	3.0199466
13		3	2	5.5	3.5	12.5	2			2558352	6396	82	2.9670375	2.6263327
14	100	3	2	5	3	12.5	2	1.5	0.1d4	1452522	3631	71.7	1.8124402	2.2144345

x/D=10

MP, *r* (mm)	Vertical division LeCroy (mV/div)	fctr (MHz)	fmin (MHz)	fmax (MHz)	fwin (MHz)	Sampling rate (MHz)	Record length (s)	Seeding pressure (bar)	Gain	Percent validation (%)	Total data rate (Hz)	Average data rate (Hz)	Mean velocity (m/s)	RMS (m/s)
0		6	4	9.7	5.7	25	1			98	12941316	32353	21.126093	4.2851948
0		7	4	9.5	5.5	25	1			98	16862792	42157	21.806259	4.5628256
1		6.5	4	9.5	5.5	25	1			97.8	14143483	35359	20.439553	4.3796227
2		6.5	3.8	9	5.2	25	1			98.2	15833203	39583	20.166548	4.642599
3		6	3.5	9	5.5	25	1			95.7	12943850	32360	18.52955	4.508776
4		6	3	9	6	25	1			98.8	13043481	32609	17.545485	4.6381315
5		5.5	3.5	9	5.5	25	1			97.2	12097264	30243	16.13086	4.5598904
6		5.5	3	8.5	5.5	25	1			98.6	9779080	24448	14.47856	4.4255361
7		5	3	8.5	5.5	25	1			97.6	10839257	27098	13.486883	4.4655708
8		5	3	8	5	25	1			98.3	8671098	21678	11.971399	4.2388481
9		4.5	2.5	7.5	5	25	1			97.4	7502233	18756	10.697243	4.0336326
10		4	3	7.3	4.3	25	1			97.7	6523266	16308	9.4782773	3.8510671
11		4	3	7	4	25	1			97.3	4627030	11568	8.1380143	3.5847218
12		4	2	6.5	4.5	25	1			97.8	3554846	8887	7.05002	3.3688404
13		3.5	2.5	6.5	4	25	1			97.9	2992256	7481	6.0717439	3.1765604
14		3.5	2	6	4	12.5	2			94.6	5024475	12561	5.1633501	2.9401885
15		3.2	2.2	6	3.8	12.5	2			94.7	4705456	11764	4.4353213	2.7732998
16		3.2	2	5	3	12.5	2			90.5	3985370	9963	3.6903142	2.567668
17		3.2	2	5	3	12.5	2			86.6	1967641	4919	2.808255	2.2447468
18	100	3.2	2	5	3	12.5	2	1.4	0.1d4	79.6	1330462	3326	2.2600678	2.1203691

x/D=15

MP, *r* (mm)	Vertical division LeCroy (mV/div)	fctr (MHz)	fmin (MHz)	fmax (MHz)	fwin (MHz)	Sampling rate (MHz)	Record length (s)	Seeding pressure (bar)	Gain	Percent validation (%)	Total data rate (Hz)	Average data rate (Hz)	Mean velocity (m/s)	RMS (m/s)
0		6	3.5	8	4.5	25	1			99.2	8174135	20435	15.117962	3.3070433
1.5		5.7	3.5	8	4.5	25	1			98.6	7732178	19330	14.926897	3.278978
3		5.7	3.5	8	4.5	25	1			98.9	8722536	21806	14.702567	3.3722859
4.5		5.5	3.5	8	4.5	25	1			98.5	8954658	22387	14.021536	3.4248013
6		5.2	3.2	7.5	4.3	25	1			98.8	8305160	20763	13.207675	3.4674247
7.5		5	3	7.5	4.5	25	1			98.9	7910306	19776	12.188542	3.4615505
9		5	3	7.2	4.2	25	1			98.8	7892498	19731	11.178754	3.4603343
10.5		4.5	3	7	4	25	1			99	6876441	17191	10.001972	3.3544346
12		4.3	2.9	6.7	3.8	25	1			98.9	5658623	14147	8.7883664	3.2519745
13.5		4	2.5	6.5	4	25	1			98.4	4634675	11587	7.7008962	3.1186115
15		4	2.5	6.4	3.9	25	1			98.1	3574559	8936	6.6207898	2.9597331
16.5		3.6	2.5	6.3	3.8	25	1			97.8	3305369	8263	5.8184199	2.7873896
18		3.3	2.3	6	3.7	12.5	2			97.6	4767709	11919	4.9861453	2.5936518
19.5		3.3	2.3	5.5	3.2	12.5	2			94.4	3534785	8837	4.217077	2.4092137
21		3.2	2.5	5.5	3	12.5	2			93.2	2607457	6519	3.5538391	2.2418401
22.5		3	2.2	5	2.8	12.5	2			87.3	1709064	4273	2.8580036	2.03595
24		3	2.2	4.8	2.6	12.5	2			87.5	1506093	3765	2.4144148	1.9409653
25.5		3	2.2	4.8	2.6	12.5	2			75.6	824608	2062	1.8239893	1.681052
27	50	3	2.2	4.8	2.6	12.5	2	1.4	0.1d4	71.8	466965	1167	1.4076028	1.5460798

x/D=20

MP, *r* (mm)	Vertical division LeCroy (mV/div)	fctr (MHz)	fmin (MHz)	fmax (MHz)	fwin (MHz)	Sampling rate (MHz)	Record length (s)	Seeding pressure (bar)	Gain	Percent validation (%)	Total data rate (Hz)	Average data rate (Hz)	Mean velocity (m/s)	RMS (m/s)
0		5.1	3.5	7	3.7	25	1			99.2	4099073	10248	11.163838	2.536531
2		5.1	3	7	3.5	25	1			99.3	5722952	14307	11.181498	2.591739
4		4.9	3.5	6.5	3.5	25	1			99.3	7009934	17525	11.057757	2.6739547
6		4.9	3.2	6.5	3.6	25	1			99.2	4580355	11451	10.162453	2.6251294
8		4.8	3	6.5	3.6	25	1			99.1	5984313	14961	9.8854836	2.730433
10		4.7	3	6.4	3.6	25	1			99.2	3777893	9445	8.7574604	2.6285364
12		4.6	3.2	6.3	3.6	25	1			98.9	4858352	12146	8.2246779	2.6792722
14		4.4	3	6.2	3.6	25	1			99.1	3395114	8488	7.2604822	2.5871212
16		4.3	3	6	3.5	12.5	2			98.5	5451371	13628	6.4527613	2.4718716
18		4.2	2.6	6	3.6	12.5	2			98	4649559	11624	5.6946035	2.362706
20		3.9	2.8	5.3	2.6	12.5	2			97.6	4088325	10221	5.0341165	2.22518
22		3.8	2.6	5.2	2.6	12.5	2			96.5	2755259	6888	4.2416372	2.0611271
24		3.8	2.6	5.2	2.6	12.5	2			94.4	2766719	6917	3.8392822	1.9968507
26		3.6	2.5	5	2	12.5	2			91.5	1576498	3941	3.1323933	1.7624694
28		3.6	2.5	4.6	2	12.5	2			86.3	1468712	3672	2.7656015	1.7113004
30		3.4	2.5	4.5	1.8	12.5	2			76	701593	1754	2.0706	1.5357596
32		3.4	3.5	4.5	1.5	12.5	2			73.2	754259	1886	1.8003792	1.4702199
34		3.3	3.5	4.5	1.5	12.5	2			57.6	360151	900	1.303215	1.3516426
36	50	3	3.5	4.5	1	12.5	2	1.4	0.1d4	45.3	248015	620	0.98247948	1.2470158

x/D=30

MP, *r* (mm)	Vertical division LeCroy (mV/div)	fctr (MHz)	fmin (MHz)	fmax (MHz)	Sampling rate (MHz)	Record length (s)	Seeding pressure (bar)	Gain	Percent validation (%)	Total data rate (Hz)	Average data rate (Hz)	Mean velocity (m/s)	RMS (m/s)
0		4.4	3	5.5	12.5	2			99.7	10131004	25328	7.5908512	1.7933666
3		4.4	3	5.3	12.5	2			99.7	9796388	24491	7.3963878	1.7937238
6		4.3	3.2	5.2	12.5	2			99.5	9960895	24902	7.151487	1.8357148
9		4.3	3	5.2	12.5	2			99.7	5942753	14857	6.628351	1.8285186
12		4	2.9	5.2	12.5	2			99.6	4930472	12326	6.1487452	1.8179885
15		4	3.1	5.2	12.5	2			99.6	3479521	8699	5.5643846	1.7789599
18		3.8	2.7	5.2	12.5	2			99.5	2677572	6694	5.0568853	1.7392173
21		3.5	2.8	5	12.5	2			99.3	3137079	7843	4.7251761	1.7323382
24		3.5	2.8	5	12.5	2			98.6	3748594	9371	4.2439749	1.7008819
27		3.5	2.6	4.8	12.5	2			97.9	1840727	4602	3.5516413	1.5303556
30		3.5	2.7	4.7	12.5	2			95.9	1947395	4868	3.2550514	1.4961509
33		3.2	2.7	4.7	12.5	2			93.3	1324776	3312	2.8071842	1.3786204
36		3.2	2.6	4.5	12.5	2			91	921060	2303	2.4190331	1.3103643
39		3.1	2.6	4.3	12.5	2			79.6	759508	1899	2.0875799	1.2127097
42		3.1	2.6	4	12.5	2			78.1	551307	1378	1.770869	1.0909638
45	20	3	2.7	4	12.5	2	1.5	0.1d4	72.5	312497	781	1.4989769	1.0875588

Appendix VIII(d) – Measurement points and processing parameters for **Paper V**

MP, x/D	Sampling rate (MHz)	Record length (s)	Vertical division LeCroy (mV/div)	fctr (MHz)	fwin (MHz)	Gain	Percent validation (%)	Total data rate (Hz)	Average data rate (Hz)	Mean velocity (m/s)	RMS (m/s)
10	25	1		8.2	6.5	0.4d4	98.93	9685322	24213	28.253428	5.8020722
11	25	1		8	6.5	0.4d4	99.17	8576229	21441	26.221322	5.4918416
12	25	1		7.5	6.5	0.4d4	99.36	5665465	14164	23.96661	5.1691007
13	25	1		7.3	6.2	0.4d4	99.09	6311024	15778	22.504187	4.9182579
14	25	1		7.1	6.2	0.4d4	98.81	5788252	14471	21.115859	4.6882314
15	25	1		6.8	6	0.4d4	98.16	5114119	12785	19.745829	4.4680656
16	25	1		6.6	5	0.4d4	99.02	5079755	12699	18.651218	4.1153304
17	25	1		6.4	5	0.4d4	99.26	4568354	11421	17.591997	3.9430273
18	25	1		6.2	5	0.4d4	98.98	4172366	10431	16.589536	3.789757
19	25	1		6	5	0.4d4	98.79	3789890	9475	15.69414	3.6248462
20	25	1		5.8	4.8	0.4d4	99.05	3830969	9577	14.898243	3.4288525
21	25	1		5.7	4.8	0.4d4	98.96	3258188	8145	14.096785	3.2792716
22	25	1		5.6	4.6	0.4d4	98.67	2899939	7250	13.488336	3.1313351
23	25	1		5.4	4.6	0.4d4	98.64	2830740	7077	12.845714	3.0100776
24	25	1		5.4	4.6	0.4d4	98.81	2813849	7035	12.340762	2.8840509
25	25	1		5.1	4.2	0.4d4	98.77	2406678	6017	11.686517	2.7355544
26	25	1		5.1	4.2	0.4d4	98.87	2243167	5608	11.177339	2.6170239
27	25	1		5	4	0.4d4	98.83	2094105	5235	10.756829	2.531878
28	12.5	2		4.9	2.65	0.4d4	99.68	3688379	9221	10.279567	2.4091282
29	12.5	2		4.8	2.65	0.4d4	99.76	3469635	8674	9.9050562	2.3326325
30	12.5	2		4.8	2.6	0.4d4	99.7	3202574	8006	9.5336491	2.2447074
31	12.5	2		4.7	2.6	0.4d4	99.77	2953598	7384	9.1768806	2.1699324
32	12.5	2		4.7	2.6	0.4d4	99.89	3004668	7512	8.9113592	2.1135664
33	12.5	2		4.6	2.6	0.4d4	99.67	3228501	8071	8.6678234	2.0583933
34	12.5	2		4.5	2.1	0.4d4	99.86	3447507	8619	8.4277139	1.9891699
35	12.5	2		4.4	1.9	0.4d4	99.77	2732813	6832	8.0122657	1.8676885
36	12.5	2		4.4	2.6	0.4d4	99.67	3187954	7970	7.9430107	1.920068
37	12.5	2	50	4.4	2	0.4d4	99.83	2505392	6263	7.6002319	1.8056199

DTU Mechanical Engineering
Section of Fluid Mechanics, Coastal and Maritime Engineering
Technical University of Denmark

Nils Koppels Allé, Bld. 403
DK-2800 Kgs. Lyngby
Denmark

Tlf.: +45 4525 1360
Fax: +45 4525 1961

www.mek.dtu.dk

June 2019

ISBN: 978-87-7475-563-0

DCAMM
Danish Center for Applied Mathematics and Mechanics

Nils Koppels Allé, Bld. 404
DK-2800 Kgs. Lyngby
Denmark
Phone (+45) 4525 4250
Fax (+45) 4525 1961

www.dcamm.dk

DCAMM Special Report No. S262

ISSN: 0903-1685